

Improving Synchrotron Methods for Advanced Characterisation of Heterogeneous Catalysts

Eleanor Kathleen Dann

Department of Chemistry
University College London

Thesis submitted for the degree of Doctor of Philosophy
2019

Declaration

I, Eleanor Kathleen Dann, confirm that the work presented in this thesis is my own. Where information has been derived from other sources, I confirm that this has been indicated in the thesis.

.....

Abstract

Heterogeneous catalyst materials, in particular supported metal nanoparticles, are hugely important in industrial processes such as emissions control technology. In order to design new catalyst materials with improved catalytic performance, the catalytic properties and mechanistic pathways must be well understood. The work presented in this thesis makes advances to *operando* spectroscopy methods for the characterisation of industrial heterogeneous catalyst materials operating in realistic reaction conditions. A multi-technique approach, employing XAFS and DRIFTS simultaneously, has been used to probe the electronic and structural properties of metal nanoparticles as well as the molecular vibrations of reactants and intermediates at the catalyst surface.

In this work, the preparation of supported metal nanoparticle catalysts have been investigated using time-resolved XAFS and DRIFTS spectroscopy approach. Structure-activity relationships of the supported Pd nanoparticle catalysts have been identified during their operation for an important reaction used in diesel after-treatment technology; the selective catalytic oxidation of NH_3 . The selectivity of the reaction towards the different reaction products (N_2 , N_2O and NO), within the relevant temperature window for industrial application, has been linked to the different structural phases of Pd, including a previously unidentified PdN_x species.

The major challenges for *operando* measurements, concerning improved time resolution and spatial resolution, have been addressed with the development of a new reactor for combined XAFS and DRIFTS of a catalyst bed operating in plug-flow reaction conditions. The advantage of this reactor design for *operando* characterisation has been demonstrated in the investigation of a supported Pd nanoparticle catalyst ($\text{Pd}/\gamma\text{-Al}_2\text{O}_3$) during oscillating CO oxidation. This reactor improves on previous designs by allowing spectroscopic measurements to be performed with spatial resolution along the axial length of a catalyst bed. In this way, there is scope for elucidating the structure-function relationships of many other heterogeneous catalysts.

Impact Statement

This work has made advances to the characterisation of heterogeneous catalysts for understanding the structure and function of industrial catalyst materials. By working closely with the Johnson Matthey Clean Air division, characterisation methods have been developed to aid the research of optimised catalytic materials for abatement of harmful gases in emissions control technology.

A combination of spectroscopy techniques, employing synchrotron x-ray radiation and lab-based IR radiation, have been performed to study the formation and operation of industrial catalyst materials. In particular, a new and improved reactor has been designed for spatially resolved, *operando* x-ray absorption fine structure spectroscopy (XAFS) and diffuse reflectance infrared Fourier transformed spectroscopy (DRIFTS). These techniques can be performed simultaneously to study a catalyst contained in plug-flow configuration during a range of different reaction conditions. By combining the two spectroscopic techniques, and correlating with end-pipe activity data from mass spectrometry, confident characterisation of the catalyst structure and functionality is achieved.

The time-resolved XAFS/DRIFTS spectroscopy approach has been used to investigate the formation of supported metal nanoparticle catalysts from conventional industrial methods. The disadvantage of using certain metal salts for achieving high metal dispersion of the resulting catalyst is attributed to the decomposition mechanism of the molecular precursor which can promote or delay the formation of metal oxide nanoparticles. There is scope for this time-resolved, multi-technique approach to investigate the preparation of a number of other industrial metal nanoparticle catalysts.

The selective catalytic oxidation of NH_3 (NH_3 -SCO) over a Pd catalyst is an important reaction in diesel exhaust technology. NH_3 -derived chemicals - used in excess for the reduction of harmful NO_x from diesel exhaust - must also be removed to avoid NH_3 emissions. The combined, time-resolved XAFS/DRIFTS spectroscopy approach has been used to elucidate the relationship between Pd nanoparticle structure, surface speciation and product selectivity during NH_3 -SCO, finding that high selectivity is due to a previously unidentified PdN_x phase. This has great significance in the future design of Pd catalysts for improved selectivity in the abatement of NH_3 and NO_x gases.

The improved time resolution and spatial resolution of the combined XAFS/DRIFTS method has allowed for the investigation of supported Pd nanoparticle catalysts during oscillating CO oxidation. CO oxidation is an extensively studied reaction, however, the explanation for oscillating reaction kinetics under certain reaction conditions has remained a topic of discussion. By investigating the extent of Pd oxidation and CO

coverage at the nanoparticle surface at multiple positions of a catalyst bed, the oscillating behaviour is found to depend on the position within the reactor.

The advanced characterisation methodology developed and demonstrated in this work presents opportunity to investigate not only the catalytic reactions in this study, but a number of other heterogeneous catalytic reactions that play a significant role in industrial processes for now and in the future. By understanding the chemical and physical properties of the catalyst during the most active and selective phase, new catalysts can be designed with desirable properties for improved catalytic performance.

Acknowledgements

I would like to thank my supervisor Dr Peter Wells for giving me the opportunity to embark on this project. Peter has been a great mentor throughout my doctorate study, he has provided guidance and given me freedom to explore my own research interests. I am grateful for the close knit research team that Peter has brought together over the past few years, and it has been a pleasure to work amongst a group of supportive peers.

I would like to thank Professor Alexandre Goguet for his continued support and ambitious research plans. He has been committed to the success of this research, providing thought-provoking questions and answers. I owe a large thank you to Dr Emma Gibson who has educated me in performing successful *in situ* beam time experiments. Professor Christopher Hardacre is acknowledged for helping me get this research project off the ground and giving me the initial inspiration for the work. Professor Richard Catlow is acknowledged for his support throughout the entire duration of the project and for acting as my official supervisor at UCL.

Johnson Matthey have played a significant role in this research project, providing the incentive, the funding, the resources and much of the expertise. I feel privileged to have worked closely with Johnson Matthey throughout my PhD, giving me the opportunity to develop professional skills both in the lab and in presenting in regular progress meetings. I must thank Agnes Raj for training me in catalyst preparation and testing, Tugce Eralp Erden for general support in material characterisation, and particular thanks to Paul Collier who has facilitated the ongoing collaboration between academia and industry.

The research in this thesis would be insignificant without the access to the synchrotron radiation facilities that were used to conduct XAFS and XPS measurements; Diamond Light Source, the Swiss Light Source (Paul Scherrer Institute) and the European Synchrotron Facility (ESRF). I owe great thanks to all the staff at these facilities for making these experiments possible; Diego Gianolio and Phil Robbins for helping with the setup and execution of beamtimes at B18 (Diamond Light Source), Maarten Nachtegaal for facilitating experimental time at SuperXAS (Swiss Light Source), Paul Thompson for the design and implementation of experiments at XMaS beamline (ESRF), and Monica Amboage, Trevor Orpin and Darren Neville for assisting in experimental setup and operation of I20-EDE (Diamond Light Source).

I must thank all the HR and technical support staff at the Research Complex at Harwell for making it possible to conduct my research. June Callison, Josie Goodall and all other students and post docs from the UK Catalysis Hub are thanked for their continued support, and for creating an enjoying atmosphere to work in.

Lastly I must thank my friends and family, for without whom this PhD would not have been possible. Thanks for endlessly listening to the problems and challenges, for keeping my spirits high, and for giving me encouragement when I needed it most.

Conferences

Oral Presentations

UCL Ramsay Symposium 2018, London (26/09/18)

17th International Congress on X-ray Absorption Spectroscopy 2018, Krakow (26/07/19)

UCL Clark Symposium 2018, London (26/06/18)

Johnson Matthey Academic Conference 2018, Loughborough (11/04/18)

UK Catalysis Conference 2018, Loughborough (03/01/18)

Poster Presentations

Celebrating 50 years of synchrotron radiation in the UK and its global impact, 2018

Johnson Matthey Academic Conference 2017 and 2016

13th European Congress on Catalysis, EuropaCAT, 2017

UK Catalysis Conference 2017

Awards

UCL Ramsay Medal, September 2018.

Ken Seddon OBE, Student Poster prize, UKSR50 conference, July 2018.

UCL 'Clark' Prize, Best student presentation in Inorganic Materials Chemistry, July 2018.

UCL Poster presentation prize, June 2017.

Publications

Combined spatially resolved *operando* spectroscopy: New insights into kinetic oscillations of CO oxidation on Pd/ γ -Al₂O₃, *Journal of Catalysis*, **373** (2019), 201-208.

Structural Selectivity of Supported Pd Nanoparticles for Catalytic NH₃ Oxidation Resolved using combined *Operando* Spectroscopy, *Nature Catalysis*, **2** (2019), 157-163

Combined In Situ XAFS/DRIFTS Studies of the Evolution of Nanoparticle Structures from Molecular Precursors, *ACS Chemistry of Materials*, **29** (17), (2017), 7515-7523;

Table of Contents

Chapter One. Introduction

1.1 Catalysis in Industry.....	1
1.2 Heterogeneous Catalysis.....	2
1.3 Metal Nanoparticles for Catalysis.....	4
1.3.1 Examples of commercial precious metal nanoparticle catalysts.....	5
1.4 Solid Material Characterisation.....	6
1.4.1 <i>In Situ</i> Spectroscopy.....	7
1.4.2 <i>Operando</i> Spectroscopy.....	7
1.4.3 Combined, <i>operando</i> spectroscopy.....	9
1.5 Aims and objectives.....	12
1.6 References.....	13

Chapter Two. Methods

2.1 Introduction.....	19
2.2 Synchrotron Radiation.....	19
2.3 X-ray Absorption Fine Structure.....	20
2.3.1 Theory.....	20
2.3.2 XAFS Data Acquisition.....	23
2.3.3 Quick-EXAFS (QEXAFS).....	25
2.3.4 Energy Dispersive X-ray Absorption Fine Structure (EDE-XAFS).....	26
2.3.5 XAFS Data Analysis.....	27
2.4 Infrared (IR) Spectroscopy.....	28
2.4.1 Diffuse reflectance infrared Fourier transform spectroscopy (DRIFTS).....	29
2.4.2 Transmission FTIR.....	30
2.5 Mass Spectrometry.....	30
2.6 Combined XAFS/DRIFTS/MS Set-up.....	31
2.7 Additional Characterisation Techniques.....	32
2.7.1 Transmission Electron Microscopy (TEM).....	32
2.7.2 X-ray Photoelectron Spectroscopy (XPS).....	34
2.7.3 X-ray Diffraction (XRD).....	35
2.8 Catalyst Preparation.....	36
2.9 References.....	36

Chapter Three. Following the evolution of metal nanoparticles from their molecular precursors by *in situ* XAFS/DRIFTS

3.1 Introduction.....	38
3.1.1 Preparation of Supported Metal Nanoparticles.....	38
3.1.2 Conventional Preparation Routes.....	38
3.2 Methods.....	40
3.2.1 Sample Preparation.....	40

3.2.2	<i>In situ</i> XAFS/DRIFTS/MS.....	41
3.2.3	EXAFS Analysis.....	42
3.2.4	<i>Ex situ</i> Characterisation.....	44
3.2.5	Catalytic Testing.....	45
3.3	Results.....	45
3.3.1	<i>In situ</i> XAFS.....	45
3.3.2	<i>In situ</i> DRIFTS and MS.....	54
3.3.3	<i>Ex situ</i> characterisation.....	58
3.3.3.1	TEM Analysis.....	58
3.3.3.2	XRD.....	59
3.3.3.3	<i>Ex situ</i> EXAFS.....	60
3.3.3.4	FTIR CO adsorption.....	63
3.3.4	Catalytic Testing.....	64
3.4	Discussion.....	64
3.5	Conclusions.....	65
3.6	References.....	66

Chapter Four. Identifying structure-function relationships of Pd catalysts for NH₃-SCO using an *operando* XAFS/DRIFTS/MS approach

4.1	Introduction.....	70
4.1.1	Diesel Exhaust After-treatment.....	70
4.1.2	Noble metal catalysts for NH ₃ -SCO.....	71
4.1.3	Alternative non-noble metal catalysts for NH ₃ -SCO.....	73
4.1.4	<i>In situ</i> studies of NH ₃ -SCO catalysts.....	73
4.2	Methods.....	74
4.2.1	Sample Preparation.....	74
4.2.2	<i>Ex situ</i> Characterisation.....	74
4.2.3	Catalytic Testing.....	74
4.2.4	<i>In situ</i> Pd L ₃ -edge XANES.....	75
4.2.5	XPS.....	75
4.2.5.1	<i>In situ</i> XPS.....	75
4.2.5.2	<i>Ex situ</i> XPS.....	76
4.2.6	Combined, <i>operando</i> Pd K-edge XAFS/DRIFTS/MS.....	76
4.2.7	DFT + D3 Calculations.....	77
4.3	Results.....	78
4.3.1	<i>Ex situ</i> characterisation.....	78
4.3.2	Catalytic Testing.....	80
4.3.3	<i>In situ</i> Pd L ₃ -edge XANES.....	82
4.3.4	XPS.....	83
4.3.5	<i>In situ</i> XPS.....	83

4.3.6	<i>Ex situ</i> XPS.....	85
4.3.7	<i>Operando</i> XAFS/DRIFTS/MS.....	86
4.3.7.1	On-line catalytic activity.....	86
4.3.7.2	<i>Operando</i> Pd K-edge XAFS.....	87
4.3.7.3	<i>Operando</i> DRIFTS.....	93
4.3.8	DFT + D3.....	96
4.4	Discussion.....	97
4.5	Conclusions.....	99
4.6	References.....	100

Chapter Five. Cell Design for combined, *operando* XAFS and DRIFTS

5.1	Introduction.....	104
5.2	XAFS and DRIFTS cell specification.....	104
5.2.1	X-rays.....	104
5.2.2	Infrared.....	107
5.2.3	Reactor Considerations.....	108
5.3	Literature Review: Design of the spectroscopic cell.....	109
5.4	Cell Design Iterations.....	121
5.4.1	3D Printed Plastic Model.....	121
5.4.2	Boron Nitride Cell.....	123
5.4.3	Aluminium Cell.....	125
5.5	Improvements for Future Models.....	127
5.6	Conclusions.....	128
5.7	References.....	129

Chapter Six. Kinetic Oscillations of Pd nanoparticle catalysts for CO oxidation; spatially resolved *operando* EDE/DRIFTS/MS

6.1	Introduction.....	133
6.1.1	CO oxidation at a metal surface.....	133
6.1.2	Kinetic Oscillations.....	134
6.2	Methods.....	137
6.2.1	Sample Preparation.....	137
6.2.2	Spatially resolved, <i>operando</i> EDE/DRIFTS.....	137
6.2.3	EDE Data Processing.....	140
6.2.4	IR Thermography Imaging.....	141
6.3	Results.....	142
6.3.1	Spatially resolved, <i>operando</i> EDE/DRIFTS.....	142
6.3.1.1	End-pipe Catalytic Activity.....	142
6.3.1.2	Position 8 – End of the catalyst bed (+ 14.6 mm).....	144
6.3.1.3	Position 1 – Front of the catalyst bed (+ 0.4 mm).....	152

6.3.1.4 Spatio-temporal analysis.....	155
6.3.2 Thermographic Imaging.....	158
6.4 Discussion.....	159
6.5 Conclusions.....	162
6.6 References.....	163

Chapter Seven. Summary and Conclusions

7.1 Summary and Future Outlooks.....	166
7.2 Final Remarks.....	168

Chapter One. Introduction

Life in the developed world would not be as we know it without the scientific advances in catalysis, and the development of new catalytic processes hold great potential for future technology as we strive towards a sustainable future. In order to design new heterogeneous catalysts, we must have a thorough understanding of the material properties and functionality that govern their catalytic behaviour. To do this, a number of characterisation techniques must be employed to examine their chemical and physical properties, whilst operating under realistic reaction environments.

1.1 Catalysis in Industry

The phenomenon of catalysis has huge significance in industry to facilitate reactions that would otherwise be economically unfeasible, and allow the control of product selectivity. It is now widely acknowledged that over 90% of commercial chemicals and processed materials utilize a catalytic step at least once during their industrial production.^{2, 3} The current socio-economic climate presents an interesting period for the development of new catalytic technologies, as society recognises the negative impact of consumerism on both human health and the environment, and the need to strive towards a more sustainable future. The drive to devise cleaner chemical processes to improve air quality in cities, address diminishing fossil fuel resources, clean up plastic waste and hinder global warming requires research into new and improved catalytic materials. Global pollution, from chemical waste, plastic waste and gaseous emissions, is a pressing issue that has received increased attention over the last decade. In 2015 it was estimated that nine million premature deaths worldwide were caused by pollution and, despite the emissions control technologies in place, air pollution accounted for six million of those.⁴ It is currently estimated that 90% of the world's population are living in areas that exceed the air pollution limits set by the World Health Organisation⁵ – with an alarming number of those located in cities in developed countries, such as London.⁶ The major pollutants concerning human health in cities are nitrogen oxides, NO_x (NO and NO_2), and particulate matter (PM), which are released from automotive vehicle exhaust and directly inhaled by nearby pedestrians. The monitoring of NO_2 levels in one location in London found that the hourly $200 \mu\text{g}/\text{m}^3$ limit was breached 18 times in January 2018 alone, which was the total limit set for NO_2 levels for that entire year.⁷ In order to curb the dangerous incline in air pollution levels, the Euro emission standards that set out the legal limits of pollutants from automotive vehicles in Europe, are becoming increasingly stringent.⁸ Consequently, the world's largest technology companies are competing to find solutions to lower emissions and capitalise on the 'greener' technology initiatives that will shape our future. There is no doubt that development of new technologies for abatement of pollutants from the atmosphere requires thorough understanding of heterogeneous catalysis.

1.2 Heterogeneous Catalysis

A catalyst is a material that increases the kinetic rate of a chemical reaction by providing an alternative reaction pathway with a lower activation energy than that of the uncatalysed pathway. The reaction rate, Equation 1.1, is determined by the concentration of reactants, the order of reaction with respect to those reactants and the rate coefficient, k . The relationship between the rate coefficient, k , the activation energy, E_a , and the temperature, T , is given by the Arrhenius equation (Equation 1.2), where A is a constant and R is the gas constant.

$$\text{rate} = k[A]^x[B]^y \quad \text{Equation 1.1}$$

$$k = A \exp\left(\frac{-E_a}{RT}\right) \quad \text{Equation 1.2}$$

The catalyst is not consumed in the process and so *does not* appear in the stoichiometric equation for the overall reaction, but *will* be involved in the reaction mechanism and thus the rate law of that particular reaction.

A heterogeneous catalyst, as opposed to a homogeneous catalyst, is one that occupies a different phase from that of the reactants and products; often a solid catalyst in a liquid or gaseous reaction mixture. Heterogeneous catalysts are usually preferred in industrial processes as they are generally easier to separate from the reaction products and so can be reused many times.

Heterogeneous catalysts generally operate by providing an active site at its surface for adsorption, reaction and desorption of at least one reagent in the reaction. There are two broad classes of adsorption which can subsequently lead to the catalysed reaction; physisorption and chemisorption. Physisorption involves the long-range, weak Van der Waals interactions between the molecule (the adsorbate) and the solid surface (the substrate). The low attraction energy means that the adsorbate can move around at the surface and has low desorption energy, but the molecule may be held in a preferred orientation for reaction. Alternatively, chemisorption involves a stronger interaction of the adsorbate with the surface by transfer of electrons between the gas-phase molecule and the solid surface. Dissociative chemisorption, whereby donation of electron density from the surface into an antibonding orbital of the adsorbing molecule weakens that molecular bond sufficiently to break it, resulting in reactive 'activated' adsorbates at the catalyst surface. For example dissociative H_2 adsorption over Pd(111) catalyst surface,⁹ which is the elementary step for catalysed hydrogenation reactions.^{10, 11} After reaction at the surface, the products (or modified reaction products) desorb back into the gas phase. The 'Sabatier Principle', illustrated by the volcano plot in Figure 1.1, states that the interaction between a catalyst and substrate must be strong enough – such that adsorbed molecules can be immobilized on the surface for

reaction – but weak enough for neighbouring molecules to react and for fast desorption of products back into the gas phase.^{1, 3}

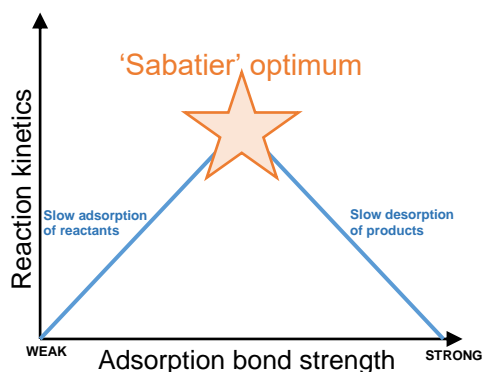


Figure 1.1. Schematic representation of the Sabatier volcano plot showing reaction kinetics as a function of adsorbate bond strength on a catalyst surface.¹

Generally accepted classes of mechanism for heterogeneous catalysis can be categorized into three types; Eley-Rideal mechanism,¹² Langmuir-Hinshelwood mechanism¹³ and Mars-Van Krevelen mechanism¹⁴. The Eley-Rideal mechanism involves the adsorption of just one of the reactants to the catalyst surface, followed by reaction with a gas phase molecule and subsequent desorption of the products. The Langmuir-Hinshelwood mechanism involves the adsorption of more than one reactant to the catalyst surface, reaction between the neighbouring adsorbates and desorption of the products. The Mars-Van Krevelen mechanism involves reaction of an adsorbed reactant with an atom from the surface layer of the catalyst, subsequently leaving a vacancy in the surface when the products desorb. The surface vacancy is filled either with an atom from the catalyst bulk structure or from the gas phase to regenerate the catalytic surface.

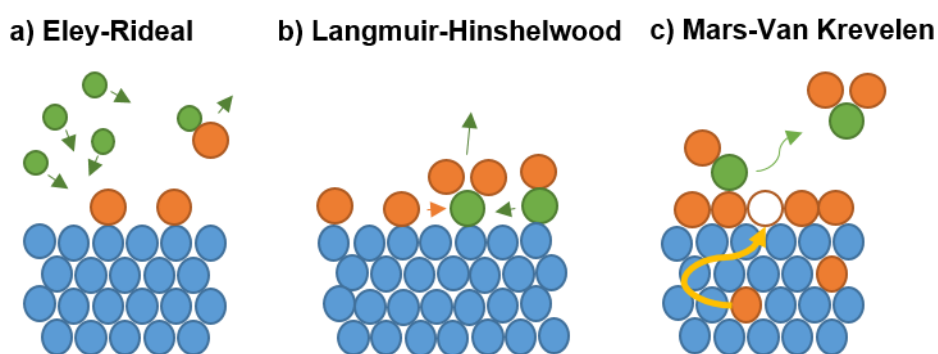


Figure 1.2. Schematic drawing of the three generally accepted catalytic mechanisms; a) Eley-Rideal, b) Langmuir-Hinshelwood, and c) Mars-Van Krevelen.

1.3 Metal Nanoparticles for Catalysis

A catalyst material must be carefully designed to achieve optimal performance for the desired reaction. The solid heterogeneous catalysts in this work have been studied for gas phase reactions, in an effort to address the abatement of harmful, pollutant gases from the atmosphere. Specific requirements for each catalyst depend upon their final application and operating conditions, but in any case they should achieve high activity and selectivity towards the desired products. Metal surfaces, in particular those of transition metals and precious metals, often provide desirable catalytic activity due to their electronic properties. The electronic structure of a bulk metal can be described by the band theory, by which bonds between metal atoms form a collection of molecular orbitals so close in energy that they form an almost continuous 'band' of energy levels then referred to states. The density of states (DOS) in a metal describes the number of states at each defined energy, and the Fermi level describes the occupancy of those states. The DOS is unique for different metals, with a general trend of narrowing d-band in moving from left to right across the periodic table. At a metal surface, the surface atoms have fewer neighbours and have effectively 'broken' metal bonds with isolated surface orbitals, thus the band is narrowed but the Fermi level is still dictated by the bulk. Donation of electrons from the Fermi level of the metal are used to create chemisorption bonds by donation to the adsorbate.¹⁵

The catalyst must possess the surface sites required for the adsorption of gaseous reactant(s), which may be the external surface of nanoparticle materials or the internal surface of a porous material. When a crystal is cleaved and a surface is created, the orientation of atomic orbitals depends on the crystal structure and the type of surface exposed. Even a polished surface or freshly cleaved crystal will not have a surface that is flat on the atomic scale and it is often the under coordinated defect sites – kinks, steps, adatoms – that provide the lowest energy adsorption sites. The use of metal nanoparticles for catalysis benefit from a large number of under coordinated surface defect sites, larger surface area per unit mass and high surface energy. The higher surface area to unit mass of metal nanoparticles has economic implications for industrial catalyst production, lowering the (often expensive) wt% metal loading required for the catalyst and thus keeping down the raw material costs. This is a notable consideration when using expensive precious metals, which also pose a concern of limited reserves and ethics of mining.

Additionally, the catalyst material must have suitable stability under the operating reaction environment and resistance against deactivation mechanisms to allow a sufficient operating lifetime. There are different types of deactivation mechanisms that result in gradual decay of catalytic activity during time on stream, caused by thermal, chemical and mechanical factors. The most common deactivation mechanisms for metal nanoparticles are poisoning (adsorption of unreactive species that block the

active sites) and sintering (the agglomeration of nanoparticles to result in loss of surface area).¹⁶ The anchoring of metal nanoparticles to a high surface area metal oxide or carbon support helps to stabilize against sintering mechanisms and maintain high dispersion. The greater the strength of metal-support interactions, the lower the thermodynamic force for sintering and lower the sintering rate.^{17, 18} The support material must also have high thermal and mechanical resistance, and is usually considered inert (although some studies have shown that the support may play a role in the catalytic mechanism by charge transfer¹⁹). The preparation of supported metal nanoparticle catalysts can be achieved by different methods which can affect their physicochemical properties and catalytic activity. The route to prepare such nanoparticle materials with optimal catalytic properties should therefore be carefully designed.

1.3.1 Examples of commercial precious metal nanoparticle catalysts

The use of gold nanoparticles in catalysis has been widely researched for a number of different applications. Many early studies used gold nanoparticles for CO oxidation²⁰⁻²², other oxidation reactions (eg. glycerol to glyceric acid)²³⁻²⁵ and hydrogenation reactions^{18, 26, 27}. Hydrogen purification, for the removal of CO impurities from the H₂ gas feed used for fuel cell operation, requires the use of a selective catalyst for the preferential oxidation of CO to CO₂, without the oxidation of H₂ to H₂O. The commercial product *AUROPureH₂*TM, consists of an Au/TiO₂ catalyst and operates at room temperature to selectively remove CO down to 1 ppm concentrations.^{28, 29}

The water gas shift (WGS) reaction is important for the industrial production of hydrogen, providing fuel for hydrogen fuel cells and a feedstock for many other chemical processes such as the Haber-Bosch production of ammonia. The WGS reaction to form H₂ and CO₂ from CO and H₂O is exothermic and reversible, thus a catalyst is required to increase the reaction kinetics at low temperature. Multiple studies have reported the superior catalytic activity of Pt nanoparticle catalysts for low temperature WGS reaction when supported on CeO₂^{30, 31} and Ce-modified TiO₂.³² Similarly to other supported precious metal catalysts, these Pt/CeO₂ catalysts benefit from a high dispersion of Pt over the support and resistance against sintering, with the CeO₂ support thought to also assist in oxygen transfer and oxygen storage.³³ Other applications for Pt nanoparticle catalysts include fuel cell electrocatalysts,³⁴ hydrogen production by catalytic methane decomposition³⁵ and glycerol oxidation.³⁶

Supported palladium nanoparticle catalysts also play a significant role in catalysing industrial chemical processes, particularly selective hydrogenation reactions of olefins^{37, 38}, alkynes^{39, 40} and dienes^{41, 42}. For example, the manufacture of nylon-6 from caprolactone, requires the selective hydrogenation of phenol to cyclohexanone over a Pd/TiN catalyst.⁴³ The selective hydrogenation of furfural can be achieved with a Pd catalyst, for the production of the biomass derived fuel, furfuryl alcohol,⁴⁴⁻⁴⁶ and the synthesis of hydrogen peroxide involves the Pd catalysed hydrogenation of 2-ethyl-

anthraquinone.⁴⁷⁻⁴⁹ As well as hydrogenation reactions, the ability of Pd nanoparticles to catalyse oxidation reactions is important for emissions control technology. In 1994, Ford motors reported the benefits of using Pd as the active component of their three-way catalysts for abatement of hydrocarbons, CO and NO from gasoline engine exhaust.⁵⁰ Due to the alternative fuels used today, the use of Pd catalysts for a range of other emissions control applications has been investigated; low temperature CH₄ oxidation (Chapter 3), selective NH₃ oxidation (Chapter 4) and CO oxidation (Chapter 5). Each of the above mentioned catalytic reactions require different electronic and physical properties of the active Pd nanoparticle catalyst to facilitate the different catalytic pathways. Further investigation is therefore required to understand the material properties that govern the catalytic activity so that new catalysts can be designed with optimal performance for the desired reactivity.

1.4 Solid Material Characterisation

In order to design new catalysts, it is important to understand the nature of the active phase and the chemistry facilitating the catalysed reaction pathway on the surface. There are a number of physical techniques that can be used to characterise the chemical and physical properties of solid materials, as well as their surface reactivity. Microscopy techniques such as (i) transmission electron microscopy (TEM), scanning electron microscope (SEM) and scanning tunnelling microscopy (STM) are used to obtain high resolution images of solid materials for information about particle size and morphology, (ii) diffraction techniques, such as X-ray diffraction (XRD), are able to identify atomic structure of crystalline materials which can then be combined with computed tomography (XRD-CT) for chemical imaging and phase identification, (iii) spectroscopy techniques use different frequencies of electromagnetic radiation to probe electronic, vibrational and rotational energy levels of the investigated material. Microwave radiation can be used to probe transitions between rotational energy levels. Infrared (IR) and Raman spectroscopy can be used to probe molecular and atomic vibrations. X-ray absorption spectroscopy (XAS) and X-ray photoelectron spectroscopy (XPS) can be used to probe the high energy electronic transitions from core atomic orbitals, and ultraviolet-visible spectroscopy (UV-Vis) is able to probe the lower energy electronic transitions from the valence band. X-ray absorption fine structure (XAFS) spectroscopy is able to give additional information for the local atomic structure and does not rely on long-range ordering of the material, meaning that XAFS is an ideal technique for studying the structure of supported metal nanoparticle catalysts. IR, Raman, UV-Vis and XPS spectroscopy are frequently used for catalyst characterisation due to the accessibility of these techniques in the lab, whereas the use of X-ray spectroscopy techniques are restricted by limited access to synchrotron radiation facilities.

1.4.1 *In situ* Spectroscopy

The dynamic nature of catalyst materials is well-recognized and so it is important to consider the environment in which a catalyst is investigated, and how this may differ from its real operating reaction environment. Advances in spectroscopic methods over the last ~40 years have recognised the need to progress from *ex situ* characterisation towards *in situ* and *operando* characterisation in order to obtain information for the operating catalyst. *Ex situ* refers to methods in which the material is investigated in an ambient or static environment that is most suited to the spectroscopic technique, which is often very different to the environment in which the catalyst would be exposed in its application. The *pre natal* and *post mortem* analysis, whereby the catalyst is examined by *ex situ* methods before and after catalyst testing, often miss important changes to the catalyst that occur under reaction conditions.⁵¹⁻⁵³ For example, the active phase may be formed after an initial induction period^{54, 55} and return to an inactive state upon removing from the high temperature and pressure of the reactor. It is also recognised that the investigation of model catalysts contained under high vacuum systems can give insightful information to the fundamental surface science but do not represent the real catalytic systems used in industry. This concept is often referred to as the materials and pressure gap, *i.e.* the difference between the single crystal surface studied in ambient conditions compared to the 'real' industrial catalyst in its operating environment.^{56, 57} *In situ* describes a characterisation technique whereby the 'real' catalyst is investigated under a controlled atmosphere, replicating the environment that would be seen by the catalyst during reaction. Some spectroscopy methods are more easily adapted to *in situ* studies, such as infrared, Raman, UV-Vis and X-ray spectroscopy, due to penetration of the spectroscopic probe through the reaction medium and development of a suitable spectroscopic cell (this will be discussed in more detail later). The use of synchrotron radiation is particularly useful for *in situ* measurements by providing a collimated beam and high flux of the incident radiation to penetrate the catalyst sample and reaction medium. The development of *in situ* methods for techniques usually conducted in high vacuum systems such as near ambient pressure-XPS (NAP-XPS) and electron microscopy have been more challenging but have undergone significant advances in recent years; the opening of a new near ambient pressure X-ray photoelectron spectroscopy (NAP-XPS) beamline, B07 at Diamond Light Source,⁵⁸ and the development of an *in situ* TEM cell was used successfully at the electron Physical Sciences Imaging Centre (ePSIC) to study the formation of Pt nanocrystals in real time.⁵⁹

1.4.2 *Operando* Spectroscopy

Although *in situ* spectroscopy has provided invaluable information about catalyst properties under controlled environments, the direct relationship between these structural changes and the catalytic activity can only be confidently assigned by

operando spectroscopy. *Operando* is used in this context to describe the time-resolved spectroscopic measurements of an operating catalyst that are coupled with simultaneous measurements of the reaction kinetics. In this way, the experimentalist can be certain that the structural properties investigated by the spectroscopic technique relate to the catalytic activity and selectivity observed by the product analysis. The term '*operando*' was introduced in 2002 by A. Bañares,⁶⁰⁻⁶² but the pioneering work of others before this time must be recognised in their attempts to complement spectroscopic measurements with online product analysis.

The use of *operando* IR spectroscopy is particularly useful to observe how reactant molecules interact with the catalyst surface and how they are transformed into the reaction product(s) during the catalytic mechanism. The earliest study of this kind was reported by J. Ward *et al.* in 1968 which describes 'using an IR cell which could function as a flow reactor with effluent gas flow analysed by gas chromatography' to study the role of zeolite acid sites in the catalytic alkylation of cumene.⁶³ Although activity data was not reported, this is the first mention of such experimental setup with an intention to collect both spectroscopy and activity data sets simultaneously. Conclusions resulting from simultaneous IR and GC data collection were not reported until 1991 by J.F. Joly *et al.*⁶⁴ who were able to elucidate active acid sites for dealuminated HY zeolites during cyclohexene conversion, then by P. Maetz *et al.*⁶⁵ in 1994 for accessing the operation of Pt/SiO₂ for butyne hydrogenation. *In situ* Raman spectroscopy was also established around this time, reported by Wachs *et al.* to study vanadium oxide catalysts for butane oxidation.⁶⁶

The early *operando* measurements of catalyst materials using X-ray techniques took advantage of the highly penetrating nature of the bright, tunable X-ray flux from a synchrotron source to probe the catalyst sample contained within a reaction chamber. *In situ* XRD measurements by Clausen *et al.* were able to follow the change in structural phases of Cu/Zn/Al catalysts during their operation for WGS and methanol synthesis reactions.⁶⁷ By analysing the effluent gas from the XRD capillary with on-line gas chromatography, they were able to correlate the variation in WGS activity with changes in the formation and growth of a metallic Cu phase. Early *in situ* XANES measurements were also achieved by D. Liu *et al.* in 1993 to identify the role of Cu(I) species in a redox mechanism for catalysis of NO decomposition.⁶⁸

The advantage of Fourier transform spectroscopy for faster data acquisition,⁶⁹ coupled with measurements of the diffusely reflected IR radiation gave rise to diffuse reflectance infrared Fourier transformed spectroscopy (DRIFTS) for time-resolved *operando* characterisation of heterogeneous catalysts.⁷⁰ Reaction intermediates at the catalyst surface were probed in real time, using DRIFTS, in the form of 'active reservoirs of CO_{ads} and HCOO⁻_{ads}' at the surface of a Ru/TiO₂ catalyst during catalysed CO₂ methanation.⁷¹ Sampling aliquots from the reactor were continuously sent to an on-line

mass spectrometer for analysis. A. Banares *et al.* published work using DRIFTS in 1995 with catalytic activity data, although these measurements were performed in different reactors.⁷² Weckhuysen *et al.* published early reports of simultaneous collection of diffuse reflectance spectroscopy (in the ultraviolet, visible and near-infrared regions) and catalytic activity by on-line gas chromatography of the exhaust.⁷³ ⁷⁴ Since these early experiments, there has been significant development of *in situ* spectroscopy methods for understanding structure-activity relationships of heterogeneous catalysts, and increasing recognition of the advantage of a combined, multi-technique approach.⁷⁵

1.4.3 Combined, *operando* spectroscopy

The techniques discussed above are each able to provide different information about the catalyst material; electronic structure, atomic arrangement, surface reactivity, particle morphology, *etc.* There is not one technique that can yield all this information in a single shot; therefore the combination of multiple *operando* techniques applied simultaneously to the study of a single sample can provide a more detailed understanding of the material. The first time-resolved, multi-technique experiment used a combination of X-ray diffraction and X-ray absorption spectroscopy (XRD/XAFS) to follow the formation of a Cu/ZnO catalyst during the calcination of a layered mineral aurichalchite ($\text{Cu}_{5-x}\text{Zn}_x(\text{OH})_6(\text{CO}_3)_2$) to 450°C. This was amongst some of the first studies to recognise the advantage of using a combination of X-ray techniques to study the structural and chemical changes of a material in real time.⁷⁶ Other studies during the 1990s used the same time resolved XRD/XAFS approach to study the formation of catalyst materials and structural changes under controlled environments.⁷⁶⁻⁷⁹ Around the same time, the use of combined XRD/XAFS to study catalysts under simple reaction conditions, such as the oxidation of cyclohexane was reported.⁸⁰ Due to the long-range atomic order required for XRD, this combination of techniques has been more useful for the study of larger crystallite materials (such as zeolites) rather than the supported metal nanoparticle catalysts. For the structural characterisation of metal nanoparticle catalysts XAFS is the preferred technique (rather than XRD), as long range order is not required and the high sensitivity of XAFS to the selected element is suitable for studying industrial catalysts which often contain a low wt% of the active metal component. Many successful experiments have used *in situ* XAFS in combination with other time-resolved spectroscopic techniques; UV-Vis (homogeneous catalysts⁸¹⁻⁸⁵ and heterogeneous catalysts^{86, 87}), FTIR (heterogeneous catalysts)⁸⁸⁻⁹³ and Raman (heterogeneous catalysts)^{86, 94}. For the characterisation of supported metal nanoparticles, the combination of XAFS with DRIFTS is desirable as it provides information of both the bulk nanoparticle structure (XAFS) and the surface reactivity (DRIFTS). XAFS and DRIFTS can be acquired on similar timescales and length scales for confident structure-function analysis of the catalyst. Improvements to the combined,

in situ XAFS/DRIFTS methodology for the advanced characterisation of heterogeneous catalysts will be investigated in this work.

The collective goal for *operando* spectroscopy of heterogeneous catalysts is to gain a detailed insight into their operation, to obtain a specification for the design of new, improved catalyst materials. Some scientists have expressed the desire to obtain 'motion pictures' of the operating catalyst in action,⁹⁵ similarly to those obtained for the conformational changes of cells and proteins in biological pathways.⁹⁶ The experimental tools required to achieve this detailed mechanistic understanding of heterogeneous catalysts are still far from well-established. The spectroscopic techniques and *operando* methods must achieve improved time resolution and spatial resolution in order to gain greater understanding of catalytic processes in real time.

Improved time resolution is required to observe each mechanistic step in the catalytic pathway, ideally including the bond-breaking and bond-making at the catalyst surface. The remarkable development of spectroscopic instrumentation in the past 50 years for improved signal-to-noise, energy resolution and faster data acquisition has opened up the possibility for improved time resolution in *operando* spectroscopy methods. In particular, the advances to synchrotron radiation have seen vast improvements for time-resolved X-ray absorption spectroscopy. The commission of the quick scanning EXAFS (QEXAFS) technique in 1988 has allowed for fast scanning of the EXAFS spectrum by using a monochromator that is driven by a motor in continuous motion.^{97, 98} The advantage of this high time-resolved technique for *in situ* studies of catalyst materials was demonstrated a few years later^{78, 99}, and since then has been used extensively for catalyst characterisation at synchrotrons around the world.¹⁰⁰⁻¹⁰² The possibility for the entire EXAFS spectrum to be collected in a 'single shot' measurement on the millisecond timescale was made available by the development of energy dispersive EXAFS (EDE) in 1983 (method discussed in detail in Chapter 2).¹⁰³ Although this technique was developed around the same time period as QEXAFS, its use for *in situ* measurements of catalyst materials has been less extensive due to the difficulty in performing such experiments. The first reports of successful time resolved, *in situ* studies of catalyst materials using the EDE technique came during 1997 from P. Lee *et al.* for the characterisation of vanadium catalysts during n-butane oxidation,¹⁰⁴ and also Ressler *et al.* for the characterisation of Pd nanoparticle catalysts during CO oxidation.¹⁰⁵ Realistically, the process of making and breaking bonds occurs on the femtosecond timescale and is beyond the time resolution of most spectroscopic techniques. The recent development of the free electron laser (XFEL) does present an opportunity to observe bond making and breaking at the catalyst surface in real time,^{106, 107, 108} however, these experiments present many challenges and remain out of reach to most experimentalists. More commonly, transient spectroscopic measurements performed on the millisecond timescale are used to monitor the change

in population of active states after initiating changes in the reaction conditions (change in temperature, gas concentrations *etc.*).

Spatial resolution in spectroscopic measurements is particularly important when combining multiple techniques to obtain collective information of a catalyst sample. In order to relate the catalyst structure and function of a catalyst by performing simultaneous spectroscopic techniques of one single sample, the multiple techniques must be sure to probe exactly the same spatial position of the sample, or be confident in the homogeneity of the sample at the two positions. In this way, the two data sets and the information obtained by analysis of each technique can be confidently linked to give a holistic view of the catalytic properties responsible for the catalytic reactivity. Typically, heterogeneous catalysts for industrial catalytic reactions will be used in a plug-flow arrangement, whereby gases flow continuously through the catalyst bed from the reactor inlet towards the reactor outlet. Industrial catalysts, particularly for emissions control applications, are used under integral conditions whereby the high conversion of reactants to products results in a steep gradient in reactant and product concentrations from inlet to outlet, as illustrated in Figure 1.3.¹⁰⁹ The reaction conditions are expected to have minimal variation across the radial cross section of the reactor, but vary with position along the axial length of the reactor. This has been evidenced by spatially resolved mass spectrometry measurements of a powdered catalyst bed, using a technique named the Spaci-FB.¹¹⁰ In this technique, a sampling capillary is drawn along the length of fixed catalyst bed during operation for the desired catalytic reaction, for example a Pd/Al₂O₃ catalyst during CO oxidation.^{111, 112} High catalytic activity and fast reaction kinetics were found at the front of the catalyst bed, nearest to the reactor inlet, where reactant concentration was at its greatest. With increasing distance downstream of the inlet, the reactant concentration decreased as did the reaction rate. Therefore spectroscopic techniques applied to study heterogeneous catalysts operating in plug-flow reaction conditions must be able to probe the catalyst at multiple spatial positions along the length of the reactor, with sufficient resolution to capture the changes in catalyst structure and function on a suitable length scale.

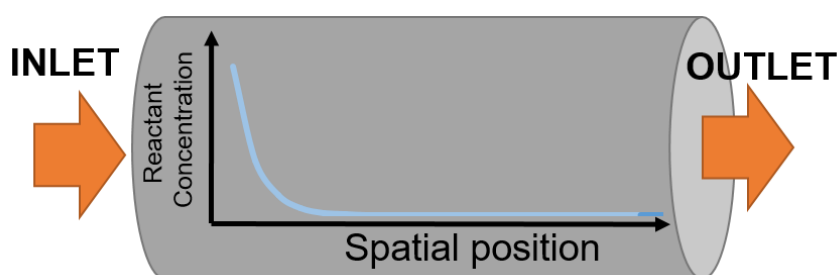


Figure 1.3. Schematic illustration of a plug flow reactor, showing the reactant concentration as a function of spatial position along the length of the reactor.

The limitation for ideal *operando* measurements currently lies with the design of a suitable spectroscopic cell to contain the catalyst in its operating environment, whilst permitting time-resolved and spatially resolved spectroscopy. For true *operando* measurements, taking spectroscopic and activity measurements of the catalyst in its normal operating environment (eg. at the catalytic converter within the exhaust of a vehicle driving on the road) would ensure the catalyst is unaltered from its real working state. Clearly this arrangement is not possible, particularly when the spectroscopy instrument is not portable. Therefore a spectroscopic cell must be designed that is able to replicate the 'real' working conditions of the catalyst as closely as possible, without compromising the quality of the spectroscopic data.

1.5 Aims and objectives

The fundamental aim of this thesis is to provide a greater understanding of the structure-function properties of heterogeneous catalyst materials, in particular supported Pd nanoparticle catalysts for emissions control technology. In order to achieve this, combined XAFS and DRIFTS spectroscopy will be used, making improvements to the existing methodology for this combined spectroscopic approach by designing a new spectroscopic cell for improved time resolution and spatial resolution of *operando* measurements. The preparation of supported Pd nanoparticle catalysts will be investigated in Chapter 3, using combined, time-resolved spectroscopy to understand the formation of these nanoparticle catalysts from their molecular precursors. The operation of supported Pd nanoparticle catalysts for two important reactions used in emission control technology will be discussed; the selective catalytic oxidation of ammonia (Chapter 4) and carbon monoxide oxidation (Chapter 6). The structure-function relationships of the Pd nanoparticle catalyst operating under these different working conditions are investigated by probing the Pd nanoparticle structure, oxidation state and particle size with Pd K-edge XAFS and the surface reactivity by simultaneous DRIFTS. The theory and design for a new spectroscopic cell is detailed in Chapter 5, which allows for improved temporal resolution and spatial resolution of combined, *operando* XAFS and DRIFTS spectroscopy. The operation of this improved spectroscopic cell will be tested for a spatially resolved study of a Pd catalyst during kinetic oscillations of CO oxidation (Chapter 6). This work is aimed to provide greater insight into the operation of the Pd nanoparticle catalysts, providing new information for the spatial variance in structure-function relationships on a millimetre length-scale and millisecond time-scale.

1.6 References

1. P Sabatier, *La catalyse en chimie organique*, Nouveau Monde éditions, 2014.
2. JG de Vries and SD Jackson, *Cat. Sci. Tech.*, 2012, **2**, 2009-2009.
3. AJ Medford, A Vojvodic, JS Hummelshøj, J Voss, F Abild-Pedersen, F Studt, *et al.*, *J. Catal.*, 2015, **328**, 36-42.
4. H Wang, M Naghavi, C Allen, RM Barber, ZA Bhutta, A Carter, *et al.*, *The Lancet*, 2016, **388**, 1459-1544.
5. World Health Organisation. Ambient (outdoor) air quality and health [online]. May 2018. Available from: [https://www.who.int/news-room/fact-sheets/detail/ambient-\(outdoor\)-air-quality-and-health](https://www.who.int/news-room/fact-sheets/detail/ambient-(outdoor)-air-quality-and-health). [Accessed 02 February 2019].
6. CD Beevers S, Dajnak D, Stewart G, Williams M, Fussell J, Kelly F, *Energy and Emission Control Technologies*, 2015, **4**, 27-39.
7. Carrington D., Holder J., London air pollution live data – track the breaches of legal limits in 2018. *The Guardian* [online]. 2018. Available from: <https://www.theguardian.com/environment/ng-interactive/2018/jan/01/london-air-pollution-live-data-where-will-be-first-to-break-legal-limits-in-2018>. [Accessed 02 February 2019].
8. European Union. Regulation (EC) No 715/2007 on type approval of motor vehicles 2007. European Environment Agency, Denmark.
9. K Christmann, *Surface Science Reports*, 1988, **9**, 1-163.
10. I Horiuti and M Polanyi, *Trans. Faraday Soc.*, 1934, **30**, 1164-1172.
11. JM Moses, AH Weiss, K Matusek and L Gucci, *J. Catal.*, 1984, **86**, 417-426.
12. WH Weinberg, *Accounts Chem. Res.*, 1996, **29**, 479-487.
13. I Langmuir, *J. Am. Chem. Soc.*, 1918, **40**, 1361-1403.
14. P Mars and DW van Krevelen, *Chem. Eng. Sci.*, 1954, **3**, Supplement 1, 41-59.
15. A Beale, J Ruiz-Martinez, BM Weckhuysen, In-situ characterization of Heterogeneous Catalysts. In: JA Rodriguez, JC Hanson, PJ Chupas, (eds.) In-situ Characterization of Heterogeneous Catalysts. John Wiley & Sons; 2013. p. 441-475.
16. TW Hansen, AT DeLaRiva, SR Challa and AK Datye, *Accounts Chem. Res.*, 2013, **46**, 1720-1730.
17. JA Farmer and CT Campbell, *Science*, 2010, **329**, 933-936.
18. CT Campbell, *Accounts Chem. Res.*, 2013, **46**, 1712-1719.
19. M Boronat, P Concepción, A Corma, S González, F Illas and P Serna, *J. Am. Chem. Soc.*, 2007, **129**, 16230-16237.
20. M Haruta, N Yamada, T Kobayashi and S Iijima, *J. Catal.*, 1989, **115**, 301-309.
21. H Falsig, B Hvolbæk, IS Kristensen, T Jiang, T Bligaard, CH Christensen, *et al.*, *Angew. Chem. Int. Ed.*, 2008, **47**, 4835-4839.

22. M Valden, X Lai and DW Goodman, *Science*, 1998, **281**, 1647-1650.
23. S Carrettin, P McMorn, P Johnston, K Griffin, CJ Kiely, GA Attard, *et al.*, *Top. Catal.*, 2004, **27**, 131-136.
24. JJ Bravo-Suárez, KK Bando, T Akita, T Fujitani, TJ Fuhrer and ST Oyama, *Chem. Comm.*, 2008, DOI: 10.1039/b800620b, 3272-3274.
25. A Abad, P Concepción, A Corma and H García, *Angew. Chem. Int. Ed.*, 2005, **44**, 4066-4069.
26. J Jia, K Haraki, JN Kondo, K Domen and K Tamaru, *J. Phys. Chem. B*, 2000, **104**, 11153-11156.
27. M Juliusa, S Roberts and JCQ Fletchera, *Gold Bull.*, 2010, **43**, 298-306.
28. DT Thompson, *Nano Today*, 2007, **2**, 40-43.
29. GP J. Steyn, E. van der Lingen, M. Scurrrell and D. Hildebrandt, *South African Patent Application*, 2006.
30. AA Phatak, N Koryabkina, S Rai, JL Ratts, W Ruettinger, RJ Farrauto, *et al.*, *Catal. Today*, 2007, **123**, 224-234.
31. D-W Jeong, HS Potdar, J-O Shim, W-J Jang and H-S Roh, *Int. J. Hydrogen Energ.*, 2013, **38**, 4502-4507.
32. ID González, RM Navarro, W Wen, N Marinkovic, JA Rodríguez, F Rosa, *et al.*, *Catal. Today*, 2010, **149**, 372-379.
33. G Dutta, UV Waghmare, T Baidya, MS Hegde, KR Priolkar and PR Sarode, *Catal. Lett.*, 2006, **108**, 165-172.
34. S Sui, X Wang, X Zhou, Y Su, S Riffat and C-j Liu, *J. Mater. Chem. A*, 2017, **5**, 1808-1825.
35. M Caballero, G Del Angel, I Rangel-Vázquez and L Huerta, *Catal. Today*, 2018, DOI: <https://doi.org/10.1016/j.cattod.2018.05.024>.
36. R Garcia, M Besson and P Gallezot, *Appl. Catal. A: General*, 1995, **127**, 165-176.
37. Y Zhang, S Liao, Y Xu and D Yu, *Appl. Catal. A: General*, 2000, **192**, 247-251.
38. F Wang, Z Zhang, X Wei, Q Fang and X Jiang, *Appl. Catal. A: General*, 2017, **543**, 196-200.
39. H Bazzazzadegan, M Kazemeini and AM Rashidi, *Appl. Catal. A: General*, 2011, **399**, 184-190.
40. Z Guo, Y Liu, Y Liu and W Chu, *Appl. Surf. Sci.*, 2018, **442**, 736-741.
41. VV Chesnokov, IP Prosvirin, NA Zaitseva, VI Zaikovskii and VV Molchanov, *Kinet. Catal.*, 2002, **43**, 838-846.
42. B Bachiller-Baeza, J Peña-Bahamonde, E Castillejos-López, A Guerrero-Ruiz and I Rodríguez-Ramos, *Catal. Today*, 2015, **249**, 63-71.
43. H-F Li, Q-S Zhang, Z-B Pang, M Tian, P Gao and L-L Wang, *Chinese Chem. Lett.*, 2016, **27**, 1500-1504.
44. J Du, J Zhang, Y Sun, W Jia, Z Si, H Gao, *et al.*, *J. Catal.*, 2018, **368**, 69-78.

45. R Albilali, M Douthwaite, Q He and SH Taylor, *Cat. Sci. Tech.*, 2018, **8**, 252-267.
46. SM Rogers, CRA Catlow, CE Chan-Thaw, A Chutia, N Jian, RE Palmer, *et al.*, *ACS Catal.*, 2017, **7**, 2266-2274.
47. X Shi, E Yuan, G Liu and L Wang, *Chinese J. Chem. Eng.*, 2016, **24**, 1570-1576.
48. E Yuan, C Wu, X Hou, M Dou, G Liu, G Li, *et al.*, *J. Catal.*, 2017, **347**, 79-88.
49. X Li, H Su, D Li, H Chen, X Yang and S Wang, *Appl. Catal. A: General*, 2016, **528**, 168-174.
50. MS Chatta, WLH Watkins, HS Gandhi, Three-way catalyst for automotive emission control and method of making the catalyst, US4992405. *US Patent* 1991.
51. F Tao and M Salmeron, *Science*, 2011, **331**, 171-174.
52. GA Somorjai, *Langmuir*, 1991, **7**, 3176-3182.
53. SD Senanayake, JT Sadowski, J Evans, S Kundu, S Agnoli, F Yang, *et al.*, *J. Phys. Chem. Lett.*, 2012, **3**, 839-843.
54. W Ding, S Li, G D Meitzner and E Iglesia, *J. Phys. Chem. B*, 2001, **105**, 506-513.
55. G Malta, SA Kondrat, SJ Freakley, CJ Davies, L Lu, S Dawson, *et al.*, *Science*, 2017, **355**, 1399-1403.
56. M Bron, D Teschner, A Knop-Gericke, B Steinhauer, A Scheybal, M Hävecker, *et al.*, *J. Catal.*, 2005, **234**, 37-47.
57. R Imbihl, RJ Behm, R Schlögl, *Phys. Chem. Chem. Phys.*, 2007, **9**, 3459-3459.
58. Diamond Light Source. 2016. Beamline Update: B07's ambient pressure soft X-ray beamline now available for users. [online] Available from: <https://www.diamond.ac.uk/Home/Corporate-Literature/newsletter/Spring2016/News/B07.html>. [Accessed 02 February 2019].
59. S Wang, H Sawada, Q Chen, GGD Han, C Allen, AI Kirkland, *et al.*, *ACS Nano*, 2017, **11**, 9057-9067.
60. MA Bañares, MO Guerrero-Pérez, JLG Fierro and GG Cortez, *J. Mater. Chem.*, 2002, **12**, 3337-3342.
61. MA Bañares and IE Wachs, *J. Raman Spectrosc.*, 2002, **33**, 359-380.
62. MO Guerrero-Pérez and MA Bañares, *Chem. Comm.*, 2002, DOI: 10.1039/b202556f, 1292-1293.
63. JW Ward, *J. Catal.*, 1968, **11**, 259-260.
64. JF Joly, N Zanier-Szydłowski, S Colin, F Raatz, J Saussey and JC Lavalley, *Catal. Today*, 1991, **9**, 31-38.
65. P Maetz, J Saussey, JC Lavalley and R Touroude, *J. Catal.*, 1994, **147**, 48-56.
66. IE Wachs, J-M Jehng, G Deo, BM Weckhuysen, VV Guliants, JB Benziger, *et al.*, *J. Catal.*, 1997, **170**, 75-88.

67. BS Clausen, G Steffensen, B Fabius, J Villadsen, R Feidenhans'l and H Topsøe, *J. Catal.*, 1991, **132**, 524-535.
68. D-J Liu and HJ Robota, *Catal. Lett.*, 1993, **21**, 291-301.
69. HN Rundle, *J. Res. Nat. Bur. Stand.*, 1964, **69C**.
70. MP Fuller and PR Griffiths, *Anal. Chem.*, 1978, **50**, 1906-1910.
71. JG Highfield, M Prairie and A Renken, *Catal. Today*, 1991, **9**, 39-46.
72. MA Banares, L Dauphin, V Calvoperez, TP Fehlner and EE Wolf, *J. Catal.*, 1995, **152**, 396-409.
73. BM Weckhuysen, AA Verberckmoes, J Debaere, K Ooms, I Langhans and RA Schoonheydt, *J. Mol. Catal. A-Chem*, 2000, **151**, 115-131.
74. BM Weckhuysen and RA Schoonheydt, *Catal. Today*, 1999, **49**, 441-451.
75. MA Newton and W van Beek, *Chem. Soc. Rev.*, 2010, **39**, 4845-4863.
76. JW Couves, JM Thomas, D Waller, RH Jones, AJ Dent, GE Derbyshire, *et al.*, *Nature*, 1991, **354**, 465.
77. G Sankar, PA Wright, S Natarajan, JM Thomas, GN Greaves, AJ Dent, *et al.*, *J. Phys. Chem.*, 1993, **97**, 9550-9554.
78. BS Clausen, L Gråbæk, G Steffensen, PL Hansen and H Topsøe, *Catal. Lett.*, 1993, **20**, 23-36.
79. JD Grunwaldt, AM Molenbroek, NY Topsøe, H Topsøe and BS Clausen, *J. Catal.*, 2000, **194**, 452-460.
80. IJ Shannon, T Maschmeyer, G Sankar, JM Thomas, RD Oldroyd, M Sheehy, *et al.*, *Catal. Lett.*, 1997, **44**, 23-27.
81. M Tromp, JRA Sietsma, JA van Bokhoven, GPF van Strijdonck, RJ van Haaren, AMJ van der Eerden, *et al.*, *Chem. Comm.*, 2003, DOI: 10.1039/b206758g, 128-129.
82. JG Mesu, AMJ van der Eerden, FMF de Groot and BM Weckhuysen, *J. Phys. Chem. B*, 2005, **109**, 4042-4047.
83. JG Mesu, AM Beale, FMF de Groot and BM Weckhuysen, *J. Phys. Chem. B*, 2006, **110**, 17671-17677.
84. M Bauer, G Heusel, S Mangold and H Bertagnolli, *J. Synchrotron Radiat.*, 2010, **17**, 273-279.
85. M Tromp, GPF van Strijdonck, SS van Berkel, A van den Hoogenband, MC Feiters, B de Bruin, *et al.*, *Organometallics*, 2010, **29**, 3085-3097.
86. AM Beale, AMJ van der Eerden, K Kervinen, MA Newton and BM Weckhuysen, *Chem. Comm.*, 2005, DOI: 10.1039/b504027b, 3015-3017.
87. SDM Jacques, O Leynaud, D Strusevich, P Stukas, P Barnes, G Sankar, *et al.*, *Catal. Today*, 2009, **145**, 204-212.
88. MA Newton, B Jyoti, AJ Dent, SG Fiddy and J Evans, *Chem. Comm.*, 2004, DOI: 10.1039/b405694a, 2382-2383.

89. MA Newton, AJ Dent, SG Fiddy, B Jyoti and J Evans, *Catal. Today*, 2007, **126**, 64-72.
90. MA Newton, AJ Dent, SG Fiddy, B Jyoti and J Evans, *Phys. Chem. Chem. Phys.*, 2007, **9**, 246-249.
91. MA Newton, *Top. Catal.*, 2009, **52**, 1410-1424.
92. A Kubacka, A Martínez-Arias, M Fernández-García and MA Newton, *Catal. Today*, 2009, **145**, 288-293.
93. E Becker, P-A Carlsson, L Kylhammar, MA Newton and M Skoglundh, *J. Phys. Chem. C*, 2011, **115**, 944-951.
94. C Kongmark, V Martis, A Rubbens, C Pirovano, A Löfberg, G Sankar, *et al.*, *Chem. Comm.*, 2009, DOI: 10.1039/b907935a, 4850-4852.
95. J Sá and J Szlachetko, *Catal. Lett.*, 2014, **144**, 197-203.
96. T Hussain, JL Llácer, BT Wimberly, JS Kieft and V Ramakrishnan, *Cell*, 2016, **167**, 133-144.e113.
97. R Frahm, *Nucl. Instrum. Meth. A*, 1988, **270**, 578-581.
98. R Frahm, *Physica B*, 1989, **158**, 342-343.
99. K Tomishige, K Asakura and Y Iwasawa, *Catal. Lett.*, 1993, **20**, 15-22.
100. C Prestipino, O Mathon, R Hino, A Beteva and S Pascarelli, *J. Synchrotron Radiat.*, 2011, **18**, 176-182.
101. AJ Dent, G Cibin, S Ramos, AD Smith, SM Scott, L Varandas, *et al.*, *J. Phys. Conf. Ser.*, 2009, **190**, 012039.
102. O Müller, M Nachtegaal, J Just, D Lützenkirchen-Hecht and R Frahm, *J. Synchrotron Radiat.*, 2016, **23**, 260-266.
103. RP Phizackerley, ZU Rek, GB Stephenson, SD Conradson, KO Hodgson, T Matsushita, *et al.*, *J. Appl. Crystallogr.*, 1983, **16**, 220-232.
104. GW Coulston, SR Bare, H Kung, K Birkeland, GK Bethke, R Harlow, *et al.*, *Science*, 1997, **275**, 191-193.
105. T Ressler, M Hagelstein, U Hatje and W Metz, *J. Phys. Chem. B*, 1997, **101**, 6680-6687.
106. WA Barletta, J Bisognano, JN Corlett, P Emma, Z Huang, KJ Kim, *et al.*, *Nucl. Instrum. Meth. A*, 2010, **618**, 69-96.
107. JMJ Madey, in *Reviews of Accelerator Science and Technology*, DOI: 10.1142/9789814340397_0001, pp. 1-12.
108. M Dell'Angela, T Anniyev, M Beye, R Coffee, A Föhlisch, J Gladh, *et al.*, *Science*, 2013, **339**, 1302-1305.
109. K Morgan, J Touitou, J-S Choi, C Coney, C Hardacre, JA Pihl, *et al.*, *ACS Catal.*, 2016, **6**, 1356-1381.
110. A Goguet, C Stewart, J Touitou and K Morgan, in *Advances in Chemical Engineering*, eds. A. G. Dixon, O. Deutschmann, Academic Press, 2017, vol. 50, pp. 131-160.

111. J Touitou, K Morgan, R Burch, C Hardacre and A Goguet, *Cat. Sci. Tech.*, 2012, **2**, 1811-1813.
112. J Touitou, R Burch, C Hardacre, C McManus, K Morgan, J Sa, *et al.*, *Analyst*, 2013, **138**, 2858-2862.

Chapter Two. Methods

2.1 Introduction

This chapter will cover the experimental details and theoretical principles behind the characterisation methods used in this study. The two techniques that are predominantly used in this study are x-ray absorption fine structure (XAFS) and diffuse reflectance infrared Fourier transformed spectroscopy (DRIFTS). The development of synchrotron radiation, spectroscopic instrumentation and data analysis techniques that have facilitated the *operando* spectroscopy experiments performed in this study will be outlined. Additional lab-based characterisation techniques that have been used to complement the results in this study will also be detailed.

2.2 Synchrotron Radiation

Synchrotron radiation has developed rapidly in the last 50 years and opened the possibility for a huge range of characterisation methods and scientific investigations that were previously not possible, or gave far inferior data quality when using lab based radiation sources. The main advantage of radiation from a synchrotron source is the increased brightness which is a measure of photon flux in a certain small bandwidth per surface area, per solid angle and has the units (photons/sec/mm²/mrad²/0.1%BW). X-rays from 3rd generation synchrotron light sources are 10¹² times brighter than from an x-ray tube,¹ which means that more photons of a given wavelength and direction are focussed into the same position in a given unit of time. The synchrotron x-rays are well-collimated, polarized and can be tuned to a range of different wavelengths allowing a high degree of control in spectroscopy and diffraction measurements.

A synchrotron consists of an electron gun, linear accelerator (LINAC), booster ring, storage ring, bending magnets, beamlines and end stations. The electron gun generates electrons from a high voltage cathode, which are then accelerated at the LINAC in 'bunches' for injection into the booster ring. The booster ring accelerates the electrons to $\sim 3 \times 10^8$ m s⁻¹, which are injected into the storage ring during a 'top up'. The electrons travel in circular motion around the storage ring, under vacuum ($\sim 10^{-9}$ mbar) at near relativistic speeds. Electromagnetic radiation is emitted when these high speed electrons are deflected by a magnetic field. Insertion devices located around the storage ring maintain the electron beam on its circular path and generate radiation as multiple thin beams that make up each individual beamline. The characteristics of each beamline is dictated by the details of the insertion device, which may use either a bending magnet (Figure 2.1a) or an undulator (Figure 2.1b). An undulator consists of a stack of small magnets alternating in polarity, which cause the electron beam to be accelerated back and forth in an 'undulating' trajectory. Radiation emitted at each bend in the trajectory interfere with one another to generate a highly

focused radiation beam. A bending magnet deflects the electrons from their straight path, to turn a corner of the storage ring. A wide beam of radiation is emitted from the bending magnet - tangentially to the plane of the electron beam. Radiation from a bending magnet has a broader range of energies and poorer focus than the beam emitted from an insertion device.

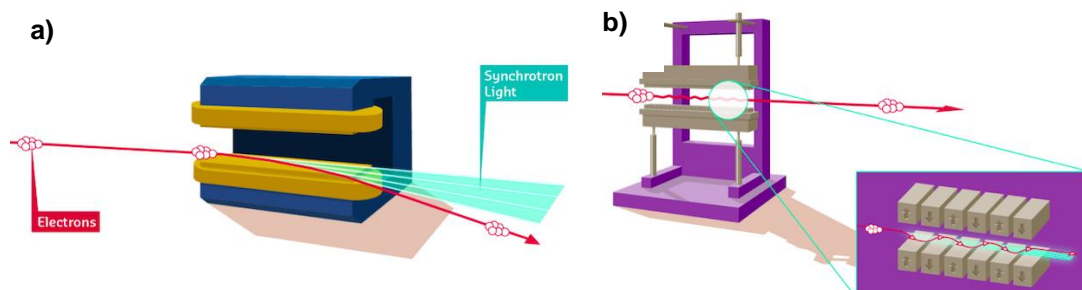


Figure 2.1. Schematic drawing of synchrotron insertion devices, showing path of accelerated electron beam (red) and emitted electromagnetic radiation (blue). **a)** bending magnet, **b)** undulator.

Typically a synchrotron beamline consists of an optics hutch, an experimental hutch and the control room. The radiation first reaches the optics hutch where it is filtered, focussed and tuned to the desired energy by a Si crystal monochromator. In this study, synchrotron radiation has been used as a source of tunable, collimated, high energy x-rays for XAFS spectroscopy of heterogeneous catalyst materials.

2.3 X-ray Absorption Fine Structure

2.3.1 Theory

X-ray absorption fine structure (XAFS) refers to the information obtained by the absorption of photons with x-ray energies at or close to the core-electron binding energy of the element of interest, which results in the transition of a core-electron to vacant states. Each XAFS spectrum measures the absorption coefficient, μ , as a function of x-ray energy, E . The value of μ is calculated from the x-ray flux transmitted through the sample, I_t , relative to the incident x-ray flux, I_0 , and is defined by the Beer Lambert relationship given in Equation 2.1, whereby x is the path length of x-rays through the sample.

$$I = I_0 e^{-\mu E x} \quad \text{Equation 2.1}$$

The attenuation of x-rays by an element depends on its atomic number Z , atomic mass A , and the incident x-ray energy, E , as Equation 2.2. Where ρ is the density of that element in the measured sample. The XAFS spectrum is an averaged signal combining information from all atoms of the selected element within the x-ray path length through the sample.

$$\mu = \frac{\rho Z^4}{A E^3} \quad \text{Equation 2.2}$$

At most x-ray energies, μ is inversely proportional to the value of E , however, when E approaches the binding energy of a core-electron within the sample, there is a sharp increase in μ due to absorption of the x-ray photon by the core-electron. Absorption of the incident photon can result in transition of the core-electron to a vacant atomic or valence orbital, or emission of that electron from the absorbing atom into the continuum (Figure 2.2). This sharp increase in μ is referred to as the 'edge' energy, E_0 , which is characteristic of the element and electronic properties of the absorbing atom. The absorption edges are conventionally named according to the principle quantum number, n , of the energy level from which the core electron is excited, detailed in Table 2.1.

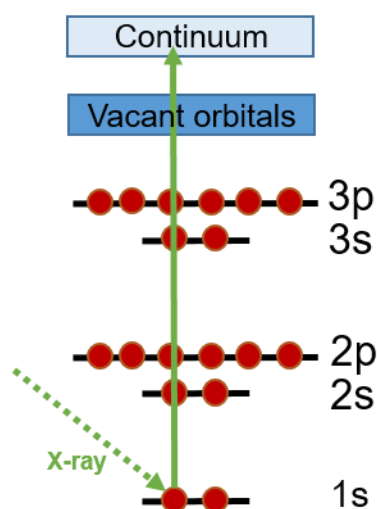


Table 2.1. Conventional names of x-ray absorption edges and the corresponding orbitals of the excited core electron.

Absorption edge	Orbital	Quantum number
K	1s	$n = 1, l = 0, j = 1/2$
L ₁	2s	$n = 2, l = 0, j = 1/2$
L ₂	2p _{1/2}	$n = 2, l = 1, j = 1/2$
L ₃	2p _{3/2}	$n = 2, l = 1, j = 3/2$

Figure 2.2. Energy level diagram showing the absorption of an x-ray photon at the K-edge to result in the excitation of a core electron to the continuum.

The XAFS spectrum can be divided into two parts; the x-ray absorption near-edge spectrum (XANES) and the extended x-ray absorption fine structure (EXAFS). The region of the x-ray absorption spectrum from just before the edge to 50 eV past the edge is called the x-ray absorption near-edge spectrum (XANES). For example, the Pd K-edge XAFS of Pd foil is shown in Figure 2.3a which is annotated with the pre-edge region (A), the XANES region (B) and the EXAFS region (C). The value of E_0 is taken as the maximum of the first derivative, E/E_0 , (Figure 2.3b).

The XANES region gives information for the empty density of states of the absorbing atom within the measured sample – provided that the electronic transition is allowed by dipole selection rules. The dipole selection rules state that transitions of a core electron to a vacant state may only occur if $\Delta l = \pm 1$. Exceptions to this rule occur when there is significant orbital mixing or an allowed electric quadrupole transition.² The EXAFS region gives information for the local atomic environment surrounding the absorbing atoms in the sample. At incident x-ray energies above the edge energy,

$h\nu > E_0$, the core-electron absorbs sufficient energy to be ejected from the absorbing atom with kinetic energy, E_{kin} , as defined by Equation 2.3.

$$E_{kin} = h\nu - E_0 \quad \text{Equation 2.3}$$

Where h is Planck's constant and ν is the frequency of the incident x-ray.

The outgoing photoelectron is described as a spherical wave function, with wavelength $\lambda = 2\pi/k$, and wave vector, k , defined by:

$$k = \sqrt{\left[\left(\frac{8\pi^2 m_e}{h^2}\right)(h\nu - E_0)\right]} \quad \text{Equation 2.4}$$

Where m_e is the electron mass.

The outgoing photoelectron wave can experience backscattering from electron density of surrounding neighbouring atoms, which gives rise to oscillations in the extended region of the EXAFS spectrum. The nature of these oscillations therefore depends on the number and type of neighbouring atoms surrounding the absorbing atoms. In order to interpret the EXAFS region to obtain information about the local atomic structure, the EXAFS fine structure function, $\chi(E)$, should be obtained by subtracting a smooth background function, $\mu_0(E)$ which represents the absorption of the isolated atom. The normalised EXAFS are given by

$$X(E) = \frac{\mu(E) - \mu_0(E)}{\Delta\mu_0(E)} \quad \text{Equation 2.5}$$

The normalised EXAFS, plotted as a function of k (Figure 2.3c) can then be interpreted by considering the amplitude and phase of the oscillations, as defined by the EXAFS equation

$$X(k) = \sum_j \frac{N_j f_j(k) e^{-2k^2 \sigma_j^2}}{k R_j^2} \sin[2kR_j + \delta_j(k)] \quad \text{Equation 2.6}$$

Which is a sum of all the neighbouring atoms, j , that contribute to the EXAFS oscillations. Where $\frac{N_j f_j(k) e^{-2k^2 \sigma_j^2}}{k R_j^2}$ defines the amplitude, and $[2kR_j + \delta_j(k)]$ defines the phase of the oscillations. $f_j(k)$ and $\delta_j(k)$ are scattering properties of the atomic neighbour, j . N_j is the number of neighbouring atoms found at the defined radial distance R_j from the absorbing atom. σ_j^2 is the EXAFS Debye-Waller factor which is a measure of disorder that accounts for the vibrational displacement of the neighbouring atoms. The scattering contribution from neighbouring atoms at greater radial distances can be emphasised by multiplying $\chi(E)$ by a factor of k^n , where n is generally 1 to 3. By performing a Fourier transform of the EXAFS data, the backscattering from near atomic neighbours is displayed as a function of real space, R (Figure 2.3d).

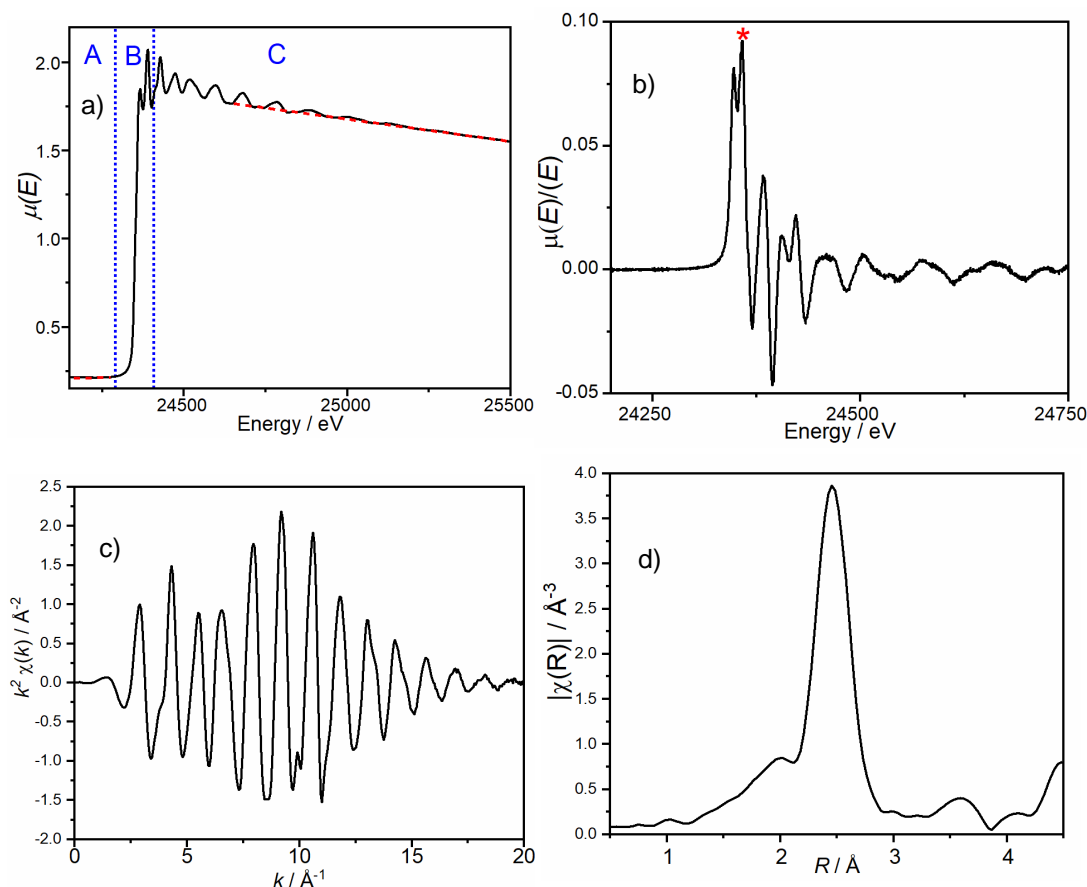


Figure 2.3. Pd K-edge XAFS data of Pd foil. **a)** $\mu(E)$ plotted as a function of energy, annotated to show the pre-edge region (A), the XANES region (B) and the EXAFS region (C). The pre-edge and post-edge lines used to subtract the background function $\mu(E_0)$ are plotted in red dashed lines. **b)** First derivative of $\mu(E)/E$ plotted as a function of energy, annotated with an asterisk to show the position of E_0 . **c)** EXAFS fine structure with k -weighting of 2 plotted as a function of wavenumber, k . **d)** Fourier transformed EXAFS data plotted as a function of real space, R .

An appropriate fitting model can be constructed by using a sum of multiple scattering components with scattering properties $f_j(k)$ and $\delta_j(k)$ to obtain values of N_j , R_j and hence interpret the average local atomic structure surrounding the absorbing atom. The example shown in Figure 2.4 is the Fourier transformed Pd K-edge EXAFS data of Pd foil, fitted with a sum of two scattering paths Pd-Pd1 and Pd-Pd2. The fitting parameters N and R for these scattering paths are set to the values known for metallic Pd fcc crystal structure. (Pd-Pd1 $N = 12$, $R = 2.73$ Å; Pd-Pd2 $N = 6$, $R = 3.86$ Å.) The imaginary part of the Fourier transformed EXAFS is often used in addition to the magnitude part, to help fit complex atomic structures.

2.3.2 XAFS Data Acquisition

The majority of the XAFS spectra acquired in this work were performed in transmission mode (beamline schematic shown in Figure 2.5), whereby the sample is placed in the x-ray path between two ion chambers. The ion chambers are filled with a gas (typically Ar, He or N_2) that is ionised by incoming x-ray photons. The ionised gas molecules

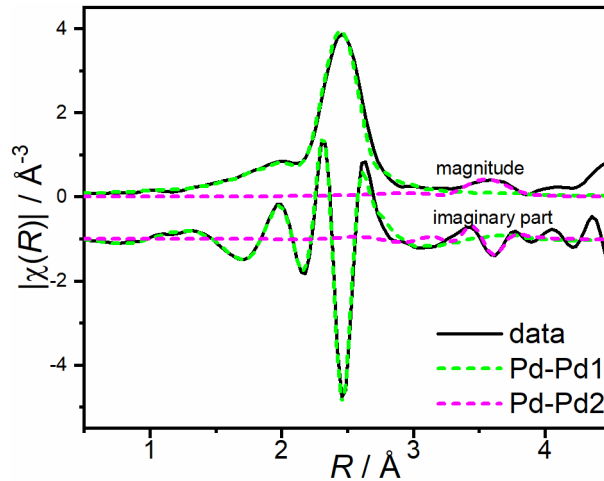


Figure 2.4. Magnitude and imaginary parts of Fourier transformed Pd K-edge EXAFS data of Pd foil, plotted as a function of R , showing scattering paths Pd-Pd1 and Pd-Pd2 due to neighbouring Pd atoms at 2.73 Å and 3.86 Å, respectively.

travel towards an electrode generating a current that is proportional to the intensity of incoming radiation. The ion chambers are positioned on the beamline to detect the intensity of x-rays before (I_0) and after (I) transmission through the sample, for acquisition of the XAFS spectrum. The XAFS spectrum of a reference sample can be collected simultaneously by positioning a selected reference sample (eg. metal foil) between the second ion chamber (I_i) and a third ion chamber (I_r). The known edge jump, E_0 , of the reference XAFS spectrum can be used to calibrate the x-ray energies.

The photon energy of the x-ray beam is controlled by using a double crystal monochromator. Diffraction of the x-ray beam from the Si crystal monochromator follows Bragg's law (Equation 2.7). The wavelength of the diffracted x-ray beam, λ , therefore depends on the angle of the crystal with respect to the incident beam, θ , and the atomic spacing within the polished crystal, d . Depending on the energy range required, this is usually a Si(111) crystal ($\sim 2 - 20$ KeV) or Si(311) crystal ($\sim 4 - 35$ KeV). The purpose of the monochromator is to scan through a range of wavelengths that make up the spectral range of the desired XAFS spectrum.

$$n\lambda = 2d \sin \theta \quad \text{Equation 2.7}$$

The entrance and exit slits positioned before and after the monochromator control the size and shape of the resulting monochromatic beam. In a standard data acquisition mode, the angle of the crystal is increased in a step-by-step motion to scan through the required energy range of the XAFS spectrum.

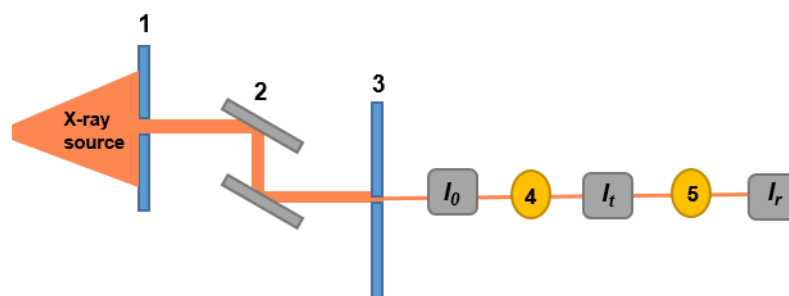


Figure 2.5. Schematic drawing of beamline set-up for XAFS data acquisition in transmission mode. Figure shows (1) the entrance slit, (2) the double crystal monochromator, (3) the exit slit, (4) the sample position, (5) the reference sample position and the ion chamber detectors I_0 , I_t and I_r .

For dilute samples, or low edge energy measurements, where the XAFS signal is only a small fraction of the total x-ray absorption, the absorption coefficient, $\mu(E)$, may be measured in fluorescence mode. X-ray fluorescence results from the relaxation of the excited state after an absorption event. A core hole, created by the excitation of the core electron during absorption, can be filled by decay of electrons from a higher core energy level. The core hole in the excited state exists only for a short time, typically a few femtoseconds, before the decay process. Relaxation of higher energy electrons into the core hole results in the emission of photons with well-defined energies, known as the fluorescence lines. The intensity of a selected fluorescence line, I_f , is measured by a detector positioned at a 90° trajectory from the incident beam at the sample, and can be used to plot the energy dependence of the absorption coefficient, $\mu(E)$.

2.3.3 Quick-EXAFS (QEXAFS)

The QEXAFS set-up allows for faster acquisition times of EXAFS spectra due to fast scanning of a continuously moving monochromator. The double crystal monochromator is mounted to a goniometer and driven by stepper motors to move the monochromator at a constant speed through the complete range of angles required to achieve the spectral range of x-ray energies.^{3,4} The energy and time resolution of the XAFS spectra is defined by the detector read-out time, and the achievable angular velocity of the moving monochromator. QEXAFS spectra can be acquired during the forward and reverse motion of the monochromator, for quickly scanning multiple spectra with minimal downtime between scans, eg. QEXAFS acquisition at beamline X10DA (SuperXAS), Swiss Light Source at its highest speed achieves a frequency of 50 Hz, meaning that 100 spectra (collected in both the forward and reverse direction) can be collected each second.⁵ The disadvantage of EXAFS data acquisition in the scanning mode, including QEXAFS, is that changes to the sample during the scan time will disproportionately affect the quality of the resulting spectrum. Additionally, small changes in the beam position during a scan are a problem for spatially resolved measurements.

2.3.4 Energy Dispersive X-ray Absorption Fine Structure (EDE-XAFS)

The EDE-XAFS approach is different from the scanning XAFS experiments described above in that the entire energy range of the EXAFS spectrum is exposed to the sample in a single shot, rather than scanning through the individual energies in a stepwise manner. A curved crystal operating in the Bragg or Laue condition is used to spatially separate the energies of a polychromatic beam.^{6, 7} For the EDE measurements performed in this work at the dispersive beamline I20-EDE at Diamond light source, the polychromatic 'pink' x-ray beam at the Pd K-edge spectral energy range was achieved by diffraction from a curved Si(311) crystal cut, operating in the Bragg condition.^{8, 9} The beamline schematic for EDE-XAFS set-up in Figure 2.6 shows the path of the x-ray beam from the synchrotron source. The trajectory of the x-rays of each wavelength from the polychromator intersect at a single focal point, which is where the sample was positioned for measurements. The cross section of the spot size at the focal point is on the scale of micrometres, e.g. the minimum spot size achieved at I20-EDE is 30 μm x 100 μm .⁹ A position sensitive detector located at the other side of the sample is used to detect the x-ray intensity of each wavelength of the transmitted polychromatic beam. Typically, the position sensitive detector at EDE beamlines uses a charge coupled device (CCD), which is able to measure the photon intensity at each pixel on the screen and translate the positional information into photon intensity as a function of energy.¹⁰ The acquisition time of the EDE-XAFS spectrum is then determined by the saturation time of each pixel in the CCD camera, the amount of spectra needed to generate acceptable signal-to-noise, and the read-out time of the detector, which can range from microseconds to seconds.

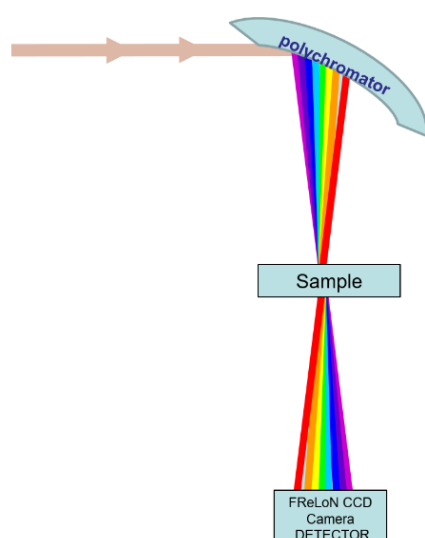


Figure 2.6. Schematic drawing of the x-ray path at an EDE-EXAFS beamline, showing the dispersion from the polychromator, transmission through the sample to be measured and detection at the CCD camera.

There are experimental challenges associated with performing successful EDE-XAFS measurements. Firstly, the high photon flux of the polychromatic beam at the focal point on the sample means that the sample is more vulnerable to beam damage. The stability of the sample in the beam must be checked before time-resolved measurements. Secondly, the intensity of the beam before, I_0 , and after transmission through the sample, I_t , cannot be measured simultaneously in an EDE-XAFS setup. The value of I_0 must therefore be measured at a different time point, and is sensitive to beam instability. In order to reduce the effect of beam instabilities, an average value of I_0 may be calculated from two I_0 measurements collected before and after the time-resolved I_t measurements. For high data quality, the measurement environment for I_0 should be as close as possible to the sample environment such that the x-ray absorption and scattering from materials other than the element of interest in the sample can be accounted for.

2.3.5 XAFS Data Analysis

Normalisation and processing of XAFS data was performed using the IFEFFIT software with the Horae package (Athena and Artemis).¹¹ Raw XAFS spectra were opened in Athena, using measured values of E , I_t , I_r and I_0 . The value of E_0 was set as the maximum in the plot of the first derivative ($\mu(E)/E$). Values of E were calibrated by aligning the E_0 of the reference spectrum, $\ln(I_t/I_r)$, to the known edge energy, and shifting all E values of the measured spectra by the same value. For *ex situ* measurements, or *in situ* measurements under static conditions, the multiple acquisitions of the same sample were merged to obtain an averaged spectrum with improved data quality. A smooth pre-edge function was subtracted from $\mu(E)$ to remove any instrumental background and a smooth post-edge background spline function was subtracted to remove absorption of the isolated atom, $\mu(E_0)$. The EXAFS function was plotted, applying a k -weighting of 2 to obtain suitable emphasis of scattering contributions from atomic neighbours with both low and high masses.¹² The EXAFS function was truncated at an appropriate range and the Fourier transform was performed across a defined k range.

Artemis was used to make appropriate fitting models to the Fourier transformed EXAFS data. Artemis uses FEFF calculations to calculate the scattering amplitude and phase of different coordination shells of known compounds.¹³ These theoretical scattering components were used to construct a model to best fit the measured EXAFS data, obtaining values of N and R for different atomic neighbours.

For the large volume of data collected during time-resolved EDE-XAFS measurements, the Data Analysis Workbench (DAWN) was used to view and process a collection of data.¹⁴ Firstly, any glitches in the data were removed, then the spectra were cropped

to 24030 – 35380 eV, calibrated and normalised in a batch process, using the same parameters as described above.

2.4 Infrared (IR) Spectroscopy

Vibrations in molecules or in solid lattices can be excited by the absorption of photons with frequencies, ν , in the mid-infrared range (400 – 4000 cm^{-1}). The vibrations of atoms within a molecule can be approximated by the harmonic oscillator (Equation 2.8), in which $V(r)$ is the potential, r is the distance between the vibrating atoms, r_{eq} is the equilibrium distance between the atoms and k is the force constant of the vibrating bond.

$$V(r) = \frac{1}{2}k(r - r_{eq})^2 \quad \text{Equation 2.8}$$

The vibrational frequency is related to the force constant of the vibrating bond, k , and the reduced mass of the vibrating atoms, μ , by Equation 2.9.

$$\nu = \frac{1}{2\pi} \sqrt{\frac{k}{\mu}} \quad \text{Equation 2.9}$$

Thus, vibrational frequencies increase with increasing bond strength and decreasing mass of the vibrating atoms. Molecular vibrations may only be excited by the absorption of a photon if the resulting transition between vibrational levels obeys the selection rules. Allowed transitions are those for which the vibrational quantum number changes by ± 1 , and it is required that the dipole moment of the molecule must change during the vibration. The different types of vibrations of molecules are stretches, bending in one plane (rock, twist or wag), bending out of plane and torsion vibrations. The typical absorption bands in IR spectra of heterogeneous catalysts can be divided into three regions; the X-H region (4000 - 2500 cm^{-1}), C≡O region (2500 – 2000 cm^{-1}) and the fingerprint region (1500 – 500 cm^{-1}). IR spectroscopy can be performed in different modes. In this work, the IR spectroscopy has been performed in transmission mode and diffuse reflectance mode.

All IR spectra acquired in this work made use of Fourier transform spectroscopy which refers to the method of data collection using a Michelson interferometer.¹⁵ The Michelson interferometer, schematic shown in Figure 2.7, consists of a beamsplitter and two perpendicular mirrors; one mirror is stationary and the other is able to move in a smooth continuous motion. The beamsplitter splits the collimated IR beam into two paths which are directed towards the stationary and moving mirror, respectively. As the movable mirror moves back and forth, the path difference of the reflected beams - and thus the interference upon recombination - creates a sinusoidal signal called an interferogram. The interferogram contains information about the IR absorption intensities at each wavelength, which can be transformed into the IR absorption spectrum by Fourier transformation. The Fourier transform spectroscopy allows for

faster acquisition times on the millisecond timescale, which is essential for following time-resolved spectroscopy of dynamic catalytic processes, and for synchronising with time-resolved XAFS spectroscopy.

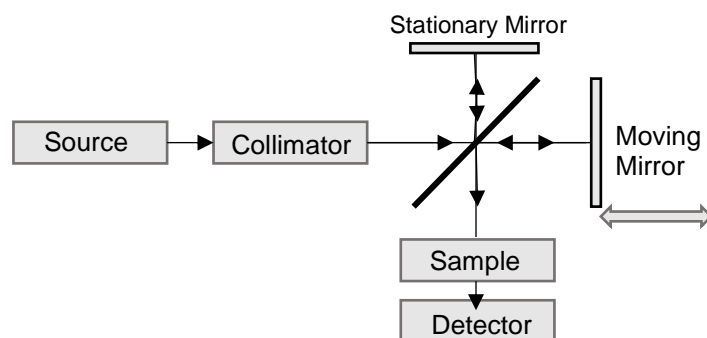


Figure 2.7. Schematic drawing of the parts making up the Michelson interferometer for Fourier transform IR spectroscopy.

2.4.1 Diffuse reflectance infrared Fourier transform spectroscopy (DRIFTS)

For measurements in the diffuse reflectance mode, strongly absorbing samples can be investigated as a powder as the diffusely scattered IR radiation from the sample surface is collected by an ellipsoidal mirror and focussed towards the detector. The Harrick 'praying mantis' accessory (Figure 2.8) has been utilised in this work, for focussing the IR beam to the sample and the reflected beam from the sample to the detector.¹⁶ The praying mantis optics were installed inside the Agilent Carey 680 Fourier transform IR spectrometer, for DRIFTS measurements using a KBr beamsplitter and a mercury-cadmium-telluride semiconducting material (MCT) as the detector.

The sample environment for DRIFTS measurements used a Harrick high temperature reaction chamber. The Harrick reaction chamber contains the sample in a cup in the centre of a dome shaped reactor, with canted ZnSe windows to allow the entry and exit of IR radiation to and from the surface of the sample. The reactor is fitted with a heating rod beneath the sample cup, and a K-type thermocouple inside the sample cup to control the temperature of the sample up to temperatures of 900°C.¹⁷ Three stainless steel tube fittings soldered to the reaction chamber allow for evacuating the chamber and connecting to inlet and outlet gas lines. Two other inlet and outlet fittings are provided for a water cooling circulation that cools the exterior stainless steel frame of the reactor vessel.

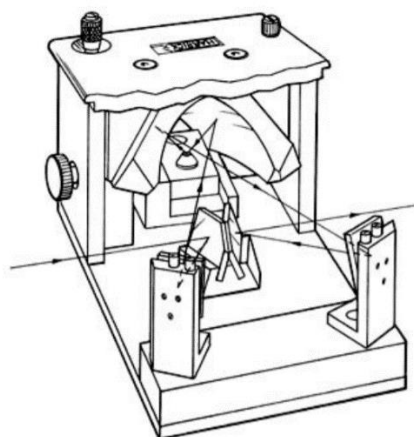


Figure 2.8. Schematic drawing of Harrick 'praying mantis' accessory for DRIFTS measurements. Image courtesy of Harrick Scientific.¹⁶

2.4.2 Transmission FTIR

For transmission IR, the sample (10 – 100 mg) was pressed into a thin, self-supporting disk (1.3 cm²). The mass of sample used to make the pellet was determined by the absorptivity of the sample, such that there was sufficient transmission of IR intensity through the sample to the detector. The sample pellet was mounted into the Harrick transmission accessory installed within the FTIR spectrometer. The Harrick transmission accessory uses two KBr windows either side of the sample to allow the entry and exit of the IR beam. A heating rod and K-type thermocouple inserted inside the chamber are used to control the sample temperature up to 350°C, and inlet and outlet gas lines allow introducing a controlled gas environment.

2.5 Mass Spectrometry (MS)

Mass spectrometry was used to analyse gas mixtures from the exhaust of the catalytic reactor, identifying the reactants and products of the catalytic reaction and quantifying the catalytic activity. The mass spectrometer used for the analysis in this thesis was a Hiden QGA mass spectrometer. A heated capillary was used to direct a small sample (~25 cm³ min⁻¹) of the exhaust gas mixture from the reactor outlet to the mass spectrometer. Inside the mass spectrometer, the gas mixture entered a vacuum (~10⁻⁶ mbar) where it was ionised and then accelerated towards the mass analyser. The mass analyser used a quadrupole (Figure 2.9), which causes the ions to travel in sinusoidal pathways bringing them in and out of focus with the detector depending on their mass-to-charge (m/z) value. The mass spectrometer was used to continuously scan for a list of programmed m/z values, with a time resolution of ~2 seconds between each scan. The generated current at the detector was calibrated using controlled concentrations of known gas for quantitative analysis of the gas mixture.

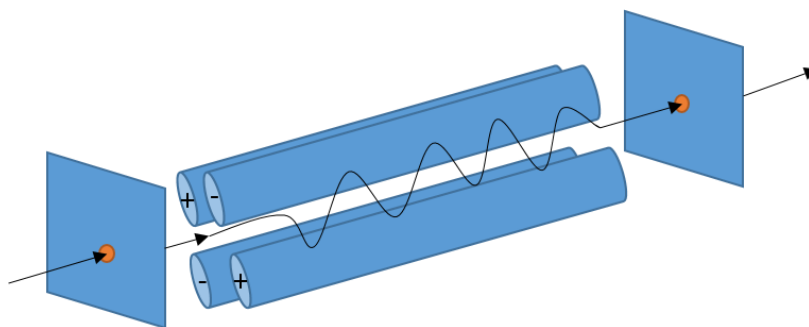


Figure 2.9. Schematic drawing of the quadrupole mass analyser within the mass spectrometer. The sinusoidal pathway of an ion within the sample is shown by the black arrow.

2.6 Combined XAFS/DRIFTS/MS Set-up

In this study the combination of XAFS and DRIFTS spectroscopy has been applied to investigate heterogeneous catalytic systems. In order to couple both spectroscopic techniques at the same sample at the same time, careful experimental set-up was required to align both the x-ray and IR beams in the correct geometry for simultaneous XAFS and DRIFTS spectroscopy. Additionally, gas lines to and from the sample environment, a heater, thermocouple and mass spectrometer were required for *in situ* and *operando* measurements under controlled reaction environments. A schematic drawing of the experimental setup is shown in Figure 2.10. A portable gas trolley, able to safely secure gas cylinders, was fitted with Brookes mass flow controllers (MFCs) and a Valco 2-way switching valve. This set-up allowed for the controlled flow of 6 different gases via the 6 MFCs to two separate mixing chambers (A and B). The mixing chambers were connected to the single switching valve (C) to allow for fast switching between two different gas mixtures. One gas line from the switching valve was used to send gases to the sample in the reaction chamber, and the second gas line from the switching valve was used as a bypass straight to vent. The gas lines used 1/8" stainless steel tubing, which could be heated up to 200°C using a flexible heating tape. The Harrick Da Vinci arm accessory with 'praying mantis' optics was used to redirect the IR beam from the IR spectrometer to the sample, which was positioned just outside the IR spectrometer in the x-ray beam. The entire optical path within the Da Vinci arm was purged with dry N₂ to avoid absorption of IR by IR active gas molecules in the air. The sample was contained in a reaction chamber beneath the Da Vinci arm accessory, which allowed for focussing of the IR beam at the surface of the sample and transmission of the x-ray beam through the sample.

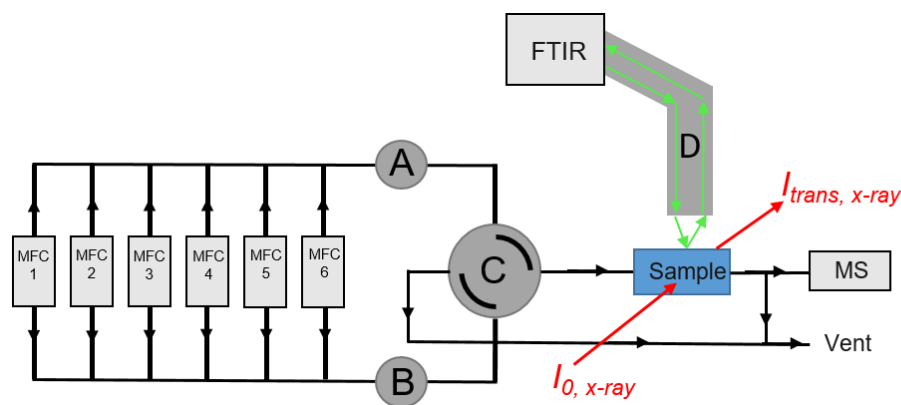


Figure 2.10. Schematic drawing of experimental set-up for in situ combined XAFS/DRIFTS/MS, showing gas lines linking the 6 MFCs, mixing chambers A and B, switching valve C, the sample environment and the mass spectrometer. Path of IR beam through the Da Vinci arm accessory D is shown by green arrows. Path of x-ray beam through the sample is shown by red arrows.

The specific sample environments for the combined XAFS/DRIFTS measurements are detailed in Chapter 5. The combined XAFS/DRIFTS/MS experiments reported in Chapters 3 and 4 used the modified Harrick high temperature XAFS/DRIFTS reaction chamber, whereas the spatially resolved XAFS/DRIFTS/MS experiment reported in Chapter 6 used a new reactor design.

2.7 Additional Characterisation Techniques

In order to validate the results obtained by combined XAFS/DRIFTS measurements in this study, additional characterisation techniques were employed. These largely consisted of transmission electron microscopy (TEM) to obtain images of the supported nanoparticle catalysts, x-ray photoelectron spectroscopy (XPS) to confirm the chemical composition of the material, and x-ray diffraction (XRD) to uncover the bulk crystalline components of the supported catalyst.

2.7.1 Transmission Electron Microscopy (TEM)

TEM is used to obtain high resolution images of thin material samples, thus making it a useful tool to observe the particle size and morphology of supported metal nanoparticle catalyst materials. The TEM microscope operates upon the same basic principles as a classic optical microscope but using a beam of electrons instead of visible light. The resolution achieved by TEM is governed by the de Broglie wavelength of the accelerated electron beam, given by Equation 2.10, where m_e is the mass of the electron and v is the velocity of the accelerated electron beam. The wavelength of the electron beam, λ_e , is smaller than the wavelength of visible light and so is able to resolve atomic structures on the Å length scale.

$$\lambda_e = \frac{h}{m_e v} \quad \text{Equation 2.10}$$

The path of the electron beam through the TEM microscope is shown in Figure 2.11. An electron gun (hot filament) is used to emit a beam of high energy electrons into the TEM column. The speed of the emitted electron beam is controlled by the voltage applied to the filament (80 – 200 KeV), and the TEM column is maintained under vacuum (10^{-5} mbar) so that the electron beam is not slowed down by collision with gas molecules. The electron beam travels through the column, passing through a series of electromagnetic lenses which focus the beam onto the sample. The electron beam is transmitted through the sample, depending on the electron transparency and thickness of the material. The transmitted electron beam then passes through a projection lens which projects the beam onto a fluorescent screen to be viewed by the user. The projected image can alternatively be captured digitally by installing a CCD camera in place of the fluorescent screen. The TEM images in this work were performed using a JEOL JEM 2100 microscope located at the Research Complex at Harwell.

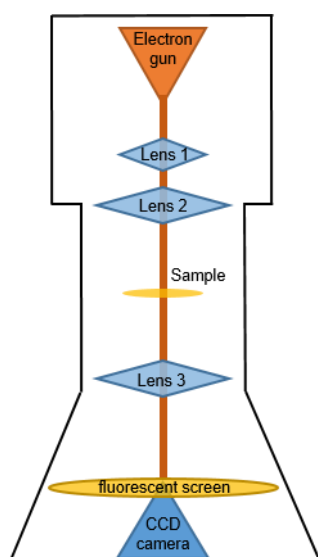


Figure 2.11. Simple diagram showing the components of a TEM microscope contained within a vacuum column; electron gun, focussing lenses, fluorescent screen and CCD camera.

The most common imaging mode is bright field (BF) imaging which uses the unscattered, transmitted electron beam through the sample to construct an inverted 2D image of the sample. The transmission of the electron beam through the sample depends on the absorption coefficient of the different components within the sample, so more absorbing components will appear as darker regions in the projected image and less absorbing components as brighter regions. In the dark field (DF) imaging mode, an image is constructed from the diffracted electron beam which is collected at the objective aperture and then magnified at the viewing screen. Images collected in the DF mode will show brighter regions corresponding to more crystalline components of the sample, which are contrasted against a dark background. The TEM images in this study were collected in the BF mode.

2.7.2 X-ray Photoelectron Spectroscopy (XPS)

XPS is used to investigate the chemical composition of surfaces by measuring the kinetic energy of photoelectrons emitted as a result of the photoelectric effect. The photoelectric effect, as described by Equation 2.3, is the phenomenon by which electrons within a material absorb x-ray radiation with sufficient energy, $h\nu$, to overcome the electron binding energy, E_0 , and be ejected as a photoelectron with kinetic energy, E_{kin} . The electron binding energy is the difference in energy between the initial and final states after emission of the photoelectron. Each element has a characteristic set of binding energies, which may be shifted depending on its chemical environment within the sample. Hence the XPS spectrum gives information for the elemental composition and oxidation state of elements within the sample.

Each XPS spectrum is obtained by irradiating the sample with a monochromatic x-ray beam and measuring the kinetic energy of the emitted photoelectrons. An additional term for the spectrometer work function, φ_{sp} , is often included in the calculation of binding energies from XPS measurements. This φ_{sp} term accounts for the energy cost in travelling from the sample to the analyser of the spectrometer. XPS spectra can be acquired using a lab-source spectrometer, which typically uses x-rays from a tube source of Mg K α (1253.6 eV) or Al K α (1486.6 eV). XPS spectra acquired at a synchrotron have the advantage of being able to rapidly switch between different monochromatic x-ray beams. Due to the poor penetrating power of the emitted photoelectrons, only photoelectrons from the surface (< 6 nm) will have sufficient kinetic energy to reach the detector, thus XPS is a surface sensitive technique.

Each XPS spectrum will display a range of peaks for photoelectrons emitted from different atoms and different energy levels within each atom. As well as these emitted photoelectrons, relaxation of electrons from higher energy orbitals to fill the core hole of the excited ions results in the emission of Auger electrons (Figure 2.12). The emitted Auger electrons that have sufficient kinetic energy to reach the detector will also be observed as peaks in the XPS spectrum but with low kinetic energies, representing the difference in energy between the initial ion and the doubly charged final ion.

The low penetrating power of emitted photoelectrons and Auger electrons means that the sample must be contained within ultra-high vacuum. The sample is prepared as a self-supported pellet or as a wash coat on a Si wafer, and mounted within the vacuum chamber of the XPS spectrometer. Positive charge can build up within electrically insulating samples due to continual loss of electrons from the sample, resulting in a shift of all measured peaks in the XPS spectrum by the same amount to higher binding energies.¹⁸ This can be corrected for by calibrating the entire spectrum to a known peak for a particular element within the sample. Electrically conductive samples do not suffer

the same charging effects as they are able to receive current through the sample holder which acts to neutralise the positive charge.

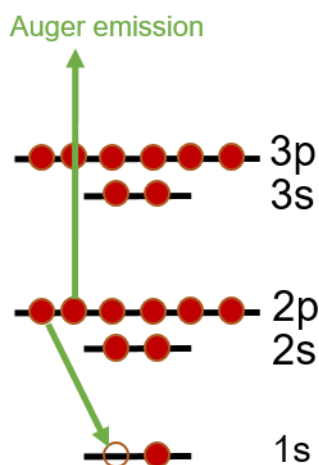


Figure 2.12. Energy level diagram showing the emission of an Auger electron following the relaxation of an electron from a higher energy orbital to fill the core-hole of the excited ion.

2.7.3 X-ray Diffraction (XRD)

XRD is able to give information about the crystalline structure of a material by studying the scattering of monochromatic x-ray waves incident at the sample. The periodically spaced atoms within a crystalline sample act as a 3D diffraction grating to the x-ray beam in accordance with Bragg's law (Equation 2.7). When Bragg's law is satisfied (Figure 2.13), the atomic spacing within the crystal lattice, d , causes constructive interference of the x-ray waves of wavelength, λ , to give rise to diffraction peaks at a defined diffraction angle, θ . The measured XRD diffraction pattern is a plot of the intensity of the diffracted beam at the detector as a function of incident angle, θ .

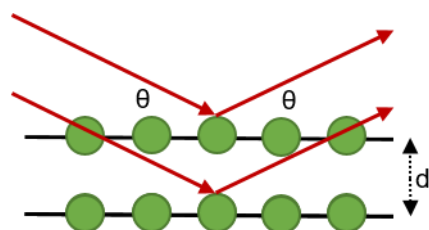


Figure 2.13. Schematic diagram of x-ray beams that are diffracted by lattice planes of separation distance, d , within a crystalline material that satisfy the Bragg Law at an incident angle, θ .

The crystalline phases present in a material can be identified by 'fingerprint' comparison of the measured XRD pattern with those of reference compounds. Often the measured sample will contain a mixture of multiple crystalline phases, and so comparison with many reference compounds is required. The precise atomic structure of a sample can be achieved by Rietveld refinement, which uses a least-squares refinement method to fit the position and intensity of all diffraction peaks within the pattern to a calculated model.¹⁹

The Scherrer equation (Equation 2.11), describes the relationship between the broadening of XRD diffraction peaks and the crystallite size.²⁰ The smaller the crystallite size, D_p , the increased broadening of the diffraction peaks, β . The constant of proportionality, k , depends on how the width is determined, the shape of the crystal and the size distribution.²¹ The value of k for full width half maximum (FWHM) of diffraction peaks from spherical crystals with cubic symmetry is 0.94. At crystallite sizes below a certain value, the diffraction peaks will be so broad that they cannot be determined. This makes XRD unsuitable for studying metal nanoparticle catalysts that have particles sizes below the detectable limit, or catalyst materials with largely amorphous character. Moreover, for supported metal nanoparticle catalysts, the largely crystalline component of the support material can dominate the XRD diffraction pattern, making it difficult to observe diffraction peaks of the active catalytic component.

$$D_p = \frac{k\lambda}{\beta \cos \theta} \quad \text{Equation 2.11}$$

2.8 Catalyst Preparation

The supported metal nanoparticle catalysts prepared in this work used an incipient wetness impregnation method, detailed and investigated in Chapter 3. The metal precursors and commercial metal oxide supports used to prepare the catalysts were supplied by Johnson Matthey Technology Centre, Sonning Common.

2.9 References

1. ESRF. **2018**. ESRF in brief and key figures [online]. Available from: <https://www.esrf.eu/about/press-room/intro-esrf-journalists>. [Accessed 02 February 2019].
2. T Yamamoto, *X-Ray Spectrometry*, 2008, **37**, 572-584.
3. R Frahm, *Nucl. Instrum. Meth. A*, 1988, **270**, 578-581.
4. AJ Dent, G Cibin, S Ramos, AD Smith, SM Scott, L Varandas, *et al.*, *J. Phys. Conf. Ser.*, 2009, **190**, 012039.
5. O Muller, M Nachtegaal, J Just, D Lutzenkirchen-Hecht and R Frahm, *J. Synchrotron Radiat.*, 2016, **23**, 260-266.
6. J Pellicer-Porres, A San Miguel and A Fontaine, *J. Synchrotron Radiat.*, 1998, **5**, 1250-1257.
7. A San-Miguel, M Hagelstein, J Borrel, G Marot and M Renier, *J. Synchrotron Radiat.*, 1998, **5**, 1396-1397.
8. A Fontaine, E Dartyge, JP Itie, A Jucha, A Polian, H Tolentino, *et al.*, Time-resolved X-ray absorption spectroscopy using an energy dispersive optics: Strengths and limitations. *Synchrotron Radiation in Chemistry and Biology III*. Berlin, Heidelberg, 1989.
9. S Diaz-Moreno, M Amboage, M Basham, R Boada, NE Bricknell, G Cibin, *et al.*, *J. Synchrotron Radiat.*, 2018, **25**, 998-1009.

10. J-C Labiche, O Mathon, S Pascarelli, MA Newton, GG Ferre, C Curfs, *et al.*, *Rev. Sci. Instrum.*, 2007, **78**, 091301.
11. B Ravel and M Newville, *J. Synchrotron Radiat.*, 2005, **12**, 537-541.
12. DC Koningsberger, BL Mojet, GE van Dorssen and DE Ramaker, *Top. Catal.*, 2000, **10**, 143-155.
13. M Newville, *J. Synchrotron Radiat.*, 2001, **8**, 322-324.
14. M Basham, J Filik, MT Wharmby, PCY Chang, B El Kassaby, M Gerring, *et al.*, *J. Synchrotron Radiat.*, 2015, **22**, 853-858.
15. AA Michelson, 1927. *Studies in Optics*. Chicago: The University of Chicago Press.
16. Harrick Scientific Products, Inc. Data Sheet Praying Mantis document [online]. Available from: https://www.harricksci.com/sites/default/files/pdf/data_sheets/Data_Sheet_Praying_Mantis.pdf. [Accessed: 02 February 2019].
17. Harrick Scientific Products, Inc. High Temperature Reaction Chamber for the Praying Mantis. [online]. Available from: https://www.harricksci.com/sites/default/files/pdf/data_sheets/Data_Sheet_HVC_High_Temp_Praying_Mantis_Reaction_Chamber.pdf. [Accessed: 06 February 2019].
18. A Cros, *J. Electron Spectrosc.*, 1992, **59**, 1-14.
19. HM Rietveld, *J. Appl. Crystallogr.*, 1969, **2**, 65-71.
20. P Scherrer, *Nachr. Ges. Wiss. Göttingen* 1918, **26**, 98-100.
21. JI Langford and AJC Wilson, *J. Appl. Crystallogr.*, 1978, **11**, 102-113.

Chapter Three. Following the evolution of metal nanoparticles from their molecular precursors by *in situ* XAFS/DRIFTS

3.1 Introduction

3.1.1 Preparation of Supported Metal Nanoparticles

The preparation of supported metal nanoparticle catalysts in industry requires a process that achieves the desired material with optimal catalytic performance, whilst operating in a cost effective manner in terms of the raw materials, energy and labour input. Improvements to the preparation route are constantly investigated in order to optimise both the efficiency of the process and also the resulting catalytic properties. Improvements to the catalytic properties of a material refer to increased catalytic activity, tailored selectivity towards the desired reaction products, and stability against poisoning mechanisms to increase the catalyst lifetime.¹

High dispersion of the metal nanoparticles over the metal oxide support is often an important criteria for increasing catalytic activity, as smaller nanoparticles have greater surface area of the active component per mass of catalyst. Moreover, the active metal component of the supported nanoparticle catalyst is often an expensive platinum group metal or rare transition metal, and so increasing the metal dispersion ensures that a greater proportion of the expensive active metal is positioned at the surface and is available for catalysis, rather than being hidden in the bulk. However, it is well known that small nanoparticles have a tendency to sinter, particularly at elevated temperatures, which reduces the active surface area and decreases catalytic activity.^{2,3} Therefore, as well as high dispersion, the preparation route to small metal nanoparticles must ensure a strong interaction with the support to prevent nanoparticle migration and sintering. The key challenges faced by industries to optimise catalyst materials are to increase the metal dispersion, decrease nanoparticle size, lower precious metal content, and increase metal-support interfacial regions, without compromising the active catalytic sites.

3.1.2 Conventional Preparation Routes

The conventional preparation methods used in industry are precipitation and impregnation routes.⁴ Precipitation involves the nucleation and growth of metal nanoparticles from a precursor solution, induced by a change in the conditions (temperature or pH). In co-precipitation methods the active metal and metal oxide support are precipitated simultaneously from a solution containing both precursor salts. Co-precipitation results in metal nanoparticles < 50 nm in size, with strong metal-support interactions. However, unlike the catalysts investigated in this study, co-precipitation is often used to produce catalysts with high wt% loading of the active metal, such as the supported Ni catalyst, 30wt% Ni/Al₂O₃, with particle sizes between

12 – 20 nm used for steam reforming.⁵ One of the main drawbacks to the coprecipitation method is the need for multiple washing steps to remove the precursor salt which produces large amounts of contaminated waste solvent.

The conventional impregnation route involves wetting the preformed metal oxide support with a solution containing the active metal salt. The impregnation may be achieved with an excess volume of precursor solution, referred to as 'wet impregnation', or a calculated volume of precursor solution that does not completely saturate the pore volume of the support, referred to as 'incipient wetness impregnation'. The latter method has the advantage of producing less waste as the entire precursor solution is contacted with the support. The metal oxide support material usually contains a number of hydroxyl groups at its surface which act as adsorption sites for interaction with the impregnated metal precursor. The point of zero charge (PZC) of a metal oxide support (eg. Al_2O_3) is the pH at which these hydroxyl groups have zero net charge. If the pH of the impregnated precursor solution is above the PZC of the support, there will be a large concentration of negative charge at the surface (eg. Al-O^-), whereas if the pH is below PZC then there will be a large concentration of positive charge at the surface (eg. Al-OH^+). This dictates the electrostatic interaction of the metal ion with the support via ion exchange or ligand substitution.⁶ The formation of the metal nanoparticles are achieved during the final heat treatment of the impregnated sample. The temperature, duration and gas environment of the heat treatment have a strong influence on the resulting nanoparticle size.⁷⁻¹⁰ It is usually preferred to perform a calcination treatment in oxidising atmospheres in order to remove nitrates, carbonates and other salts from the precursor solution and form metal oxide nanoparticles. If the catalyst is then required in the reduced form, a subsequent reduction step may be performed after the calcination. However, some studies have reported the advantage in treating the catalyst directly in a reducing atmosphere for maintaining small particle size.¹⁰

There have been many studies in the past to investigate the effect of changing certain parameters in the impregnation methods on the resulting catalyst; change in the molecular precursor,¹¹ change in concentration^{12, 13} or pH¹⁴ of the impregnating solution, and change in the calcination temperature or calcination environment.¹⁵ Many of these studies have used *ex situ* characterisation techniques to compare the different catalysts produced in each case. The use of time-resolved, *in situ* methods for studying the formation of catalyst materials has been limited to XRD or combined XRD/XAFS techniques to follow the formation of large crystalline microporous materials.¹⁶⁻¹⁹ To our knowledge, an *in situ* DRIFTS method has yet been applied to follow the decomposition mechanism of metal precursors during their calcination to metal nanoparticles. In this work, the role of the molecular precursor will be investigated for its influence on the resulting nanoparticle catalyst. *Ex situ* characterisation in the past has found that metal

nanoparticles prepared from chloride containing precursors often suffer from residual Cl⁻ that block active sites at the resulting catalyst surface.^{20, 21} Whereas organic precursors such as acetate, acetylacetonate, ammonia containing salts and nitrate precursors have been found to yield greater dispersion of the active metal over the support.^{11, 20, 22} In this work, time-resolved *in situ* spectroscopy will be used to follow the preparation of Pd nanoparticle catalysts from a conventional Pd(NO₃)₂ precursor and an alternative Pd(NH₃)₄(OH)₂ precursor.

The supported Pd nanoparticle materials prepared in this chapter serve as catalysts for the low temperature CH₄ oxidation reaction which are used in compressed natural gas engines (CNGs). CNGs have become a popular option for heavy duty vehicles, particularly in the USA, due to relatively high abundance of natural gas reserves compared to oil and reduced emission of nitrogen oxides, particulate matter and carbon dioxide emissions compared to diesel and gasoline engines.²³ However, the main component of natural gas, CH₄, has a high ignition temperature (600°C)²⁴ and so a catalyst is required to promote CH₄ oxidation during the cold start up period of operation to avoid slip of unburned CH₄ from the vehicle exhaust. Highly dispersed PdO nanoparticles have repeatedly been found to achieve the greatest activity for CH₄ oxidation.^{25, 26} The correlation between catalytic activity and nanoparticle dispersion is rationalised by mechanistic studies proposing the oxidation of CH₄ to occur at the PdO nanoparticle surface, close to the metal oxide support interface where oxygen migration from the support can assist in re-oxidation of the nanoparticle surface via a Mars-Van Krevelen mechanism.^{27, 28} Additionally, smaller particles possess a greater specific surface area meaning a greater number of active sites for higher turn-over frequencies, with a large number of under coordinated surface sites which permit lower activation energy for dissociative CH₄ adsorption.^{29, 30}

In the present chapter the preparation of two supported 3wt% Pd catalysts (Pd/γ-Al₂O₃) from an impregnation method are investigated by combined *in situ* XAFS and DRIFTS spectroscopy. This work uses the time-resolved *in situ* spectroscopic techniques to follow the decomposition of the molecular precursor and formation of the PdO nanoparticles during the calcination treatment of the impregnated precursor. The differences in nanoparticle dispersion of the resulting PdO catalyst from the two different Pd precursors will be explained and the implication for their catalytic reactivity for methane oxidation.

3.2 Methods

3.2.1 Sample Preparation

The preparation of 3wt% PdO nanoparticles supported on γ-Al₂O₃ was investigated from an incipient wetness impregnation method using two different Pd precursors. The route to supported PdO nanoparticle catalysts, (PdO/γ-Al₂O₃) by incipient wetness

impregnation of a Pd salt onto the γ -Al₂O₃ support (SASOL, specific surface area = 140 m² g⁻¹), was investigated from two different precursor solutions. The first precursor used an acidified aqueous solution of palladium nitrate, (15.11 wt% Pd, Johnson Matthey) and a defined quantity of HNO₃, corresponding to a molar ratio NO₃/Pd = 3.8. The second precursor used an aqueous solution of tetraamminepalladium hydroxide (5.96 wt% Pd assay, Johnson Matthey), prepared from dissolution of tetraamminepalladium(II) hydrogen carbonate (JM, 99.99%) in aqueous NH₄OH solution (28 wt%). Incipient wetness impregnations were performed at room temperature with calculated quantities of the Pd salt to achieve a catalyst loading of 3wt% Pd. The volume of aqueous precursor solution used for the impregnation was calculated to be less than the total pore volume of the γ -Al₂O₃ support (0.5 cm³ g⁻¹). The mixture of the γ -Al₂O₃ support and the impregnated precursor solution were dried in the oven (100°C) for 12 hours to obtain the samples Pd(NO₃)₂/ γ -Al₂O₃ and Pd(NH₃)₄(OH)₂/ γ -Al₂O₃, respectively. For *ex situ* analysis, 10 g of the dried, impregnated precursor samples Pd(NO₃)₂/ γ -Al₂O₃ and Pd(NH₃)₄(OH)₂/ γ -Al₂O₃ were calcined in a conventional furnace at 500°C in air for 2 hours to achieve the calcined PdO/ γ -Al₂O₃ catalysts.

3.2.2 *In situ* XAFS/DRIFTS/MS

Combined, *in situ* XAFS and DRIFTS measurements of the dried, impregnated precursor samples were collected during a calcination treatment at beamline B18, Diamond Light Source using a previously reported Harrick XAFS/DRIFTS cell integrated with an Agilent Carey 680 FTIR spectrometer.³¹ A DaVinci arm accessory fitted with praying mantis optics was used to refocus the IR beam outside the FTIR spectrometer for positioning of the Harrick XAFS/DRIFTS cell in the X-ray beam. The dried, impregnated precursor (~20 mg) was loaded as a powder into the sample cup of the Harrick XAFS/DRIFTS cell. The experiment used a controlled flow of compressed air (30 cm³ min⁻¹) into the reaction chamber at atmospheric pressure using Brooks mass flow controllers, and the temperature of the sample was controlled and monitored by a thermocouple positioned inside the sample bed. XAFS measurements were performed at the Pd K-edge in transmission mode using QEXAFS setup with a fast scanning Si(311) double crystal monochromator. The acquisition time of each XAFS spectrum was 21 seconds spectrum⁻¹, collecting to a *k* range of 15.9 Å⁻¹. All XAFS spectra were acquired with a Pd foil placed between *I_t* and *I_{ref}*. DRIFTS spectra were collected taking 64 scans with a resolution of 4 cm⁻¹ using the liquid nitrogen cooled MCT detector, at a rate of 30 seconds per spectrum (400 – 4000 cm⁻¹). The effluent gas flow from the reactor was continuously monitored by online mass spectrometry using a Hiden QGA spectrometer to detect *m/z* 4, *m/z* 17, *m/z* 18, *m/z* 28, *m/z* 30, *m/z* 44 and *m/z* 46. The sample was heated from room temperature to 500°C at a ramp rate of 10°C min⁻¹, then maintained at 500°C for a dwell period of 2 hours before cooling

to room temperature. Combined XAFS and DRIFTS spectra were collected continuously throughout the ramp, dwell and cooling period, and the effluent gas monitored continuously by mass spectrometry.

3.2.3 EXAFS analysis

Processing EXAFS data was performed using IFEFFIT with the Horae package (Athena and Artemis). Athena was used to calibrate, align and normalise the spectra with respect to the Pd foil, for which E_0 was set at 24358 eV. EXAFS data processing used a k weighting of 2 and an appropriate k range for the data. Analysis of the Fourier transformed data was performed by using fitting paths generated from crystallographic data of Pd metal,³² PdO³³ and Pd(NO₃)₂³⁴. The amplitude reduction factor, S_0^2 , was derived from fitting the Pd foil to a single scattering path of known coordination number of 12 to give a S_0^2 value of 0.8.

In order to obtain quantification of Pd coordination numbers from the EXAFS data collected during the calcination ramp period, the Fourier transformed EXAFS data was fitted to models using three scattering paths; Pd-O at a distance 2.03 Å, Pd-Pd(1) at a distance 3.06 Å and Pd-Pd(2) at a distance 3.46 Å. These are the scattering paths used to fit reference bulk PdO.³³ The linear dependence of σ^2 with temperature was found by fitting the Fourier transformed Pd K-edge data of the calcined PdO/ γ -Al₂O₃ sample during the cooling period from 500°C to 20°C. The Fourier transformed EXAFS data of the calcined PdO/ γ -Al₂O₃ (prepared from Pd(NO₃)₂) show the increase in amplitude of EXAFS scattering features upon cooling the sample (Figure 3.1), which is due to a decrease in thermal motion and mean squared disorder, σ^2 .³⁵ The sample is assumed to remain as PdO nanoparticles upon cooling, with no change in Pd coordination numbers or distances, and so the EXAFS data were fitted with the same three scattering paths of PdO; Pd-O, Pd-Pd(1) and Pd-Pd(2). All parameters were fixed, allowing only the value of σ^2 to be varied for each scattering path, which are detailed in Table 3.1. The linear dependence of σ^2 with temperature is shown in Figure 3.2, the values of which were used to make appropriate fits to the EXAFS data collected during the calcination ramp period.

Table 3.1 Dependence of σ^2 with temperature, found by fitting Fourier transformed EXAFS data of calcined PdO/ γ -Al₂O₃ catalyst during cooling from 500°C to room temperature. Fitting model used scattering paths of Pd-O and Pd-Pd with fixed coordination numbers and coordination distances; Pd-O coordination number 4, coordination distance 2.03 Å. Pd-Pd(1) coordination number 5.5, coordination distance 3.06 Å. Pd-Pd(2) coordination number 4.5, coordination distance 3.46 Å.

Temperature / °C	$\sigma^2 / \text{Å}^2$		
	Pd-O	Pd-Pd(1)	Pd-Pd(2)
48	0.0030(6)	0.011(1)	0.010(2)
100	0.0031(6)	0.012(2)	0.011(2)
145	0.0036(7)	0.014(2)	0.012(2)
195	0.0039(7)	0.015(2)	0.012(3)
225	0.0040(7)	0.016(2)	0.013(3)
245	0.0042(7)	0.017(2)	0.012(2)
295	0.0045(7)	0.017(3)	0.014(3)
345	0.0050(8)	0.018(3)	0.014(3)
395	0.0054(8)	0.020(3)	0.015(3)
445	0.0056(8)	0.021(4)	0.016(4)

Note: Fit range $3.1 < k / \text{Å}^{-1} < 13.4$, $1.15 < R / \text{Å} < 3.5$.

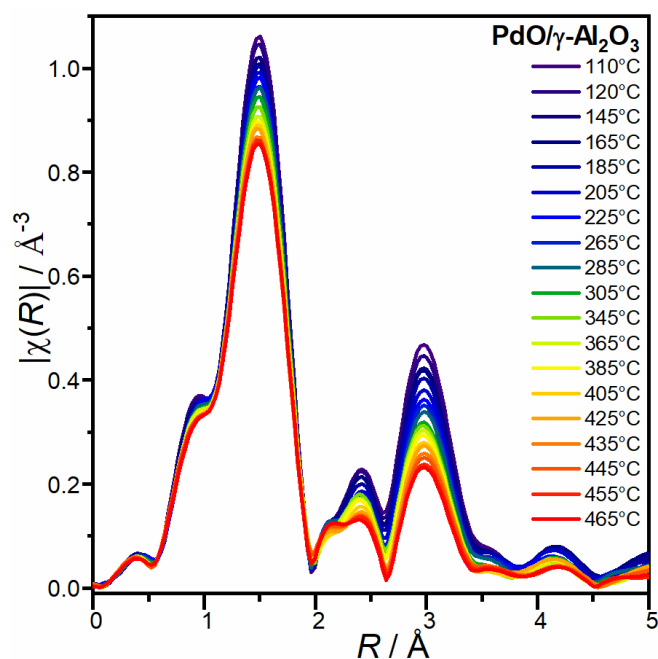


Figure 3.1. Fourier transformed Pd K-edge EXAFS of PdO/ γ -Al₂O₃ during cooling period of calcination in air flow from 500°C to room temperature.

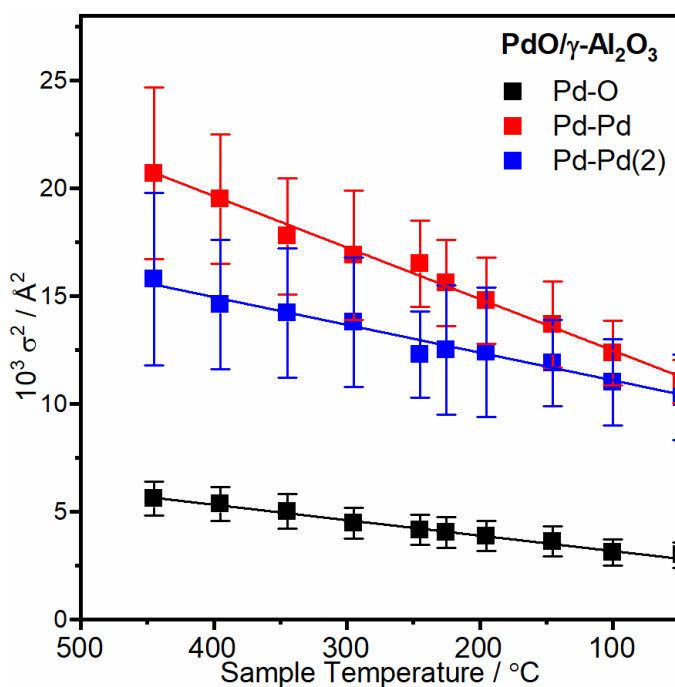


Figure 3.2. Linear dependence of EXAFS Debye Waller factor, σ^2 , with temperature. Values obtained by fitting the Fourier transformed EXAFS data PdO/ γ -Al₂O₃ during cooling period of calcination treatment.

3.2.4 *Ex situ* Characterisation

TEM images of the samples were obtained using a JEOL JEM 2100 transmission electron microscope. Samples were prepared for TEM analysis by dispersing the catalyst powder in high-purity ethanol using ultrasonication. 1 μ L of the sonicated suspension was pipetted onto a holey carbon supported Cu grid and the solvent was evaporated.

Ex situ Pd K-edge XAFS spectra of the calcined catalyst samples after reducing in H₂ were taken in transmission mode on B18 at Diamond light source, using QEXAFS setup with fast scanning Si(311) double crystal monochromator and with a Pd foil placed between I_t and I_{ref} .

CO chemisorption of the calcined catalyst samples were investigated by FTIR spectroscopy in transmission mode. Samples (20 mg) were pressed into self-supporting wafers (1.35 cm²), mounted in the transmission FTIR cell and dried at 100°C under constant flow of He. The sample cell was cooled to room temperature before introducing several pulses of CO (5% CO/He) into the cell until the catalyst surface became saturated (*i.e.* additional pulses of CO did not further increase the intensity of CO_{ads} absorption bands). The CO adsorption FTIR spectra were recorded (400 – 4500 cm⁻¹, 4 cm⁻¹ resolution) after purging the cell with He (15 minutes).

XRD diffraction patterns were collected using Rigaku Miniflex diffractometer (ISIS Characterisation Lab) with Cu tube source 600 mW of 45 kV and 15 mA and a 1D Si strip detector.

3.2.5 Catalytic Testing

The catalytic testing was conducted at Johnson Matthey Technology centre, Sonning Common. The temperature of the reactor used 0.2 g of catalyst, which was sieved to a controlled pellet fraction (425 – 250 μm). The reactor was increased to 150°C before introducing the synthetic natural gas mixture (0.5% CH_4 , 10% O_2 , 0.01% C_2H_6 , 0.01% C_3H_8 , 0.01% NO , 10% CO_2 , and 10% H_2O) at a total flow rate of 2000 $\text{cm}^3 \text{min}^{-1}$. The reactor temperature was increased linearly at a rate of 15 $^\circ\text{C min}^{-1}$, and the catalyst temperature recorded using an internal thermocouple positioned at the inlet of the catalyst bed. The exhaust gases were analysed by a MKS 2000 multi-gas FTIR analyser, and conversion values calculated relative to the inlet CH_4 signal.

3.3 Results

3.3.1 In Situ XAFS

Pd K-edge XANES of the dried, impregnated precursors (before calcination treatment) are plotted in Figure 3.3 together with the Pd K-edge XANES of their corresponding unsupported precursor salt. The XANES spectrum of $\text{Pd}(\text{NH}_3)_4(\text{OH})_2/\gamma\text{-Al}_2\text{O}_3$ matches closely with that of the aqueous $[\text{Pd}(\text{NH}_3)_4][(\text{OH})_2]$ solution, showing that the Pd species of impregnated $\text{Pd}(\text{NH}_3)_4(\text{OH})_2/\gamma\text{-Al}_2\text{O}_3$ exist in +2 oxidation state with the same coordination geometry as the unsupported precursor. Similarly, the XANES spectrum of $\text{Pd}(\text{NO}_3)_2/\gamma\text{-Al}_2\text{O}_3$ was compared with that of the crystalline Pd nitrate hydrate, showing that there was no change to the Pd oxidation state or coordination geometry

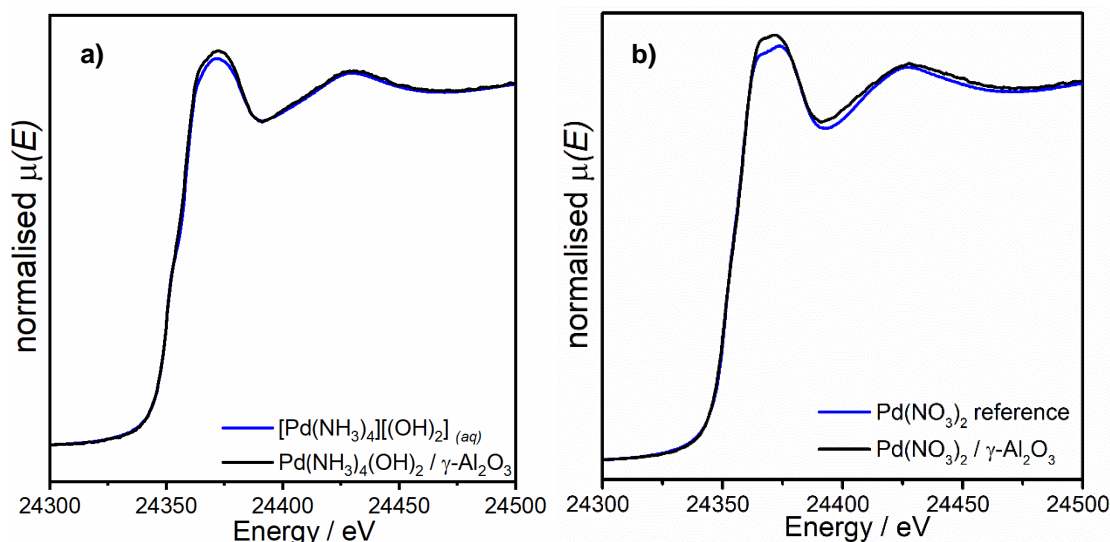


Figure 3.3. Pd K-edge XANES of impregnated precursor samples with the corresponding unsupported precursor salt. **a)** $\text{Pd}(\text{NH}_3)_4(\text{OH})_2/\gamma\text{-Al}_2\text{O}_3$ (black) and aqueous $[\text{Pd}(\text{NH}_3)_4][(\text{OH})_2]$ solution (blue), **b)** $\text{Pd}(\text{NO}_3)_2/\gamma\text{-Al}_2\text{O}_3$ (black) and $\text{Pd}(\text{NO}_3)_2$ (blue).

upon impregnation. The structure is assumed to be a *trans*-[Pd(NO₃)₂(H₂O)₂] complex, where the square planar environment of Pd is coordinated to 4 oxygen atoms (two belonging to H₂O and two belonging to (NO₃)).³⁶

The Fourier transformed Pd K-edge EXAFS data of the two dried, impregnated precursors are shown in Figures 3.4a and 3.4b together with those of the unsupported precursors. The Pd K-edge EXAFS data gives information for the local coordination environment of Pd species in each sample upon initial impregnation onto the γ -Al₂O₃ support. The EXAFS spectrum of Pd(NH₃)₄(OH)₂/ γ -Al₂O₃ matches closely with that of the unsupported aqueous precursor solution [Pd(NH₃)₄][(OH)₂] (Figure 3.4a). However, the EXAFS spectrum of Pd(NO₃)₂/ γ -Al₂O₃, shows an additional scattering feature at 9.2 Å⁻¹ (annotated with an asterisk in Figure 3.4b) that is absent from the corresponding EXAFS spectrum of the unsupported Pd(NO₃)₂ precursor salt. A simple model - constructed from one scattering path for Pd coordinated to 4 light atomic neighbours at an average radial distance of 2.04 Å - was able to fit the Fourier transformed EXAFS data of the impregnated Pd(NH₃)₄(OH)₂/ γ -Al₂O₃ (data and fit plotted in Figure 3.4c and fitting parameters detailed in Table 3.2). This data shows that the Pd species of Pd(NH₃)₄(OH)₂/ γ -Al₂O₃ remain as well-isolated, 4-coordinate Pd²⁺ complexes upon impregnation onto the γ -Al₂O₃ support. This simple fitting model was not sufficient to fit the Fourier transformed EXAFS data of Pd(NO₃)₂/ γ -Al₂O₃. In order to make a suitable fit to this data, additional scattering paths were required (data and fitting model plotted in Figure 3.4d, and fitting parameters detailed in Table 3.1). An additional three scattering paths to light neighbouring atoms at radial distances of 2.005 Å, 2.92 Å and 3.17 Å, can be attributed to O and N atoms of nitrate ligands, and an additional scattering path to a heavier neighbouring atom at a radial distance of 3.43 Å, which can be attributed to Pd atoms of neighbouring molecular complexes. This data shows that the molecular Pd complexes of the impregnated Pd(NO₃)₂/ γ -Al₂O₃ must experience intermolecular interactions that position Pd centres at a separation of 3.43 Å.

Changes to the local coordination environment of Pd species during the calcination ramping period were followed by plotting the Fourier transformed Pd K-edge EXAFS data collected at increasing temperatures (Figure 3.5). For the Pd(NO₃)₂/ γ -Al₂O₃ sample, Figure 3.5a shows that the scattering feature at 3.0 Å, previously identified as scattering from a heavy atomic neighbour, increases in amplitude with increasing temperature from 203°C to 255°C. This means that despite increase in σ^2 with temperature, there must have been considerable increase in coordination to neighbouring Pd atoms at that defined distance to cause such an increase in amplitude.

Table 3.2. Fitting parameters for Fourier transformed Pd K-edge EXAFS of impregnated precursors before calcination treatment.

	Scattering Path	N	$R / \text{\AA}$	$\sigma^2 / \text{\AA}^2$	E_0 / eV	R_{factor}
Pd(NH₃)₄(OH)₂ γ-Al₂O₃^a	Pd-N	3.9(2)	2.037(4)	0.0020(8)	-1.4(5)	0.02
Pd(NO₃)₂ γ-Al₂O₃^b	Pd-O	4 (set)	2.005(3)	0.0015(4)	1.4	0.02
	Pd-N	2.7(9)	2.92(2)	0.002 (set)		
	Pd-O	2(1)	3.17(3)	0.002 (set)		
	Pd-Pd	1.1(7)	3.43(2)	0.003(3)		

Note: ^a $S_0^2 = 0.8$. Fit range $3.1 < k / \text{\AA}^{-1} < 13.4$, $1.15 < R / \text{\AA} < 2.5$, number of independent points 10. ^b $S_0^2 = 0.8$. Fit range $3.1 < k / \text{\AA}^{-1} < 13.4$, $1.15 < R / \text{\AA} < 3.5$, number of independent points 15.

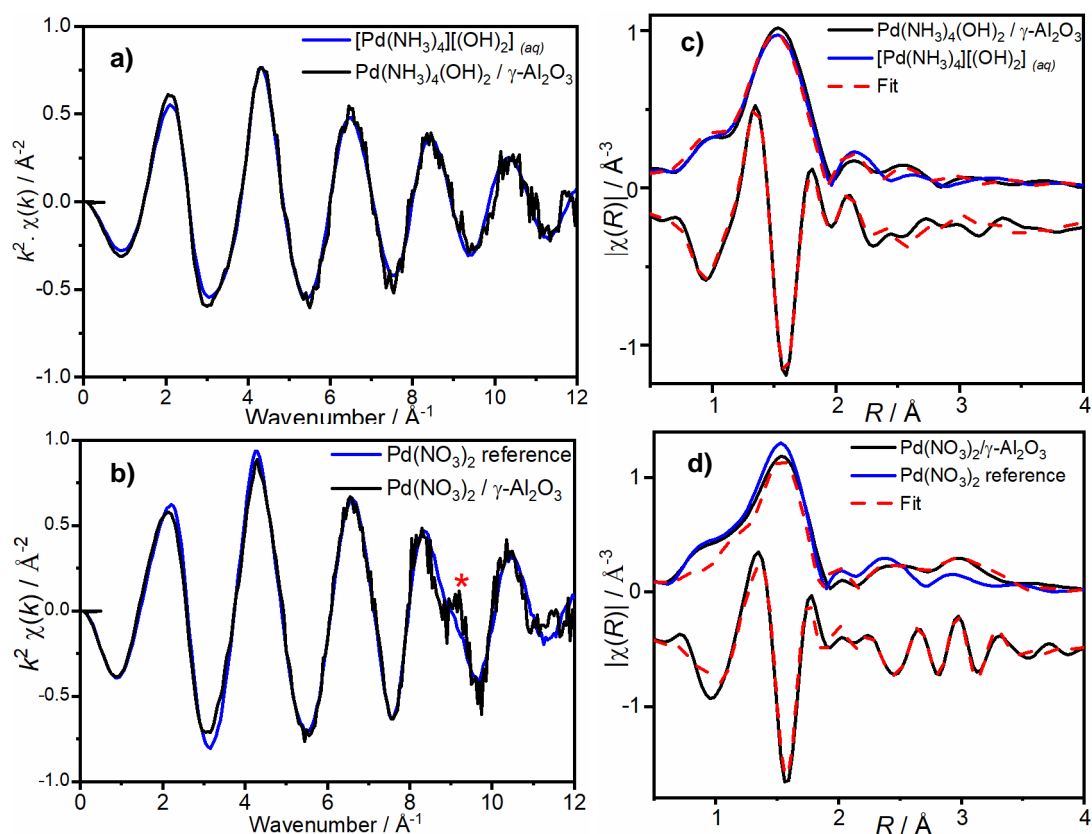


Figure 3.4. Pd K-edge EXAFS data of impregnated precursors, plotted together with the corresponding reference spectrum **a**) Pd(NH₃)₄(OH)₂/γ-Al₂O₃ (black) and [Pd(NH₃)₄][(OH)₂] (blue) and **b**) Pd(NO₃)₂/γ-Al₂O₃ (black) and Pd(NO₃)₂ (blue). Corresponding Fourier transformed EXAFS data of impregnated precursors **c**) Pd(NH₃)₄(OH)₂/γ-Al₂O₃ and **d**) Pd(NO₃)₂/γ-Al₂O₃, plotted together with the corresponding reference spectrum and the fitting model detailed in Table 3.2.

By fitting the Fourier transformed EXAFS data to scattering paths of bulk PdO (fitting parameters given in Table 3.3), and by comparison with the Fourier transformed Pd K-edge EXAFS of the PdO reference sample (Figure 3.5), it can be shown that the increase in amplitude of this EXAFS feature can be attributed to an increasing number of Pd atoms positioned at 3.43 Å from the absorbing Pd atom. Considering the tetragonal crystal structure of bulk PdO, shown by the unit cell diagram in Figure 3.6, formation of PdO would expect each Pd atom to be coordinated to four oxygen atoms in a square planar orientation, and two Pd-Pd distances of 3.07 Å and 3.43 Å with corresponding coordination values of 4 and 8, respectively.^{33, 37} For Pd atoms within nanocrystalline PdO particles, a large number of under-coordinated atoms means that the expected Pd-Pd coordination numbers will be much lower than the reference values of bulk crystalline PdO. Therefore, increase in Pd-Pd coordination at a radial distance of 3.43 Å is indicative of the nucleation and growth of PdO nanoparticle structure, which occurs for the sample prepared from Pd(NO₃)₂/γ-Al₂O₃ between 203°C and 255°C of the calcination ramp period.

The Fourier transformed EXAFS data of the impregnated Pd(NH₃)₄(OH)₂/γ-Al₂O₃ sample at increasing temperatures of the calcination ramp period are shown in Figure 3.5b. The scattering feature at 3.0 Å in the Fourier transformed EXAFS data of Pd(NH₃)₄(OH)₂/γ-Al₂O₃ was not observed until 393°C, suggesting that the location of Pd neighbours at a coordination distance of 3.43 Å for the formation of PdO structure did not occur until higher calcination temperature than was observed for Pd(NO₃)₂/γ-Al₂O₃.

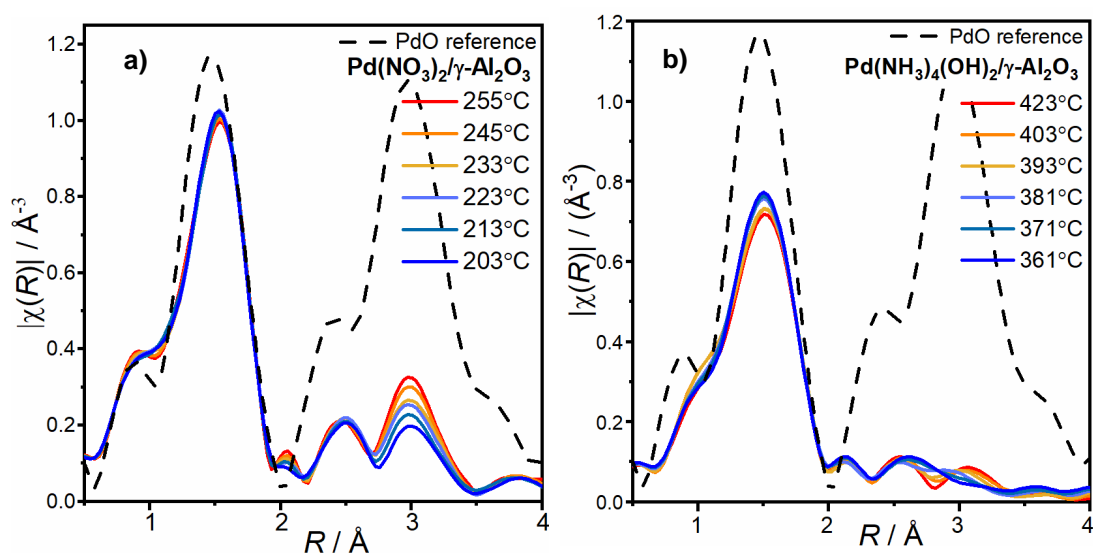


Figure 3.5. Non-phase corrected Fourier transformed EXAFS data of impregnated Pd precursors **a)** Pd(NO₃)₂/γ-Al₂O₃ and **b)** Pd(NH₃)₄(OH)₂/γ-Al₂O₃ at increasing temperatures during calcination ramping period.

The corresponding fitting models are plotted with the Fourier transformed EXAFS data of the impregnated precursors Pd(NO₃)₂/γ-Al₂O₃ and Pd(NH₃)₄(OH)₂/γ-Al₂O₃ in Figures 3.7 and 3.8, respectively, and the fitting parameters are detailed in Table 3.3 and Table

3.4, respectively. The EXAFS data was fitted using the same three scattering paths of PdO; Pd-O, Pd-Pd(1) and Pd-Pd(2), at the defined distances (2.01 Å, 3.07 Å and 3.42 Å, respectively). The value of σ^2 was adjusted accordingly for each temperature, so that the coordination numbers could be found. The Pd-Pd(2) coordination number is plotted as a function of temperature in Figure 3.9, showing the difference in PdO formation from the two different precursors. The impregnated Pd(NO₃)₂/γ-Al₂O₃ precursor has intermolecular interactions at low temperatures of the calcination ramping period (<150°C) which facilitate the positioning of Pd centres at a neighbouring distance of 3.43 Å, for the early formation of PdO structure between 200-250°C. Conversely the Pd centres of Pd(NH₃)₄(OH)₂/γ-Al₂O₃ remain well isolated until ~400°C and the growth of PdO nanoparticles was to a lesser extent.

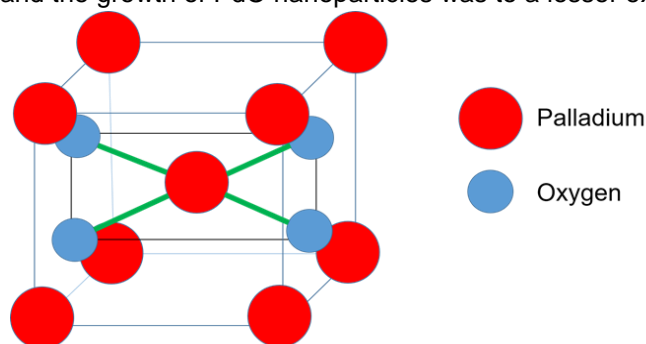


Figure 3.6. Unit cell diagram of tetragonal palladium oxide, not drawn to scale, showing the palladium atoms coordinated to four oxygen atoms in a square planar orientation.

The EXAFS data collected during the first 5 minutes of the dwell period at 500°C match closely to the EXAFS data collected after two hours of the dwell period at 500°C, as shown in Figure 3.10. This data shows that there was no change to the Pd coordination environment throughout the duration of the calcination dwell period, and so the resulting spectra of both samples could be identified as PdO nanoparticles. It is also shown that the PdO nanoparticles prepared from Pd(NH₃)₄(OH)₂/γ-Al₂O₃ maintained smaller particle size throughout the duration of the calcination dwell period, due to the lower amplitude of EXAFS scattering features compared to Pd(NO₃)₂/γ-Al₂O₃. By following the increase in amplitude of the scattering feature at 3.0 Å of the Fourier transformed EXAFS data, we have been able to identify the temperature for nucleation and growth of PdO nanoparticles from the two different precursors during the calcination treatment.

Table 3.3. Coordination numbers of Pd to neighbouring O and Pd atoms found by fitting the Fourier transformed EXAFS data of Pd(NO₃)₂/γ-Al₂O₃ collected during the calcination ramp period to scattering paths Pd-O and Pd-Pd, using fixed values of S₀², R and σ.

Temperature / °C	Coordination Number			R _{factor}
	Pd-O (2.01 Å)	Pd-Pd (3.07 Å)	Pd-Pd (3.42 Å)	
144	4.0(2)	-	2(1)	0.03
203	4 (set)	-	2.1(9)	0.03
213	4 (set)	2.6(8)	4.1(9)	0.02
223	4 (set)	2.9(8)	5(1)	0.02
233	4 (set)	3.0(8)	4.8(9)	0.02
243	4 (set)	3.0(8)	4.8(9)	0.02
253	4 (set)	3.4(9)	6(1)	0.02
304	4 (set)	4(1)	6(1)	0.02
345	4 (set)	4(1)	6(1)	0.02
405	4 (set)	4(1)	5(1)	0.02
425	4 (set)	4(1)	5(1)	0.02
473	4 (set)	4(1)	5(1)	0.02

Note: S₀² = 0.8. Fit range 3.1 < k / Å⁻¹ < 13.4, 1.15 < R / Å < 3.5, number of independent points 15. E₀ = -3.1 eV

Table 3.4. Coordination numbers of Pd to neighbouring O and Pd atoms found by fitting the Fourier transformed EXAFS data of Pd(NH₃)₄(OH)₂/γ-Al₂O₃ collected during the calcination ramp period to scattering paths Pd-O and Pd-Pd, using fixed values of S₀², R and σ.

Temperature / °C	Coordination Number			R _{factor}
	Pd-O (2.01 Å)	Pd-Pd (3.17 Å)	Pd-Pd (3.43 Å)	
361	3.6(1)	-	-	0.02
371	3.6(1)	-	-	0.04
381	3.6(1)	-	0.9(8)	0.03
393	3.6(1)	1(1)	2(1)	0.03
403	3.6(1)	1.5(9)	2.2(9)	0.02
413	3.6(1)	0.5(9)	2.1(8)	0.02
423	3.6(1)	1.4(8)	2.1(7)	0.01
433	3.6(1)	1.8(8)	2.5(8)	0.02
443	3.6(1)	1.8(9)	2.2(8)	0.02
453	3.6(1)	1.5(8)	2.1(8)	0.02
463	3.6(1)	1.4(1)	2.4.(1)	0.02

Note: S₀² = 0.8. Fit range 3.1 < k / Å⁻¹ < 12, 1.15 < R / Å < 3.5, number of independent points 15. E₀ = -3.6 eV

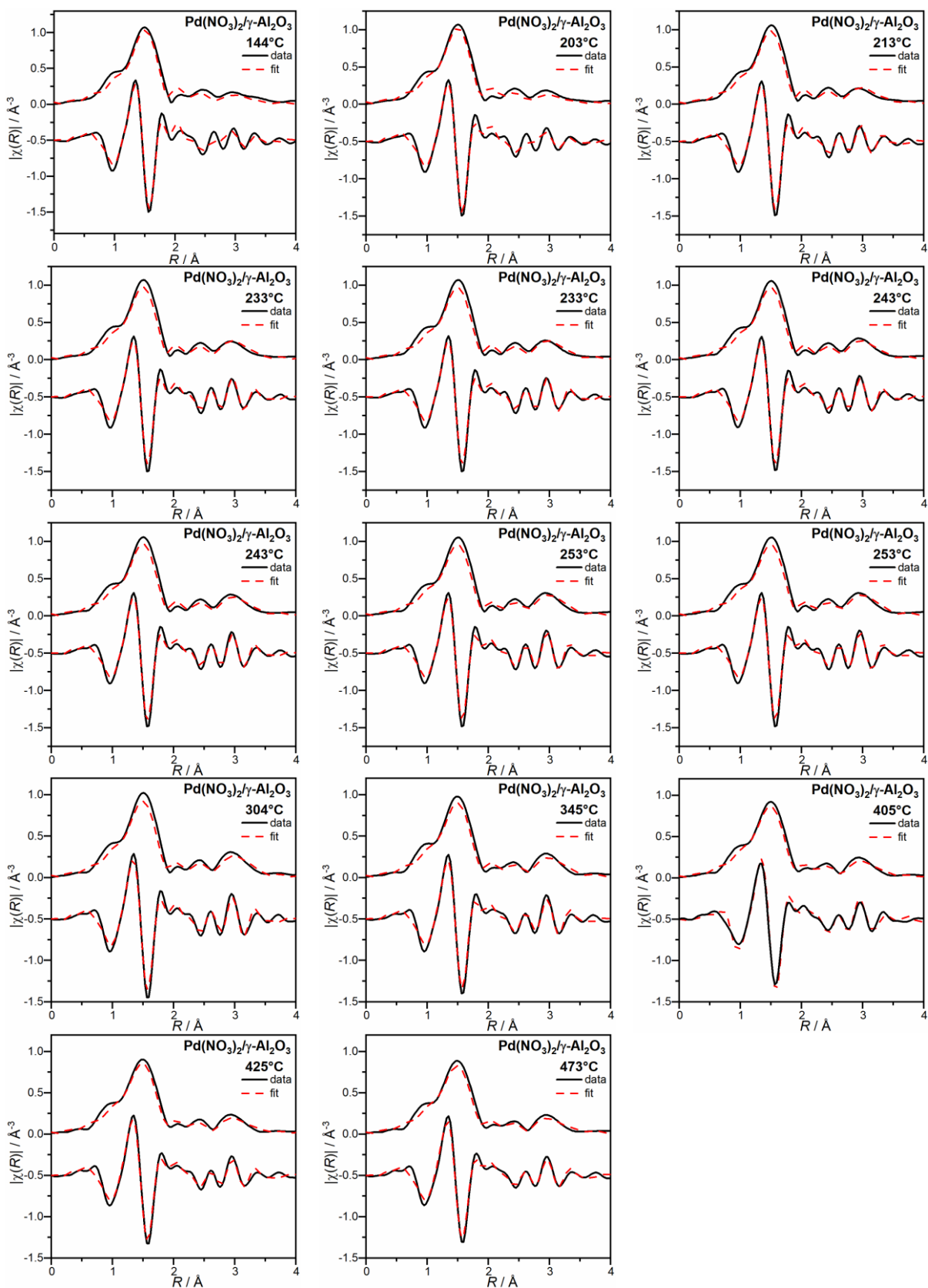


Figure 1.7. Fourier transformed EXAFS data of impregnated precursor $\text{Pd}(\text{NO}_3)_2/\gamma\text{-Al}_2\text{O}_3$ at increasing temperatures during the calcination ramp period, plotted together with the corresponding fitting models constructed using scattering paths Pd-O and Pd-Pd of PdO.

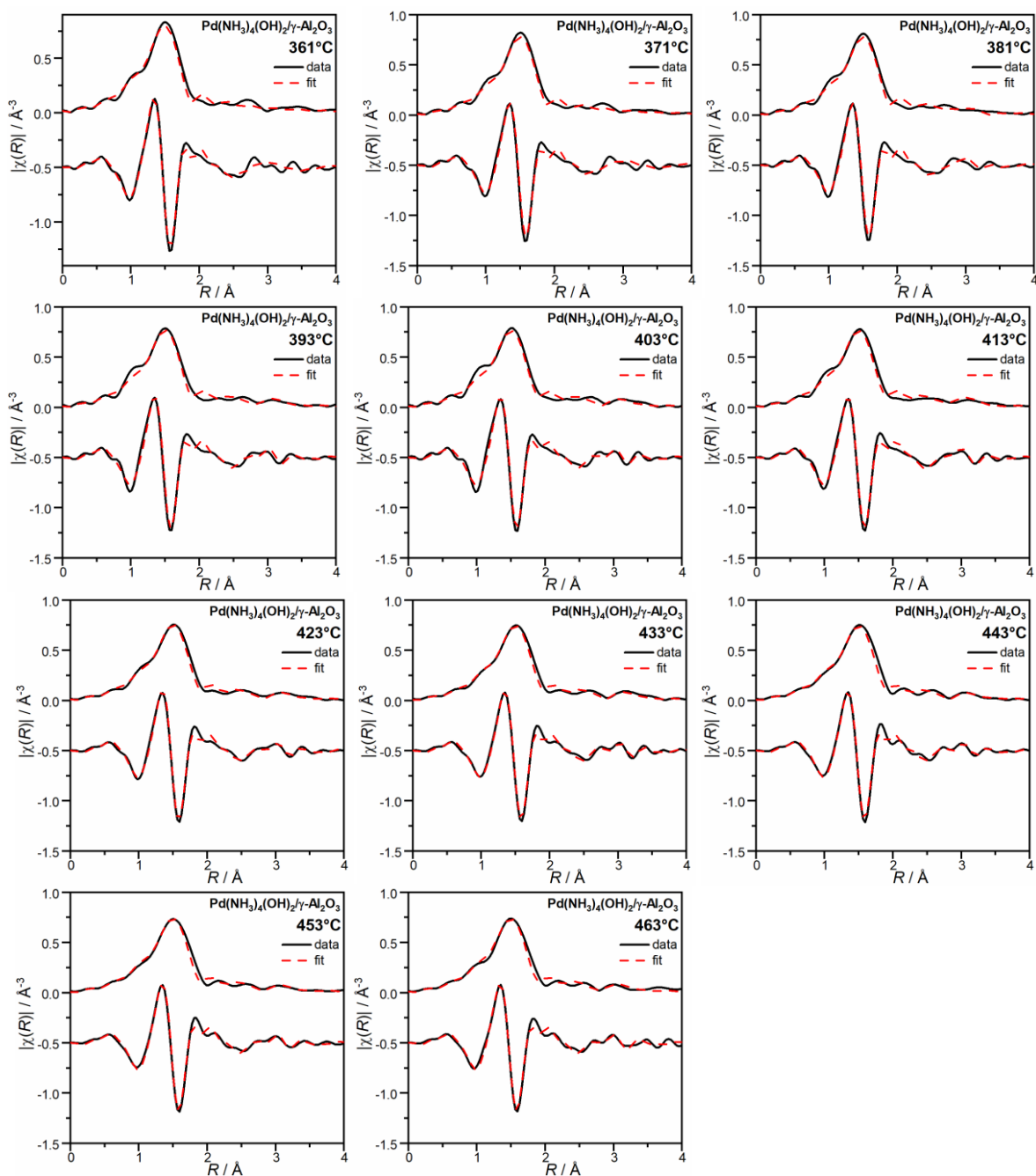


Figure 3.8. Fourier transformed EXAFS data of impregnated precursor $\text{Pd}(\text{NH}_3)_4(\text{OH})_2/\gamma\text{-Al}_2\text{O}_3$ at increasing temperatures during the calcination ramp period, plotted together with the corresponding fitting models constructed using scattering paths Pd-O and Pd-Pd of PdO.

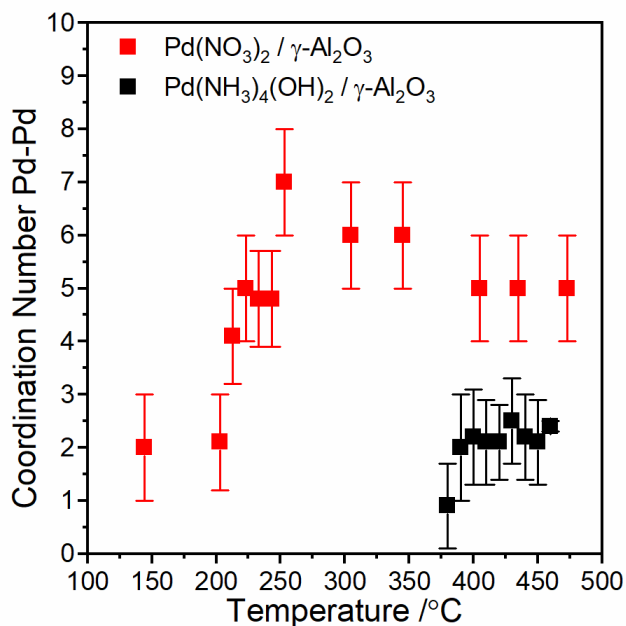


Figure 3.9. Coordination numbers for Pd coordination to neighbouring Pd (at radial distance 3.43 Å) calculated from fitting Pd-Pd scattering path of PdO to the Fourier transformed EXAFS data of impregnated precursors, Pd(NH₃)₄(OH)₂/γ-Al₂O₃ and Pd(NO₃)₂/γ-Al₂O₃ at increasing temperatures during calcination ramping period.

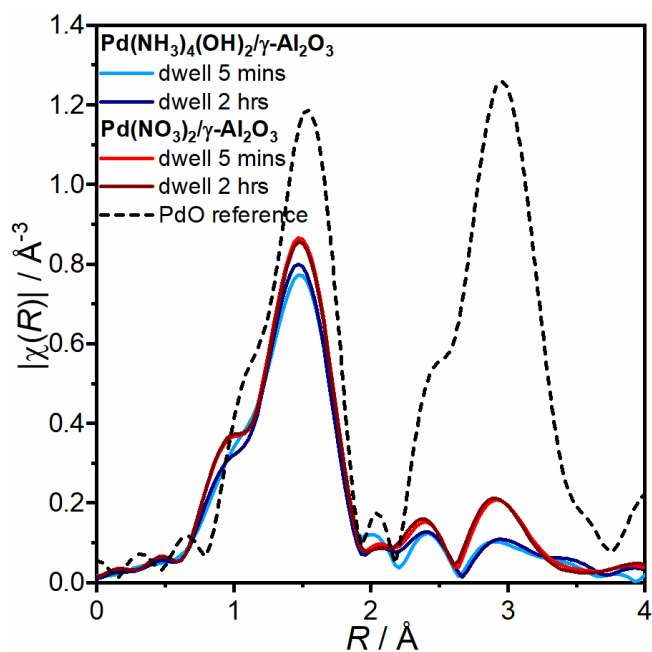


Figure 3.10. Non-phase corrected Fourier transformed EXAFS data of impregnated Pd precursors Pd(NH₃)₄(OH)₂/γ-Al₂O₃ (blue) and Pd(NO₃)₂/γ-Al₂O₃ (red) at increasing temperatures during calcination ramping period.

3.3.2 *In Situ* DRIFTS and MS

The DRIFTS spectra of the impregnated precursor samples before calcination, $\text{Pd}(\text{NH}_3)_4(\text{OH})_2/\gamma\text{-Al}_2\text{O}_3$ and $\text{Pd}(\text{NO}_3)_2/\gamma\text{-Al}_2\text{O}_3$, show the characteristic vibrational absorption bands for the molecular ligands surrounding each metal complex (Figure 3.11). The broad absorption band centred at 3500 cm^{-1} , present in the initial DRIFTS spectra of both impregnated samples, can be assigned to symmetric and antisymmetric O-H stretching vibrations of lattice water. The more intense stretching band observed between 3000 cm^{-1} and 3400 cm^{-1} from the $\text{Pd}(\text{NH}_3)_4(\text{OH})_2/\gamma\text{-Al}_2\text{O}_3$ sample can be attributed to N-H stretching of NH_3 species, and the sharp band at 1420 cm^{-1} is assigned to carbonate ions on the oxide support of both samples.³⁸ Loss of these absorption bands upon heating the samples to 200°C indicates removal of H_2O and CO_3^{2-} groups from the surface and pores of the support. The negative absorption band at 2350 cm^{-1} is due to a decrease in gas phase CO_2 during the *in situ* measurement conditions compared to the ambient background measurement. The nitrate species of sample $\text{Pd}(\text{NO}_3)_2/\gamma\text{-Al}_2\text{O}_3$ can be identified by two molecular vibrational bands for N=O stretching between 1650 cm^{-1} and 1500 cm^{-1} , and O-N-O asymmetrical stretching between 1350 cm^{-1} and 1200 cm^{-1} .^{39, 40} The H-N-H vibrational modes of ammonia ligands of $\text{Pd}(\text{NH}_3)_4(\text{OH})_2/\gamma\text{-Al}_2\text{O}_3$ can be identified by absorption bands at 1490 cm^{-1} and 1345 cm^{-1} .⁴¹⁻⁴⁴ The evolution of the molecular precursors can be followed by the DRIFTS spectra collected at increasing temperatures during the calcination ramp.

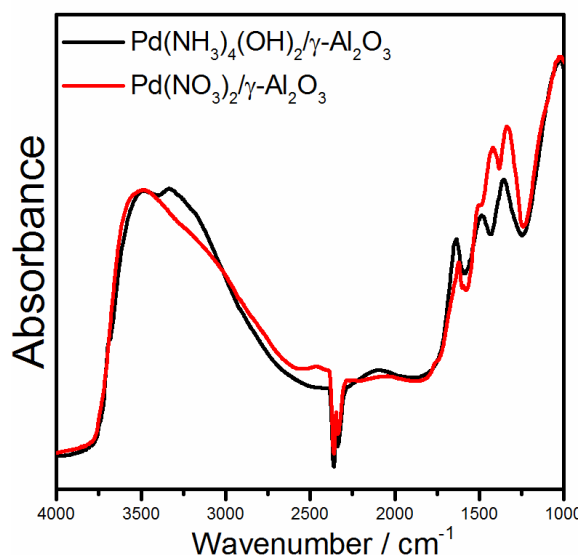


Figure 3.11. DRIFTS spectra of the impregnated precursors $\text{Pd}(\text{NH}_3)_4(\text{OH})_2/\gamma\text{-Al}_2\text{O}_3$ (black) and $\text{Pd}(\text{NO}_3)_2/\gamma\text{-Al}_2\text{O}_3$ (red) before calcination treatment.

The change in intensity of absorption bands from DRIFTS spectra of $\text{Pd}(\text{NH}_3)_4(\text{OH})_2/\gamma\text{-Al}_2\text{O}_3$ collected during the calcination ramp are shown by the colour map in Figure 3.12. The NH_3 absorption bands, located in DRIFTS spectra of $\text{Pd}(\text{NH}_3)_4(\text{OH})_2/\gamma\text{-Al}_2\text{O}_3$ at 1490 cm^{-1} and 1345 cm^{-1} , decrease in intensity upon increasing the temperature above 100°C and are completely removed by 225°C . The online mass spectrometry analysis of the effluent gas flow from the reactor during this

time (Figure 3.13) shows the presence of N_2O gas (measured by m/z 44) which suggests that the NH_3 molecules are oxidised before leaving the reactor. The ability of Pd to catalyse the oxidation of NH_3 to N_2O is well known⁴⁵⁻⁴⁷ and so it is likely that the oxidation of NH_3 was facilitated by coordination to Pd centres. Following the removal of these NH_3 bands, the presence of two weak intensity absorption bands at 1510 cm^{-1} and 1556 cm^{-1} are revealed (circled in red in Figure 3.12), which can be attributed to N=O stretching vibrations of surface nitrosyl species (NO^-_{ads}).^{48, 49} The formation of nitrosyl species can result from the oxidative decomposition of NH_3 ligands, which are known to form strong interactions with the $\gamma\text{-Al}_2\text{O}_3$ surface.⁵⁰ The N=O stretching bands exist in the DRIFTS spectra of $\text{Pd}(\text{NH}_3)_4(\text{OH})_2/\gamma\text{-Al}_2\text{O}_3$ up to 400°C , at which temperature they are desorbed from the sample surface and detected as NO gas in the exhaust by online mass spectrometry measurements (m/z 30). It is important to note the significance in the temperature for removal of the NO^-_{ads} from the $\gamma\text{-Al}_2\text{O}_3$ surface, which coincided with the temperature for PdO formation that was observed by the *in situ* EXAFS data of this sample. It is suggested that the NO^-_{ads} species at the surface of the $\gamma\text{-Al}_2\text{O}_3$ support could prevent the movement of Pd species across the support which is required for nucleation and growth of PdO nanoparticles.

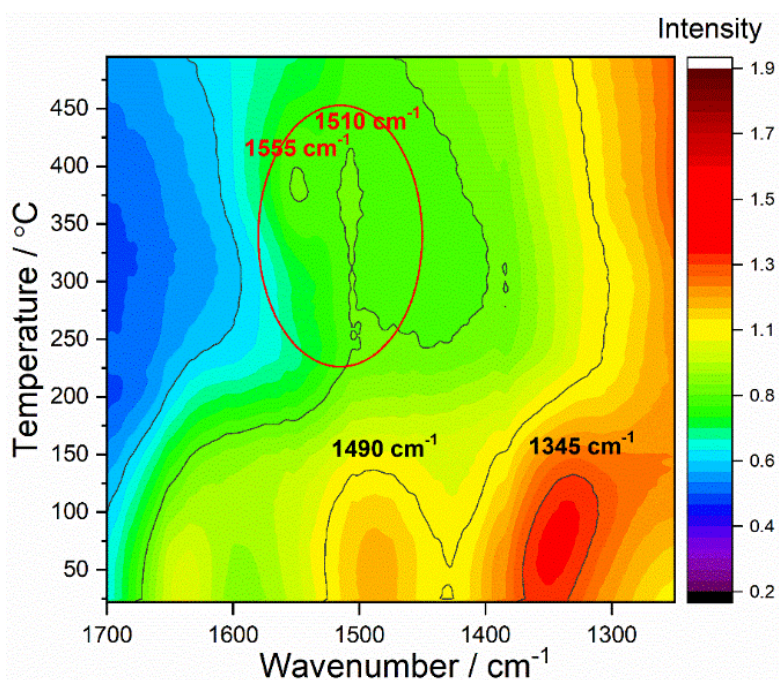


Figure 3.12. Colour map showing intensity of absorption bands of DRIFTS spectra collected from $\text{Pd}(\text{NH}_3)_4(\text{OH})_2/\gamma\text{-Al}_2\text{O}_3$ at increasing temperatures (25°C - 500°C) during the calcination ramp period.

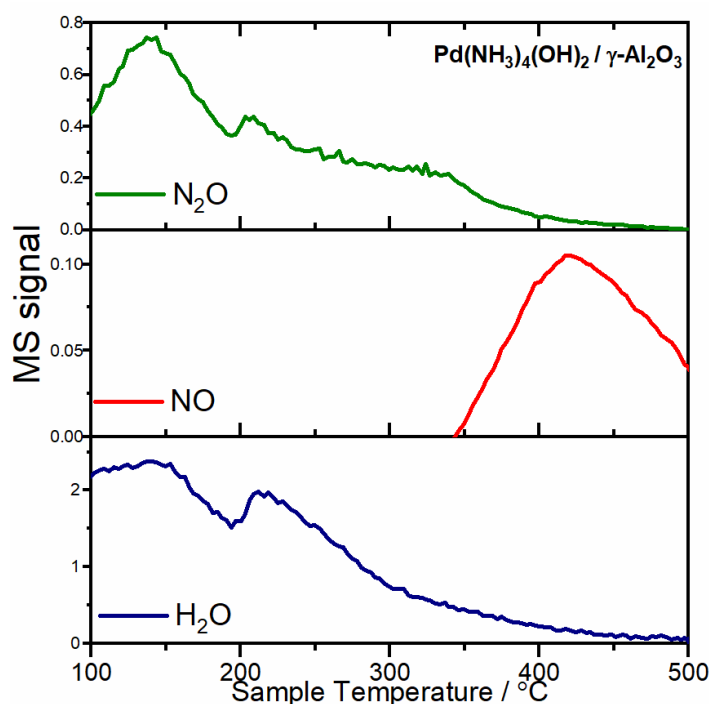


Figure 3.13. Mass spectrometry signals for N_2O , NO and H_2O gases at the exhaust from the XAFS/DRIFTS reactor during calcination ramp.

The change in intensity of absorption bands from DRIFTS spectra of $\text{Pd}(\text{NO}_3)_2/\gamma\text{-Al}_2\text{O}_3$ collected during the calcination ramp are shown by the colour map in Figure 3.14. The O-N-O and N=O stretching bands of nitrate groups from $\text{Pd}(\text{NO}_3)_2/\gamma\text{-Al}_2\text{O}_3$ are initially shown to have vibrational frequencies of 1320 cm^{-1} and 1510 cm^{-1} , respectively. Upon increasing the temperature of the sample beyond 100°C , these nitrate bands started to shift in frequency. At 200°C the band initially centred at 1320 cm^{-1} shifted to 1270 cm^{-1} , and the band initially centred at 1510 cm^{-1} shifted to 1570 cm^{-1} . The shift in nitrate bands to greater separation is consistent with increased bidentate nitrate coordination to a metal centre.⁵¹ This evidence for bidentate coordination of nitrate ligands at such low temperatures of the calcination treatment provides an explanation for the early neighbouring of Pd species that was identified by analysis of the Pd EXAFS data. The bidentate coordination of nitrate ligands to form bridging interactions between neighbouring Pd complexes is able to position Pd centres at a bridging separation distance of 3.4 \AA , which was the coordination distance reported by the EXAFS analysis. This is significant for the early formation of PdO structure, which is found to be facilitated by the early association of Pd centres. The temperature that NO and N_2O gases reached the mass spectrometer (Figure 3.15) coincided with the temperature for slow decomposition and removal of nitrates from the DRIFTS spectra. There was no evidence for the presence of trapped NO^-_{ads} at the $\gamma\text{-Al}_2\text{O}_3$ surface of this sample, which suggests that nitrosyl species were not formed from the decomposition of nitrate ligands in the oxidising atmosphere.

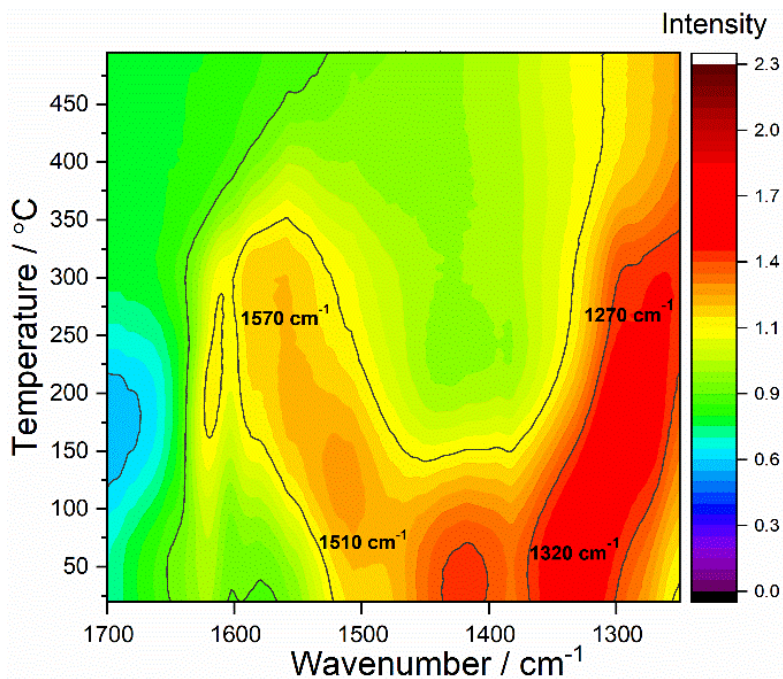


Figure 3.14. Colour map showing intensity of absorption bands of DRIFTS spectra collected from $\text{Pd}(\text{NO}_3)_2/\gamma\text{-Al}_2\text{O}_3$ at increasing temperatures (25°C - 500°C) during the calcination ramp period

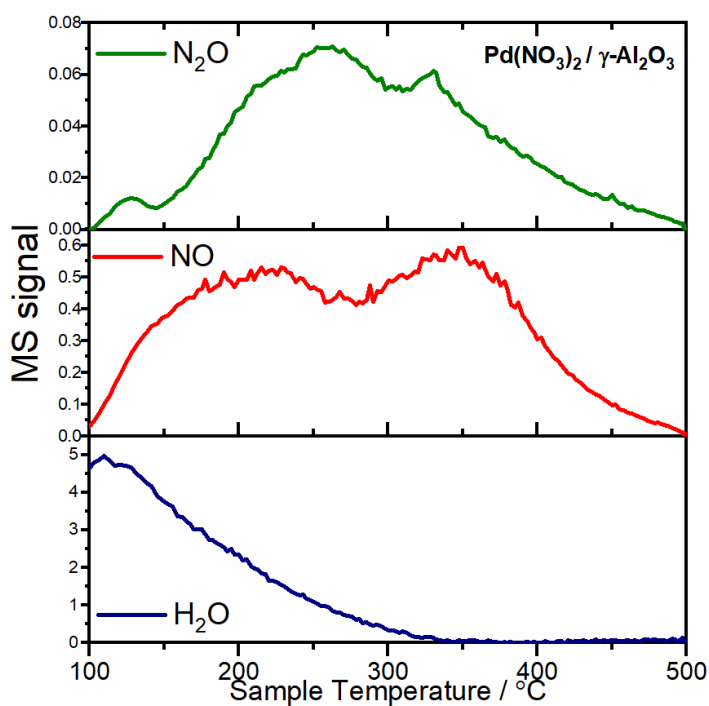


Figure 3.15. Mass spectrometry signals for N_2O , NO and H_2O gases at the exhaust from the XAFS/DRIFTS reactor during calcination ramp.

3.3.3 Ex situ Characterisation

The resulting, calcined catalyst samples were investigated by various *ex situ* characterisation techniques to confirm the difference in material properties between the two supported Pd catalysts that were prepared from the precursors $\text{Pd}(\text{NO}_3)_2$ and $\text{Pd}(\text{NH}_3)_4(\text{OH})_2$, respectively.

3.3.3.1 TEM Analysis

The TEM images of the calcined catalysts (Figure 3.16) show the size and shape of dark PdO nanoparticles contrasting against the $\gamma\text{-Al}_2\text{O}_3$ support. Particle size analysis was conducted over a sample of 100 particles from the TEM images of each sample, giving the particle size distributions plotted in Figure 3.17. It is apparent from the images and the particle size distribution that the catalyst prepared from $\text{Pd}(\text{NO}_3)_2$ resulted in presence of few large particles measuring > 15 nm in diameter. The presence of these large particles were not observed from images of the catalyst

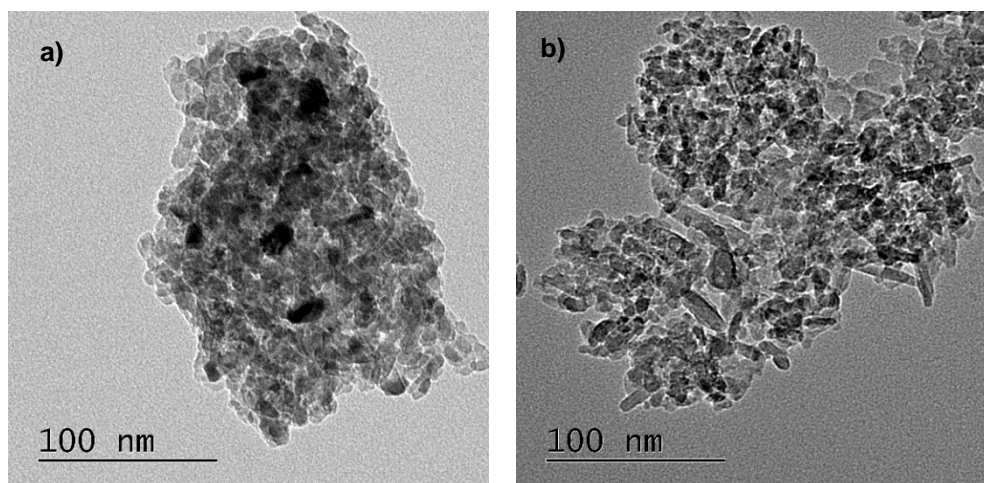


Figure 3.16. TEM images of calcined catalysts $\text{Pd}/\text{Al}_2\text{O}_3$ prepared by incipient wetness impregnation from **a)** $\text{Pd}(\text{NO}_3)_2$ (left) and **b)** $\text{Pd}(\text{NH}_3)_4(\text{OH})_2$ (right).

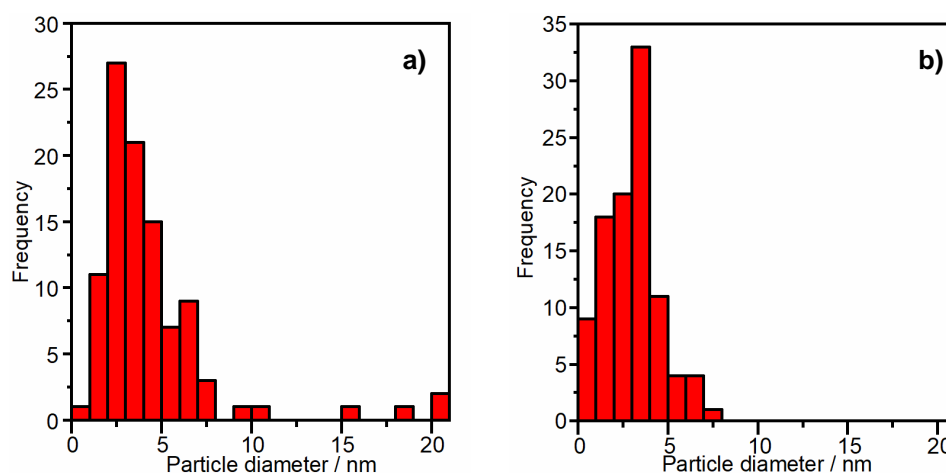


Figure 3.17. Histograms of particle size distribution of calcined $\text{PdO}/\text{Al}_2\text{O}_3$ catalysts prepared by incipient wetness impregnation from **a)** $\text{Pd}(\text{NO}_3)_2$ (left) and **b)** $\text{Pd}(\text{NH}_3)_4(\text{OH})_2$ (right), conducted from a sample of 100 particles measured from the corresponding TEM images.

prepared from $\text{Pd}(\text{NH}_3)_4(\text{OH})_2$, which appeared to have a narrower particle size distribution and smaller average particle size.

3.3.3.2 XRD

X-ray diffraction patterns of both calcined catalyst samples are shown in a stacked plot in Figure 3.18, together with the diffraction lines of cubic $\gamma\text{-Al}_2\text{O}_3$ ⁵² and tetragonal PdO ³⁷. Both catalysts show diffraction peaks assigned to $\gamma\text{-Al}_2\text{O}_3$ which are annotated with arrows in Figure 3.18. The broad, low intensity diffraction peaks located at 2θ angles of 42.6, 55.6, and 72.7° can be attributed to small, crystalline domains of tetragonal PdO . The relative crystallite size of these PdO domains can be inferred from the full width half-maximum (FWHM) of these peaks, as defined by the Sherrer equation.⁵³ The diffraction peak at 2θ angle of 55.6° was used to calculate the PdO crystallite size as this peak experienced the least interference from close diffraction lines of $\gamma\text{-Al}_2\text{O}_3$. The FWHM was measured to be 1.3° and 2.4°, for the catalysts prepared from $\text{Pd}(\text{NO}_3)_2$ and $\text{Pd}(\text{NH}_3)_4(\text{OH})_2$, respectively. These values corresponded to calculated PdO crystallite sizes of 11.4 nm and 6.0 nm, respectively (detailed in Table 3.5). For these samples there were a considerable number of particles observed by TEM to be less than 5 nm in diameter which may be insufficient in size to contribute to the XRD diffraction pattern of PdO crystal structure.⁵⁴ It is therefore likely that the PdO crystallite size calculated from the Sherrer equation may not represent the average particle size of all Pd nanoparticles in these samples.

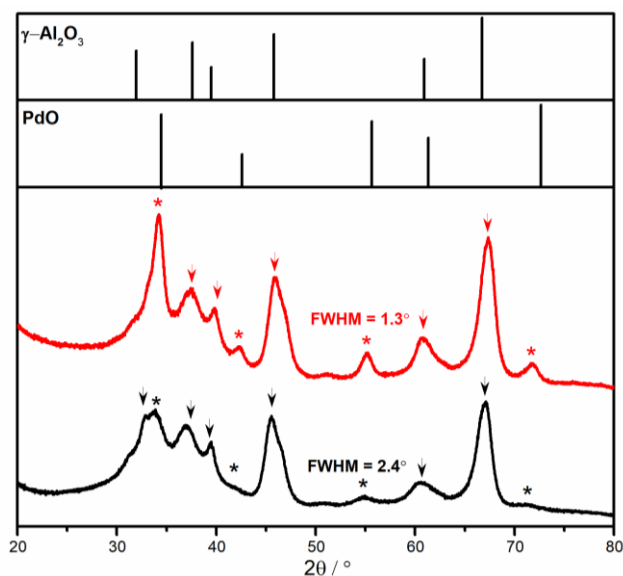


Figure 3.18. XRD patterns of $\text{PdO}/\gamma\text{-Al}_2\text{O}_3$ catalysts prepared by incipient wetness impregnation from $\text{Pd}(\text{NO}_3)_2$ (red) and $\text{Pd}(\text{NH}_3)_4(\text{OH})_2$ (black), and calcination. The XRD patterns of cubic $\gamma\text{-Al}_2\text{O}_3$ and tetragonal PdO are shown in the top panel.

Table 3.5. Average PdO crystallite size calculations from XRD diffraction peak (at 2θ of 55°) of calcined catalysts PdO/ γ -Al₂O₃ prepared by incipient wetness impregnation from Pd(NO₃)₂ and Pd(NH₃)₄(OH)₂ precursors. Calculations performed using the Scherrer equation.

Catalyst precursor	λ / nm	2θ / deg	FWHM / deg	Crystallite Size / nm
Pd(NO ₃) ₂	0.154	55.1	1.27	11.4
Pd(NH ₃) ₄ (OH) ₂	0.154	54.6	2.37	6.0

3.3.3.3 Ex Situ XAFS

Pd K-edge XAFS spectra of the resulting calcined catalyst samples were collected in transmission mode by pressing the samples into homogeneous pellets. The XANES region (Figure 3.19) shows that the Pd species of each sample exist in the same oxidation state and with the same coordination geometry as the bulk PdO reference. The Fourier transformed Pd K-edge EXAFS data (Figures 3.20a and 3.20b) can be fitted using a model constructed of Pd-O and Pd-Pd scattering paths for tetragonal PdO structure. The relatively low coordination numbers, compared to bulk PdO, are a result of a significant number of under coordinated Pd atoms at the surface of the small nanoparticles. The decreased amplitude of EXAFS scattering features for the catalyst prepared from Pd(NH₃)₄(OH)₂ is indicative of smaller PdO nanoparticle size and thus larger specific surface area. The Pd-Pd coordination numbers obtained by fitting the Fourier transformed EXAFS data of the *ex situ*, calcined catalyst samples in Figure 3.20 differ from those obtained by fitting that of the *in situ* EXAFS data. This can be explained by the correlation between multiple unknown parameters; the coordination number, *CN*, and mean square disorder parameter, σ^2 . The higher than expected coordination number for the closest Pd neighbours (at 3.07 Å from the absorbing Pd

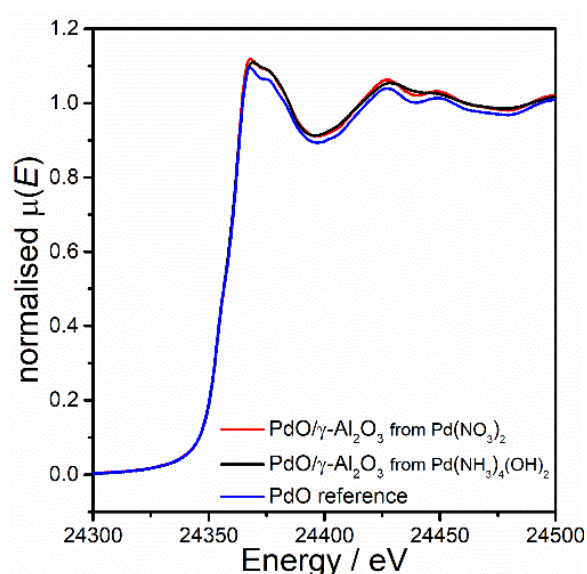


Figure 3.19. Pd K-edge XANES spectra of calcined PdO/ γ -Al₂O₃ catalysts prepared by incipient wetness impregnation from Pd(NO₃)₂ (red) and Pd(NH₃)₄(OH)₂ (black), plotted together with Pd K-edge XANES of a bulk PdO reference sample.

atoms) can result from the high mean square disorder value, which were both calculated from the amplitude of the EXAFS scattering features. In this case, the fitting parameters obtained from the *in situ* EXAFS data may provide a more accurate description of the atomic structure, as the mean square disorder parameter was set at incremental values in line with the change in temperature.

Pd K-edge EXAFS of the calcined catalyst samples were collected in the absence of oxygen after a reduction treatment in H₂ (200°C), in order to directly compare the particle size from Pd-Pd coordination numbers. The coordination environment of the Pd nanoparticles can be compared more easily in their reduced metallic state because the Pd K-edge EXAFS scattering only results from Pd atoms in the nanoparticle (rather than scattering from Pd and O atoms for PdO nanoparticles). The reduced Pd/γ-Al₂O₃ catalysts were investigated in the absence of oxygen to prevent the formation of a surface oxide layer, known to form in ambient conditions.⁵⁵

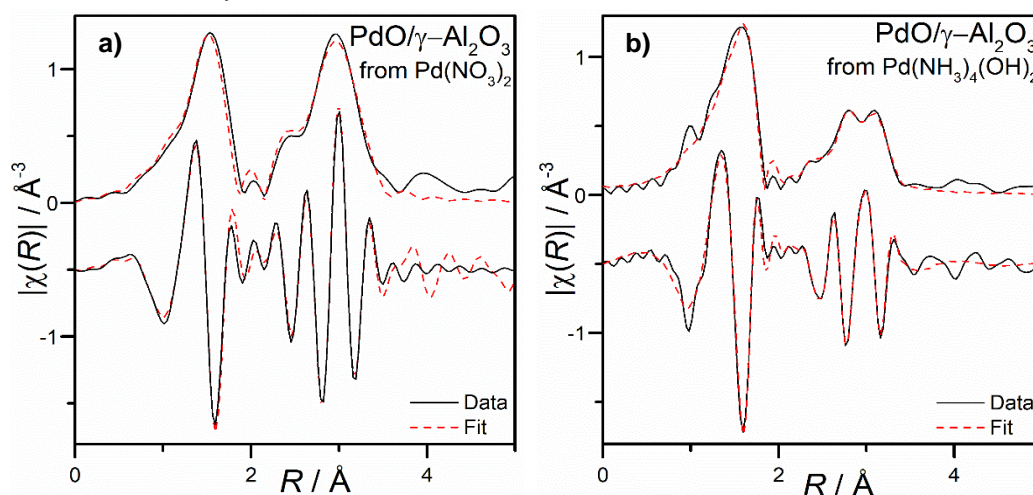


Figure 3.20. Fourier transformed Pd K-edge EXAFS of PdO/γ-Al₂O₃ catalysts prepared from incipient wetness impregnation of **a)** Pd(NO₃)₂ (left) and **b)** Pd(NH₃)₄(OH)₂ (right), after calcination treatment. Plotted as a stacked plot showing magnitude (top) and (imaginary) parts of the data (black) and the corresponding fitting model (red, dashed).

Table 3.6 Fitting parameters for the Pd K-edge EXAFS of calcined catalysts PdO/γ-Al₂O₃ prepared by incipient wetness impregnation from Pd(NO₃)₂ and Pd(NH₃)₄(OH)₂.

Sample	Catalyst precursor	Scattering path	CN	R / Å	σ ² / Å ²	R factor
PdO/ γ-Al ₂ O ₃	Pd(NO ₃) ₂	Pd-O	4.2(1)	2.031(2)	0.0021(3)	0.01
		Pd-Pd	5.9(3)	3.066(3)	0.0061(3)	
		Pd-Pd	5.0(3)	3.453(3)	0.0041(3)	
PdO/ γ-Al ₂ O ₃	Pd(NH ₃) ₄ (OH) ₂	Pd-O	3.92(9)	2.021(2)	0.0019(3)	0.1
		Pd-Pd	2.9(2)	3.050(5)	0.0058(5)	
		Pd-Pd	3.2(3)	3.438(5)	0.0055(5)	

Note: Fitted from three scattering paths of the absorbing Pd atom to the nearest neighbour O and Pd atoms, using $S_0^2 = 0.8$ as determined by the use of a Pd foil standard; Fit range $3 < k / \text{Å}^{-2} < 18.7$, $1 < R / \text{Å} < 3.5$; number of independent points = 25.

The Fourier transformed Pd K-edge EXAFS of the reduced Pd/ γ -Al₂O₃ catalysts are shown in Figure 3.21, plotted together with that of the Pd foil. By fitting the EXAFS data to a model using a single scattering path to neighbouring Pd atoms at a distance of 2.74 Å, the Pd-Pd coordination distance can be compared with that of Pd foil, which is known to be a value of 12. The fitting parameters, detailed in Table 3.7, show that the Pd nanoparticles prepared from Pd(NO₃)₂ and Pd(NH₃)₄(OH)₂ are found to have coordination numbers of 10.3 ± 4 and 7.5 ± 2, respectively. These coordination numbers were used to calculate the average particle size of the Pd nanoparticles which gave values of 2.7 ± 6 and 1.1 ± 1 nm, respectively, using an exponential Hill calculation with parameters defined previously.⁵⁶ The model assumes perfectly spherical nanoparticles with cubic fcc crystal structure and that the size of these nanoparticles are within the tolerable limit (structures comprising less than 200 atoms).

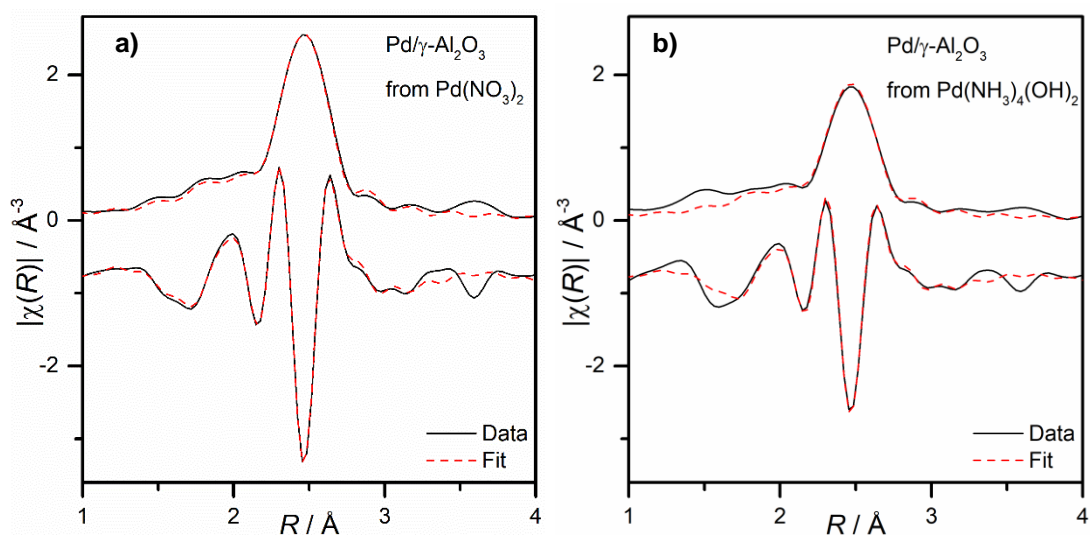


Figure 3.21. Fourier transformed Pd K-edge EXAFS of Pd/ γ -Al₂O₃ catalysts prepared from incipient wetness impregnation of **a)** Pd(NO₃)₂ (left) and **b)** Pd(NH₃)₄(OH)₂ (right) after calcination treatment and subsequent reduction in H₂.

Table 3.7. Fitting parameters for the Pd K-edge EXAFS of catalysts Pd/ γ -Al₂O₃ prepared by incipient wetness impregnation from Pd(NO₃)₂ and Pd(NH₃)₄(OH)₂, then calcination (air, 500°C) and subsequent reduction in (H₂, 200°C).

Sample	Catalyst precursor	Scattering path	CN	R / Å	$\sigma_2 / \text{Å}^2$	R factor
Pd/ γ -Al ₂ O ₃	Pd(NO ₃) ₂	Pd-Pd	10.3(4)	2.7412(8)	0.0065(3)	0.001
Pd/ γ -Al ₂ O ₃	Pd(NH ₃) ₄ (OH) ₂	Pd-Pd	7.5(2)	2.7435(7)	0.0065(3)	0.004

Note: Fitted from one scattering path of the absorbing Pd atom to the nearest neighbour Pd atoms, using $S_\sigma^2 = 0.8$ as determined by the use of a Pd foil standard; Fit range $3 < k / \text{Å}^{-2} < 14.5$, $2 < R / \text{Å} < 3$; number of independent points = 7.

3.3.3.4 FTIR CO adsorption

The available surface area of the two PdO/ γ -Al₂O₃ catalysts were investigated by using CO as a probe molecule and FTIR spectroscopy to examine the available catalytic adsorption sites. The FTIR spectra of both catalysts were performed in transmission mode, after saturating with CO adsorption (Figure 3.22). The FTIR spectra of both catalysts show the presence of CO adsorbed linearly atop of the Pd metal surface as a sharp peak at 2071 cm⁻¹.⁵⁷⁻⁶⁰ Bridged and multi-coordinate CO adsorption is also evidenced at the surface of both Pd catalysts by the broad FTIR absorption band between 1969 cm⁻¹ and 1830 cm⁻¹.⁵⁷⁻⁶⁰ The FTIR spectra in Figure 3.22 were normalised with respect to the mass of catalyst, therefore the relative intensity of CO adsorption bands corresponds to the number of CO molecules at the Pd surface. It is clear from the difference in intensity of the CO absorption bands from each catalyst that the PdO nanoparticles prepared from Pd(NH₃)₄(OH)₂ were able to accommodate a larger number of CO molecules at both the linear and bridge bonded adsorption sites, and thus this catalyst must have a larger surface area to mass ratio. Furthermore, the ratio between the integrated area of the linearly bonded CO adsorption band (at 2071 cm⁻¹) compared to that of the bridge bonded CO adsorption band (1969 cm⁻¹), is thought to give indication for the type of sites dominating the nanoparticle surface. The linear to bridged ratio of CO absorption bands was found to be greater for the catalyst prepared from Pd(NH₃)₄(OH)₂ at a value of 0.27, compared to 0.14 for the catalyst prepared from Pd(NO₃)₂. It is known that the fraction of linearly bonded CO increases with decreasing particle size, indicating that the Pd nanoparticles prepared from the Pd(NH₃)₄(OH)₂ catalyst have a surface with a greater number of edge and step sites.⁶¹ This is most likely a result of the improved metal dispersion and smaller average

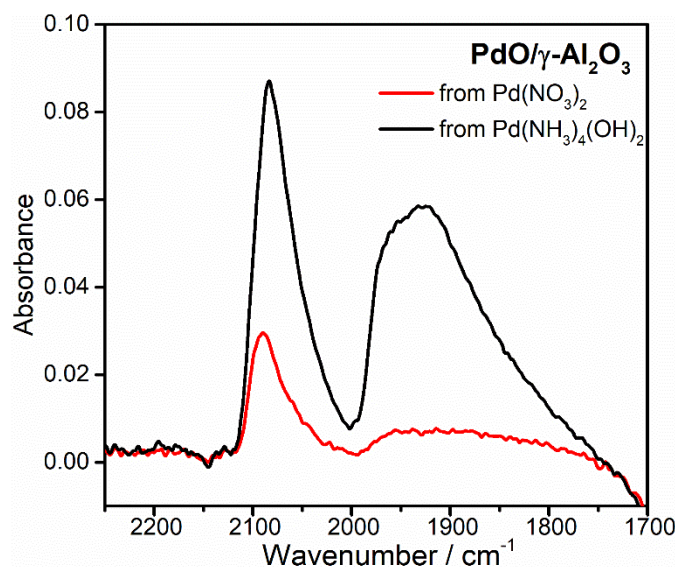


Figure 3.22. FTIR spectra of PdO/ γ -Al₂O₃ catalysts prepared by incipient wetness impregnation from Pd(NO₃)₂ (red) and Pd(NH₃)₄(OH)₂ (black) and calcination, then saturation of the surface sites with CO.

nanoparticle size – concluded from analysis of TEM images and Pd K-edge EXAFS - which means that a greater fraction of the Pd atoms in this catalyst are located at a nanoparticle surface which is composed of a greater number of step and edge sites rather than smooth terraces which would be found at the surface of larger particles.^{59, 62}

3.3.4 Catalytic Testing

The two calcined PdO/ γ -Al₂O₃ catalysts were tested for their catalytic activity in the low temperature methane oxidation. The light off tests, plotted in Figure 3.23, were conducted by measuring the CH₄ conversion as a function of temperature during a controlled temperature ramp experiment in a flow of synthetic natural gas feed, using a 'lean' fuel to oxygen ratio to replicate the conditions found with the CNG engine.⁶³ The light off curves suggest that the PdO/ γ -Al₂O₃ catalyst prepared from Pd(NH₃)₄(OH)₂ was able to achieve CH₄ oxidation at lower temperatures (50% CH₄ conversion at 385°C) than the PdO/ γ -Al₂O₃ catalyst that was prepared from Pd(NO₃)₂ (50% CH₄ conversion at 394°C). Considering the fast ramp rate of these light off tests (10°C min⁻¹), a difference in light off temperature of 9°C may be close to the experimental error, and so further tests are required to confidently assess the difference in catalytic activity for CH₄ oxidation between the two supported Pd/ γ -Al₂O₃ catalysts.

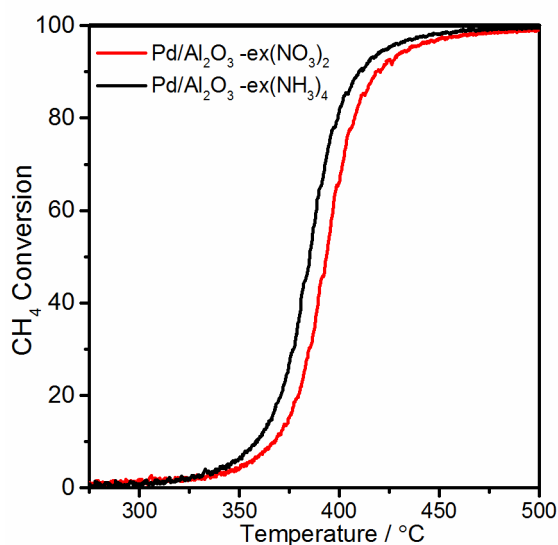


Figure 3.23. Percentage of CH₄ conversion over the PdO/ γ -Al₂O₃ catalysts during a temperature ramp with synthetic natural gas feed (0.5% CH₄, 10% O₂, 10% CO₂, 10% H₂O, 0.01% C₂H₆, 0.01% C₃H₈, 0.01% NO), measured by FTIR analysis of CH₄ concentration at the outlet compare to that at the inlet.

3.4 Discussion

The temperature range for PdO nanoparticle formation during the calcination treatment from two different impregnated Pd salts on γ -Al₂O₃ has been identified by Pd K-edge EXAFS. The Pd(NO₃)₂ precursor was found to form PdO nanoparticles at lower

temperature (203°C - 250°C) and with larger average particle size whereas the Pd species from the Pd(NH₃)₄(OH)₂ precursor remained well isolated up to high temperatures of the calcination treatment (400°C) and formed PdO nanoparticles with smaller average diameter. Pd(NO₃)₂/γ-Al₂O₃ showed significant intermolecular interaction before heat treatment, whereas Pd(NH₃)₄(OH)₂/γ-Al₂O₃ showed isolation of Pd centres. This is thought to be due to strong initial interactions of [Pd(NH₃)₄]²⁺ cations with negatively charged Al–O[−] surface sites (as surface Al–OH groups are deprotonated by OH[−] ions during incipient wetness impregnation), similarly to that reported for ion exchange of Pt(NH₃)₄(OH)₂ onto a SiO₂ surface.⁶⁴ The evidence for bidentate nitrate coordination to two Pd centres from the DRIFTS spectra of Pd(NO₃)₂/γ-Al₂O₃ shows that the nitrate ligands of the Pd(NO₃)₂ precursor have the ability to create bridging interactions between neighbouring Pd complexes at low temperatures of the calcination treatment (< 200°C). The separation distance of Pd centres of these bridging complexes was found to be ~3.43 Å which is the known separation distance of neighbouring Pd atoms in the crystal structure of PdO. Therefore, the early association of Pd centres from bridging nitrate interactions are thought to create an arrangement of Pd atoms that is favourable for the early formation of PdO nanoparticle structure. The formation of PdO from the Pd(NH₃)₄(OH)₂ precursor occurred simultaneously to the desorption of surface nitrosyl species from the γ-Al₂O₃ surface, which are formed by decomposition of NH₃ ligands and have been suggested to prevent the migration of Pd across the support. The stabilizing effect of NO[−]_(ads) species has been previously postulated in multiple studies by Sietsma *et al.*, whereby introducing NO gas into the calcination atmosphere was shown to suppress nanoparticle agglomeration over metal oxide support.^{65, 66} Therefore a combination of both high initial Pd dispersion and NO[−]_(ads) stabilization contributed to the later formation and suppressed growth of PdO nanoparticles from the Pd(NH₃)₄(OH)₂ precursor. The resulting supported Pd nanoparticle catalysts were found to show different characteristics in terms of their particle size and surface area. The PdO/γ-Al₂O₃ catalyst prepared from Pd(NH₃)₄(OH)₂ had a smaller average particle size, a larger specific surface area and a larger number of surface adsorption sites for CO adsorption. Consequently, the PdO/γ-Al₂O₃ catalyst prepared from Pd(NH₃)₄(OH)₂ is expected to have higher catalytic activity for CH₄ oxidation compared to the PdO/γ-Al₂O₃ catalyst prepared from Pd(NO₃)₂, which is indicated by the preliminary CH₄ oxidation light off tests.

3.5 Conclusions

A combined, *in situ* XAFS/DRIFTS method has been able to follow the formation of supported nanoparticle catalysts from oxidative decomposition of an impregnated molecular precursor. In this study two PdO/γ-Al₂O₃ catalysts were prepared from incipient wetness impregnation of two different precursors that resulted in catalysts with

different properties. The catalyst prepared from $\text{Pd}(\text{NH}_3)_4(\text{OH})_2$ benefited from smaller Pd particle size and improved dispersion over the support, which in turn favoured a lower light off temperature for CH_4 oxidation compared to the PdO catalyst prepared from $\text{Pd}(\text{NO}_3)_2$. By investigating the temperature of nucleation for nanoparticle formation and the decomposition pathways of the molecular precursor during the calcination process, it was possible to identify intermolecular reactions and stabilising mechanisms that dictated the dispersion of the resulting nanoparticle catalyst. The nucleation and growth of PdO nanoparticles during calcination was identified from the Pd K-edge EXAFS data by an increase in the scattering contribution from Pd neighbours located at a coordination distance (3.43 Å), consistent with the Pd–Pd distance of crystalline PdO. For $\text{Pd}(\text{NO}_3)_2/\gamma\text{-Al}_2\text{O}_3$, early association of Pd neighbours was observed in the EXAFS data of the sample before heat treatment; attributed to the bridging nature of nitrate ligands, evidenced by bidentate N=O and O–N–O nitrate stretching frequencies in DRIFTS spectra. For $\text{Pd}(\text{NO}_3)_2/\gamma\text{-Al}_2\text{O}_3$, there was significant PdO nanoparticle growth between 200°C – 250°C, whereas $\text{Pd}(\text{NH}_3)_4(\text{OH})_2/\gamma\text{-Al}_2\text{O}_3$ remained well isolated on the support until 400°C. Although NH_3 ligands were shown to decompose from the impregnated sample below 200°C, NH_3 was partially oxidized and small amounts of NO^- were captured by the $\gamma\text{-Al}_2\text{O}_3$ surface. This was evidenced by N=O stretching vibrations (1510 cm^{-1} and 1556 cm^{-1}) in DRIFTS spectra and evolution of m/z 30 in online mass spectrometry of the effluent gas upon their desorption. Strong ionic interaction of $[\text{Pd}(\text{NH}_3)_2]^{2+}$ with the support and the role of adsorbed NO^- resulted in stabilization of isolated Pd species on $\gamma\text{-Al}_2\text{O}_3$, such that PdO nanoparticle formation was suppressed until higher temperatures.

In this way, a combined XAFS and DRIFTS methodology has been used to study the formation of metal oxide nanoparticles from two different molecular precursors. There is scope for this method to be applied to study the formation of many other metal oxide nanoparticle catalysts. The method can be applied to study catalyst preparation routes from other metal precursors, provided that the molecular precursor has IR active bands that can be observed by DRIFTS, and the edge energy of the metal of interest is within the energy range of the beamline employed for XAFS measurements. Another aspect to consider is the path length through the sample within the XAFS/DRIFTS reactor used in this chapter. Modification of the sample chamber for the XAFS/DRIFTS measurements may allow an increased range of metals to be investigated.

3.6 References

1. P Munnik, PE de Jongh and KP de Jong, *Chem. Rev.*, 2015, **115**, 6687-6718.
2. CT Campbell, SC Parker and DE Starr, *Science*, 2002, **298**, 811-814.
3. A Cao, R Lu and G Veser, *Phys. Chem. Chem. Phys.*, 2010, **12**, 13499-13510.
4. JA Schwarz, C Contescu and A Contescu, *Chem. Rev.*, 1995, **95**, 477-510.

5. JI Villacampa, C Royo, E Romeo, JA Montoya, P Del Angel and A Monzón, *Appl. Catal. A: General*, 2003, **252**, 363-383.
6. JP Brunelle, *Pure Appl. Chem.*, 1978, **5**, 1211 - 1229.
7. RF Hicks, H Qi, ML Young and RG Lee, *J. Catal.*, 1990, **122**, 280-294.
8. C Chen, J Cao, M Cargnello, P Fornasiero and RJ Gorte, *J. Catal.*, 2013, **306**, 109-115.
9. S Yang, A Maroto-Valiente, M Benito-Gonzalez, I Rodriguez-Ramos and A Guerrero-Ruiz, *Appl. Catal. B: Environmental*, 2000, **28**, 223-233.
10. GHt Brink, G Krishnan, BJ Kooi and G Palasantzas, *J. Appl. Phys.*, 2014, **116**, 104302.
11. J Panpranot, S Kaewkun, P Praserttham and JG Goodwin, *Catal. Lett.*, 2003, **91**, 95-102.
12. M Schreier and JR Regalbuto, *J. Catal.*, 2004, **225**, 190-202.
13. T Cukic, M Holena, D Linke, D Herein and U Dingerdissen, in *Stud. Surf. Sci. Catal.*, eds. E. M. Gaigneaux, M. Devillers, D. E. De Vos, S. Hermans, P. A. Jacobs, J. A. Martens, P. Ruiz, Elsevier, 2006, vol. 162, pp. 195-202.
14. C Conțescu and MI Vass, *Appl. Catal.*, 1987, **33**, 259-271.
15. JT Miller, M Schreier, AJ Kropf and JR Regalbuto, *J. Catal.*, 2004, **225**, 203-212.
16. F Meneau, G Sankar, N Morgante, S Cristol, CRA Catlow, JM Thomas, *et al.*, *Nucl. Instrum. Meth. B*, 2003, **199**, 499-503.
17. AM Beale, AMJ van der Eerden, SDM Jacques, O Leynaud, MG O'Brien, F Meneau, *et al.*, *J. Am. Chem. Soc.*, 2006, **128**, 12386-12387.
18. G Sankar, T Okubo, W Fan and F Meneau, *Faraday Discuss.*, 2007, **136**, 157-166.
19. S Nikitenko, AM Beale, AMJ van der Eerden, SDM Jacques, O Leynaud, MG O'Brien, *et al.*, *J. Synchrotron Radiat.*, 2008, **15**, 632-640.
20. N Mahata and V Vishwanathan, *J. Catal.*, 2000, **196**, 262-270.
21. A Moronta, ME Troconis, E González, C Morán, J Sánchez, A González, *et al.*, *Appl. Catal. A: General*, 2006, **310**, 199-204.
22. M Benkhaled, S Morin, C Pichon, C Thomazeau, C Verdon and D Uzio, *Appl. Catal. A: General*, 2006, **312**, 1-11.
23. A Thiruvengadam, M Besch, V Padmanaban, S Pradhan and B Demirgok, *Energy Policy*, 2018, **122**, 253-259.
24. C Robinson and DB Smith, *J. Hazard Mater.*, 1984, **8**, 199-203.
25. H Yoshida, T Nakajima, Y Yazawa and T Hattori, *Appl. Catal. B: Environmental*, 2007, **71**, 70-79.
26. B Stasinska, A Machocki, K Antoniak, M Rotko, JL Figueiredo and F Gonçalves, *Catal. Today*, 2008, **137**, 329-334.
27. WR Schwartz and LD Pfefferle, *J. Phys. Chem. C*, 2012, **116**, 8571-8578.

28. RE Hayes, ST Kolaczowski, PKC Li and S Awdry, *Chem. Eng. Sci.*, 2001, **56**, 4815-4835.
29. A Hellman, A Resta, NM Martin, J Gustafson, A Trincherro, PA Carlsson, *et al.*, *J. Phys. Chem. Lett.*, 2012, **3**, 678-682.
30. NM Martin, M Van den Bossche, A Hellman, H Grönbeck, C Hakanoglu, J Gustafson, *et al.*, *ACS Catal.*, 2014, **4**, 3330-3334.
31. EK Gibson, AM Beale, CRA Catlow, A Chutia, D Gianolio, A Gould, *et al.*, *Chem. Mater.*, 2015, **27**, 3714-3720.
32. WP Davey, *Phys. Rev.*, 1925, **25**, 753-761.
33. WJ Moore and L Pauling, *J. Am. Chem. Soc.*, 1941, **63**, 1392-1394.
34. J Bruns, T Klüner and MS Wickleder, *Chemistry – A European Journal*, 2015, **21**, 1294-1301.
35. W Bohmer and P Rabe, *J. Phys. C Solid State*, 1979, **12**, 2465.
36. SP Khranenko, IA Baidina and SA Gromilov, *J. Struct. Chem.*, 2007, **48**, 1152-1155.
37. J Waser, HA Levy and SW Peterson, *Acta Crystallographica*, 1953, **6**, 661-663.
38. M Schmal, MMVM Souza, VV Alegre, MAP da Silva, DV César and CAC Perez, *Catal. Today*, 2006, **118**, 392-401.
39. FC Meunier, JP Breen, V Zuzaniuk, M Olsson and JRH Ross, *J. Catal.*, 1999, **187**, 493-505.
40. B Wichterlová, P Sazama, JP Breen, R Burch, CJ Hill, L Čapek, *et al.*, *J. Catal.*, 2005, **235**, 195-200.
41. X Chen, T Zhang, M Zheng, Z Wu, W Wu and C Li, *J. Catal.*, 2004, **224**, 473-478.
42. G Ramis and M Angeles Larrubia, *J. Mol. Catal. A-Chem*, 2004, **215**, 161-167.
43. MA Larrubia, G Ramis and G Busca, *Appl. Catal. B: Environmental*, 2000, **27**, L145-L151.
44. MA Larrubia, G Ramis and G Busca, *Appl. Catal. B: Environmental*, 2001, **30**, 101-110.
45. RQ Long and RT Yang, *Catal. Lett.*, **78**, 353-357.
46. J Taguchi and T Okuhara, *Appl. Catal. A: General*, 2000, **194–195**, 89-97.
47. M Jabłońska, A Król, E Kukulska-Zajac, K Tarach, L Chmielarz and K Góra-Marek, *J. Catal.*, 2014, **316**, 36-46.
48. B Westerberg and E Fridell, *J. Mol. Catal. A-Chem*, 2001, **165**, 249-263.
49. S Tamm, N Vallim, M Skoglundh and L Olsson, *J. Catal.*, 2013, **307**, 153-161.
50. S Kameoka, Y Ukisu and T Miyadera, *Phys. Chem. Chem. Phys.*, 2000, **2**, 367-372.
51. X Zhang, H He, H Gao and Y Yu, *Spectrochim. Acta A*, 2008, **71**, 1446-1451.

52. L Smrcok, V Langer and J Krestan, *Acta Crystallographica Section C*, 2006, **62**, i83-i84.
53. JI Langford and AJC Wilson, *J. Appl. Crystallogr.*, 1978, **11**, 102-113.
54. AV Vorontsov and SV Tsybulya, *Industrial & Engineering Chemistry Research*, 2018, **57**, 2526-2536.
55. MM Wolf, H Zhu, WH Green and GS Jackson, *Appl. Catal. A: General*, 2003, **244**, 323-340.
56. AM Beale and BM Weckhuysen, *Phys. Chem. Chem. Phys.*, 2010, **12**, 5562-5574.
57. D Tessier, A Rakai and F Bozon-Verduraz, *J. Am. Chem. Soc., Faraday Trans.*, 1992, **88**, 741-749.
58. RP Eischens, SA Francis and WA Pliskin, *J. Phys. Chem.*, 1956, **60**, 194-201.
59. GC Cabilla, AL Bonivardi and MA Baltanás, *Catal. Lett.*, 1998, **55**, 147-156.
60. M Haneda, M Todo, Y Nakamura and M Hattori, *Catal. Today*, 2017, **281**, Part 3, 447-453.
61. M Bäumer and H-J Freund, *Prog. Surf. Sci.*, 1999, **61**, 127-198.
62. RF Hicks and AT Bell, *J. Catal.*, 1984, **90**, 205-220.
63. A Raj, *Johnson Matthey Technology Review*, 2016, **60**, 228-235.
64. A Goguet, M Aouine, FJ Cadete Santos Aires, A De Mallmann, D Schweich and JP Candy, *J. Catal.*, 2002, **209**, 135-144.
65. JRA Sietsma, JD Meeldijk, JP den Breejen, M Versluijs-Helder, AJ van Dillen, PE de Jongh, *et al.*, *Angew. Chem. Int. Ed.*, 2007, **46**, 4547-4549.
66. JRA Sietsma, H Friedrich, A Broersma, M Versluijs-Helder, A Jos van Dillen, PE de Jongh, *et al.*, *J. Catal.*, 2008, **260**, 227-235.

Chapter Four. Identifying structure-function relationships of Pd catalysts for NH₃-SCO using an *operando* XAFS/DRIFTS/MS approach

4.1 Introduction

The selective catalytic oxidation of NH₃ (NH₃-SCO) is a viable solution for abatement of NH₃ slip from diesel exhaust. It relies on the performance of an efficient, selective catalyst material that is able to operate at low temperatures (< 500°C), with high conversion of ppm concentrations of NH₃. Currently the supported Pd nanoparticle catalysts possess the most promising catalytic performance in terms of high activity at low temperature with improved selectivity to N₂. However, the catalytic properties and reaction pathway over these materials is not well understood and so a combined, *operando* XAFS, DRIFTS and MS technique has been employed to identify structure-function relationships of the Pd nanoparticle catalyst during NH₃-SCO.

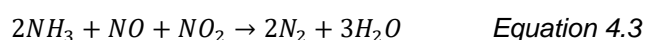
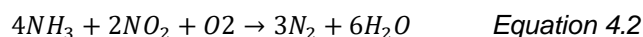
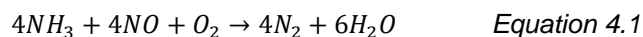
4.1.1 Diesel Exhaust After-treatment

Harmful emissions from the untreated exhaust of a diesel engine typically consist of gaseous hydrocarbons (HCs), carbon monoxide, nitrogen oxides (NO_x) and unburnt carbon particulates. A diesel oxidation catalyst (DOC) is able to remove HCs and CO, and a particulate filter removes the unburnt particulate matter however removal of NO_x is more challenging.

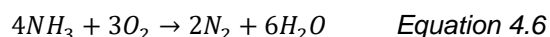
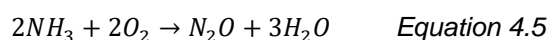
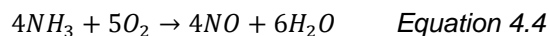
The abatement of NO_x from diesel exhaust has received much attention recently, as the Euro 6 emission legislation (Regulation (EC) No 715/2007)¹ implemented a 56% reduction of NO_x emissions (0.08 g km⁻¹) permitted from diesel vehicles compared to Euro 5 legislations (0.18 g km⁻¹).² NO_x refers collectively to nitric oxide and nitrogen dioxide gases, which cause respiratory problems upon inhalation and formation of acid rain. Vehicle manufacturers struggling to meet the Euro 6 legislation have been accused of cheating emission tests, reporting lower NO_x emissions from their testing vehicles than those driven on the roads³ and in June 2018 a young girl fell victim to NO_x pollution, reported as the first case of mortality directly linked to air pollution in the UK.⁴ This has put increased pressure on the performance of emissions control technology to improve the efficient removal of NO_x from both vehicle exhaust and industrial flue gases.

One of the current leading solutions for deNO_x technology is the reduction of NO_x using NH₃ (ammonia selective catalytic reduction, NH₃-SCR). The commercialised diesel exhaust fluid (DEF), AdBlue®⁵, is an NH₃-derived chemical that decomposes to NH₃ upon injection into the vehicle exhaust. NH₃ reacts with NO and NO₂ (Equations 4.1-4.3) to yield the benign products N₂ and H₂O. Improved efficiency of NO_x conversion

may be achieved by using a greater stoichiometry of NH₃, however, this results in a greater amount of NH₃ slip from the exhaust. NH₃ has now been added as an additional provision to the Euro 6 emission legislation, restricting NH₃ concentration from diesel exhaust to 10 ppm.²



An estimated 44 million tons of gaseous NH₃ are emitted globally each year.⁶ There are various methods for the removal of unreacted NH₃ leaving exhaust systems; absorption to the liquid phase with dilute acid solution,⁷ adsorption to the surface of highly porous materials,⁸ low temperature and high pressure liquefaction,⁹ biofiltration,¹⁰ thermal oxidation¹¹ and selective catalytic oxidation.¹² Selective catalytic oxidation of NH₃ (NH₃-SCO) poses a promising solution for efficient elimination of small concentrations of gaseous NH₃, that can be implemented downstream of the NH₃-SCR converter of stationary or mobile exhaust systems. Oxidation of NH₃ in air would lead to the unwanted NO_x products, via Equations 4.4 and 4.5, therefore research into a high performance catalyst for the selective reaction pathway, Equation 4.6, is required to achieve high conversion of NH₃ to N₂ and H₂O.



The catalyst must operate with high selectivity to N₂ in a relatively low temperature (150 - 400°C) range due to significant cooling of the exhaust gas downstream of the engine. The catalyst must be resistant to additional gases found in diesel exhaust such as H₂O, CO₂ and SO₂, and be able to tolerate fluctuating NH₃ concentrations and temperatures as the exhaust changes with different drive cycles of the engine.

4.1.2 Noble metal catalysts for NH₃-SCO

There has been little research into heterogeneous catalysts for NH₃-SCO in the gas phase until 2010s, with most literature before then focused on the catalytic oxidation in wet conditions.¹³ Noble metals supported on metal oxide have repeatedly been used to catalyse oxidation reactions at relatively low temperatures, and promising activity for NH₃ oxidation has been reported with Pt, Pd, Ag, Rh, Ir and Ru catalysts.¹⁰⁸⁻¹¹³ The catalytic activity for NH₃ conversion and selectivity towards N₂ are given in Table 4.1, for a variety of supported noble metal catalysts. Direct comparison between these catalysts is difficult due to the different reactant concentrations, flow rate and quantity of catalyst used in each case. The greatest activity was reported for the 1%Pt/γ-Al₂O₃

and 1.2% Rh/ γ -Al₂O₃ reduced catalysts, which achieved complete NH₃ conversion at 200°C, although only 75% selectivity to N₂.¹⁴ Improved N₂ selectivity was achieved on the Pd/ γ -Al₂O₃, Rh/ γ -Al₂O₃ and Pd/zeolite-Y catalysts, with the best combination of activity and selectivity achieved with 1.5% Pd/zeolite-Y. Jabłońska *et al.* have investigated the effect in catalytic performance of different Pd loading on the zeolite-Y (0.05% - 2.5%), and found that 1.5wt% Pd achieved the greatest activity without compromising selectivity.¹⁵

Table 4.1. Comparison of NH₃ conversion and N₂ selectivity of a selection of supported noble metal catalysts reported in the literature.

Catalyst	NH ₃ Conversion / %	N ₂ selectivity / %	Reaction Conditions	Ref.
1% Pt/ γ -Al ₂ O ₃	34	48	220°C, 500 ppm NH ₃ , 10% O ₂ , 200 cm ³ min ⁻¹ , 0.2 g catalyst	¹⁶
1.2% Pt/ γ -Al ₂ O ₃ reduced	100	75	200°C, 1.14% NH ₃ , 8.21% O ₂ , 74.7 cm ³ min ⁻¹ , 0.2 g catalyst	¹⁴
1.5% Pt/ZSM-5	98	41	250°C, 1000 ppm NH ₃ , 2% O ₂ , 500 cm ³ min ⁻¹ , 0.06 g catalyst	¹⁶
4.2% Pd/ γ -Al ₂ O ₃	84	97	250°C, 1000 ppm NH ₃ , 4% O ₂ , 100 cm ³ min ⁻¹ , 0.1 g catalyst	¹⁷
1.2% Pd/ γ -Al ₂ O ₃ reduced	60	97	250°C, 1.14% NH ₃ , 8.21% O ₂ , 74.7 cm ³ min ⁻¹ , 0.2 g catalyst	¹⁴
4.1% Pd/ ZSM-5	94	75	250°C, 1000 ppm NH ₃ , 4% O ₂ , 100 cm ³ min ⁻¹ , 0.1 g catalyst	¹⁷
1% Pd/zeolite-Y	87	97	250°C, 0.5% NH ₃ , 2.5% O ₂ , 40 cm ³ min ⁻¹ , 0.1 g catalyst	¹²
2.7% Rh/ γ -Al ₂ O ₃	84	97	250°C, 1000 ppm NH ₃ , 4% O ₂ , 100 cm ³ min ⁻¹ , 0.1 g catalyst	¹⁷
1.2% Rh/ γ -Al ₂ O ₃ reduced	100	75	200°C, 1.14% NH ₃ , 8.21% O ₂ , 74.7 cm ³ min ⁻¹ , 0.2 g catalyst	¹⁴
2.7% Rh/ZSM-5	9	95	250°C, 1000 ppm NH ₃ , 4% O ₂ , 100 cm ³ min ⁻¹ , 0.1 g catalyst	¹⁷

Although high NH₃ conversion may have been achieved with these catalyst materials, the major drawback is the lack of selectivity to N₂ which is an essential criteria for these catalysts to avoid the reformation of harmful NO_x. The catalyst selectivity is a crucial requirement of these NH₃-SCO catalysts that must be considered before efforts to optimise for long term stability against H₂O, CO₂ and SO_x in the exhaust, and lowering their production cost.

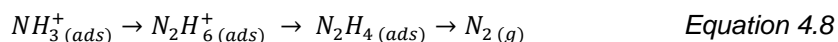
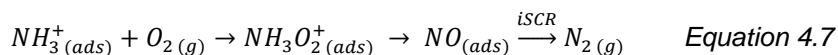
4.1.3 Alternative non-noble metal catalysts for NH₃-SCO

The most promising reported zeolite based catalysts – apart from those impregnated with precious metals – are Cu-exchanged and Fe-exchanged zeolites. Gang *et al.* found that zeolite-Y exchanged with 8.4wt% Cu was able to achieve 88% NH₃ conversion and 98% selectivity to N₂ at 300°C.¹⁸ Comparably a study by Long *et al.* found the Fe-ZSM-5 catalyst to be highly selective, able to achieve 99% selectivity to N₂ at 500°C.¹⁹ Of the tested transition metal oxide catalysts, the most promising was the CuO/Al₂O₃, deposited as 10wt% Cu, which was reported to achieve 90% NH₃ conversion and 97% N₂ selectivity at 300°C.^{14, 18} The active component of the Cu/Al₂O₃ catalyst has repeatedly been attributed to the formation of a CuAl₂O₄ spinel phase.^{12,15,20}

Of course moving away from the use of precious metals in new technologies is always desirable, due to the finite reserve of noble metals and the expense associated with extracting them. For some industrial processes, the exchange of conventional precious metal catalysts for alternative materials has not only reduced the cost of the process but has been able to achieve improved reaction kinetics and efficiency.^{21, 22} The main drawback to these transition metal ion exchanged zeolite catalysts is the poor activity in the low temperature range < 400°C, compared to precious metal analogues. Therefore, supported precious metal catalysts are still regarded as the most promising materials for the NH₃-SCO reaction.

4.1.4 *In situ* studies of NH₃-SCO catalysts

According to DFT studies, the catalytic mechanism for NH₃-SCO has been proposed to proceed by two different reaction mechanisms; the first is an indirect pathway suggested to prevail under oxygen abundant conditions (Equation 4.7), and the second is a direct pathway suggested to occur under anaerobic conditions (Equation 4.8). The indirect route involves first the oxidation of NH₃ to NO, which is subsequently reduced by reaction with another NH₃. The indirect route is expected to proceed through the formation of a nitrosyl intermediate [NH₃O₂⁺_(ads)], whereas the direct route is expected to involve nitrogen coupling to hydrazine species [N₂H₂_(ads)].²³ *In situ* FTIR studies have been able to evidence both of these species on metal oxide surfaces, so the residing mechanism has remained unclear.^{24, 25}



The above mentioned studies for NH₃-SCO catalysts have used conventional *ex situ* characterisation techniques such as XRD,²⁶⁻²⁸ XPS²⁷ and XAFS²⁰ in the material characterisation. NH₃-TPD has been used frequently to look at the adsorption properties of the catalyst²⁸⁻³⁰ and few studies have been able to draw conclusions for the catalyst function by using *in situ* DRIFTS³¹, *in situ* FTIR^{32, 33} and DFT methods³¹. However, the lack of combined spectroscopic techniques – or *operando* spectroscopy – means that there is a lack of understanding for the catalyst structure-function relationships, particularly for the highly selective Pd-based catalysts.

4.2 Methods

4.2.1 Sample Preparation

Supported 1.5wt% Pd catalysts were prepared by incipient wetness impregnation of an acidified aqueous solution of palladium nitrate (15.11 wt% Pd, Johnson Matthey) onto the commercial support; γ -Al₂O₃ (SASOL) and zeolite–Y (Zeolyst, CBV600, H-form, SiO₂/Al₂O₃ molar ratio of 5.2). Incipient wetness impregnation was carried out at room temperature. The impregnated supports were subsequently dried at 100°C, then calcined in air at 500°C for 2 hours.

4.2.2 Ex situ Characterisation

TEM images of the samples were obtained using a JEOL JEM 2100 transmission electron microscope. Samples were prepared for TEM analysis by dispersing the catalyst powder in high-purity ethanol using ultrasonication. 1 μ L of the sonicated suspension were pipetted onto a holey carbon supporting Cu grid, and the solvent evaporated.

4.2.3 Catalytic Testing

The catalytic testing was conducted at Johnson Matthey Technology Centre, Sonning Common. The reactor used 0.4 g catalyst as pressed pellets (425 – 250 μ m), loaded into a cylindrical fixed bed with a diameter of 11.3 mm and height of 15 mm. The activity test involved increasing the temperature of the reactor to 100°C before introducing the reactant gas feed (0.5% NH₃, 2.5% O₂, 97% N₂) at a total flow rate 1800 cm³ min⁻¹. The reactor temperature was increased at a constant rate of 5°C min⁻¹ and the catalyst temperature was recorded using an internal thermocouple positioned at the inlet of the fixed catalyst bed. The exhaust gases were sent to an FTIR analyser (recording the IR active gaseous products NO, H₂O, NO₂ and NH₃) and conversion values calculated relative to the inlet NH₃ signal. The N₂ formation was calculated by considering the nitrogen mass balance.

4.2.4 *In situ* Pd L₃-edge XANES

In situ Pd L₃-edge XANES (3175 eV) were collected in fluorescence mode at the XMaS beamline of the ESRF. The catalyst sample (125-250 μm pellet fraction) was contained between two Kapton windows as a packed bed within a 100 μm trench of a flow reactor, reported elsewhere.³⁴ The reactor was mounted within a He chamber and connected to gas lines for flow of reactant gases to the sample. The effluent flow from the reactor was sent to a Hiden QGA mass spectrometer. The temperature was controlled by a thermocouple inserted close to the catalyst bed. The energy range (3150 – 3220 eV) was selected using a double crystal Si(III) monochromator and spectra were collected using a fluorescence detector at 90° to the x-ray beam and with the sample orientated 45° to the incoming beam. The detector was tuned to measure the intensity of the Pd Lα₁ (2838 eV) fluorescence line. Each scan measured 265 points with a counting time of 5 seconds per point, taking a total time of 22 minutes per spectrum. The experimental procedure consisted of online pre-treatment at 200°C in a reducing (5% H₂/He) atmosphere. The reactant gas mixture was introduced (0.5% NH₃, 2.5% O₂, 97% He) at 100°C with a total flow of 40 cm³ min⁻¹, before ramping 2.5°C min⁻¹ to 200°C. The experimental procedure was repeated with a fresh sample, performing the same pre-treatment but then introducing an NH₃ only gas mixture (0.5% NH₃, 99.5% He) to characterise the sample in the absence of oxygen. The Pd hydride reference sample was formed *in situ* by cooling the sample to room temperature in 10% H₂/He.

4.2.5 XPS

4.2.5.1 *In situ* XPS

The *in situ* XPS measurements were conducted at beamline B07 Diamond Light Source, using an *in situ* sample chamber with mbar gas pressure. The catalyst powder (100 mg) was pressed to an 8 mm diameter pellet and held in place on the sample holder with tungsten foil, shown in Figure 4.1. The sample holder was positioned in the measurement chamber at 10⁻⁹ bar, and heated to 200°C. After cooling to 100°C, 0.5 mbar Ar atmosphere was introduced and XPS spectra of Pd 3d, Al 2p and N1s were collected using incident photon energy 900 eV, pass energy 50 eV and exposure 0.5 seconds. The sample was treated *in situ* with 49.5 mbar NH₃/0.5 mbar Ar atmosphere at 100°C for 15 mins, before measuring XPS spectra of Pd 3d, Al 2p and N 1s in 1 mbar NH₃ at 100°C using the same acquisition method.

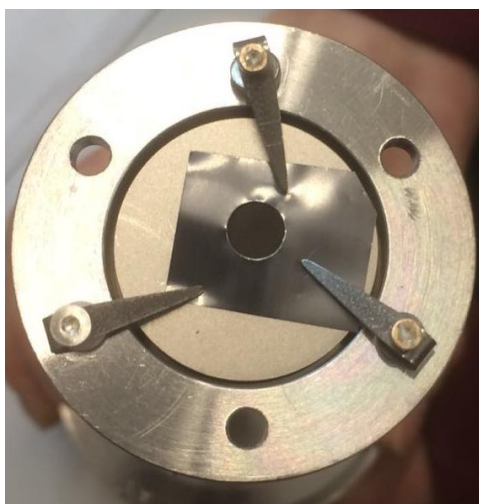


Figure 4.1. Supported Pd catalyst pressed into an 8 mm diameter pellet and mounted onto the mounting post of the tea cup reaction chamber for *in situ* XPS using Tungsten wire.

4.2.5.2 *Ex situ* XPS

Ex situ XPS analysis was performed with a Kratos AXIS Ultra DLD apparatus, equipped with monochromated Al K α radiation x-ray source, a charge neutralizer and a hemispherical electron energy analyser. During data acquisition, the chamber pressure was kept below 10 mbar. The spectra were analysed using the CasaXPS software package and binding energies calibrated by using the C 1s binding energy peak as the reference at 284.8 eV.

4.2.6 Combined, *operando* Pd K-edge XAFS/DRIFTS/MS

Operando XAFS and DRIFTS measurements were conducted at SuperXAS X10DA, Swiss Light Source, Paul Scherrer Institute, using a previously reported Harrick DRIFTS cell^{35, 36} integrated with an Agilent Carey 680 FTIR spectrometer. A DaVinci arm accessory fitted with praying mantis optics was used to refocus the IR beam outside the FTIR spectrometer for positioning of the Harrick DRIFTS cell in the x-ray path. The Harrick DRIFTS cell has an x-ray path length of 3.17 mm through the sample positioned 1.04 mm below the surface of the catalyst bed. The experiment used a controlled flow of mixed gases into the reaction chamber under atmospheric pressure using Brooks mass flow controllers, and the temperature of the catalyst was controlled and monitored by a thermocouple positioned inside the catalyst bed. Each run used ~10 mg of pelletized (125 - 250 μm) catalyst. XAFS measurements were performed at the Pd K-edge (24358 eV) in transmission mode using QEXAFS setup with an oscillating Si(311) double crystal monochromator operating at 1 Hz. All XAFS spectra were acquired with a Pd foil placed between I_t and I_r , and the time resolution was 0.5 seconds per spectrum ($k_{\text{max}} = 16.2 \text{ \AA}^{-1}$). DRIFTS spectra were collected taking 64 scans with a resolution of 4 cm^{-1} using the liquid nitrogen cooled MCT detector. The time resolution of DRIFTS were 30 seconds per spectrum (400 – 4000 cm^{-1}). At the

same time, the composition of effluent gas was measured using a mass spectrometer (Hiden QGA) for H₂ ($m/z = 2$), He ($m/z = 4$), NH₃ ($m/z = 17$), H₂O ($m/z = 18$), N₂ ($m/z = 28$), NO ($m/z = 30$), O₂ ($m/z = 32$), N₂O ($m/z = 44$) and NO₂ ($m/z = 46$). The experimental procedure consisted of online pre-treatment at 400°C in a reducing (5% H₂/He) atmosphere, then cooling to 100°C in He. The reactant gas mixture was introduced (0.5% NH₃, 2.5% O₂, 97% He) at 100°C with a total flow of 50 cm³ min⁻¹, before ramping at a rate of 2.5°C min⁻¹ to 400°C. Background DRIFTS spectra were recorded during a flow of He at 100°C and subtracted from the sample spectrum for each measurement.

The *ex situ* Pd K-edge XAFS spectrum of a reference PdO sample was measured at ambient conditions on B18, Diamond Light Source. The XAFS spectrum was acquired in transmission mode using QEXAFS setup with a fast scanning Si(311) double crystal monochromator. Calibration was achieved using a Pd foil placed between I_t and I_{ref} . The acquisition time was 21 seconds, collecting to a k range of 14.7 Å⁻¹.

4.2.7 DFT + D3 Calculations.

All computational work in this chapter was carried out by Dr Arunabhiram Chutia and Dr Constantinos Yeinalipour-Yazdi. All the spin polarized periodic density functional theory based calculations were performed using Vienna Ab Initio Simulation Package (VASP).³⁷⁻³⁹ The projector augmented wave (PAW) method was used and the cut-off energy for the expansion of the plane-wave basis sets was set to 550 eV, which gave bulk energies converged to within 10⁻⁵ eV.⁴⁰ A convergence criterion of 0.01 eV Å⁻¹ was chosen for structural optimizations and a k -point grid of 3×3×1 was employed for all slab calculations. Benchmark calculations were used to check the results obtained with Monkhorst-Pack k -point grids of different grid densities which gave negligible differences in adsorption energies. A smearing value of 1 was used, which is recommended in the VASP manual to be appropriate for metals,⁴¹ and a partial occupancy value of 0.2. Benchmark calculations were used to check the influence of the partial occupancy value on the calculated adsorption energies. The Perdew-Burke-Ernzerhof (PBE) version of generalized gradient approximation (GGA) was used to carry out geometry optimizations and the total energy calculations.⁴² The ideal Pd(111) surfaces were modelled by a 2×2 cell with seven atomic layers. For calculations involving the adsorption of NH₃, of the seven atomic layers the bottom four layers were fixed to mimic the bulk of the material. The slabs were cut from bulk Pd with a calculated energy minimized lattice constant of 3.904 Å (which compares well with the experimental value of 3.891 Å) while in the direction perpendicular to the surface, a vacuum gap of ~15 Å was used. To check the increase in the Pd–Pd distances due to the presence of interstitial N-atoms series of calculations were performed by systematically increasing the number of N-atoms at the interstitial positions. For all these calculations, N-atoms were placed close to both the exposed surfaces and

relaxed the atomic coordinates within a fixed cell. This study was extended to clarify the influence of the interstitial N-atoms on the adsorption properties of NH₃ molecule on the Pd(111) surface. The adsorption of the NH₃ molecule was allowed on only one of the two exposed surfaces. The dipole moment, due to the adsorbed species, was taken into account by using the methods implemented in VASP according to the procedures of Markov *et al.* and Neugebauer *et al.*^{43, 44} In this study, Grimme's dispersion correction (DFT+D3) were employed as dispersive effects might be significant for such systems.⁴⁵ The climbing-image nudged elastic band (CI-NEB) method was employed to determine the minimum energy path for evaluating the activation energy barrier for the diffusion of interstitial N-atom.⁴⁶

4.3 Results

4.3.1 *Ex situ* characterisation

Two supported 1.5wt% Pd catalysts were prepared by incipient wetness impregnation to yield PdO/ γ -Al₂O₃ and PdO/zeolite-Y. The Pd K-edge XANES of the supported PdO catalysts after impregnation and calcination (Figure 4.2) can be matched with that of the PdO reference sample, showing that the Pd species exist as PdO.

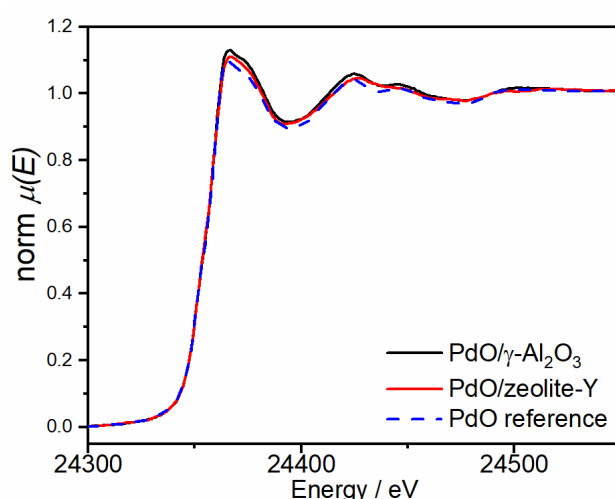


Figure 4.2. Normalised Pd K-edge XANES of PdO/ γ -Al₂O₃ and PdO/zeolite-Y after calcination treatment in air, plotted together with that of a reference PdO sample.

TEM images of the supported PdO catalysts, shown in Figure 4.3, show the contrast of dark PdO nanoparticles imaged against the less absorbing support material. The images show that the particles are fairly uniform in size and shape and are well dispersed over the support, in each case. By measuring the diameter of 100 particles, the average particle sizes of PdO/ γ -Al₂O₃ and PdO/zeolite-Y were found to be 4.1 nm and 5.7 nm, respectively. The histogram of particle size distribution in Figure 4.3 shows that PdO/ γ -Al₂O₃ has a narrow particle size distribution compared to Pd/zeolite-Y which has a number of particles > 8 nm.

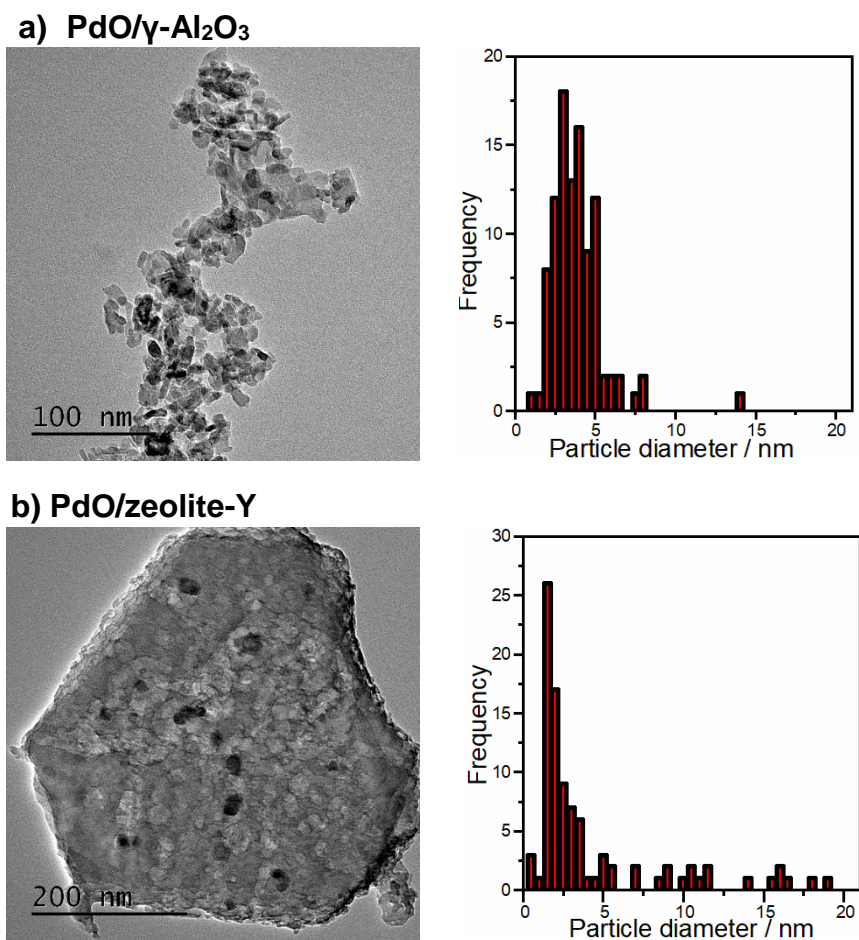


Figure 4.3. TEM images and corresponding histogram of particle size distribution of calcined catalysts **a)** PdO/ γ -Al₂O₃ (top) and **b)** PdO/zeolite-Y (bottom).

After treating the catalyst samples in 5%H₂/He, the measured Pd K-edge XANES could be matched to that of Pd foil (shown in Figure 4.4), with small differences attributed to particle size and temperature effects.⁴⁷ The reduction treatment in H₂/He was performed at elevated temperature (200°C) and the gas flow switched to inert (He) before cooling to avoid formation of Pd hydride species. The XANES spectra in Figure 4.4 therefore confirm that the PdO nanoparticles, PdO/ γ -Al₂O₃ and PdO/zeolite-Y, were reduced to metallic Pd nanoparticles, Pd/ γ -Al₂O₃ and Pd/zeolite-Y, respectively. The Fourier transformed Pd K-edge EXAFS spectra of the reduced Pd catalysts (Figure 4.4b) were fitted with a model constructed from a single scattering path of Pd-Pd at a coordination distance of 2.734 Å. The amplitude reduction factor, S_0^2 , was found to be 0.8 by fitting the model first to the Pd K-edge EXAFS of Pd foil, and setting the coordination number of the single Pd-Pd scattering path to 12. Pd K-edge EXAFS of Pd/ γ -Al₂O₃ and Pd/zeolite-Y could be fitted with a Pd-Pd coordination number of 9.7 and 11.3, respectively, using a value of 0.8 for S_0^2 . The average particle diameters of the reduced Pd nanoparticles were calculated from these Pd-Pd coordination numbers using the exponential Hill function, (a method reported by Beale *et al.*⁴⁸), which gave average particle diameters of 2.1 nm and 5.2 nm for Pd/ γ -Al₂O₃ and Pd/zeolite, respectively. These values are in agreement with the average particle size calculated

from TEM images, considering EXAFS is able to account for the isolated Pd atoms that are not observed by TEM and thus always give a slightly smaller average particle size.

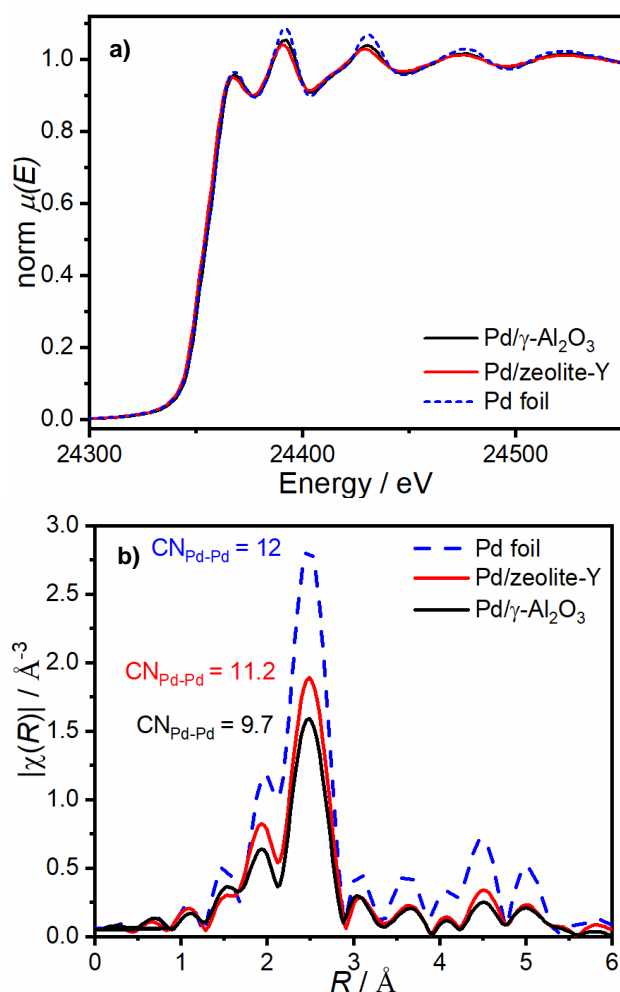


Figure 4.4. **a)** Pd K-edge XANES of Pd/ γ -Al₂O₃ and Pd/zeolite-Y after reduction treatment in H₂, plotted with Pd K-edge XANES of Pd foil reference. **b)** Fourier transformed Pd K-edge EXAFS of Pd/ γ -Al₂O₃ and Pd/zeolite-Y after reduction treatment in H₂, plotted with Pd foil reference, annotated with coordination numbers found by fitting to a model constructed from a single scattering path Pd-Pd.

4.3.2 Catalytic Testing

The calcined PdO catalysts were tested for catalytic NH₃ oxidation using a reactant gas feed of 0.5% NH₃, 2.5% O₂ and 97% N₂, at increasing temperatures from 100°C - 500°C. Figures 4.5a and 4.5b show the NH₃ conversion and product distribution from NH₃ oxidation over catalysts PdO/ γ -Al₂O₃ and PdO/zeolite-Y, respectively. Both catalysts show similar reactivity with a sharp increase of NH₃ consumption beyond 215°C, 50% NH₃ conversion achieved by 250°C, and 100% conversion achieved by 285°C. This is in line with previous literature for high activity of Pd catalysts for NH₃-SCO,¹² in particular 1.5wt% Pd supported on zeolite-Y.¹⁵ The product distribution from these catalysts changes upon increasing the temperature. In the low temperature region $T_1 < 250^\circ\text{C}$, there was high selectivity to N₂. In the mid-temperature region there was significant formation of nitrous oxide (N₂O), a decrease in N₂ formation and onset of

nitric oxide (NO). In the high temperature region $> 300^{\circ}\text{C}$, there was further decrease in the formation of N_2 , decrease in N_2O formation but a large increase in formation of NO. These tests show that the different support material does not have a significant effect on the catalytic activity or selectivity of NH_3 oxidation. The Pd nanoparticles achieved high activity and selectivity at low temperature, with unfavourable formation of nitrogen oxides at high temperatures $> 250^{\circ}\text{C}$.

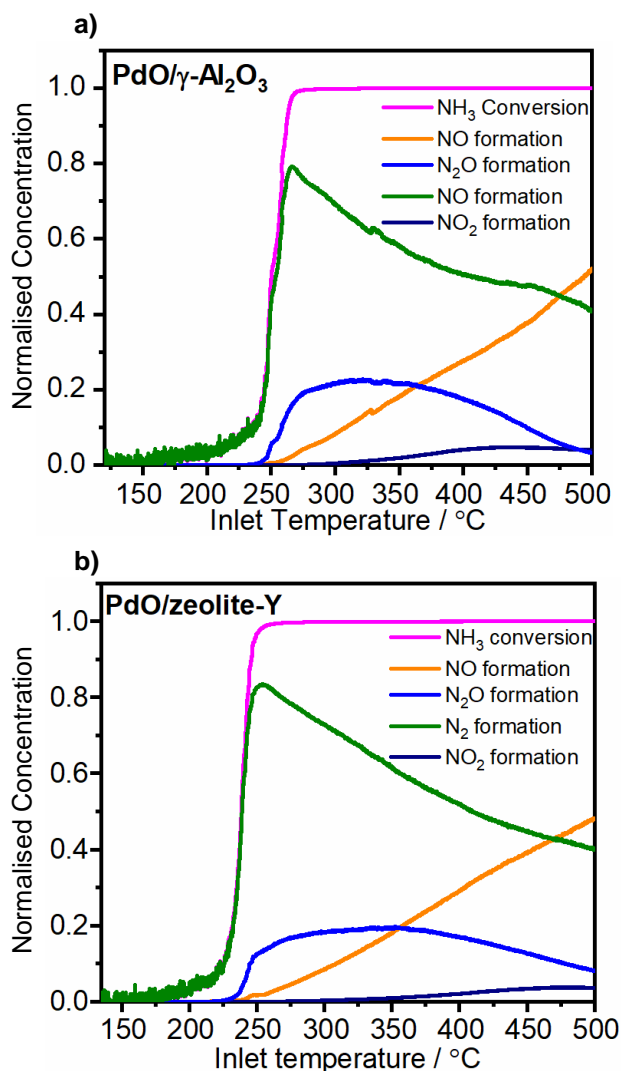


Figure 4.5. NH_3 conversion and product distribution of $\text{NH}_3\text{-SCO}$ over supported Pd catalysts **a)** $\text{PdO}/\gamma\text{-Al}_2\text{O}_3$ (top) and **b)** $\text{PdO}/\text{zeolite-Y}$ (bottom), during temperature ramp with 0.5% NH_3 , 2.5% O_2 , 97% N_2 reactant gas feed. At a total flow rate of $1800\text{ cm}^3\text{ min}^{-1}$. Gases (NH_3 , NO , N_2O and NO_2) detected by FTIR, N_2 formation calculated by mass balance.

4.3.3 *In situ* Pd L₃-edge XANES

Both supported Pd catalysts were investigated during the low temperature reaction conditions for NH₃-SCO by Pd L₃-edge XANES. The Pd L₃-edge involves absorption of x-rays by electrons in the Pd 2p orbitals, allowing transition into vacant d orbitals, therefore probing the empty d density of states. This can provide useful information for the oxidation state of the Pd atoms and any molecular bonding. The catalyst was loaded into a bespoke *in situ* cell – used for XANES measurements of a sample under gas flow at relatively low x-ray energies. The sample was heated to 100°C and treated with different gas environments. The Pd L₃-edge XANES of the calcined catalyst, PdO/γ-Al₂O₃, and the catalyst after a reduction pre-treatment (in 5% H₂ at 200°C), Pd/γ-Al₂O₃, are shown in Figure 4.6 against the Pd L₃-edge XANES spectrum of Pd foil. The strong, sharp and symmetric white line for the spectrum of PdO/γ-Al₂O₃ is characteristic of Pd²⁺ species of PdO, due to transition of 2p electron to the partially occupied Pd 4d band.⁴⁹ Whereas the Pd L₃-edge XANES of Pd/γ-Al₂O₃ displays low intensity absorption at 3175.5 eV, matching closely to that of Pd foil, due to transition of the 2p electron into the conduction band above the Fermi level.⁴⁹ This shows that the Pd catalyst after the reduction treatment existed in the metallic state.

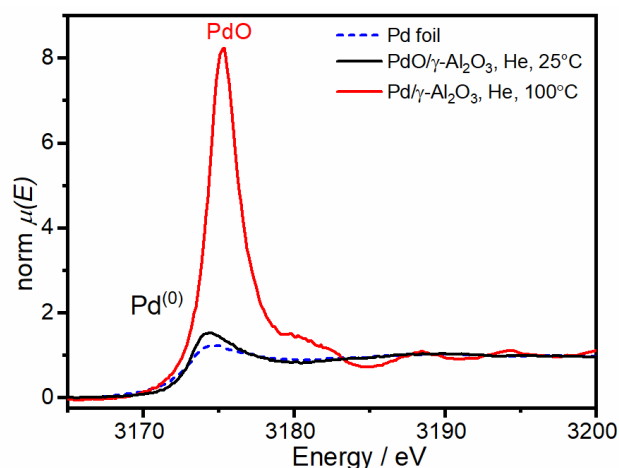


Figure 4.6. Pd L₃-edge XANES of supported Pd catalyst after calcination treatment (PdO/γ-Al₂O₃) and after a reduction treatment (Pd/γ-Al₂O₃). Plotted together with Pd L₃-edge XANES of Pd foil.

The Pd L₃-edge XANES in Figure 4.7a show the reduced, Pd/γ-Al₂O₃ catalyst measured in an inert atmosphere (He), after switching to the reactant gas feed (NH₃/O₂), and after cooling to room temperature in 5% H₂/He. The formation of palladium hydride upon cooling the sample to room temperature in H₂ is observed by the distinct absorption feature at 3182 eV in Figure 4.7a which is due to excitation of 2p electrons to the Pd-H antibonding state.⁵⁰⁻⁵² After switching to the reactant gas feed (NH₃/O₂/He), the Pd L₃-edge XANES showed increased intensity and broadening of the white line (Figure 4.7a) but without the characteristic absorption feature at 3182 eV for palladium hydride. This suggests increased vacancies in the d band, usually associated with oxidation of the Pd species. However, upon repeating this experiment

but switching from an inert (He) gas feed to the NH₃/He only gas feed at 100°C (Figure 4.7b), it is shown that the same result is obtained in the absence of oxygen. This points towards the oxidation of Pd due to electron donation to another heteroatom – such as nitrogen. The *in situ* formation of palladium carbide has previously been reported by Tew *et al.* during the hydrogenation of pent-1-yne, and is similarly characterised by increased intensity and broadening of the white line in its Pd L₃-edge XANES spectrum.^{53, 54} Therefore the formation of an interstitial compound akin to palladium carbide is suggested to form in the presence of NH₃ and the NH₃/O₂ reaction mixture, however the absence of carbon during this experiment leads us to infer the formation of a palladium nitride species (PdN_x).

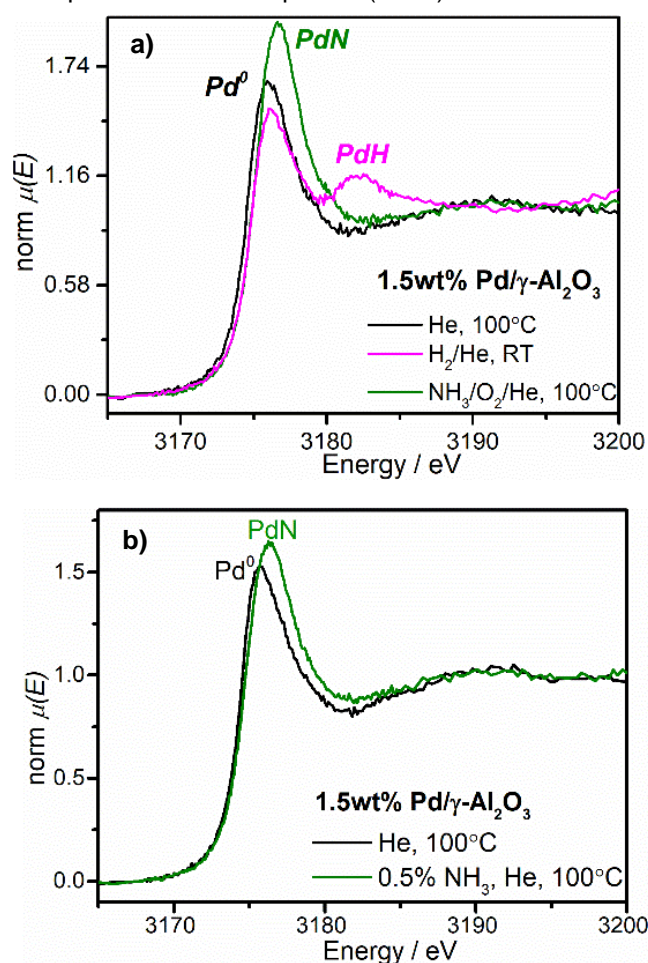


Figure 4.7. Pd L₃-edge XANES of supported Pd catalyst, Pd/ γ -Al₂O₃, after a reduction pre-treatment in H₂, then exposure to **a)** inert He at 100°C (black), 5 % H₂ at room temperature (magenta) and 0.5%NH₃/2.5%O₂/He at 100°C (green) and **b)** 0.5% NH₃/He (green) at 100°C.

4.3.4 XPS

3.3.4.1 *In situ* XPS

XPS was used as an additional characterisation technique to understand the electronic properties of the nitrogen species, as well as the Pd species of the supported Pd catalysts in an NH₃ atmosphere at elevated temperatures. Unlike XAFS, the XPS

spectra can obtain electronic information from multiple elements within the surface of the sample. The *in situ* measurements were collected at beamline B07 Diamond Light Source. The PdO/ γ -Al₂O₃ sample was reduced (in 5% H₂/He, 200°C) prior to loading into the reaction chamber so that the nanoparticles were investigated in their metallic state. The catalyst was heated to 200°C in vacuum before exposing to mbar pressures of Ar and NH₃ gases. The N 1s spectra of the Pd/ γ -Al₂O₃ catalyst before and after introducing the NH₃ atmosphere are shown in Figure 4.8a. The first spectrum collected under inert (0.5 mbar Ar) atmosphere shows one small symmetric peak at a binding energy of 399 eV which can be attributed to nitrogen-containing contaminants at the catalyst surface. The N 1s spectrum collected in NH₃ atmosphere (1 mbar NH₃) can be deconvoluted into two peaks for presence of nitrogen in two different environments. The high intensity peak at 401 eV, can be attributed to a large amount of nitrogen in NH₃ molecules adsorbed at the catalyst surface. The second broader peak with lower intensity is centred at 394 eV which is consistent with nitrogen found in metal nitrides.^{55, 56} Similarly, the Pd 3d binding energy spectra of the Pd/ γ -Al₂O₃ catalyst before and after introducing the NH₃ atmosphere are shown in Figure 4.8b. The Pd 3d spectrum collected before NH₃ treatment shows two peaks due to the separated spin orbit components of the 3d orbitals (3d_{5/2} and 3d_{3/2}) at 331 and 336 eV, which are consistent with the 3d binding energies for reduced Pd species.⁵⁶ After treatment in NH₃, these peaks shifted by ~4 eV to higher binding energies suggesting oxidation of Pd species, which can be explained by electron donation from Pd to N in the formation of the proposed PdN_x species. There was difficulty in collecting these XPS spectra due to electronic charging effects caused by the insulating properties of the Al₂O₃ support. During XPS measurements, emission of electrons from the sample caused accumulation of positive charge at the sample surface which could not be neutralised easily. Electronic charging resulted in shifting of XPS peaks to higher binding energies, making it difficult to follow real changes in the measured electronic binding energies.

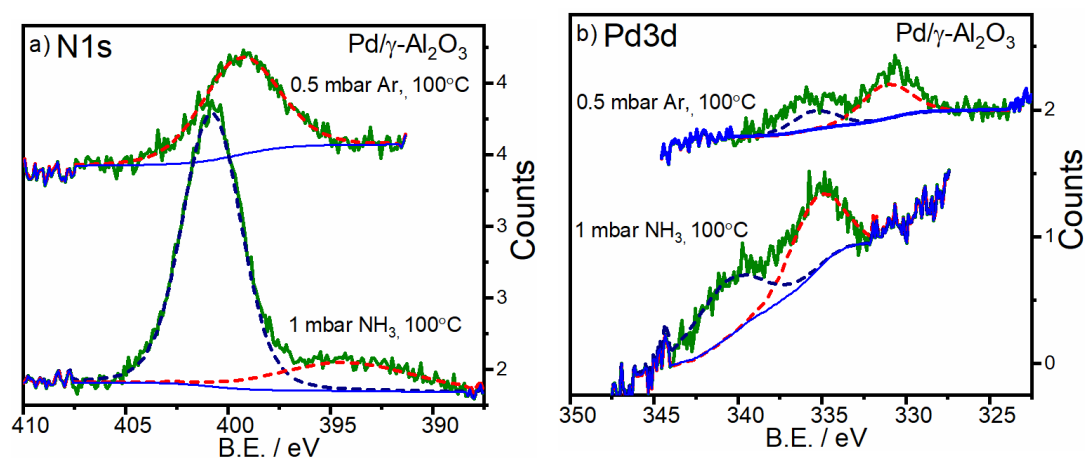


Figure 4.8. *In situ* XPS spectra of the supported Pd catalyst, Pd/ γ -Al₂O₃, after reduction pre-treatment in H₂, then exposure to inert (0.5 mbar Ar) and NH₃ (1 mbar) atmospheres at 100°C, collected with incident photon energy of 900 eV. Plots show the raw data, baseline and the deconvoluted fitting components at **a)** N1s binding energy, and **b)** Pd3d binding energy.

In order to correct for the charging effects, the Al 2p spectrum was used as a reference peak, known to have a consistent binding energy of 74.6 eV for Al₂O₃,⁵⁷ which was measured before and after the collection of N 1s and Pd 3d spectra. With increasing time in the beam, the sample underwent increasing charging. This made it increasingly difficult to align the measured spectra, and so these results may not provide conclusive evidence for the PdN_x species.

3.3.4.2 *Ex situ* XPS

Additional *ex situ* XPS measurements were performed of the supported Pd catalyst, Pd/zeolite-Y, before and after exposure to NH₃ atmosphere at 100°C. Although these measurements were collected under ultra-high vacuum at room temperature, the samples were treated at the appropriate conditions then transferred to the vacuum chamber within 1 hour with minimal exposure to air. The N 1s spectra of the catalyst before and after NH₃ treatment (Figure 4.9a) show similar features to the *in situ* spectra described earlier; a small peak before NH₃ treatment due to nitrogen-containing contaminants and a peak after NH₃ treatment that can be deconvoluted into two different nitrogen environments. The high intensity peak for nitrogen species of adsorbed NH₃ molecules gives rise to the N1s binding energy peak centred at 402 eV, whereas the small shoulder at 398 eV is again consistent with the formation of a reduced nitrogen as found in metal nitrides.^{55, 56} The *ex situ* Pd 3d binding energy spectra of the Pd catalyst after (i) a reduction treatment (H₂ 200°C), (ii) a calcination treatment (O₂, 500°C) and (iii) NH₃ treatment (NH₃, 100°C) are plotted together in Figure 4.9b. The shift in the Pd 3d binding energies of the same sample after different gas treatments shows that the calcination treatment achieved the greatest oxidation of the catalyst, shifting the Pd 3d_{5/2} peak to the highest binding energy of 337 eV, consistent with the binding energy of PdO.⁵⁶ The reduction treatment shows that the Pd 3d binding energy is consistent with that of Pd metal at 335.3 eV and the binding energy of the sample after NH₃ treatment is between the two. This shows that the electron donation from the Pd to the N in the formation of the PdN_x species is to a lesser extent than the donation of electron density from Pd to O in the formation of PdO. The binding energies of the N 1s and Pd 3d peaks from these *ex situ* measurements shown in Figure 4.9 are at slightly different values to those presented in Figure 4.8 from *in situ* measurements. This reinforces the problem with sample charging during *in situ* measurements with the synchrotron x-ray source, which did not allow for accurate determination of binding energies.

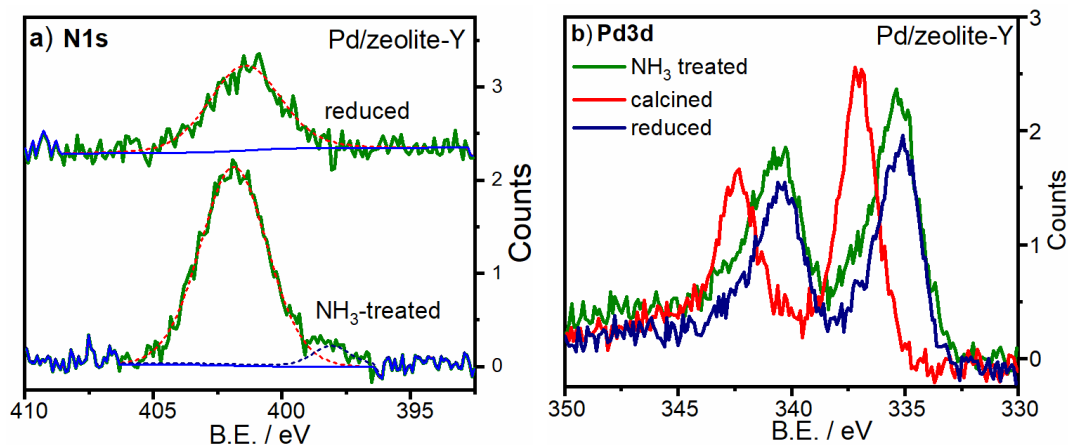


Figure 4.9. Ex situ XPS spectra of the supported Pd catalyst, Pd/zeolite-Y, collected using Al K α x-ray source (1486.6 eV) after reduction treatment (H_2 , 200°C), calcination treatment (O_2 , 500°C) and after treatment in NH_3 atmosphere (0.5% NH_3 , 100°C). **a)** N 1s binding energy showing raw data, deconvoluted fitting components and baseline. **b)** Pd 3d binding energy showing raw data only.

4.3.5 Operando XAFS/DRIFTS/MS

4.3.5.1 On-line catalytic Activity

The NH_3 conversion and product distribution of the supported Pd catalyst during NH_3 -SCO was monitored online by mass spectrometry of the exhaust from the XAFS/DRIFTS reactor during an *operando* XAFS/DRIFTS experiment. The NH_3 conversion and product distribution from both supported catalysts, Pd/ γ - Al_2O_3 and Pd/zeolite-Y are shown in Figure 4.10a and 4.10b, respectively, during a temperature ramp from 100°C to 500°C, with reactant gas feed 0.5% NH_3 , 2.5% O_2 and 97% He. The mass spectrometry signal is plotted as a function of time, with the internal temperature plotted on a second y-axis. This is to avoid complication that arises in Figure 4.10a due to a 10 minute period at reaction time 6620 seconds when the reaction temperature was held at 340°C because the x-ray beam was lost. The gas concentration and temperature range investigated during the *operando* XAFS/DRIFTS measurements were kept consistent with the catalytic activity test reported in section 3.2 of this chapter, and a lower total flow rate of 50 $cm^3 min^{-1}$ was used to achieve similar space velocity with respect to the mass of catalyst used. Figures 4.10a and 4.10b show that both supported Pd catalysts, Pd/ γ - Al_2O_3 and Pd/zeolite-Y, display similar catalytic activity for NH_3 -SCO, with a sharp onset of NH_3 conversion at 180°C and change in the product distribution with increasing temperature. The different regions of product distribution have been divided into three distinguishable regimes and are annotated in Figure 4.10. The low temperature region, T_1 , occurs in the temperature range $100^\circ C < T_1 < 240^\circ C$, where the reaction proceeds with high selectivity to N_2 . The mid-temperature region, T_2 , occurs in the temperature range $240^\circ C < T_2 < 300^\circ C$, where there is a plateau in N_2 formation and increase in the formation of nitrous oxide (N_2O). The high temperature region, T_3 , occurs in the temperature range $T_3 > 300^\circ C$, and sees the onset of increasing formation of nitric oxide (NO). This catalytic activity data measured from the exhaust of the XAFS/DRIFTS

reaction chamber confirms that the catalyst is operating in a comparable manner to the initial catalytic activity test in section 3.2 of this chapter, and thus justifies the *operando* nature of the spectroscopic measurements.

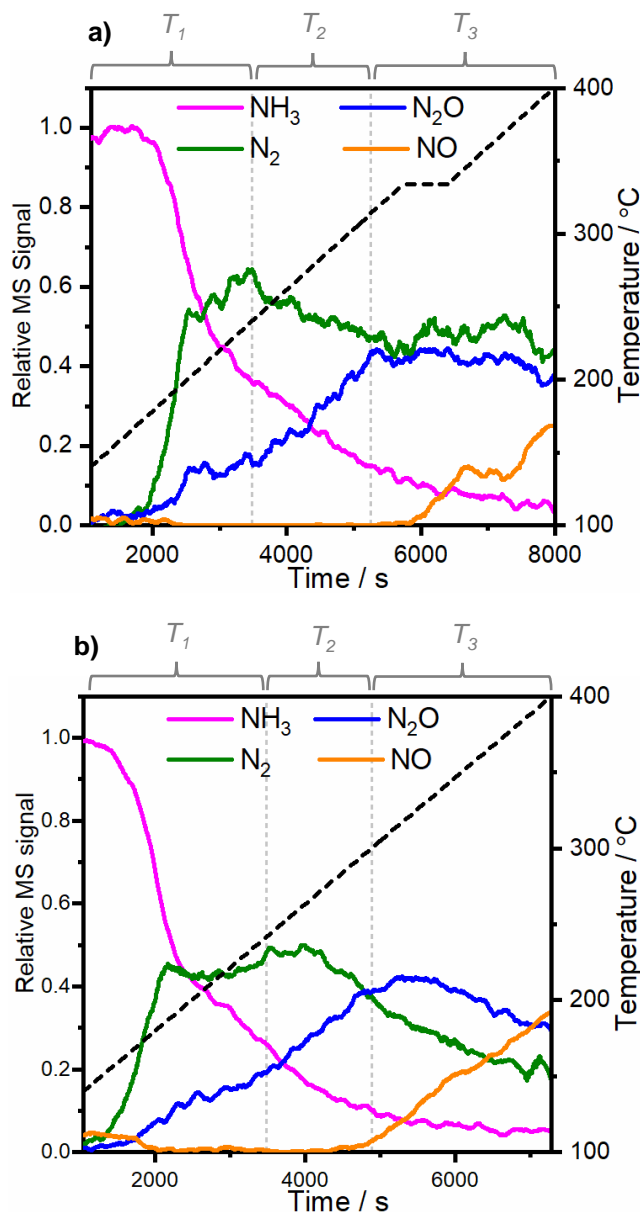


Figure 4.10. On-line catalytic activity measured by mass spectrometry of the exhaust gas (NH₃, N₂, N₂O and NO) from the XAFS/DRIFTS reaction chamber during NH₃-SCO at increasing temperatures over the supported Pd catalysts **a)** Pd/ γ -Al₂O₃ and **b)** Pd/zeolite-Y.

4.3.5.2 *Operando* Pd K-edge XAFS

The change in the Pd K-edge XANES features upon initial introduction of the supported Pd catalyst to the reactant gas feed (NH₃/O₂/He) at 100°C confirms a change in the Pd electronic structure under the reaction environment. Figure 4.11a shows the Pd K-edge XANES spectra of Pd/ γ -Al₂O₃ under the initial inert gas environment at 100°C, then upon switching to the reactant gas feed, and then after increasing the temperature to 200°C. Upon introducing the reactant gas feed, the near edge feature at 24355 eV remains in the same position with a small increase in intensity, but the absorption

features at 24393 eV and 24432 eV are shifted by ~ 4 eV to lower energies. These observations were consistent with all measurements collected between 100°C and 200°C in the reactant gas environment, and were repeated by exposing the Pd/zeolite-Y catalyst to the same conditions (Figure 4.11b). In order to eliminate any oxidation from the oxygen in the reactant gas feed, the measurements were repeated again but exposing the catalyst to an atmosphere of NH₃/He (Figure 4.12a and 4.12b). This means that the oxygen was not required to cause these changes to the palladium electronic structure. The observation of a shift in the metal Pd absorption features at 24393 eV and 24432 eV have previously been reported for the formation of a Pd carbide phase, whereby carbon atoms are inserted into the metal fcc framework of Pd nanoparticles.^{50, 54} The combination of these observations from the Pd K-edge XANES together with the changes observed at the Pd L₃-edge and XPS spectra, strongly indicate the formation of a Pd nitride phase during the low temperature regime for NH₃-SCO, whereby nitrogen is inserted into the metal Pd fcc framework of the nanoparticle structure.

The Pd K-edge EXAFS give information for the average local atomic environment of the absorbing Pd atoms in the sample. The k^2 weighted Pd K-edge EXAFS spectra of the supported Pd catalysts are shown in Figures 4.13a and 4.13b respectively, before and after introducing the reactant gas feed. Both catalysts show that there is major disruption to the local atomic arrangement of the metallic Pd nanoparticles upon introducing the reactant (NH₃/O₂) gas feed by the decrease in amplitude and phase shift of the EXAFS oscillations. The same EXAFS spectrum is also obtained by introducing the Pd catalyst to an NH₃/He gas feed, showing that the disruption to the Pd metal nanoparticle structure is also observed in the absence of oxygen. When the photoelectron is scattered by surrounding atomic neighbours that are in a regular arrangement, the constructive (and deconstructive) interference of the outgoing photoelectron waves from Pd atoms in the same environment gives rise to the large amplitude of scattering features in the recorded EXAFS spectrum. However, as is observed in these results, disruption to the Pd metal structure causes dampening of the EXAFS oscillations. This means that there must be substantial heteroatom insertion to the Pd nanoparticle, which not only causes expansion to the fcc lattice but to cause significant disruption of the local atomic ordering within the Pd nanoparticle structure.

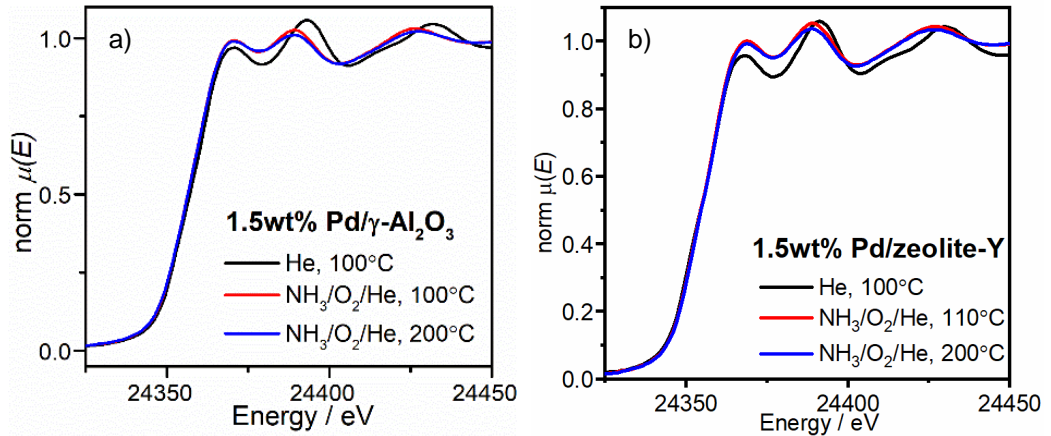


Figure 4.11. Pd K-edge XANES spectra of supported Pd catalysts **a)** Pd/ γ -Al₂O₃ and **b)** Pd/zeolite-Y in He at 100°C, NH₃/O₂/He at 100°C and NH₃/O₂/He at 200°C.

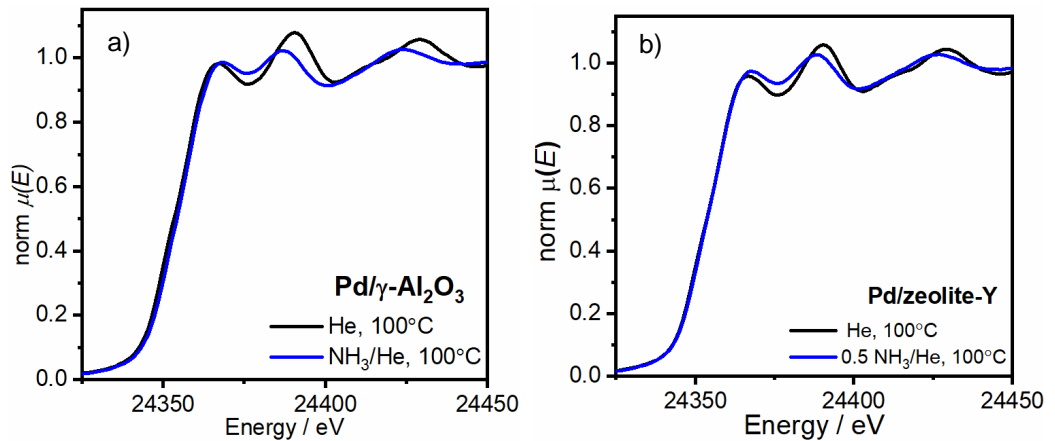


Figure 4.12. Pd K-edge XANES spectra of supported Pd catalysts **a)** Pd/ γ -Al₂O₃ and **b)** Pd/zeolite-Y in He at 100°C and NH₃/He at 100°C

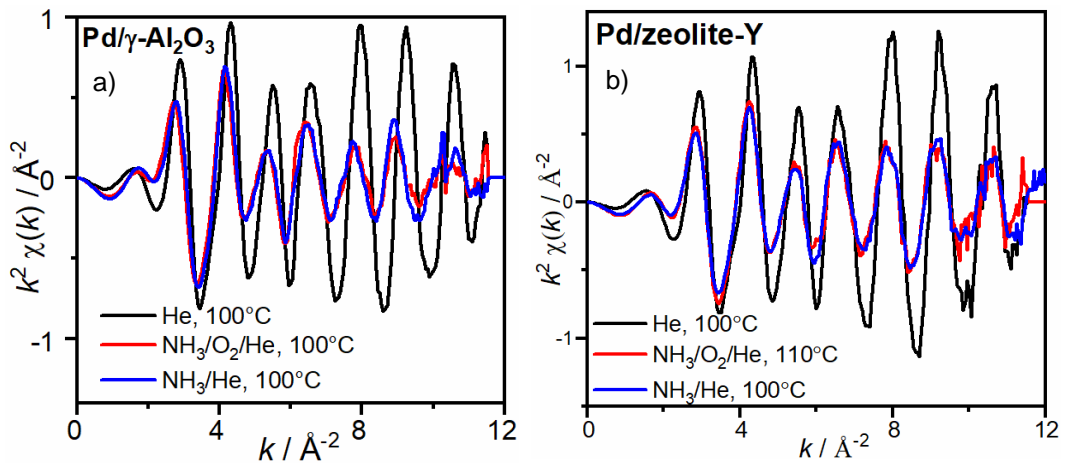


Figure 4.13. Pd K-edge EXAFS of supported catalysts **a)** Pd/ γ -Al₂O₃ and **b)** Pd/zeolite-Y in He at 100°C, NH₃/O₂/He at 100°C and NH₃/He at 100°C

The Fourier transformed Pd K-edge EXAFS spectrum of both supported catalysts during low temperature NH₃-SCO (NH₃, O₂, 100°C) are shown in Figure 4.14, together with a fitting model using first shell coordination to nitrogen ($R_{Pd-N} = 2.0 \text{ \AA}$) and a second shell coordination to palladium ($R_{Pd-Pd} = 2.8 \text{ \AA}$), with coordination numbers of 1 and 9, respectively (Table 4.2).

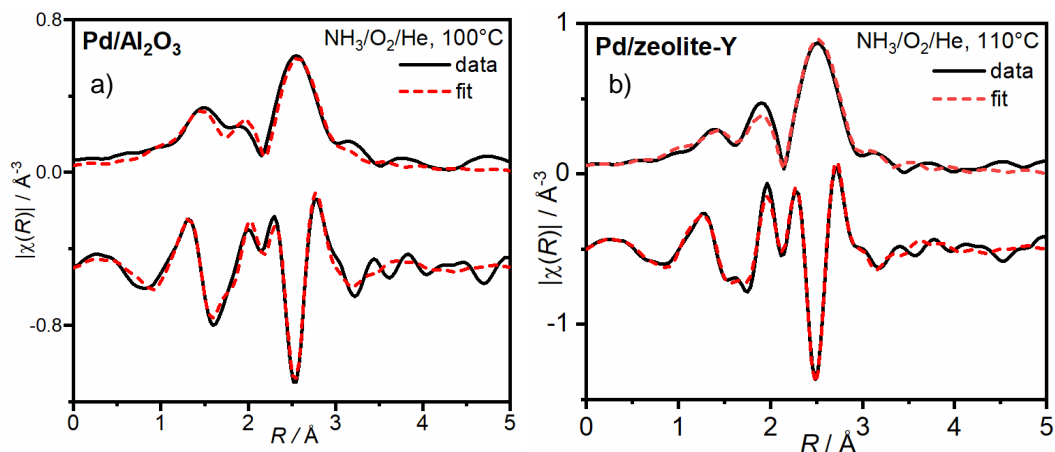


Figure 4.14. Non-phase corrected Fourier transformed EXAFS data of supported Pd catalysts **a)** Pd/ γ -Al₂O₃ and **b)** Pd/zeolite-Y, under reactant (NH₃/O₂) gas feed at 100°C plotted together with a model fitted using scattering paths Pd-N and Pd-Pd.

Table 4.2. Fitting parameters of the model used to fit Fourier transformed EXAFS data of supported Pd catalysts in reaction conditions for NH₃ oxidation (NH₃/O₂ gas feed at 100°C).

Catalyst	Abs - Scat	N	R / Å	$\sigma^2 / \text{\AA}^2$	E_0 / eV	R factor
Pd/ γ -Al ₂ O ₃	Pd-N	1.0(2)	2.00(1)	0.003(2)	-5.7(4)	0.02
	Pd-Pd	9.9(1)	2.810(5)	0.0161(8)		
Pd/zeolite-Y	Pd-N	0.9(9)	1.94(4)	0.01(1)	(-)6.4(8)	0.01
	Pd-Pd	9(1)	2.758(9)	0.013(5)		

Note: Fitting parameters $S\sigma^2 = 0.8$; Fit range $3 < k / \text{\AA}^{-2} < 10.6$, $1 < R / \text{\AA} < 3$; Number of independent points = 9.

The Pd K-edge XANES spectra collected during the mid-temperature NH₃-SCO regime ($240^\circ\text{C} \leq T_2 < 300^\circ\text{C}$) are plotted in Figure 4.15. The spectrum collected at 240°C shows that the XANES features at 24393 eV and 24432 eV - which had shifted to lower energies in the formation of the interstitial PdN_x species - return to energies that resemble the initial metal Pd⁽⁰⁾ spectrum collected initially under inert atmosphere. The difference between the XANES spectrum collected initially under inert atmosphere (He, 100°C) and that collected at 240°C under reactant (NH₃/O₂) gas feed is a small increase in the near edge feature at 24370 eV and dampening of the metallic feature at 24393 eV. This flattening of the metallic feature and increase in near-edge absorption intensity can result in part from temperature differences, but predominantly due to partial oxidation of Pd⁽⁰⁾ to Pd²⁺ at the nanoparticle surface.

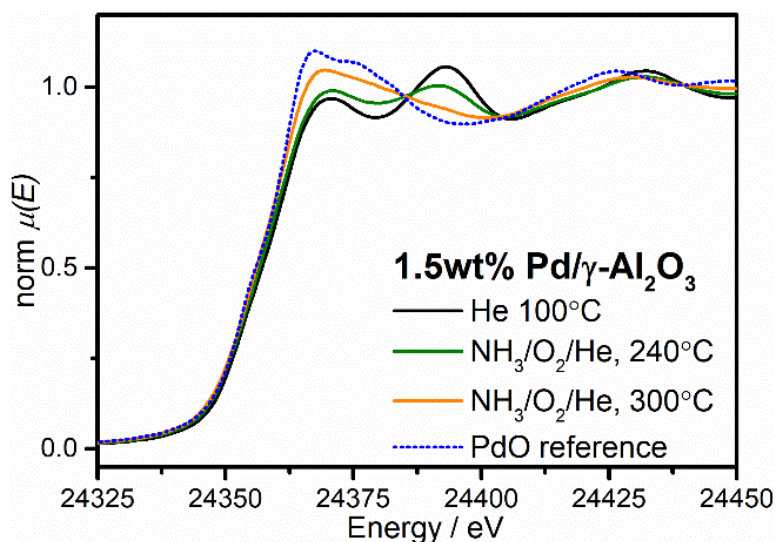


Figure 4.15. Pd K-edge XANES of supported Pd catalyst, Pd/ γ -Al₂O₃, under reactant gas feed (NH₃/O₂) at increasing temperatures.

Linear combination fitting (plotted in Figure 4.16) describes the Pd K-edge XANES collected at 240°C as an approximate summation of ~40% Pd⁽⁰⁾ and ~60% Pd²⁺ species. This fitting used the Pd K-edge XANES spectra collected at 100°C in He and at 300°C in NH₃/O₂ to represent Pd⁽⁰⁾ and Pd²⁺ species of this particle size, respectively. The ratio of 40% Pd⁽⁰⁾ and 60% Pd²⁺ is previously reported for a thin oxidic surface layer surrounding bulk metal Pd nanoparticles of 2 nm average particle diameter.⁵⁸ It is viable that a surface oxide layer has formed by 240°C at the surface of the bulk metal Pd nanoparticles in the reactant (NH₃/O₂) gas feed, which gives rise to the observed XANES spectrum. As the temperature is increased further, there is a further increase in oxide character of the XANES spectrum and a decrease in the metallic features. This

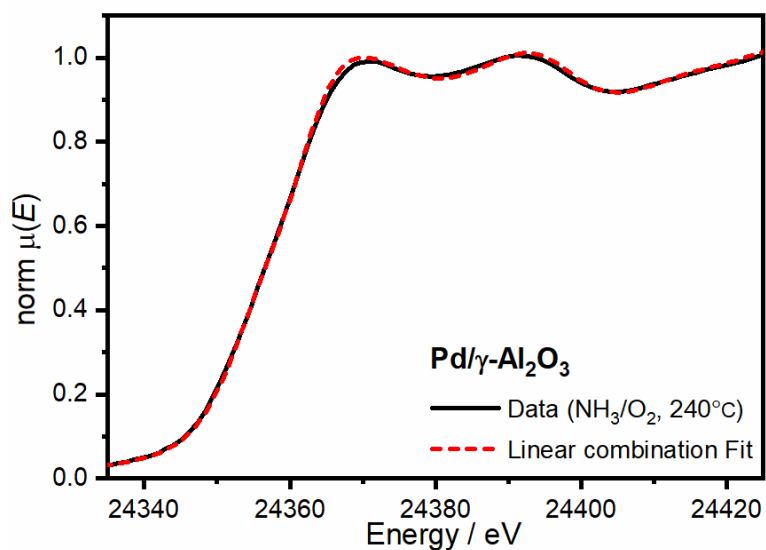


Figure 4.16. Pd K-edge XANES of supported Pd catalyst, Pd/ γ -Al₂O₃ at 240°C in reactant gas mixture (NH₃/O₂), and a fit using a linear combination of two components: 60 % Pd⁽⁰⁾ and 40% Pd²⁺. Component 1: Pd/ γ -Al₂O₃ at 100°C in He. Component 2: PdO/ γ -Al₂O₃ at 300°C in NH₃/O₂/He. Fit range 24333 ≤ E / eV ≤ 24403; Number of data points = 65. Weights forced to sum to 1.

infers the gradual oxidation of the Pd nanoparticles, starting from the formation of an oxide surface layer that penetrates to the core of the particle.

The extent of the Pd nanoparticle oxidation can be observed from the Fourier transformed EXAFS data shown in Figure 4.17. The Fourier transformed EXAFS at 240°C, show the small amplitude of a scattering feature at 1.5 Å due to Pd-O coordination at the surface of the particles, the Pd-Pd coordination distance at this temperature however remains consistent with that of Pd foil (2.81 Å). As the temperature is increased there is increase in amplitude of the Pd-O scattering feature (at non-phase corrected distance of 1.52 Å) and the Pd-Pd radial distance increases to resemble that of bulk PdO (3.01 Å). The Fourier transformed EXAFS data collected at 340°C can be fitted to a model using three scattering paths Pd-O (2.01 Å), Pd-Pd₍₁₎ (3.01 Å) and Pd-Pd₍₂₎ (3.455 Å) of bulk PdO (detailed in Table 4.4 and plotted in Figure 4.18) and thus it can be shown that the Pd nanoparticles achieve complete oxidation during the high temperature regime (>300 °C) for NH₃-SCO.

Table 4.3. Fitting parameters used to fit the Fourier transformed EXAFS data of Pd/γ-Al₂O₃ measured under reaction conditions (NH₃/O₂) at 340°C, using scattering paths Pd-O, Pd-Pd₍₁₎ and Pd-Pd₍₂₎ of PdO.

Abs - Scat	N	R / Å	σ ² / Å ²	E ₀ / eV	R factor
Pd-O	3.7(3)	2.01(1)	0.004(1)	6(1)	0.005
Pd-Pd ₍₁₎	1.0(9)	3.01(1)	0.003(1)		
Pd-Pd ₍₂₎	2(2)	3.455(5)	0.004(8)		

Note: Fitting parameters $S_0^2 = 0.8$; Fit range $3 < k / \text{Å}^{-2} < 10.6$, $1 < R / \text{Å} < 3$; Number of independent points = 14.

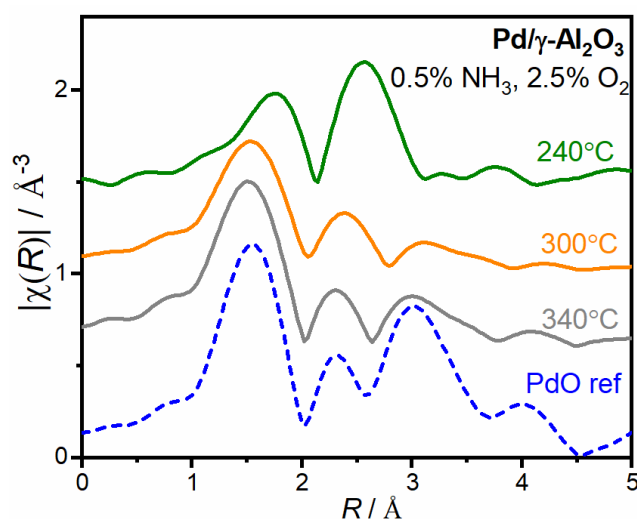


Figure 4.17. Stacked plot of non-phase corrected Fourier transformed EXAFS data of supported Pd catalyst, Pd/γ-Al₂O₃, at increasing temperatures during NH₃-SCO. Plotted together with that of a reference PdO sample.

The change in Pd nanoparticle structure during the three temperature regimes for NH₃-SCO have therefore been identified. During the low temperature regime, 100°C < T₁ < 240°C, there is insertion of nitrogen into the Pd metal framework to form an interstitial PdN_x nanoparticle structure. During the mid-temperature regime, 240°C < T₂ < 300°C, the Pd nanoparticles return to the metal fcc structure but with increasing formation of Pd oxide at the nanoparticle surface with increasing temperature. During the high temperature regime, T₃ > 300°C, oxidation at the Pd nanoparticle surface penetrates to the core achieving bulk PdO nanoparticle structure by 340°C.

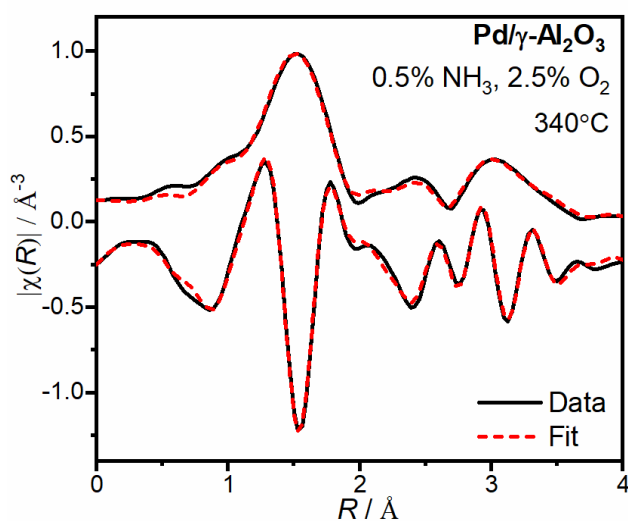


Figure 4.18 Non-phase corrected Fourier transformed EXAFS of supported Pd catalyst, Pd/γ-Al₂O₃, during NH₃-SCO at 340°C, plotted together with the fitting model constructed from Pd-O, Pd-Pd₍₁₎ and Pd-Pd₍₂₎ scattering paths of bulk PdO. Fitting parameters detailed in Table 4.4.

4.3.5.3 Operando DRIFTS

Operando DRIFTS spectra of the supported Pd catalyst were collected simultaneously to the Pd K-edge XAFS measurements during NH₃-SCO to investigate the molecular species at the catalyst surface. The difference DRIFTS spectrum collected after switching from inert (He) atmosphere at 100°C to the reactant (NH₃/O₂) gas feed are shown in Figure 4.19 for both supported Pd catalysts, Pd/γ-Al₂O₃ (Figure 4.19a) and Pd/zeolite-Y (Figure 4.19b). The sharp bands between 1250 and 1600 cm⁻¹ are typical of NH₃ adsorbed to surface acid sites. The bands at 1596 cm⁻¹ and 1256 cm⁻¹ are assigned to asymmetric and symmetric deformation of coordinated NH₃, respectively.^{12, 31, 59, 60} The band at 1450 cm⁻¹ can be assigned to asymmetric deformation of NH₄⁺ adsorbed on Brønsted sites of the support,^{15, 17, 59, 61} and the shoulder at 1490 cm⁻¹ to NH₃ coordinated to Pd.¹⁸ Low intensity combination bands of NH₃ and NH₃ dimers may give rise to the broad band around 2470 cm⁻¹.⁶² Absorption bands between 3080 and 3480 cm⁻¹ are typical of symmetric and asymmetric N-H stretching of coordinated NH₃.^{63, 64} Negative bands above 3500 cm⁻¹ show the absence of O-H stretches due to NH₄⁺ occupying surface hydroxyl Brønsted acid sites. The

dissociative adsorption of NH_3 on the Pd nanoparticle surface is shown by a weak band at 1377 cm^{-1} which is attributed to the $-\text{NH}_2$ wagging frequency,^{24, 65} usually coupled with the band at 1596 cm^{-1} . The broad, low intensity band at 1850 cm^{-1} is attributed to small amounts of neutral and positively charged nitrosyl (NO^+) species adsorbed on $\text{Pd}^{(0)}$.⁶⁶ The broad band of small intensity at 2170 cm^{-1} is present in the DRIFTS spectrum of both catalysts after switching to the NH_3/O_2 reactant gas feed at 100°C , and when switching to an NH_3/He atmosphere (Figures 4.20a and 4.20b). Absorption bands at this wavenumber have previously been associated with the vibrational frequency of an asymmetric N-N bond of bridging N_2 in multinuclear metal-dinitrogen complexes.⁵³ The observation of vibrational bands near 2200 cm^{-1} during NH_3 oxidation conditions are sometimes attributed to the N-N stretch of adsorbed N_2O species.^{67, 68} However, the absence of a corresponding N-O stretch for N_2O (expected at 1262 cm^{-1} – 1220 cm^{-1}) and absence of N_2O detected in mass spectrometry signals at 100°C means that the band at 2170 cm^{-1} cannot be assigned to N_2O species at this temperature. Similar vibrational bands at 2170 cm^{-1} are reported for NH_3 adsorption over a supported Ag catalyst, $\text{Ag}/\text{Al}_2\text{O}_3$, between 160 - 220°C , which also cannot be

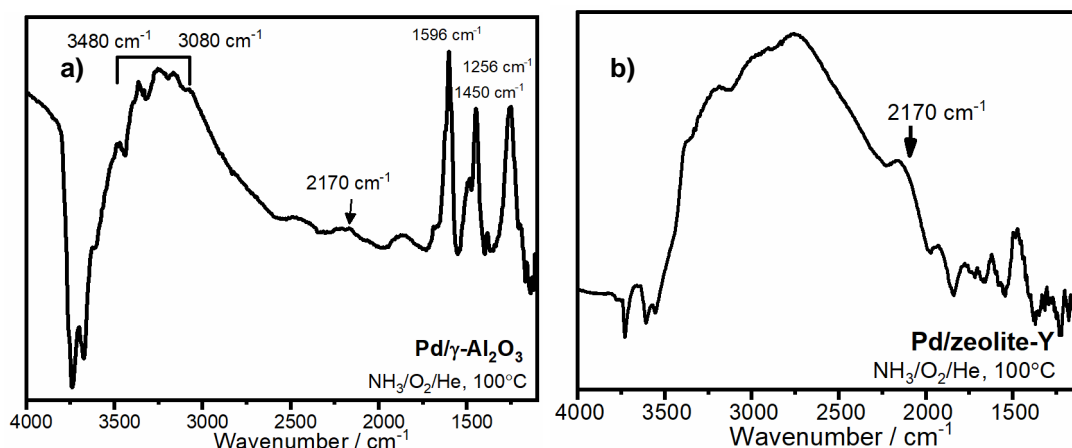


Figure 4.19. Difference DRIFTS spectra of supported Pd catalysts, **a)** $\text{Pd}/\gamma\text{-Al}_2\text{O}_3$ and **b)** $\text{Pd}/\text{zeolite-Y}$ after switching from inert (He) atmosphere to the reactant (NH_3/O_2) gas feed at 100°C .

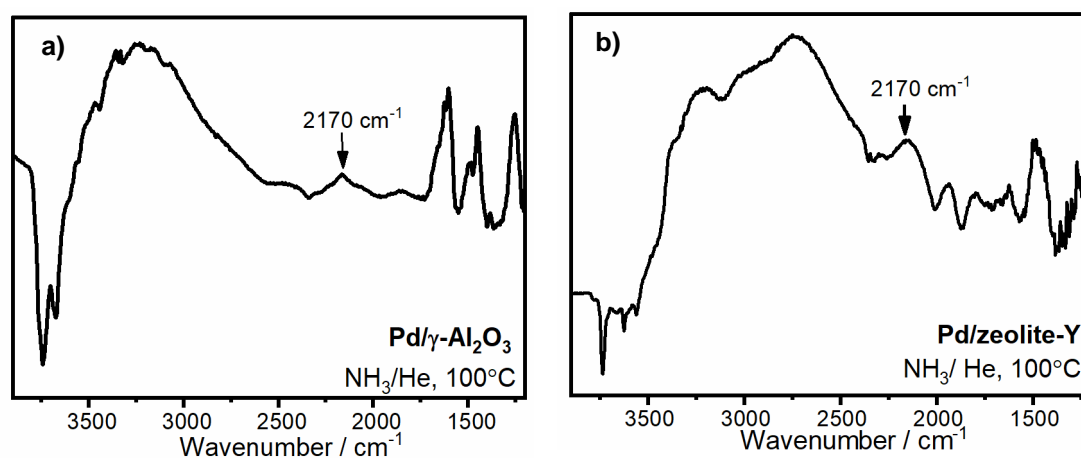


Figure 4.20. Difference DRIFTS spectra of supported Pd catalysts, **a)** $\text{Pd}/\gamma\text{-Al}_2\text{O}_3$ and **b)** $\text{Pd}/\text{zeolite-Y}$ after switching from inert (He) atmosphere to NH_3/He gas feed at 100°C .

attributed to N-N stretching of N_2O .⁶⁴ Here it is proposed that this low intensity absorption band results from an asymmetric stretch of N_2 species at the catalyst surface, following the dissociative adsorption of NH_3 molecules.

The nitrate region of the DRIFTS spectra collected from catalyst $Pd/\gamma-Al_2O_3$ between $200^\circ C$ and $300^\circ C$ are shown in Figure 4.21. An absorption band at 1455 cm^{-1} due to -NH wagging at the sample surface decreases in intensity from $200^\circ C$ to $220^\circ C$ followed by formation of small intensity bands at 2240 , 2210 , 1418 , 1302 and 1548 cm^{-1} due to the formation of adsorbed NO_x species.^{64, 69-71} The bands at 2240 , 2210 and 1418 cm^{-1} appear synchronously, reach maximum intensity at $240^\circ C$ and are attributed to the asymmetric N-N and N-O stretching modes of N_2O ,⁶⁴ this can be verified by observation of N_2O gas reaching the mass spectrometer at that temperature. The band at 1302 cm^{-1} reached maximum intensity at $280^\circ C$ and is attributed to the O-N-O asymmetrical stretching of adsorbed bidentate nitrate species.^{72, 73} The intensity of the band at 1548 cm^{-1} increased sharply from $280^\circ C$ to $300^\circ C$, and is attributed to the N=O stretching of adsorbed nitrates and nitrosyl (NO) species.⁷⁴ The increase in intensity of the N=O stretching band corresponds to the temperature for onset of NO gas detected at the mass spectrometer. The *operando* DRIFTS therefore show change in the molecular speciation at the catalyst surface during increasing operating temperatures for the NH_3 -SCO which related to the gases observed by mass spectrometry of the exhaust. Dinitrogen coupling was identified by the weak band at 2170 cm^{-1} during the low temperature regime ($100^\circ C < T_1 < 200^\circ C$), asymmetrical N-O stretches at 1302 cm^{-1} were identified in the mid-temperature region $220^\circ C < T_2 < 280^\circ C$ and N=O stretches at 1548 cm^{-1} in the high temperature region $T_3 < 280^\circ C$.

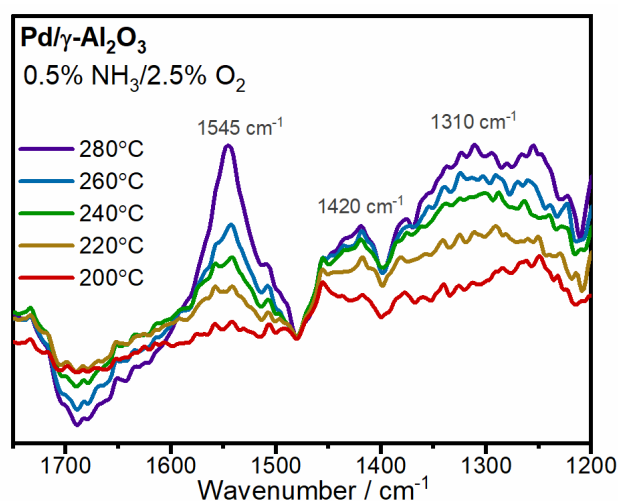


Figure 4.21. Nitrate region of DRIFTS spectra of supported catalyst $Pd/\gamma-Al_2O_3$ at increasing temperatures during NH_3 -SCO.

4.3.8 DFT + D3

To gain an improved understanding of the proposed interstitial PdN_x species, reported from XAFS and XPS measurements in this study, as the active catalytic species for NH₃-SCO during the low temperature regime (< 240°C), DFT + D3 calculations were performed by Dr Arunabhiram Chutia and Dr Constantinos Yeinalipour-Yazdi. The calculations were aimed to clarify how the presence of interstitial N-atoms influence the Pd-Pd bond distances of metal Pd nanoparticles. The DFT + D3 calculations were done in a Pd(111) system with 0.12 wt%, 0.23 wt%, 0.47 wt%, 0.70 wt%, and 1.39 wt% of interstitial N-atoms. The optimised Pd structures obtained with these values of interstitial N-atom insertion are shown in Figure 4.22. The average Pd–Pd distances in the vicinity of these interstitial N-atoms are ~2.83 Å. This is consistent with the lattice expansion observed by Pd K-edge EXAFS during N-atom insertion under NH₃/O₂ reaction conditions, reported herein. The lateral and vertical Pd-Pd distances were found to be in the range of 2.83 - 2.85 Å and 2.80 - 2.83 Å, respectively, irrespective of the concentration of N-atom insertion. The Pd-N distances were in the range 1.91 – 1.99 Å, which is in agreement with the distances found from the Pd K-edge EXAFS data. Before relaxation, distances between the interstitial N-atoms in all the above models were in the range of 2.39 – 2.47 Å and after relaxation these moved by a distance approximately in the range of 3.03 – 3.34 Å, with some of the N-atoms moving closer to the surface. The diffusion barrier for an interstitial N-atom to move from an octahedral interstitial site to a surface 3-fold hollow was low (0.25 eV), suggesting that interstitial N-atoms are able to diffuse to the surface to participate in the catalytic mechanism.

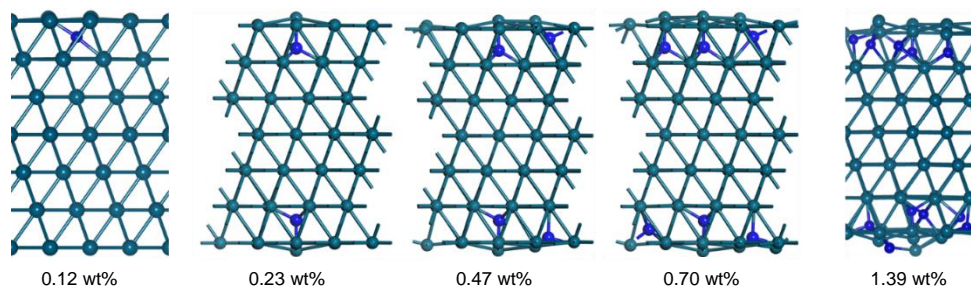
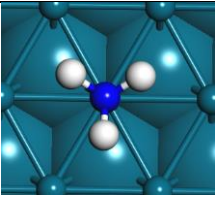
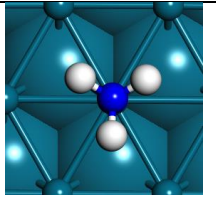
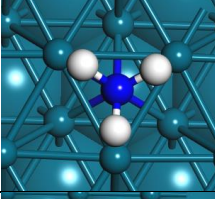
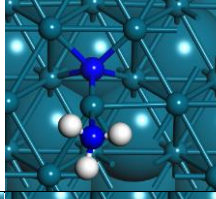
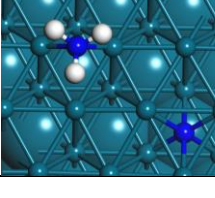
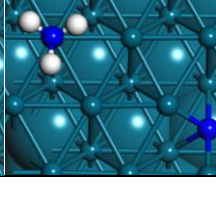


Figure 4.22. Optimised structures for the Pd(111) system with 0.12 wt%, 0.23 wt%, 0.47 wt%, 0.70 wt%, and 1.39 wt% of interstitial N-atoms, which correspond to the number of interstitial N-atoms used being 1, 2, 4, 6, and 12, respectively.

The adsorption properties of NH₃ on Pd(111) surface were considered with and without the presence of interstitial N-atoms. The adsorption energies of the most favourable configurations for an NH₃ molecule at a pristine Pd (111) surface, at a Pd (111) surface close to an interstitial N-atom and at a Pd(111) surface away from an interstitial N atom are shown in Table 4.5. The NH₃ adsorption energy is most negative when located at a surface position close to an interstitial N atom compared to away from it in the same system, and is ~0.156 eV lower in energy compared to adsorption at the pristine Pd(111) surface. This is due to the interaction of N p and Pd d molecular orbitals in the

bonding region. For pristine Pd(111) surface the Pd d_{z^2} orbital interacts with the N p orbitals whereas in the case of a Pd(111) surface with an interstitial N-atom the Pd d_{z^2} and d_{yz} interact with the N p orbital leading to a stronger bonding interaction between Pd atoms with NH₃ molecules. In the latter case there is also trace contribution from other d orbitals. From this analysis we can conclude that the Pd(111) surface with interstitial N-atoms would have greater coverage of adsorbed NH₃ as compared to the pristine Pd(111) surface.

Table 4.4. Calculated adsorption energies of an NH₃ molecule adsorbed in the lowest energy configuration on pristine Pd(111) surface, on Pd(111) close to an interstitial N-atom and on Pd(111) away from an interstitial N-atom site, showing initial configuration, relaxed configuration and the associated adsorption energy (E_{ads}).

Initial configuration	Relaxed Configuration		$E_{ads}/$ eV
	Top View	Side View	
(NH₃)_{top} (N_{top}-H_{HCP}) Adsorption of NH ₃ at the surface of pristine Pd(111)			-1.033
(NH₃)_{hcp} (Conf2) Adsorption of NH ₃ at the surface close to an interstitial N			-1.189
(NH₃)_{bdg} (Conf2) Adsorption of NH ₃ at the surface away from an interstitial N			-1.034

4.4 Discussion

Three distinct regions of catalytic activity are identified for NH₃ oxidation over supported Pd nanoparticle catalysts when tested in both the Johnson Matthey test rig and the XAFS/DRIFTS reaction chamber. By collecting together the *operando* XAFS and DRIFTS spectroscopy data, a direct link has been made between the changes in Pd nanoparticle structure, surface speciation and the observed catalytic activity. These observations are verified by *in situ* Pd L₃-edge XAFS, XPS spectroscopy and DFT+D3 calculations. In the low temperature region ($100^\circ\text{C} \leq T_1 \leq 200^\circ\text{C}$), the Pd K-edge and Pd L₃-edge XANES show that the Pd nanoparticle structure experiences lattice expansion with insertion of atomic N into the metallic Pd nanoparticle structure, which is confirmed by our DFT+D3 calculations. The XPS spectra show that there is electron donation from the palladium to the nitrogen species in the form of a Pd nitride phase. Although Pd XAFS and XPS spectroscopy have pointed towards the formation of a Pd

nitride phase, there is opportunity for further characterisation to obtain evidence of the detailed structural properties and quantity of nitrogen contained within this unusual PdN_x compound.

At the surface of the supported Pd catalysts during low temperature NH₃ oxidation, the dissociation of NH₃ is shown by DRIFTS absorption bands for –NH₂ scissoring (at 1377 cm⁻¹), –NH wagging (1455 cm⁻¹) and a low intensity vibrational band at 2170 cm⁻¹ for N-N stretching. These observations indicate dinitrogen coupling for the direct oxidation pathway of NH₃ to N₂ (Equation 4.6). The greater stability of NH₃ adsorption on the Pd nitride nanoparticle surface is calculated from molecular models and infers a high NH₃ surface coverage for dinitrogen coupling during the low temperature regime. Additionally, the low energy barrier for diffusion of interstitial N to the Pd nanoparticle surface indicates the ability for interstitial N to participate in the reaction mechanism by coupling with adsorbed NH₃ at the Pd nitride surface in a Mars-Van Krevelen type mechanism. The average coordination distance of Pd atoms to neighbouring Pd atoms in the Pd nanoparticles have been found by fitting the Fourier transformed Pd K-edge EXAFS data, which give an indication for the extent of N insertion into the Pd structure. The removal of N from the Pd lattice is therefore shown in Figure 4.23 by the contraction of Pd-Pd distances from 180°C to 240°C. Figure 4.22 also shows the simultaneous *m/z* 28 signal for N₂ reaching the mass spectrometer, and the intensity of the N-N asymmetric stretching band of dinitrogen species at the catalyst surface. The surface N-N stretch is only observed in DRIFTS spectra below 160°C when there is substantial N insertion in the Pd lattice. Desorption of these surface N-N stretching species coincides with the onset of N₂ gas reaching the mass spectrometer. Following this, the contraction of the Pd-Pd distance – indicating the removal of interstitial N from the Pd lattice – is found to occur when N₂ formation exceeds 50%, with respect to the inlet

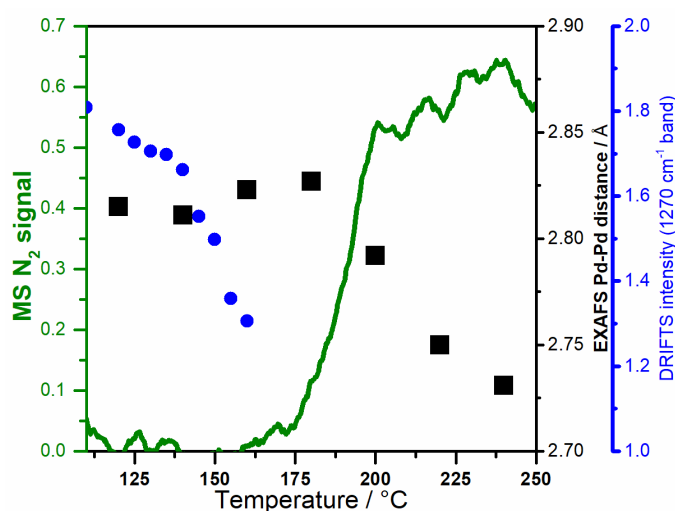


Figure 4.23. Overlay plot of Pd-Pd distance calculated from fitting models to Pd K-edge EXAFS data, N₂ signal from on-line mass spectrometry and intensity of asymmetric N-N stretching frequency from 1270 cm⁻¹ DRIFTS absorption band plotted as a function of temperature

NH₃ signal. This suggests that the interstitial N atoms play a role in the direct oxidation of NH₃ to N₂ at the catalyst surface and are depleted from the Pd nanoparticle structure when the rate of desorption of N₂ exceeds the rate of adsorption of NH₃.

The active PdN_x nanoparticle structure is observed by *operando* Pd K-edge and Pd L₃-edge XANES up to 200°C. At temperatures beyond 200°C, the interstitial N are removed from the Pd lattice and the Pd K-edge XANES show that the structure of the Pd nanoparticles return to predominantly a metallic oxidation state, with a small oxidic surface layer. During this reaction period DRIFTS spectra show the presence of absorption bands at 1418 cm⁻¹, 2240 cm⁻¹ and 2210 cm⁻¹ for molecular vibrations of N₂O at temperatures and there is an increase in N₂O gas reaching the mass spectrometer. Therefore an increasing number of nitrogen containing molecular species at the catalyst surface are combining with adsorbed oxygen to form N₂O.

The presence of N=O and O-N-O stretching bands of surface nitrates are first observed in the DRIFTS spectra at 240°C but increase significantly in intensity at 300°C which correlates with the temperature for bulk PdO formation. The oxidation of Pd nanoparticles and the increasing quantity of adsorbed nitrates at the catalyst surface is matched to the temperature for onset of NO gas reaching the mass spectrometer. The complete oxidation of the Pd nanoparticles is confirmed by fitting the Pd K-edge EXAFS data collected at 340°C to Pd-O and Pd-Pd paths of PdO. The over oxidation of NH₃ to NO, by Equation 4.4, has previously been attributed to high oxygen coverage at the precious metal surface which prevents N coupling,⁷⁵ but this study indicates that the bulk oxide nanoparticles are the active catalytic species for NH₃ oxidation to NO above 280°C.

4.5 Conclusions

The combination of *operando* DRIFTS and XAFS spectroscopy, together with verification from *in situ* Pd L₃-edge, XPS and DFT + D3 calculations, have been able to identify the changes to the Pd nanoparticle structure and the molecular speciation at the catalyst surface to provide an explanation for the change in product selectivity from the NH₃-SCO reaction at increasing temperatures. XAFS at the Pd K-edge and Pd L₃-edge have been able to identify PdN_x nanoparticle structure during the low temperature regime for NH₃-SCO (100°C < T₁ < 240°C), which is responsible for the high selectivity to N₂. At 240°C the catalyst exists as metallic Pd nanoparticles with a surface oxide layer that permits the formation of N₂O. The surface oxide layer is found to penetrate the bulk of the nanoparticle structure such that complete oxidation to PdO is achieved in the high temperature regime T₃ > 300°C which is responsible for the over oxidation of NH₃ to NO. The Pd nanoparticle structure is therefore found to dictate the product selectivity for NH₃-SCO. The favourable selectivity to N₂ achieved over the supported Pd catalyst at low temperature, T₁, is attributed to a newly identified PdN_x structure

which is able to increase surface coverage of adsorbed NH₃ and promote the dinitrogen coupling. Whereas the unfavourable over-oxidation of NH₃ to NO is found to occur at the surface of bulk PdO nanoparticles.

4.6 References

1. European Union. Regulation (EC) No 715/2007 on type approval of motor vehicles 2007. European Environment Agency, Denmark.
2. European Union. Regulation (EU) No 64/2012 on emissions from heavy duty vehicles (Euro VI) 2012. Official Journal of the European Union. L 28.
3. United States Environmental Protection Agency. 2017. Learn About Volkswagen Violations. [online] Available from: <https://www.epa.gov/vw/learn-about-volkswagen-violations>. [Accessed 06 February 2019].
4. C Marshall, 2018. Illegal levels of air pollution linked to child's death. [online] BBC news: Science and Environment. Available from: <https://www.bbc.co.uk/news/science-environment-44612642>. [Accessed 06 February 2019].
5. F Pan, CW Liu, Preparation method of Adblue, CN104341321A. Chinese Patent: 2015.
6. International Fertilizer Industry Association. 2001. Global estimates of gaseous emissions of NH₃, NO and N₂O from agricultural land. [online] Italy: Food and Agriculture Organization of the United Nations (FAO). Available from: <http://www.fao.org/docrep/004/Y2780E/y2780e00.htm>. [Accessed 06 February 2019].
7. RW Melse and NWM Ogink, Transactions of the ASAE 2005, **48**, 2303-2313.
8. TJ Bandosz and C Petit, *J. Colloid Interf. Sci.*, 2009, **338**, 329-345.
9. F Schuth, R Palkovits, R Schlogl and DS Su, *Energ. Environ. Sci.*, 2012, **5**, 6278-6289.
10. T Hartikainen, J Ruuskanen, M Vanhatalo and PJ Martikainen, *Environ. Technol.*, 1996, **17**, 45-53.
11. WD Monnery, KA Hawboldt, AE Pollock and WY Svrcek, *Industrial & Engineering Chemistry Research*, 2001, **40**, 144-151.
12. L Chmielarz and M Jablonska, *RSC Adv.*, 2015, **5**, 43408-43431.
13. J Qin and K-i Aika, *Appl. Catal. B: Environmental*, 1998, **16**, 261-268.
14. L Gang, BG Anderson, J van Grondelle and RA van Santen, *Catal. Today*, 2000, **61**, 179-185.
15. M Jabłońska, A Król, E Kukulska-Zajac, K Tarach, L Chmielarz and K Góra-Marek, *J. Catal.*, 2014, **316**, 36-46.
16. DP Sobczyk, EJM Hensen, AM de Jong and RA van Santen, *Top. Catal.*, 2003, **23**, 109-117.
17. Y Li and JN Armor, *Appl. Catal. B: Environmental*, 1997, **13**, 131-139.

18. L Gang, J van Grondelle, BG Anderson and RA van Santen, *J. Catal.*, 1999, **186**, 100-109.
19. RQ Long and RT Yang, *Chem. Comm.*, 2000, DOI: 10.1039/b004957n, 1651-1652.
20. M Jabłońska, B Wolkenar, AM Beale, S Pischinger and R Palkovits, *Catal. Comm.*, 2018, **110**, 5-9.
21. GW Huber, JW Shabaker and JA Dumesic, *Science*, 2003, **300**, 2075-2077.
22. F Jaouen, E Proietti, M Lefèvre, R Chenitz, J-P Dodelet, G Wu, *et al.*, *Energ. Environ. Sci.*, 2011, **4**, 114-130.
23. R-M Yuan, G Fu, X Xu and H-L Wan, *J. Phys. Chem. C*, 2011, **115**, 21218-21229.
24. JG Amores, VS Escribano, G Ramis and G Busca, *Appl. Catal. B: Environmental*, 1997, **13**, 45-58.
25. LI Darvell, K Heiskanen, JM Jones, AB Ross, P Simell and A Williams, *Catal. Today*, 2003, **81**, 681-692.
26. C-M Hung, *J. Hazard Mater.*, 2010, **180**, 561-565.
27. H Wang, P Ning, Q Zhang, X Liu, T Zhang, J Fan, *et al.*, *Appl. Catal. A: General*, 2018, **561**, 158-167.
28. M Rutkowska, I Pacia, S Basąg, A Kowalczyk, Z Piwowarska, M Duda, *et al.*, *Micropor. Mesopor. Mat.*, 2017, **246**, 193-206.
29. Z Qu, H Wang, S Wang, H Cheng, Y Qin and Z Wang, *Appl. Surf. Sci.*, 2014, **316**, 373-379.
30. AC Akah, G Nkeng and AA Garforth, *Appl. Catal. B: Environmental*, 2007, **74**, 34-39.
31. P Li, R Zhang, N Liu and S Royer, *Appl. Catal. B: Environmental*, 2017, **203**, 174-188.
32. G Qi and RT Yang, *Appl. Catal. A: General*, 2005, **287**, 25-33.
33. G Qi, JE Gatt and RT Yang, *J. Catal.*, 2004, **226**, 120-128.
34. PBJ Thompson, BN Nguyen, R Nicholls, RA Bourne, JB Brazier, KRJ Lovelock, *et al.*, *J. Synchrotron Radiat.*, 2015, **22**, 1426-1439.
35. NS Marinkovic, Q Wang and AI Frenkel, *J. Synchrotron Radiat.*, 2011, **18**, 447-455.
36. EK Gibson, AM Beale, CRA Catlow, A Chutia, D Gianolio, A Gould, *et al.*, *Chem. Mater.*, 2015, **27**, 3714-3720.
37. G Kresse and J Hafner, *Physical Review B*, 1993, **47**, 558-561.
38. G Kresse and J Hafner, *Physical Review B*, 1994, **49**, 14251-14269.
39. G Kresse and J Furthmüller, *Physical Review B*, 1996, **54**, 11169-11186.
40. PE Blöchl, *Physical Review B*, 1994, **50**, 17953-17979.

41. G Kresse, Marsman and J Furthmüller, VASP the GUIDE. [online]. 2018. Universität Wien, Austria. Available from: <http://cms.mpi.univie.ac.at/vasp/vasp.pdf>. [Accessed 12 February 2019].
42. JP Perdew, K Burke and M Ernzerhof, *Phys. Rev. Lett.*, 1996, **77**, 3865-3868.
43. G Makov and MC Payne, *Phys. Rev. B*, 1995, **51**, 4014-4022.
44. J Neugebauer and M Scheffler, *Phys. Rev. B*, 1992, **46**, 16067-16080.
45. S Grimme, J Antony, S Ehrlich and H Krieg, *J. Chem. Phys.*, 2010, **132**, 154104.
46. G Henkelman, BP Uberuaga and H Jónsson, *J. Chem. Phys.*, 2000, **113**, 9901-9904.
47. C-M Lin, T-L Hung, Y-H Huang, K-T Wu, M-T Tang, C-H Lee, *et al.*, *Phys. Rev. B*, 2007, **75**, 125426.
48. AM Beale and BM Weckhuysen, *Phys. Chem. Chem. Phys.*, 2010, **12**, 5562-5574.
49. I Davoli, S Stizza, A Bianconi, M Benfatto, C Furlani and V Sessa, *Solid State Commun.*, 1983, **48**, 475-478.
50. AL Bugaev, AA Guda, A Lazzarini, KA Lomachenko, E Groppo, R Pellegrini, *et al.*, *Catal. Today*, 2017, **283**, 119-126.
51. MW Ruckman, G Reisfeld, NM Jisrawi, M Weinert, M Strongin, H Wiesmann, *et al.*, *Phys. Rev. B*, 1998, **57**, 3881-3886.
52. MW Tew, JT Miller and JA van Bokhoven, *J. Phys. Chem. C*, 2009, **113**, 15140-15147.
53. MW Tew, M Janousch, T Huthwelker and JA van Bokhoven, *J. Catal.*, 2011, **283**, 45-54.
54. MW Tew, M Nachtegaal, M Janousch, T Huthwelker and JA van Bokhoven, *Phys. Chem. Chem. Phys.*, 2012, **14**, 5761-5768.
55. GM Veith, AR Lupini, L Baggetto, JF Browning, JK Keum, A Villa, *et al.*, *Chem. Mater.*, 2013, **25**, 4936-4945.
56. B D., *Surf. Interface Anal.*, 1981, **3**, v-v.
57. F Rueda, J Mendialdua, A Rodriguez, R.Casanova, Y Barboux, L Gengembre, *et al.*, *J. Electron Spectrosc.*, 1996, **82**, 135-143.
58. SM Rogers, CRA Catlow, CE Chan-Thaw, A Chutia, N Jian, RE Palmer, *et al.*, *ACS Catal.*, 2017, **7**, 2266-2274.
59. NI Il'chenko, *Russ. Chem. Rev.*, 1976, **45**, 1119.
60. J Barbier Jr, L Oliviero, B Renard and D Duprez, *Catal. Today*, 2002, **75**, 29-34.
61. C Lousteau, M Besson and C Descorme, *Catal. Today*, 2015, **241**, Part A, 80-85.
62. H Wang and N Agmon, *J Phys. Chem. A*, 2016, **120**, 3117-3135.

63. F Liu, W Shan, Z Lian, L Xie, W Yang and H He, *Cat. Sci. Tech.*, 2013, **3**, 2699-2707.
64. L Zhang and H He, *J. Catal.*, 2009, **268**, 18-25.
65. L Chmielarz, P Kuśtrowski, A Rafalska-Łasocha and R Dziembaj, *Appl. Catal. B: Environmental*, 2005, **58**, 235-244.
66. S Carré, C Dujardin and P Granger, *Catal. Today*, 2012, **191**, 59-64.
67. NU Zhanpeisov, G Martra, WS Ju, M Matsuoka, S Coluccia and M Anpo, *J. Mol. Catal. A-Chem*, 2003, **201**, 237-246.
68. A Wclaw, K Nowińska, W Schwieger and A Zielińska, *Catal. Today*, 2004, **90**, 21-25.
69. X Zhang, H He, H Gao and Y Yu, *Spectrochim. Acta A*, 2008, **71**, 1446-1451.
70. J Müslehiddinoğlu and MA Vannice, *J. Catal.*, 2003, **217**, 442-456.
71. GM Underwood, TM Miller and VH Grassian, *J Phys. Chem. A*, 1999, **103**, 6184-6190.
72. FC Meunier, JP Breen, V Zuzaniuk, M Olsson and JRH Ross, *J. Catal.*, 1999, **187**, 493-505.
73. B Wichterlová, P Sazama, JP Breen, R Burch, CJ Hill, L Čapek, *et al.*, *J. Catal.*, 2005, **235**, 195-200.
74. S Tamm, N Vallim, M Skoglundh and L Olsson, *J. Catal.*, 2013, **307**, 153-161.
75. NA Khan, S Shaikhutdinov and HJ Freund, *Catal. Lett.*, 2006, **108**, 159-164.

Chapter Five. Cell design for combined, *operando* XAFS and DRIFTS

5.1 Introduction

Ever since spectroscopic techniques were first employed for catalyst characterisation, there has been the need for a spectroscopic cell to contain the catalyst sample in a suitable geometry with respect to the incident and measured radiation. The increasing desire to perform *in situ* and *operando* spectroscopy makes the design of a spectroscopic cell an engineering challenge, as it must meet the specification to perform high quality spectroscopic measurements as well as serving as catalytic reactor. Moreover, the need to perform multiple techniques for confident structure-function analysis, creates the added complexity for the cell design. In this Chapter, the specification for a combined, *operando* XAFS and DRIFTS reactor will be outlined. The design and development of the new reactor will be described, building upon on the design of previous *in situ* and *operando* spectroscopic cell designs that have come before it.

5.2 Requirements of a spectroscopic cell

5.2.1 X-rays

For XAFS measurements in transmission mode, the sample must be positioned in the X-ray beam between the two ion chambers, I_0 and I_t , for measurement of the absorption coefficient, $\mu(E)$, as defined by the Beer Lambert law in Equation 5.1. The attenuation of X-rays through the sample depends on the incident X-ray energy, the elemental composition of the sample, the density of the sample and the path length through the sample. The sample environment must allow X-rays to penetrate a suitable path length through a uniform cross section of the sample such that a fraction of the X-ray beam is absorbed by the sample and the remaining fraction is transmitted to I_t for detection. Usually $\sim 10\%$ of I_0 is required to reach I_t , with adequate number of photons absorbed by the element of interest for sufficient signal-to-noise and an edge jump $\Delta\mu(E) \approx 1$. The attenuation length through the sample is defined as the depth into the material where the intensity of the X-ray has decreased to less than e^{-1} ($\sim 37\%$) of the incident beam, I_0 . The attenuation length through a sample can be calculated provided its elemental composition and density are known. Each element within the sample will possess a different attenuation coefficient at the incident X-ray energy, with heavier elements being more absorbing than lighter elements. The total attenuation coefficient of the sample is a weighted sum of the individual attenuation coefficients of each element making up the sample. For example, the total attenuation coefficient of a 3wt% Pd/ γ - Al_2O_3 catalyst is calculated in Table 5.1, by summing the individual attenuation coefficients of Pd, O and Al in the sample. This value can then be used to calculate the

attenuation length through the sample, provided that the density of the sample is known. Assuming that this catalyst has a density close to that of bare $\gamma\text{-Al}_2\text{O}_3$ (3.95 g cm^{-3}),¹ then the attenuation distance of an X-ray beam at the Pd K-edge (24350 eV) through this sample is 0.3 mm.

Table 5.1. Calculation for the total attenuation coefficient of a 3wt% Pd/ $\gamma\text{-Al}_2\text{O}_3$ catalyst from the sum of individual attenuation coefficients of each elemental component.

Sample Composition Element	wt%	Elemental $\mu(E)$ (at $E = 24350 \text{ eV}$) / $\text{cm}^2 \text{ g}^{-1}$	Weighted $\mu(E)$ (at $E = 24350 \text{ eV}$) / $\text{cm}^2 \text{ g}^{-1}$
Pd	3	60.4	1.81
Al	52	1.89	0.98
O	45	0.54	0.24
Total			3.04

Note: Elemental $\mu(E)$ values calculated based on data from *Lawrence Livermore National Laboratory Report UCRL-50174*.²

The absorption of X-rays through the sample is then given by the Beer Lambert law:

$$\log \left[\frac{I_t}{I_0} \right] = \mu(E) (\text{cm}^2 \text{ g}^{-1}) * \rho (\text{g cm}^{-3}) * l (\text{cm}) \quad \text{Equation 5.1}$$

Where $\mu(E)$ is the calculated absorption coefficient of the sample, ρ is the mass density of the sample and l is the path length through the sample. The attenuation of X-rays through the gas phase and the walls or windows of the reactor must also be considered, as these will also act to reduce the intensity of the X-ray beam reaching the detector (I_t). The attenuation of the beam from these sources can be reduced by using low absorbing window material, and maintaining the beam under vacuum up to the experimental stage. For the high energy X-rays used at the Pd K-edge (24350 eV), the attenuation of X-rays by air is not significant, however a suitable X-ray window material must be considered.

For XAFS measurements in transmission mode the spectroscopic cell must consist of more than one X-ray window for the entrance of the incident X-ray beam and exit of the transmitted X-ray beam. The X-ray windows must use a material with a low absorption coefficient and must not contain any crystalline components that would cause diffraction of the X-ray beam. Any diffraction or unwanted dispersion of the X-ray beam by the window material will reduce the intensity of the X-rays reaching the detector and has been found to result in broadening of the measured XANES features.³ Therefore low absorbing, amorphous materials such as polyimide film, pyrolytic carbon, graphite, beryllium, quartz or boron nitride are preferred. The X-ray attenuation values of these popular X-ray window materials are detailed in Table 5.2. DuPont™ Kapton® is a polyimide film, synthesised from an aromatic dianhydride and an aromatic diamine, containing only low absorbing elements for a low absorption coefficient.⁴ Kapton® can be supplied as a film of different thicknesses (7.5 μm – 125 μm), which has chemical resistance and thermal resistance (25 - 200°C) that makes it suitable for use in low

temperature *operando* spectroscopic cells. The microstructure of hot pressed boron nitride windows has been found to cause unwanted dispersion of the X-ray beam, resulting in broadening of the measured XANES spectra.⁵

Table 5.2. X-ray attenuation length of X-ray window materials, taken from B. L. Henke, *Atomic Data and Nuclear Data Tables*, 54 (1993) 181-342.⁶

Material		Density / g cm ⁻³	X-ray attenuation length at 24350 eV / mm
Kapton®	C ₂₂ H ₁₀ N ₂ O ₅	1.4	2.21
Boron Nitride	BN	2.3	15.7
Silicon Nitride	Si ₃ N ₄	3.4	1.90
Pyrolytic Carbon	C	2.2	17.0
Graphite	C	2.3	16.3
Beryllium	Be	1.9	31.4
Quartz	SiO ₂	2.7	2.82
Aluminium	Al	2.7	2.07

The above attenuation lengths and absorption coefficients (Table 5.2) have been reported for an X-ray beam at the Pd K-edge, which are the XAFS spectra used to study Pd nanoparticle catalysts in this work. However, in order to study the many other metal nanoparticle catalyst materials or other absorption edges, the absorption coefficients and attenuations lengths at those energies must also be considered.

For spatial resolution of the XAFS measurements, the X-ray beam should be focussed to a small spot size and the X-ray window must extend along the length of the reactor such that the X-ray beam can penetrate different spatial positions of the sample. Typically, the X-ray beam at the end station of a bending magnet is focussed to a spot size of on the order of 200 µm eg. B18 beam size at sample is 200 µm horizontally and 250 µm vertically.⁷

The nature of the polychromatic X-ray beam used in EDE measurements means that the sample must be located at the focal point of the X-ray beam. Moreover, the diverging X-ray beam before and after the focal point must be considered when designing the shape of the X-ray window, making sure not to cut off the beam at either end of the spectrum. The spot size at the focal point is also able to perform spatially resolved measurements, eg. I20-EDE spot size at the focal point is a minimum of 30 µm x 100 µm.⁸

5.2.2 Infrared

For successful DRIFTS spectroscopy, the incident IR radiation beam must approach the 'flat' surface of the sample at a grazing angle of 45°C, and the diffusely reflected IR beam must be able to travel from the surface of the sample back to the MCT detector within the IR spectrometer. The IR beam will also be attenuated by IR active molecules

in the gas phase and so efforts should be made to eliminate those gases (*i.e.* H₂O and CO₂) from the path of the IR beam. A suitable IR window material must be used to permit the transmission of IR photons to and from the sample surface, within the reactor cell. For the collection of *operando* DRIFTS spectra, the window material must retain these optical properties at a range of temperatures and atmospheres that the spectroscopic cell will be used for. A list of the commonly used IR window materials are presented in Table 5.3, together with their transmission range. The spectral range of DRIFTS spectra typically used for study of heterogeneous catalysis ranges from 4000 – 400 cm⁻¹. The high stretching frequency of O-H of water molecules, alcohol and Brønsted acid sites at zeolite surfaces⁹ absorb at the high wavenumber end of the spectrum and framework Al-O and Si-O bonds¹⁰ of the catalyst support will absorb at the low wavenumber region. The use of Al₂O₃, SiO₂ and MgF₂ are inappropriate for the spectral range required in this application. The majority of other optical materials listed in Table 5.3 are ionic crystals with high melting points, however, their optical properties are found to change at elevated temperature. ZnSe is known to oxidise in air and lose its transmission range at temperatures above 250°C, so the use of ZnSe for high temperature or oxidation reactions is not suitable, unless the windows of the cell can be cooled.¹¹ Germanium is also unsuitable at high temperatures, as thermal electrons flood the band gap above 100°C,¹² and KBr windows are unsuitable for any reaction whereby water vapour is present either in the reactant gas feed or as a reaction product because KBr has high solubility in water.¹³ According to previous investigations in the optical properties of IR window materials, Si and GaAs do not experience a decrease in the overall transmission until temperatures in excess of 500°C.¹² This leaves BaF₂ – an expensive synthetic crystal – and CaF₂, as potential IR window materials for the spectroscopic reactor.

Table 5.3. Optical properties of IR window materials, taken from E. Palik, *Handbook of Optical Constants*¹⁴

IR Window Material	Transmission Range (μm)	Transmission Range (cm^{-1})	Additional properties
BaF ₂	0.15 - 12	850 – 66, 500	
CaF ₂	0.13 - 10	1000 – 76, 900	
GaAs	0.9 - 16	625 – 11, 100	
Ge	1.8 - 23	435 – 5, 560	Ge becomes opaque at >100°C, as the band gap becomes flooded with thermal electrons
MgF ₂	0.12 - 7	1, 430 – 83, 300	
KBr	0.23 - 25	400 – 43, 000	Soluble in H ₂ O.
SiO ₂	0.18 - 3.5 and 40 - 100	2860 – 55, 500 and 100 - 250	Crystalline quartz transforms to glass at >490°C
Al ₂ O ₃	0.17 – 5.5	1820 – 58, 800	
Si	1.2 – 15 and 30 - 100	650 – 8, 300 and 100 - 300	Si containing O will have an absorption band at 1100 cm^{-1}
ZnSe	0.6 - 21	500 – 16, 500	Oxidises in air at >250°C

5.2.3 Reactor considerations

Minimal dead volume inside the reactor is required to observe the fast response of the catalyst to fast switching of the gas feed in a time-resolved manner. The conventional dome shaped reaction vessel of DRIFTS reactors creates a dead volume relating to the relatively large volume of the empty space within the dome compared to the small volume of the sample that occupies the cup within. Additionally, the flow of reactants through the catalyst must be considered. Ideally, to mimic the conditions of the catalyst in its 'real' operating environment, the reactor configuration should allow gas to flow continually through the length of the catalyst bed. The catalyst bed must allow the diffusion of gases through the reactor, as a blockage can cause overpressure in the reactor which would change the reaction conditions under investigation and create a potential safety hazard.

Most heterogeneous catalytic processes in industrial applications occur in a plug flow reactor.^{15, 16} The nature of a plug flow reactor is that reactants are consumed as they flow through the reactor, resulting in an axial concentration gradient from inlet to outlet.¹⁷ This is the basis of the necessity for spatial resolution in *operando* measurements of heterogeneous catalysts operating in plug flow configuration, whereby reaction conditions, and therefore catalyst reactivity, changes with axial position along the length of the plug flow reactor.

The spectroscopic reaction chamber must be able to be heated in a controlled manner with homogeneous heat distribution across the catalyst bed. It is inevitable that

exothermic (or endothermic) reactions during the operation of the catalyst will act to create temperature gradients within the bed, but for the isothermal measurements under steady state conditions, a homogeneous sample temperature should be achieved. In order to complement the spectroscopic measurements with measurements of the sample temperature in real time, a thermocouple must be inserted into the catalyst bed in a position as close as possible to the region measured by the spectroscopic technique, without interfering with the gas flow or spectroscopy.

The radiation probe for the spectroscopic technique must not perturb the sample or the catalytic reaction. It is known that high flux of high energy electrons can cause photoreduction of vulnerable metals, oxides or cations in solution. Preliminary tests should be conducted to check the stability of the sample, reaction environment and spectroscopic cell in the X-ray and IR beams.

Using a combined multi-technique approach requires that the XAFS and DRIFTS are able to probe the same region of the sample. This is particularly important for *operando* measurements of a catalyst in plug-flow configuration where the catalyst is exposed to different reaction environments at different positions. For DRIFTS spectroscopy the IR beam penetrates a depth of 100 – 300 μm from the sample surface (depending on the material),¹⁸ whereas the XAFS spectrum is acquired from transmission of X-rays through the entire path length through the sample, making it impossible to probe exactly the same portion of the catalyst with each technique. The IR beam and X-ray beam should be carefully aligned such that the surface and bulk measurements, respectively, examine the same axial position of the catalyst within the plug-flow configuration. In this way, one can assume that the reaction conditions and catalytic reactivity are consistent.

5.3 Literature Review: Design of the spectroscopic cell

The early reports of a spectroscopic cell used to contain a catalyst in its reaction environment for *in situ* spectroscopy were those based on FTIR spectroscopy measurements made in the transmission mode. In one particular example, the *in situ* IR spectroscopic cell was used to examine HY zeolite catalysts during the activation of cyclohexene at 370°C.¹⁹ The cell was constructed from stainless steel tubing with two CaF_2 windows installed on opposing sides of the cell for the transmission of IR radiation through the cell. The catalyst sample was pressed into a self-supporting wafer and positioned in a stainless steel holder within the cell, between the two IR windows, in the path of the IR radiation. The reactant gases were introduced into the cell via a stainless steel tube on one side of the pellet and were allowed to flow through the catalyst then leave the reactor from the tubing at the other side. The dead volume between the windows and the sample were filled with KBr rods, such that the gas flow was forced to flow through the catalyst pellet. Heating of the sample was achieved by a heater inserted close to the sample, and monitored by a thermocouple inserted into

the cell. This was one of the first reports of IR spectroscopy conducted of a catalyst in conditions similar to the 'real' operating reaction conditions. Despite being one of the first reported experimental set-ups for *in situ* spectroscopy, it was considerably advanced in being able to investigate a real catalyst material under controlled reaction environments, at elevated temperatures in a cell with limited dead-volume.

Transmission FTIR measurements of more recent studies still require the catalyst to be pressed into a self-supporting wafer. One reason for this is the absorption of IR radiation by the sample that would prevent the transmission of IR radiation through a fixed bed (self-supported pellets typically contain $<50 \text{ mg}_{\text{catalyst}} \text{ cm}^{-2}$). Additionally, there is a problem in finding a suitable IR transparent window material to contain the sample in harsh reaction environments. The major problem of conducting *operando* measurements with this type of experimental set-up whereby gases are forced to flow through the pressed catalyst pellet, is the poor diffusion of gas through the sample. This can cause build-up of high pressure of gas in front of the catalyst pellet or bypassing of the gas flow around the catalyst pellet rather than through it, resulting in poor conversion rates compared to the real operation of the catalyst.²⁰

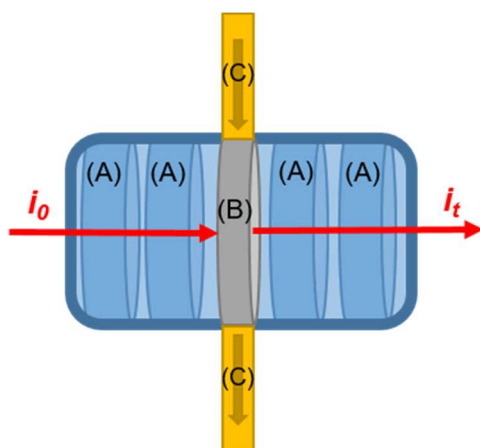


Figure 5.1. Design of an early *in situ* spectroscopic cell for infrared measurements in transmission mode, showing (A) KBr rods, (B) self-supported wafer of pressed catalyst sample, (C) Swagelok gas lines, and the incident (i_0) and transmitted (i_t) IR beam. Reconstructed from J. F. Joly, *Catal. Today* 9 (1991) 31-38.¹⁹

The challenges associated with poor diffusion and poor transmission of IR radiation through catalyst pellets can be overcome by collecting IR spectra in the diffuse reflection mode. The development of *in situ* reaction chambers for DRIFTS spectroscopy of heterogeneous catalyst materials have permitted a large number of *in situ* and *operando* experiments.^{18, 21-27} *In situ* DRIFTS measurements date back to 1986, and must acknowledge the significance of Harrick Scientific in developing the DRIFTS reaction chamber and 'praying mantis' mirror assembly to facilitate these experiments.²⁸ The early design of the Harrick DRIFTS reaction chamber (DRA-2CN), shown in Figure 5.2, allowed the catalyst sample to be examined by DRIFTS at variable temperatures and pressures. The spectroscopic cell was built around a central post (1)

which contained a heater and a thermocouple, and hosted the sample as a powder in a cup at the top of the post. The sample was enclosed by a cover (2) that was fitted with two KBr (or NaCl) windows (3a and 3b) for the entry and exit of the IR beam to and from the sample surface. The cover was fixed to the base of the cell with an o-ring to create a gas-tight seal, and an inlet and outlet for fixing gas lines or vacuum lines were provided. This setup was used repeatedly for these early *in situ* DRIFTS studies of catalyst materials during thermal decomposition and oxidation reaction conditions.^{23, 29-32}

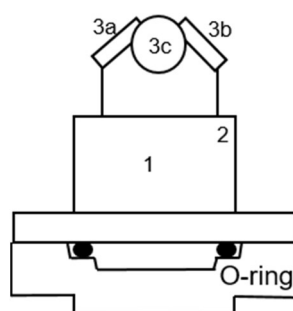


Figure 5.2. Harrick 'praying mantis' mirror (or arrangement for DRIFTS and *in situ* spectroscopic cell. Image reproduced from Leyden et. al. (1986).²⁸

Later variations of the DRIFTS reaction chamber have been devised by Harrick Scientific (Figure 5.3a)³³ and Spectra-tech³⁴ (Figure 5.3b). Both these variations of the DRIFTS reaction chamber are constructed from stainless steel, comprising a cylindrical sample cup which sits in the centre of the reactor. Both reactors make use of two interchangeable, canted IR windows for the transmission of the incident IR beam to the sample surface, and transmission of the reflected IR beam from the sample to the detector. The Harrick model fixes IR windows to a stainless steel hemispherical dome, which is sealed against the main vessel of the reactor with a gas tight Kalrez o-ring and secured with a gasket and screws. Rather than using a hemispherical dome, the Spectra-tech model has two IR windows fixed directed to the canted surfaces of the main reaction chamber. Both reaction chambers use a heating cartridge positioned directly beneath the sample cup and a K-type thermocouple inserted near to the catalyst sample for controlling the sample temperature. Both models make use of a cooling jacket that allows the exterior stainless steel casing of the reactor to be maintained at a lower temperature than the sample cup. This permits heating the sample to high temperatures (up to 500°C) without causing thermal damage to the optical windows located in the cooled exterior casing. The main difference between the Harrick and Spectra-tech models are the dead volume in each case. The dead volume of the commercial Harrick DRIFTS cell is 14 cm³ compared to a sample volume of 0.027 cm³, which results in a delay of approximately 8 seconds for an experiment using a total flow rate of 100 ml min⁻¹. The dead volume of the Spectra-Tech model is

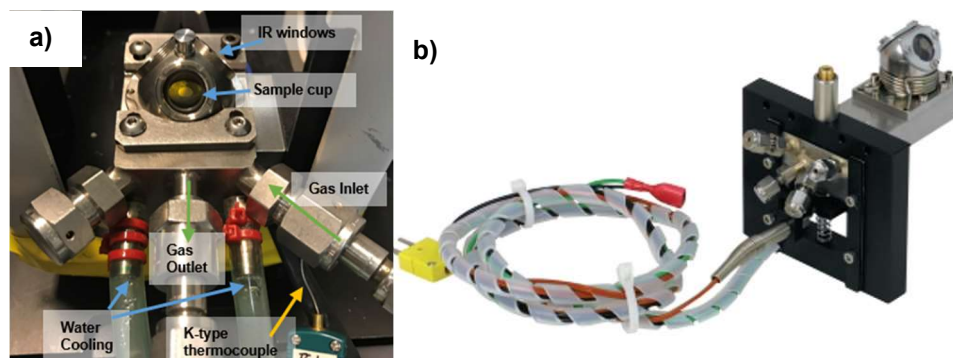


Figure 5.3. Images of commercial DRIFTS reaction chambers. a) Harrick DRIFTS reaction chamber, b) Spectra-tech DRIFTS reaction chamber. Photo Courtesy of Thermo Fisher Scientific.³⁵

improved to 3 cm³, for a delay of only 2 seconds with gas flow rate of 100 ml min⁻¹. The significance of these *in situ* DRIFTS cells in providing a way to conduct *in situ* spectroscopy of heterogeneous catalysts in controlled reaction environments has been paramount to our understanding of catalytic surface reactivity. However, there are limitations with these cell designs in terms of the requirements for advanced *operando* spectroscopy. The sample inhomogeneity due to temperature gradients within the reactor becomes a problem when the surface of the sample probed by the IR radiation is at a cooler temperature than the catalyst at the bottom of the sample cup that is closest to the heater. The temperature gradient becomes steeper as the power to the heater is increased, as the temperature at the bottom of the catalyst bed increases but the surface of the catalyst bed continues to be cooled by the cold inlet gas feed. Moreover, the flow of gases through the catalyst bed can establish plug-flow reaction conditions and therefore change in gas concentrations as a function of position in the catalyst bed. The catalytic activity measured by end-pipe analysis of the exhaust gas is therefore not a direct measurement of the catalytic activity of the catalyst investigated at the top of the bed with DRIFTS spectroscopy. An improved design of the *in situ* DRIFTS reaction chamber by Specac Ltd. has attempted to reduce the dead cell volume and temperature gradients by using just one IR window positioned on top of the surface of the sample bed.³⁵ This model still makes use of a water cooling system to maintain low temperature of the window material and so a temperature gradient – and concentration gradients – are still an apparent problem.

The development of *in situ* cells for techniques using high energy X-rays, such as *in situ* XRD and XAFS, have the advantage that high penetrating power of the X-ray radiation allows for low absorbing materials to be used to contain the sample. Early designs for *in situ* XAFS and *in situ* XRD experiments used an external furnace, with the catalyst mounted inside as a pressed pellet. In 1993, Liu *et al.* reported the use of a furnace-type spectroscopic cell for *in situ* XANES to study a Cu catalyst in reaction conditions for the catalytic reduction of NO. In this arrangement, the catalyst sample was pressed into a self-supporting wafer and mounted within a furnace in such a way that the gases were forced to flow through the permeable catalyst wafer.^{36, 37} However,

these types of spectroscopic cells often suffered a large amount of heat loss and so were unable to achieve temperatures greater than 500°C. Some other groups reported *in situ* XRD and *in situ* XAFS measurements around this time, although the experimental reaction chamber were not disclosed.³⁸⁻⁴¹

To overcome the problem of heat loss and to achieve higher temperatures, a new experimental setup was devised by Dent *et al.* in 1995 which contained the sample within a tube furnace and allowed the sample to be heated in air up to 1200°C.^{42, 43} In this tube furnace design, the sample was pressed into a self-supporting disk and mounted onto a sample holder. The sample holder was inserted into the furnace which comprised of a heated wire frame constructed from thermally resistant pyrophyllite and alumina. The wire frame was encased within an insulating heat shield fitted with Kapton® windows for transmission of X-rays to and from the sample. The wire frame and casing were then contained within an outer jacket which had two end caps cooled by an external water jacket, and the space between the heat shield and outer jacket was filled with mineral wool for further insulation. The incorporation of an insulated heat shield meant that the sample was able to be heated in a controlled way to much higher temperatures (1200°C) than previously possible. A thermocouple fixed to the sample holder and in direct contact with the sample allowed for accurate temperature monitoring during the *in situ* measurements. The same problem of poor gas diffusion through the pressed catalyst pellets in these set-ups, as experienced by the transmission IR measurements, meant that the measured catalyst was not exposed to the desired reaction conditions, and so a different approach would be needed for *in situ* measurements.

The quartz capillary sample containers used for *ex situ* XRD and XAFS were easily transformed into flow reactors, by connecting inlet and outlet gas lines via leak tight stainless steel tube fittings at either end. This created a smooth transition from *ex situ* to *in situ* measurements, whereby gases were allowed to flow through the sample in a plug flow arrangement.⁴⁴ These simple quartz tube reactors can be heated to temperatures up to 500°C using a hot air blower from beneath the reactor, as imaged in Figure 5.4.⁴⁵ To reduce the problem of temperature inhomogeneity within the quartz capillary, an X-ray transparent hood constructed from Kapton® foil or aluminium was positioned around the sample capillary to reduce heat loss to the surroundings. This experimental set-up is still used at present for *in situ* XAFS or *in situ* XRD experiments of catalysts under plug-flow reaction conditions. The photograph in Figure 5.4 shows the quartz capillary reactor used in the investigation of MoO_x/Fe₂O₃ catalysts for the selective oxidation of methanol on beamline B18 at Diamond Light Source.⁴⁶

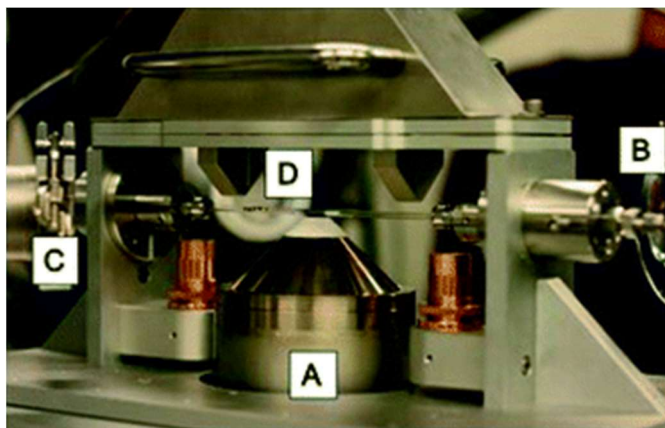


Figure 5.4. Quartz capillary microreactor used for *in situ* XAFS measurements of a catalyst under reaction conditions. (A) Hot air blower, (B) incident X-ray direction (C) transmitted X-ray (D) Fluorescence detector. Reprinted from C Brookes et al., *Cat. Sci. Tech.*, 2016, 6, 722-730.⁴⁶

Considering the specific requirements for spectroscopic reactors to conduct *operando* XAFS and DRIFTS independently, the challenge to perform both techniques simultaneously in a single reactor with the appropriate time resolution and spatial resolution requires careful design of a new spectroscopic reactor. There have been many attempts to conduct combined, *operando* XAFS and DRIFTS spectroscopy of heterogeneous catalysts using different spectroscopic cells,^{5, 47, 48} all presenting scope for improvement to the method.

The first report of a new reactor for a combined, simultaneous XAFS and DRIFTS method was published by McDougall in 1999,²⁵ and used successfully in 2004.⁴⁹ This cell was much like the stainless steel reaction chamber of the Spectra-Tech DRIFTS cell but with a flat top hosting just one IR window that sits level against the catalyst surface (Figure 5.5). Apertures were machined into the walls of the stainless steel chamber and fitted with X-ray windows of Kapton® material (or hot pressed BN) using high temperature epoxy. The IR window at the surface used a CaF₂ crystal, which has improved temperature resistance and chemical resistance compared to ZnSe – an important consideration when the window was in close proximity to the catalyst bed. A thermocouple inside the cell was positioned with its tip inside the catalyst bed to directly probe the sample temperature, and the gases were allowed to flow over the catalyst bed.^{25, 50} The main advantage of this cell design was the reduced dead volume compared to the dome shaped reaction vessel of the conventional Harrick DRIFTS cell or the canted roof of the Spectra-Tech analogue. This allowed for faster time-resolved studies of gas switching experiments, demonstrated by the combined EDE-XAFS and DRIFTS experiment at beamline ID24, ESRF whereby both datasets were collected with a time resolution of 64 ms per spectrum.⁵⁰ The limitations associated with this cell design were firstly the maximum operating temperature of the reactor which was limited to 400°C due to the proximity of the CaF₂ window to the sample. Operating the cell to temperatures higher than this would have caused the CaF₂ to degrade. Secondly, the

small aperture for X-ray transmission through the catalyst sample did not allow for any spatial resolution in the measurements, and the fixed X-ray path length through the sample limits the range of XAFS edge energies and sample materials that could be studied. Most significantly, the problem with conducting operando spectroscopy in this reactor is that the gas flow passes over the catalyst bed, rather than passing through it. This means that the observed catalytic activity would be lower than expected as much of the catalyst would not be contacted by the reactant feedstock and a plug-flow configuration could not be achieved. Despite the limitations, this cell design was used successfully to obtain information for nanoparticle catalyst structure, function and reactivity in differing reaction conditions.^{5, 49-52}

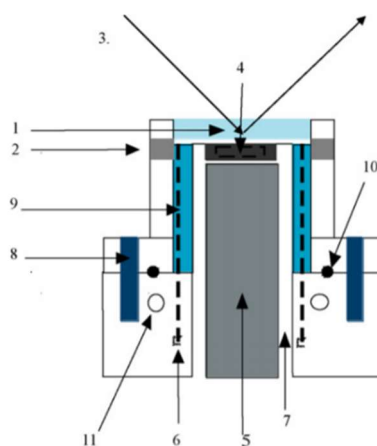


Figure 5.5. Drawing of the modified Spectra-Tech spectroscopic cell designed by McDougall *et al.*²⁵ for combined XAFS/DRIFTS spectroscopy. Drawing shows a cross-sectional plan with (1) CaF₂ IR window, (2) BN X-ray windows, (3) path of incident and diffusely reflected IR beam, (4) BN sample cup, (5) heating cartridge, (6) inlet/outlet gas lines, (7) stainless steel reactor body, (8) bolts, (9) ceramic insulation, (10) Kalrez o-ring and (11) water cooling circulation path. Image taken from Newton *et al. Catalysis Today* 126 (2007) 64.⁵⁰

An alternative approach for combined, *in situ* XAFS and IR spectroscopy was in the use of a cross-shaped cell (schematic drawing shown in Figure 5.6) designed by Bando *et al.* in 2009, which is able to perform both techniques in transmission mode.⁵³ For these combined XAFS and IR measurements, the catalyst sample was mounted as a pressed pellet in the centre of the cell. The X-ray and IR beams were oriented perpendicular to each other, and intersected at the sample in the centre. The X-ray and IR beams were allowed to enter and leave the cell via two pairs of windows; the X-ray windows were constructed from polyimide films (125 µm thick), and the IR windows used KBr crystals (3 mm thick). To reduce the dead volume within the cell, and reduce the IR absorption from gas phase molecules, CaF₂ crystal rods were sandwiched between the sample and IR windows. Gases were forced to flow through the cell via two sets of inlet and outlet valves located at each end of the arms of the cell. Although the limitations of the spectroscopic cell were not outlined by the experimental reports,^{53, 54} there are obvious problems with this cell design that relate to the large dead volume of the reactor, the ability for gases to by-pass the catalyst and the usual problems

associated with gas diffusion and poor IR transmission through pelletized catalyst samples.

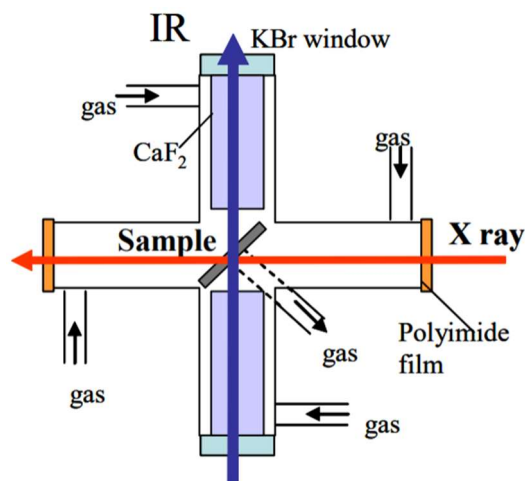


Figure 5.6. Schematic drawing of the cross-shaped *in situ* spectroscopic cell designed by Bando *et al.* for performing combined XAFS and IR in transmission mode. Figure shows the position of the sample mounted as a pellet at the centre of the reactor, the path of the IR beam (blue) and path of the X-ray beam (red). Figure taken from K. K. Bando *et al.*, *J. Phys.: Conference Series* 190 (2009) 012158.⁵³

The Harrick DRIFTS cell was modified for combined, *in situ* XAFS and DRIFTS spectroscopy at beamline X18A of the National Synchrotron Light Source in 2011.⁵⁵ The major advantage of this experimental set-up was the facilitated alignment of both X-ray and IR beams with respect to the sample, owing to the assembly of the motorised 'DaVinci arm' accessory and compatible reaction chamber. The Harrick DRIFTS cell reported in this work used two KBr windows fixed to the hemispherical dome of the reaction chamber (Figure 5.7). The X-ray beam passed through the reactor to the sample via two holes (1.7 mm in diameter), that were sealed at each end with glassy carbon windows. The sample cup containing the catalyst had an inner diameter of 3.17 mm, and allowed the transmission of the X-ray beam via two apertures located 1.04 mm from the surface of the sample cup. Akin to the conventional DRIFTS cell, there were connections for the inlet and outlet gas lines, and two additional connections for the inlet and outlet of a circulating water cooling system. The limitations of this cell design reflect the aforementioned dead cell volume associated with the dome shape of the Harrick design, which limits the time resolution of *in situ* measurements. The Harrick cell is also known to suffer from sample inhomogeneity when operated at high temperatures, however, for the maximum operating temperature in this work (200°C) this was not considered a significant problem. Akin to the McDougal cell design, the small window diameter for the X-ray beam eliminates the possibility for any spatial resolution in XAFS measurements, and the fixed path length through the sample prohibits the use of softer X-ray energies and absorbing materials. The distance of the X-ray beam fixed 1.04 mm from the sample surface means that XAFS and DRIFTS spectroscopy probe different portions of the sample, which limits the interpretation of

the combined techniques due to temperature and compositional gradients within the catalyst bed. This modified Harrick DRIFTS cell has been used by Gibson *et al.* to study the structural rearrangement of AuPd nanoparticle catalysts during reaction conditions for CO oxidation, and in Chapters 3 and 4 of this thesis.⁵⁶ These studies demonstrate the facilitated experimental setup and sample alignment at beamlines B18, Diamond Light Source and SuperXAS at the Swiss Light Source.

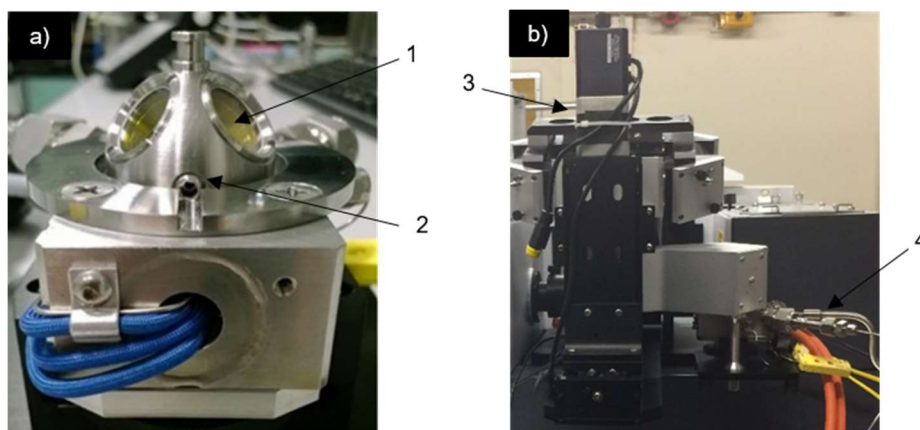


Figure 5.7. Photographs of a) modified Harrick XAFS/DRIFTS reaction chamber and b) Harrick DaVinci arm installed on FTIR spectrometer. (1) ZnSe IR windows, (2) Vitreous carbon X-ray windows, (3) DaVinci arm accessory (4) Gas tubing connected to XAFS/DRIFTS reaction chamber.

The commercial Harrick cell was modified again by Argonne National Laboratory in 2013, this time allowing for combined XAFS and DRIFTS as well as X-ray Pair Distribution Function (PDF) measurements.³ This was achieved by drilling through the Harrick DRIFTS reactor and installing two new X-ray windows (Figure 5.8). The first X-ray window, constructed from polyimide material, was fitted into a small aperture (3 mm diameter) on one side of the reactor for entrance of the incident X-ray beam into the reaction chamber. The second X-ray window, also constructed from polyimide material, was fitted into a larger aperture (12 mm diameter) on the opposing side of the reaction chamber, with its centre slightly offset from the position of the X-ray beam such that it allowed exit of the additional scattered X-ray radiation, as well as the transmitted beam, at angles up to 45° from the sample. Polyimide window materials were chosen for this cell design because they were found to interfere least with the low intensity scattered X-rays. By using larger X-ray windows than other XAFS/DRIFTS reaction chambers, there was the possibility to probe different spatial positions of the catalyst bed (within a 1.5 mm vertical slot of the sample cup) by vertically translating the spectroscopic cell with respect to the X-ray beam. Indeed, variations in the state of reaction were reported when probing different positions from the top to the bottom of the catalyst bed.

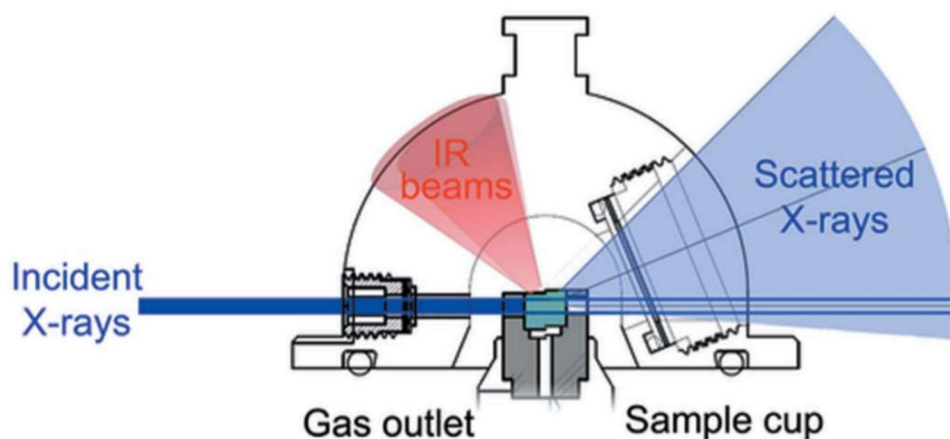


Figure 5.8. Sketch of the modified dome of the combined XAFS/DRIFTS reaction chamber designed by Beyer *et al.* showing the path of the incident, transmitted and scattered X-ray beams (blue), and the incident and diffusely reflected IR beams (red). Image taken from KA Beyer, *et al.*, *J. Appl. Crystallogr.*, 2014, 47, 95-101.³

Newton *et al.* in 2013 report the combined XAFS/DRIFTS method implemented at beamline ID24 of the European Synchrotron Radiation Facility (ESRF), using a cell design modified from the commercial Spectra-Tech DRIFTS cell.⁵¹ As with the *in situ* Spectra-Tech DRIFTS reaction chamber mentioned previously, the dead volume is smaller than that of the Harrick analogue due to the alternative shape of the reaction vessel. This group reported two main advantages of this cell, which are in line with those of the Harrick and Spectra-Tech designs; (i) gas flows through the catalyst (rather than over it) to achieve plug-flow configuration, and (ii) high maximum operating temperature of 800°C due to a water cooling exterior that maintains a cooler temperature of the IR windows. This again leads to the recognised problem of temperature and gas concentration gradients within the catalyst bed that are not considered by the fixed spatial position of spectroscopic techniques. Similarly to the Harrick cell design, this becomes a greater problem when the sample is heated to higher temperatures from beneath but continuously cooled at the surface by the cold incoming gas feed. The surface of the catalyst sample probed by DRIFTS spectroscopy would therefore be operating at lower temperature than the catalyst at a position >1 mm beneath the surface that is probed by XAFS, meaning that there is difficult correlation between the two spectroscopic techniques.

The cell design reported by D. Ferri *et al.* in 2014 was the first to move away from the commercial DRIFTS style reaction chamber.⁵⁷ In this work, a spectroscopic cell was designed to contain the catalyst sample in a capillary shaped reaction vessel, with continuous gas flow through the length of the reactor in order to comply with plug-flow conditions. In this ambitious design, it was attempted to pass both the IR and X-ray radiation beams through the same window that lay on the top face of the reactor in direct contact with the sample (Figure 5.9).⁵⁷ Due to the conflicting material properties required for transparency in IR and X-ray radiation, it was not possible to find a suitable

material to serve as both an IR and X-ray window, and so the final cell design used a CaF_2 IR window with a 500 μm carbon filled aperture at its centre to accommodate transmission of the X-ray beam. The main body of the cell was constructed from a stainless steel block, with a 5 mm x 10 mm trench extruded from the middle to contain the catalyst sample. Two stainless steel 1/16" tubes were connected to both ends of the sample trench to allow the gas to flow from one end to the other. A K-type thermocouple (0.5 mm diameter) was inserted through one of the gas tubes such that the tip was positioned in direct contact with the sample within the catalyst bed. Heating cartridges positioned in the stainless steel block either side of the sample, allowed homogeneous heating of the sample up to 500°C. The sample trench was enclosed above and below by the window material, and sealed with graphite gaskets. The sample was sandwiched between quartz wool to avoid movement in the gas flow, and additional quartz wool was used as an insulating layer across the top of the cell. The high time resolution afforded by this cell design was demonstrated for XAFS measurements at the SuperXAS beamline of the Swiss Light Source, achieving XAFS data acquisition with a 1 second time resolution and complete exchange of gas through the reactor within 5 seconds (when operating at a total gas flow rate of 100 ml min^{-1}). This allowed for the modulated excitation approach whereby continuous perturbation and response measurements were processed to enhance the sensitivity of weak spectral features in EXAFS spectra. Although this cell design achieved high resolution

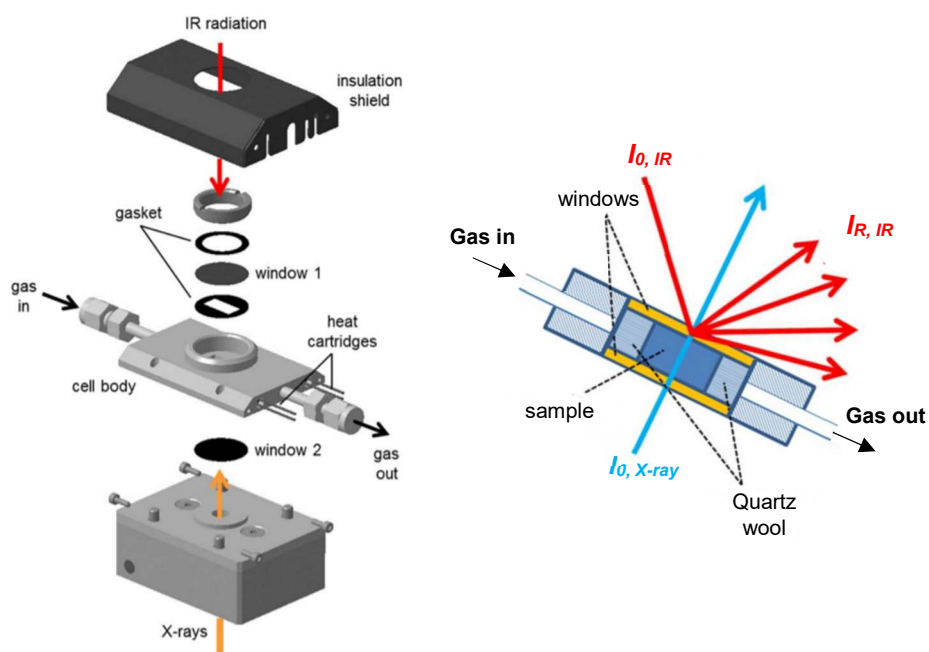


Figure 5.9. Cell design for capillary shaped XAFS/DRIFTS reaction vessel reported by Chiarello et al., a) exploded view of the different parts making up the cell and b) a simplified illustration of the cell design showing the path of the transmitted X-ray beam (blue) and the path of the diffusely reflected IR beam (red). Images modified from GL Chiarello et al., *Rev. Sci. Instrum.*, 2014, **85**, 074102.⁵⁷

in both XAFS and DRIFTS spectroscopy, it was still not possible to perform both techniques simultaneously and with any spatial resolution.

The most recent report of a new cell design for combined XAFS/DRIFTS spectroscopy has built on the original cell design by McDougall *et al.*,²⁵ making changes to ensure the gas flow does not bypass the sample and to allow higher operating temperatures.⁵⁸ This was achieved by constructing the cell in two parts; the cell body which contained the sample holder, thermocouple and gas system, and the cell dome which was fitted with two X-ray windows and one IR window (Figure 5.10). A Cu metal O-ring (CF16) was clamped between the dome and body to create a gas tight seal between the two parts, and the three windows were sealed to the dome using silicon glue (LOCTITE SI 5399). The main body of the cell was constructed from Inconel alloy, the X-ray windows used glassy carbon (200 μm) and the IR window used CaF_2 (2 mm thick). The dead volume of this cell is 0.5 cm^3 due to the 1 mm gap between the sample surface and IR window. To improve sample homogeneity compared to previous designs, and reduce the possibility for liquid condensation, there is the possibility for inlet and outlet gas lines to be heated to 150°C. This XAFS/DRIFTS cell design affords improvements to the investigation of a catalyst operating in plug flow configuration, with high time resolution and improved sample homogeneity. However, the operating temperature of the reactor was still limited due to the use of a silicon glue (resisting temperatures up to 350°C) and the small X-ray windows prevent the possibility of spatially resolved measurements beyond the front of the catalyst bed.

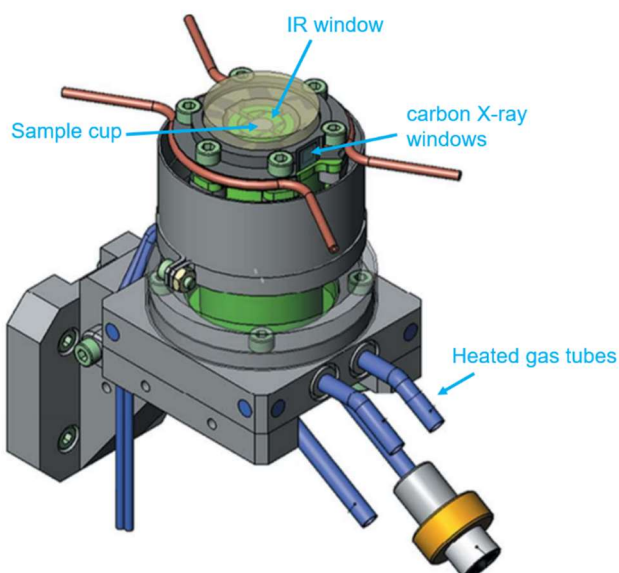


Figure 5.10. Concept design of XAFS/DRIFTS reaction chamber by Agostini *et al.* showing the IR window, X-ray windows, heated gas tubes and sample cup. Image modified from Agostini *et al.* *Journal of Synchrotron Radiation* 25 (2018) 1745.⁵⁸

Despite some constraints and measurement limitations, the above mentioned spectroscopic cells have permitted a number of *in situ* and *operando* studies to allow

new insights to the structure-function relationships of heterogeneous catalysts, and have demonstrated the worth of this combined multi-technique approach.⁵⁸ The previous articles reporting combined, *operando* XAFS/DRIFTS spectroscopy have demonstrated the difficulty in designing such experiments, and outlined the major challenges for future attempts. The main problems that need to be considered to improve future designs are reduced dead volume, plug-flow configuration and spatial resolution.

5.4 Cell Design Iterations

In order to achieve the final successful cell design for spatially resolved, combined, *operando* XAFS/DRIFTS spectroscopy in this project, multiple reaction cells were designed and constructed, each iteration building upon the problems identified with the previous design.

The fundamental concept was to construct a reactor that was based upon the capillary microreactor design used for *operando* XAFS reactors.^{45, 46} In this ideal reactor, the catalyst would be contained as a fixed bed inside the capillary and the gas would be forced to flow continuously through the length of the reactor achieving plug flow configuration. Ideally, the entire reactor would have been constructed from a single material in order to eliminate the problem of needing to join and seal two materials, and achieve uniform heating from an external source. The single chosen material would therefore need to permit transmission of both X-ray and IR radiation, whilst being resistant to the harsh reaction conditions inside the cell.

Realistically, as recognised in the ambitious work by Chiarello *et al.*,⁵⁷ finding a suitable material to serve as the main reactor body, IR window and X-ray window is not possible. Therefore, the design for the new XAFS/DRIFTS cell would require the use of more than one material that were joined by a gas tight seal. The first iteration of the proposed cell design used a single material to act as the main reactor body and the X-ray window, with a hole extruded in the top face of the capillary for installing an IR window. In order to perform DRIFTS measurements at the sample surface, the cylindrical shape of the conventional capillary shaped reactor would have to be modified to allow for a flat sample surface and a flat IR window.

5.4.1 3D Printed Plastic Model

A plastic prototype of the cell design was printed using HP DesignJet 3D printer with acrylonitrile butadiene styrene (ABS). The 3D drawing was made using the 3D CAD design software *SOLIDWORKS*, with carefully calculated dimensions such that the plastic prototype resembled the exact size and shape of the 'real' cell. This meant that the model prototype could be used to design the inlet and outlet gas connections, heating block, thermocouple and mounting posts for alignment to the 'Praying Mantis' IR optics. The dimensions of the cell were calculated according to the required X-ray

path length through the breadth of the catalyst bed, at the energies for the required XAFS acquisition. In the case of this cell design, the catalyst sample was 3wt% Pd/Al₂O₃ for Pd K-edge XAFS (24350 eV). The length of the reactor was then decided by considering the length/breadth aspect ratio of the plug flow reactors used in conventional lab based catalyst testing rigs to achieve similar space velocities. The 3D printed model and the 3D drawing of the first cell design are shown in Figures 5.11a and 5.11b. The main body of the reactor was a cuboid block with a hollow rectangular cross section (5 mm x 7 mm) and the two ends of the reactor were cylindrical (outer diameter mm, inner diameter mm) to allow for the connection of inlet and outlet gas tubing. A rectangular hole for the IR window (50 mm x 5 mm) was extruded from the top face of the reactor, with a 1 mm ledge to act as the window frame. A metal frame (Figure 5.11c), clamped together by 6 bolted rods (2 mm diameter), was designed to mount eight heating rods (3 mm diameter, 16 mm length) positioned at equal intervals along the length of the reactor and to secure the IR window. The frame was constructed

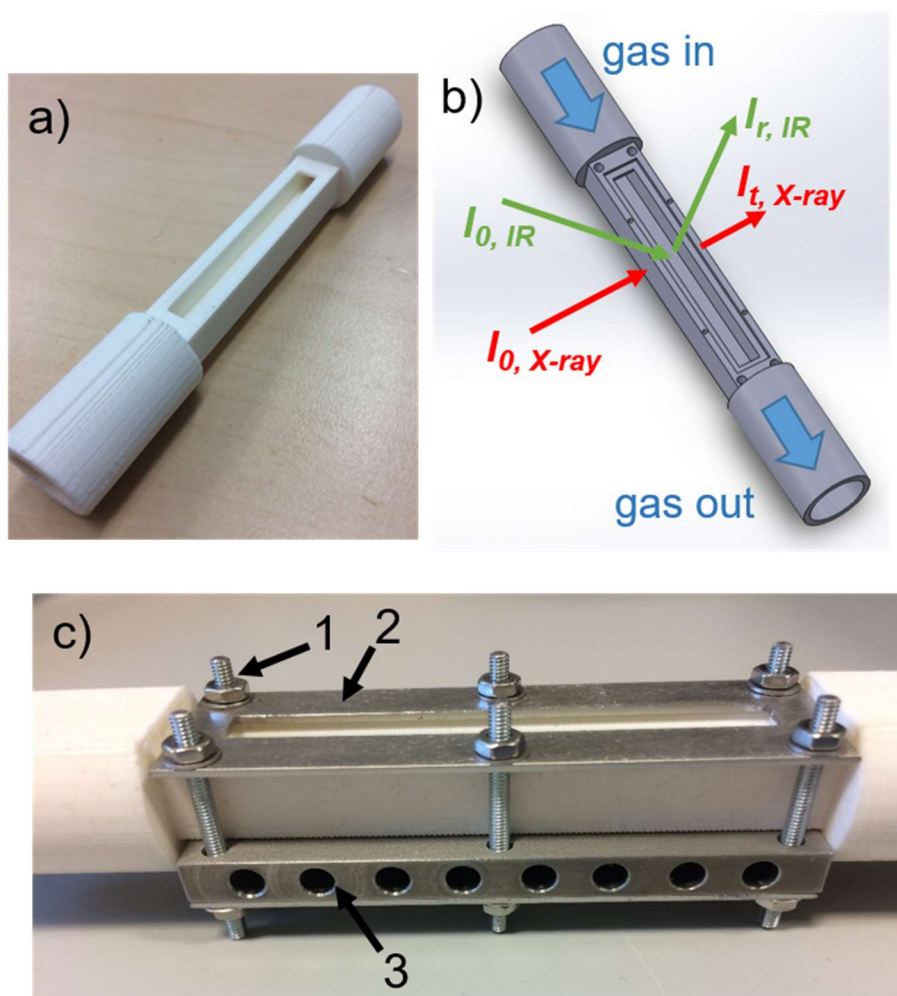


Figure 5.11. a) Photograph of 3D printed plastic prototype of new XAFS/DRIFTS cell design. b) Graphic representation of new XAFS/DRIFTS cell design showing the direction of gas flow, path of transmitted X-ray beam and path of reflected IR beam. c) Photograph of metal frame used to clamp the IR window and heating plate to the XAFS/DRIFTS cell. (1) bolted rods, (2) IR window frame (3) cavities to hold heating cartridges.

from stainless steel to aid thermal conduction for improved heat distribution around the cell.

5.4.2 Boron nitride cell

The first model of the new XAFS/DRIFTS reactor was constructed from a boron nitride material (AX05 grade) supplied from Saint Gobain. Boron nitride was chosen for its chemical inertness, resistance to high temperatures and low X-ray attenuation. The boron nitride material was supplied as a rod (20 mm diameter and 120 mm length) and machined to the desired shape. The walls of the rectangular part of the reactor were machined to a thickness of 2 mm, which allowed for 77.5% X-ray transmission (at 24350 eV) through both boron nitride walls (4 mm total). The advantage of constructing the entire cell from boron nitride means that X-rays can be transmitted through the sample compartment at any position along its length and its height, for spatial resolution in XAFS measurements.

The IR window was constructed from GaAs (52 mm x 7 mm x 2 mm), which has suitable thermal resistance but is known to suffer from oxidation and corrosion under reactive environments. Therefore a protective coating, akin to the diamond like carbon (DLC) films used for IR optics in meteorological applications,⁵⁹ was required to prevent contact of the GaAs window with the reaction environment whilst maintaining optical properties. Adapting a patent for durable anti-reflection coatings of infrared windows, a protective layer of Si (100 nm thick) was deposited onto the GaAs window surface using a chemical vapour deposition (CVD method), carried out at Queen's University Belfast Chemical Engineering workshop. The Si coated GaAs window (GaAs-Si) was then calcined at 600°C, before testing for IR transparency. The DRIFTS spectra of a supported Pd catalyst are shown in Figure 5.12, collected with the conventional canted ZnSe windows, then with the addition of the GaAs-Si window positioned between the sample surface and the ZnSe windows. In the acquisition of these DRIFTS spectra at sample temperatures of 100°C and 500°C, the ZnSe windows were continuously cooled by the water cooling of the Harrick dome, but the GaAs-Si window was allowed to reach the same temperature as the sample. There is reduced intensity of the absorption features in the spectral region $<1500\text{ cm}^{-1}$, particularly at higher temperatures, but the spectral information is not lost and there are no additional absorption bands for Si-O of the Si window surface. The transmission of IR radiation through the GaAs-Si is therefore suitable for DRIFTS acquisition up to 500°C. The advantage of using a rectangular IR window that extends the length of the sample compartment means that the DRIFTS measurements can be collected with spatial

resolution along the length of the reactor, complementing the spatially resolved XAFS measurements.

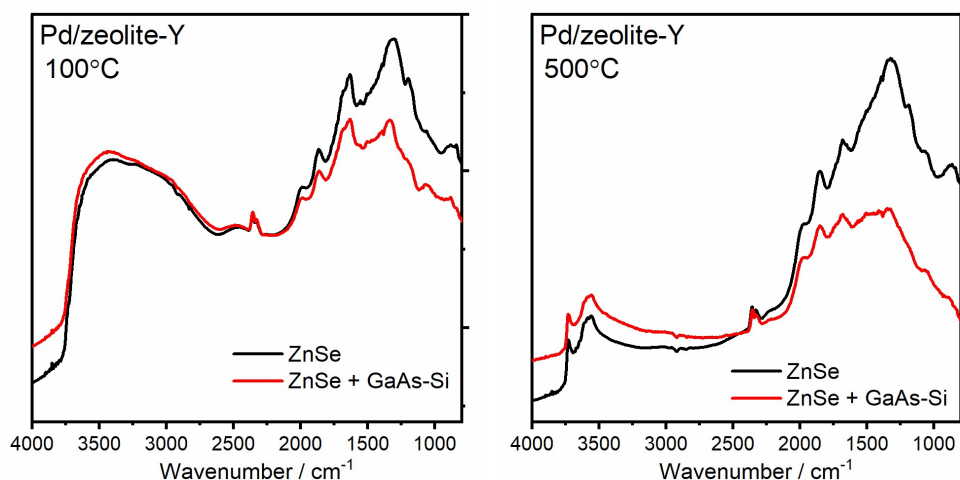


Figure 5.12. DRIFTS spectra of a supported Pd nanoparticle catalyst (Pd/zeolite-Y) contained within the Harrick DRIFTS cell with and without an additional GaAs-Si window at a) 100°C and b) 500°C.

The gas connections for the BN reactor used Swagelok stainless steel VCO fittings with a Teflon o-ring which were inserted into the cylindrical ends of the reactor and secured in place a ceramic adhesive (Aremco ceramabond 552). The photograph in Figure 5.13 shows the BN cell with the rectangular GaAs-Si window, connected to gas lines for testing gas flow through the reactor. The unforeseen problem with this initial cell design was the porosity of the BN material, which meant that the reactor was not gas tight. This made it unsuitable for testing catalytic reactions involving the use of harmful gases, and so a new cell design was required. Furthermore, the GaAs-Si window material was brittle and shattered easily – particularly when applying pressure in clamping down the window with the metal frame.

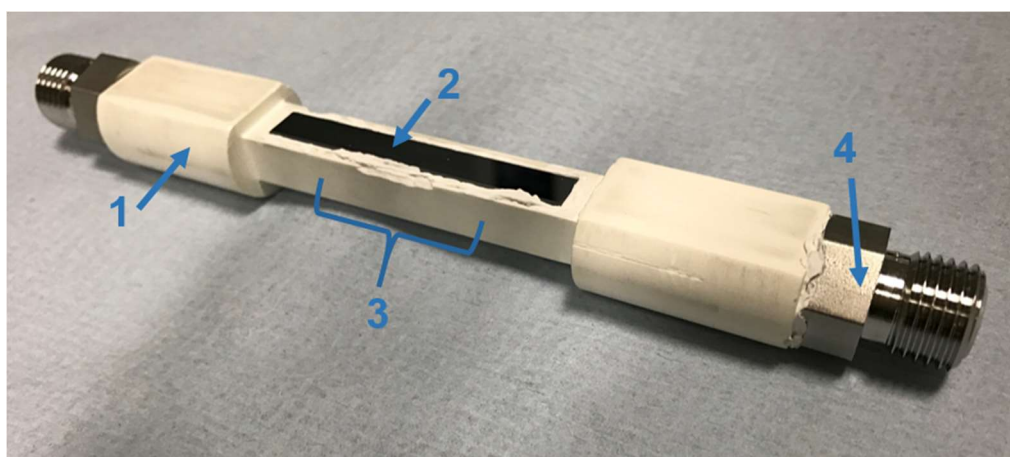


Figure 5.13. Photograph of the first iteration of the XAFS/DRIFTS reactor, showing (1) cell body constructed from BN, (2) GaAs-Si IR window, (3) square cross section capillary for containing the catalyst bed and (4) Swagelok VCO gas fittings.

5.4.3 Aluminium Cell

The second iteration of the new XAFS/DRIFTS reactor was constructed from aluminium, and the shape of the reactor body was modified to improve the integral strength (Figure 5.14). The overall dimensions of the cell were maintained (120 mm x 13 mm x 15 mm) but the entire cell was cut to a cuboidal shape. Circular holes for the inlet and outlet VCO gas connections extended a depth of 30 mm at each end of the reactor, where they met the square cross section channel which joined the two ends. A trench was extruded (50 mm x 5 mm) along the length of the two reactor walls either side of the catalyst bed, in order to thin the width of the aluminium walls for improved transmission of X-rays. The width of the walls after extruding the trench were 200 μm , which allowed for 82.4% transmission of X-rays (at 24350 eV) through both walls (total 400 μm). The new IR window was constructed from CaF_2 and used the same dimensions as the previous design (52 mm x 7 mm x 2 mm). The CaF_2 window and Swagelok gas fittings were fixed to the Al reactor using MINKON FortaFix Autostic ceramic adhesive sealant. This commercial sealant was understood to have high temperature resistance (1000°C), high resistance to oxidising and acidic environments and a low thermal expansion ($18 \times 10^{-6} \text{ C}^{-1}$).⁶⁰

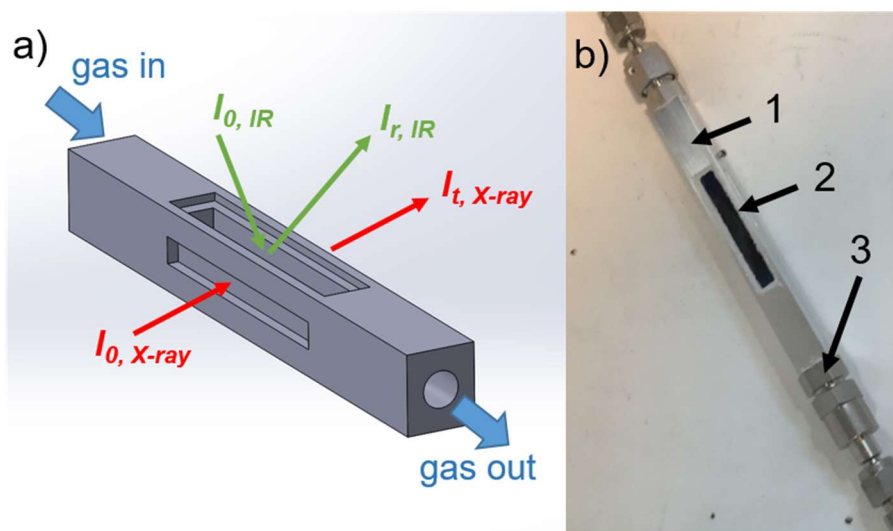


Figure 5.14. a) Graphic representation of the second iteration of the new XAFS/DRIFTS reactor showing direction of gas flow, path of transmitted X-ray beam and path of reflected IR beam. b) Photograph of the second iteration of the new XAFS/DRIFTS reactor showing (1) cell body constructed from Al, (2) CaF_2 IR window and (3) Swagelok VCO gas fittings.

A new mounting piece was designed and constructed by I20-EDE at Diamond Light Source, to secure the reactor in a fixed position on the motorised stage of the beamline. This mounting piece, shown in Figure 5.15, was machined from aluminium, using two screws at each end to clamp the XAFS/DRIFTS reactor in place with the heating plate sandwiched beneath the reactor. This arrangement eliminates the requirement for the metal frame and bolted rods (of the previous design) that were obstructing the X-ray window and exerting pressure on the fragile IR window. A K-type thermocouple

(0.75 mm diameter) was inserted through the gas line at the inlet of the reactor and sealed with a Swagelok fitting (1/16" tube fitting). The heating plate used the same dimensions as the previous design, to accommodate eight heating rods, and a smaller hole (1.1 mm diameter) was drilled into the heating plate to accommodate a second K-type thermocouple (1 mm diameter).

XAFS can be collected in transmission mode at any position along the length of the 50 mm trench, which means that XAFS measurements can be collected with a degree of spatial resolution. Both quick scanning and energy dispersive XAFS can be used in transmission mode to acquire EXAFS on the millisecond timescale. Similarly, DRIFTS spectra can be collected on the millisecond timescale at any position along the 50 mm length of the CaF_2 window, thus the spatial resolution and time resolution of DRIFTS measurements can match those of the XAFS measurements. This makes improvements on previous cell designs which have only allowed for XAFS and DRIFTS measurements at a single position of the catalyst bed.

The transfer of heat from the heating plate to the catalyst bed has been tested by performing a temperature ramp from room temperature up to 200°C. The reactor was positioned in the mount with the heating plate beneath the catalyst bed. Two thermocouples were monitored throughout the temperature ramp, the first thermocouple (T_1) was located in the centre of the catalyst bed (3wt% Pd/ $\gamma\text{-Al}_2\text{O}_3$), and the second thermocouple (T_2) was located in the heating plate. The heater was programmed to maintain a temperature ramp rate of 2°C min⁻¹, using the readout of T_2 to automatically adjust the power output supplied to the heating cartridges accordingly. The difference between T_1 and T_2 are plotted in Figure 5.16 for increasing set point

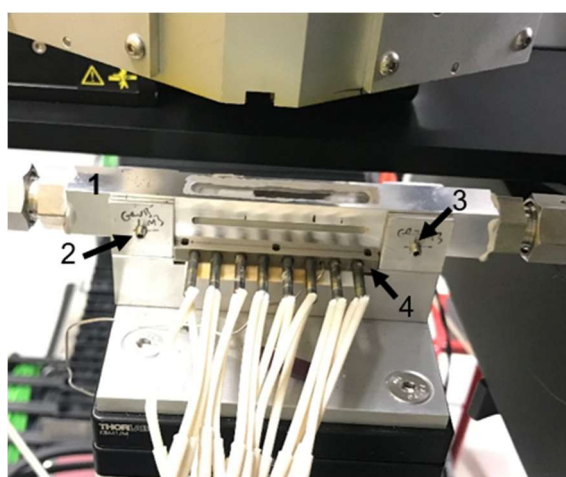


Figure 5.15. Photograph of new aluminium XAFS/DRIFTS reactor position on beamline I20-EDE at Diamond Light Source. The reactor is fixed in place by the aluminium mounting piece (1) with two screws (2) and (3), with the heating plate (4) positioned beneath the reactor.

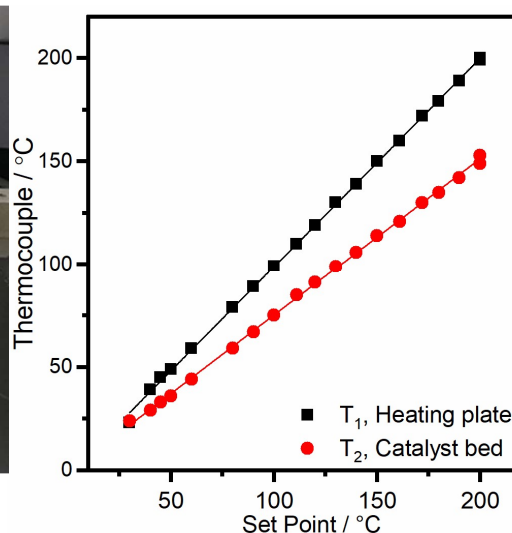


Figure 5.16. Measured temperature of catalyst bed and heating plate plotted as a function of set point during a temperature ramp experiment from room temperature to 200°C at 2.5°C min⁻¹.

temperatures, showing that the temperature measured at the catalyst sample was ~ 25% lower than that measured at the heating plate.

The capability of this new reactor to collect combined XAFS and DRIFTS measurements of a catalyst operating under plug flow conditions is demonstrated by the experiment detailed in Chapter 6. The new XAFS/DRIFTS reactor affords high time resolution due to the minimal dead volume within the reactor. When the catalyst sample is packed into the reactor, it is contained between the 3 Al walls, pressed up against the CaF₂ window and held in place between quartz wool so that there are no gaps for bypass of the gas flow. The gas is therefore forced to flow through the catalyst sample in a plug flow configuration. The catalyst sample can be sieved to a controlled sieve fraction to improve the diffusion of gas through the sample but must be small enough not to compromise the signal-to-noise ratio of acquired DRIFTS spectra. The DRIFTS spectra acquired with different sieve fractions of the same Pd/zeolite-Y catalyst are shown in Figure 5.17, which highlight the improved signal-to-noise achieved with sieve fractions smaller than that 425-250 μm .

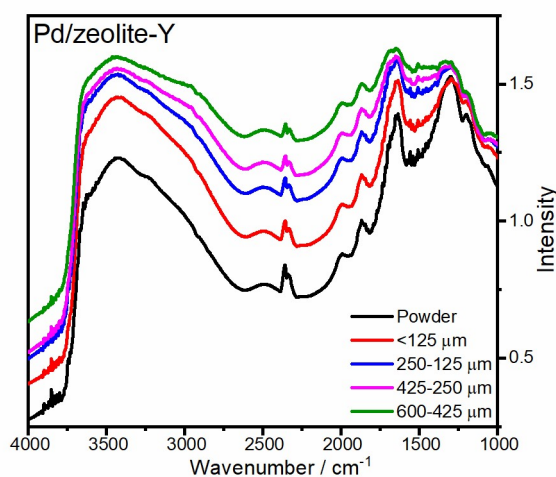


Figure 5.17. DRIFTS spectra of a supported Pd nanoparticle catalyst (Pd/zeolite-Y) contained within the Harrick DRIFTS cell, using samples prepared with different sieve fractions.

5.5 Improvements for Future Models

For improved cell designs in the future, the following problems should be addressed. An alternative method to seal the IR window to the aluminium reactor should be considered that is more forgiving of the movement caused by thermal expansion of the different parts. Ideally, an alternative seal would allow the window to be exchanged easily to assist in sample changes and cleaning of the reactor. Another challenge to consider is the temperature inhomogeneity within the sample bed. The new cell design uses a heating plate located beneath the cell, which allows for equal heat distribution along the length of the reactor but significant heat loss from the surface of the sample in contact with the IR window creates a temperature gradient in the vertical direction.

Additionally, the requirement for *operando* spectroscopy to be coupled with measurements of the catalytic activity means that it is necessary to conduct measurements of the catalytic activity with the same temporal resolution and spatial resolution as the spectroscopic measurements. The catalytic activity measurements used to complement *operando* spectroscopy in the past have most often used mass spectrometry or gas chromatography analysis of the reactor exhaust. In this way, only end-pipe analysis is obtained to give information for the activity of the catalyst bed as a whole. However, due to the variance in reaction kinetics along the length of a catalyst bed operating in plug flow configuration, the end pipe analysis may give misleading interpretation of structure-reactivity relationships of the catalyst. To overcome this problem it would be desirable to integrate this XAFS/DRIFTS reactor with an instrument capable of collecting spatially resolved catalytic activity measurements of a fixed catalyst bed, such as the Spaci-FB.⁶¹ The Spaci-FB utilises a sampling capillary (240 µm outer diameter, 150 µm inner diameter) that is inserted into the fixed catalyst bed to sample the local gas concentration and temperature at different spatial positions within the reactor. In future work there is the possibility to mount the XAFS/DRIFTS reactor to the movable stage of the Spaci-FB set-up, and insert a sampling capillary into the fixed catalyst bed via the gas tube opening at one end of the reactor. By moving the motorised stage in an axial direction with respect to the X-ray beam, IR beam and sampling capillary, there is the possibility for the catalyst bed to be examined by all three techniques, with spatial resolution achieved in each case.

5.6 Conclusions

A new, significantly improved spectroscopic cell has been designed that builds upon previous designs. The new reactor takes a different approach to the common dome-shaped reactor and affords combined XAFS and DRIFTS spectroscopy of a catalyst that is contained as a fixed catalyst bed operating in a plug-flow configuration. For the first time, simultaneous XAFS and DRIFTS measurements can be collected with spatial resolution along the length of a catalyst bed. The reactor has been tested up to temperatures of 200°C, but is expected to withstand temperatures in excess of this in a range of chemical environments. The limitations of the cell which must be considered for future designs are the method of sealing the parts of the reactor, the temperature gradient from top to bottom of the reactor and the need to integrate with the Spaci-FB instrumentation for spatially resolved MS measurements.

5.7 References

1. ILO-ICSC, *International Chemical Safety Card*. 2000. Aluminium Oxide. [online]. ILO and WHO. Available from: http://www.ilo.org/dyn/icsc/showcard.display?p_version=2&p_card_id=0351. [Accessed 06/02/19]

2. WH McMaster, NK Del Grande, JH Mallett and JH Hubbell. 1969. Compilation of X-ray Cross Sections. *Lawrence Livermore National Laboratory Report*. United States: California University.
3. KA Beyer, H Zhao, OJ Borkiewicz, MA Newton, PJ Chupas and KW Chapman, *J. Appl. Crystallogr.*, 2014, **47**, 95-101.
4. DuPont™. Dupont™ Kapton® Summary of Properties. [online]. 2017. Available from: <http://www.dupont.com/content/dam/dupont/products-and-services/membranes-and-films/polyimide-films/documents/DEC-Kapton-summary-of-properties.pdf>.
5. MA Newton and W van Beek, *Chem. Soc. Rev.*, 2010, **39**, 4845-4863.
6. BL Henke, EM Gullikson and JC Davis, *Atomic Data and Nuclear Data Tables*, 1993, **54**, 181-342.
7. AJ Dent, G Cibin, S Ramos, AD Smith, SM Scott, L Varandas, *et al.*, *J. Phys. Conf. Ser.*, 2009, **190**, 012039.
8. S Diaz-Moreno, M Amboage, M Basham, R Boada, NE Bricknell, G Cibin, *et al.*, *J. Synchrotron Radiat.*, 2018, **25**, 998-1009.
9. T Montanari, E Finocchio and G Busca, *J. Phys. Chem. C*, 2011, **115**, 937-943.
10. R Marshall, SS Mitra, PJ Gielisse, JN Plendl and LC Mansur, *J. Chem. Phys.*, 1965, **43**, 2893-2894.
11. Crystran Ltd. Handbook of Optical Materials. 2016. [online] Available from: https://issuu.com/crystran/docs/handbook_2016_web/112.
12. TR Harris, Optical Properties of Si, Ge, GaAs, GaSb, InAs and InP at Elevated Temperatures, *Thesis*, Air Force Institute of Technology, Ohio. 2010.
13. RE Stephens, EK Plyler, WS Rodney and RJ Spindler, *J. Opt. Soc. Am.*, 1953, **43**, 110-112.
14. E Palik, Handbook of Optical Constants of Solids. Burlington: Academic Press. 1998.
15. S Saeidi, M Talebi Amiri, A Saidina Amin Nor and R Rahimpour Mohammad, *Int. J. Chem. React. Eng.*, 2014, **12**, 639-664.
16. S Saeidi, F Fazlollahi, S Najari, D Iranshahi, JJ Klemeš and LL Baxter, *J. Ind. Eng. Chem.*, 2017, **49**, 1-25.
17. DW Green and RH Perry, *Perry's Chemical Engineers' Handbook, Eighth Edition*. New York: McGraw Hill. 2008.
18. C Mondelli, VD Santo, A Trovarelli, M Boaro, A Fusi, R Psaro, *et al.*, *Catal. Today*, 2006, **113**, 81-86.
19. JF Joly, N Zanier-Szydłowski, S Colin, F Raatz, J Saussey and JC Lavalley, *Catal. Today*, 1991, **9**, 31-38.
20. IE Wachs, J-M Jehng, G Deo, BM Weckhuysen, VV Guliants, JB Benziger, *et al.*, *J. Catal.*, 1997, **170**, 75-88.

21. JG Highfield, M Prairie and A Renken, *Catal. Today*, 1991, **9**, 39-46.
22. MA Banares, L Dauphin, V Calvoperez, TP Fehlner and EE Wolf, *J. Catal.*, 1995, **152**, 396-409.
23. B Klingenberg and MA Vannice, *Appl. Catal. B: Environmental*, 1999, **21**, 19-33.
24. FC Meunier, JP Breen, V Zuzaniuk, M Olsson and JRH Ross, *J. Catal.*, 1999, **187**, 493-505.
25. M Cavers, JM Davidson, IR Harkness, LVC Rees and GS McDougall, *J. Catal.*, 1999, **188**, 426-430.
26. A Martínez-Arias, M Fernández-García, A Iglesias-Juez, AB Hungría, JA Anderson, JC Conesa, *et al.*, *Appl. Catal. B: Environmental*, 2001, **31**, 51-60.
27. AI Serykh and MD Amiridis, *Micropor. Mesopor. Mat.*, 2006, **94**, 320-324.
28. RSS Murthy, JP Blitz and DE Leyden, *Anal. Chem.*, 1986, **58**, 3167-3172.
29. CF Mao and MA Vannice, *J. Catal.*, 1995, **154**, 230-244.
30. SJ Huang, AB Walters and MA Vannice, *J. Catal.*, 2000, **192**, 29-47.
31. MH Kim, JR Ebner, RM Friedman and MA Vannice, *J. Catal.*, 2001, **204**, 348-357.
32. MH Kim, JR Ebner, RM Friedman and MA Vannice, *J. Catal.*, 2002, **208**, 381-392.
33. Harrick Scientific Products, Inc. High Temperature Reaction Chamber for the Praying Mantis. [online]. Available from: https://www.harricksci.com/sites/default/files/pdf/data_sheets/Data_Sheet_HVC_High_Temp_Praying_Mantis_Reaction_Chamber.pdf. [Accessed 06/02/19]
34. Thermo Scientific. FT-IR General accessories. [online]. Available from: <http://2-lab.ru/files/catalog/2/31b17b05ef9d490c2b79b425dd947964.pdf>. [Accessed 06/02/19].
35. Specac Ltd. Environmental Chamber for Selector™ Accessory P/N GS19930. [online]. Available from: <https://www.specac.com/en/documents/data-sheets/selector-environmental-chamber>. [Accessed 06/02/19]
36. D-J Liu and HJ Robota, *Catal. Lett.*, 1993, **21**, 291-301.
37. D-J Liu and HJ Robota, *Appl. Catal. B: Environmental*, 1994, **4**, 155-165.
38. W-H Cheng, *Mater. Chem. Phys.*, 1995, **41**, 36-40.
39. U Hatje, M Hagelstein, T Reißler and H Förster, *Physica B: Condensed Matter*, 1995, **208-209**, 646-648.
40. G Sankar, PA Wright, S Natarajan, JM Thomas, GN Greaves, AJ Dent, *et al.*, *J. Phys. Chem.*, 1993, **97**, 9550-9554.
41. AR Sethuraman, *Nanostruct. Mater.*, 1994, **4**, 79-92.
42. AJ Dent, GN Greaves, MA Roberts, G Sankar, PA Wright, RH Jones, *et al.*, *Nucl. Instrum. Meth. B*, 1995, **97**, 20-22.

43. AJ Dent, M Oversluizen, GN Greaves, MA Roberts, G Sankar, CRA Catlow, *et al.*, *Physica B: Condensed Matter*, 1995, **208-209**, 253-255.
44. BS Clausen, G Steffensen, B Fabius, J Villadsen, R Feidenhans'l and H Topsøe, *J. Catal.*, 1991, **132**, 524-535.
45. AB Kroner, KMH Mohammed, M Gilbert, G Duller, L Cahill, P Leicester, *et al.*, *AIP Conference Proceedings*, 2016, **1741**, 030014-4.
46. C Brookes, M Bowker, EK Gibson, D Gianolio, KMH Mohammed, S Parry, *et al.*, *Cat. Sci. Tech.*, 2016, **6**, 722-730.
47. SJ Tinnemans, JG Mesu, K Kervinen, T Visser, TA Nijhuis, AM Beale, *et al.*, *Catal. Today*, 2006, **113**, 3-15.
48. A Bruckner, *Chem. Comm.*, 2005, DOI: 10.1039/b418790c, 1761-1763.
49. MA Newton, B Jyoti, AJ Dent, SG Fiddy and J Evans, *Chem. Comm.*, 2004, DOI: 10.1039/b405694a, 2382-2383.
50. MA Newton, AJ Dent, SG Fiddy, B Jyoti and J Evans, *Catal. Today*, 2007, **126**, 64-72.
51. MA Newton, *Top. Catal.*, 2009, **52**, 1410-1424.
52. MA Newton, AJ Dent, SG Fiddy, B Jyoti and J Evans, *Phys. Chem. Chem. Phys.*, 2007, **9**, 246-249.
53. KK Bando, T Wada, T Miyamoto, K Miyazaki, S Takakusagi, T Gott, *et al.*, *J. Phys. Conf. Ser.*, 2009, **190**, 012158.
54. KK Bando, T Wada, T Miyamoto, K Miyazaki, S Takakusagi, Y Koike, *et al.*, *J. Catal.*, 2012, **286**, 165-171.
55. NS Marinkovic, Q Wang and AI Frenkel, *J. Synchrotron Radiat.*, 2011, **18**, 447-455.
56. EK Gibson, AM Beale, CRA Catlow, A Chutia, D Gianolio, A Gould, *et al.*, *Chem. Mater.*, 2015, **27**, 3714-3720.
57. GL Chiarello, M Nachtegaal, V Marchionni, L Quaroni and D Ferri, *Rev. Sci. Instrum.*, 2014, **85**, 074102.
58. G Agostini, D Meira, M Monte, H Vitoux, A Iglesias-Juez, M Fernandez-Garcia, *et al.*, *J. Synchrotron Radiat.*, 2018, **25**, 1745-1752.
59. MJ Mirtich, D Nir, D Swec and B Banks, *J. Vac. Sci. Technol. A*, 1986, **4**, 2680-2681.
60. Minkon Ltd., Fortafix High Temperature Adhesives Data Sheet. [online] Available from: <https://fortafix.com/storage/app/media/%2Ftech-pdfs%2FAutostic%20FC%20and%20FS%20Products.pdf>. [Accessed 06/02/19].
61. J Touitou, F Aiouache, R Burch, R Douglas, C Hardacre, K Morgan, *et al.*, *J. Catal.*, 2014, **319**, 239-246.

Chapter Six. Kinetic Oscillations of Pd nanoparticle catalysts for CO oxidation; spatially resolved *operando* EDE/DRIFTS/MS

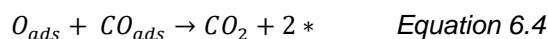
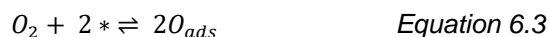
6.1 Introduction

Although a relatively simple reaction, the oxidation of CO to CO₂ is of great importance in emissions control technology to abate poisonous CO from the exhaust of internal combustion engines.¹ While CO oxidation can be catalysed at low temperature in aerobic conditions over a precious metal surface,² the onset of self-sustained kinetic oscillations is found to occur under certain reaction conditions.³⁻⁵ These kinetic oscillations are puzzling and have been the focus of many studies in the past.⁶⁻¹⁰ Many of these studies have used ultra-high vacuum (UHV) techniques with model single crystal surfaces to draw speculative conclusions for the catalytic mechanism, rather than studying the real catalytic material itself. In this work, the development of a spatially resolved, *operando* method has focussed on studying the behaviour and possible structural changes of a supported nanoparticle catalyst operating in plug-flow conditions during kinetic oscillations of the CO oxidation reaction.

6.1.1 CO oxidation at a metal surface

The oxidation of CO by O₂ to CO₂ (Equation 6.1) is one of the most widely investigated catalytic reactions. From a practical perspective, CO is a highly toxic chemical which is formed from incomplete combustion of hydrocarbon fuels and must be removed from the exhaust of combustion engines.¹¹ This can be achieved by using a high performance catalyst, which promotes the oxidation of CO by O₂ to CO₂, which can then be released to the atmosphere. Increasingly stringent emissions legislations mean that more effective catalysts are required for the efficient clean-up of CO at low temperatures.¹² The catalysed CO oxidation at a metal surface has been extensively studied, and was often used as a classic example of the Langmuir Hinshelwood reaction mechanism¹³; the two reactants from the gas phase compete for free adsorption sites on the metal surface, CO is adsorbed to one empty adsorption site (Equation 6.2) and O₂ undergoes dissociative adsorption to two empty adsorption sites (Equation 6.3), then the formation of CO₂ results from reaction of the adsorbed intermediates on the surface, CO_{ads} and O_{ads}, (Equation 6.4).^{14, 15} The Langmuir Hinshelwood mechanism was originally proposed to explain CO oxidation over single crystal metal surfaces at UHV pressures.^{16, 17} By studying the adsorption energies and the reaction rates at different partial pressures of CO and O₂, it was found that the activation energy for reaction on Pt, Pd or Rh surfaces (~110 kJ mol⁻¹) was close to the corresponding desorption energy of CO_{ads} from those metals,¹⁸ meaning that desorption of some CO_{ads} was required before the dissociative adsorption of oxygen to occur, and for the reaction to proceed.^{17, 18} The strong adsorption of CO to metal

surfaces is well known, and makes CO a poison for other catalytic processes eg. CO impurities found in H₂ poison the electrode surface of proton-exchange membrane fuel cells (PEMFCs).¹⁹



6.1.2 Kinetic Oscillations

The oscillating behaviour of catalysed CO oxidation was first reported by Beusch *et al.* in 1972, using a supported Pt/Al₂O₃ catalyst at atmospheric pressure.²⁰ Since then, self-sustained oscillations in the CO oxidation reaction kinetics have been observed with polycrystalline wires,^{8, 21} single crystal surfaces and supported Pd, Pt, Ir or Rh catalysts.²²⁻²⁶ The onset of self-sustained kinetic oscillations without external perturbation is puzzling and so many computational and experimental studies have attempted to analyse the dynamic reaction profile and physico-chemical properties of the catalyst. Despite many postulated theories, there is still a lack of clear understanding of the driving mechanism behind the oscillating behaviour, particularly in the real operating reaction conditions.

Early studies using photoemission electron microscopy (PEEM) were able to correlate the oscillating CO₂ production with patterns of adsorbed reactants, which were found to propagate in a wave-like notion over a Pt(100) surface.^{7, 14, 27} These were the first reports of such spatial separation and self-organisation of the adsorbed reactant molecules over the catalyst surface, however there was lack of convincing evidence for these adsorbate concentrations to lead to a postulated phase change and reactivity cycle of the catalyst.

Some studies have attributed the kinetic oscillations to build-up and subsequent ignition of carbon species, formed from the dissociation of CO on the catalyst surface.²⁸⁻³¹ Despite clear evidence for the adsorption of CO at the metal, there is however no evidence for atomic carbon occupying active sites at the catalyst surface. Others have attributed the kinetic oscillations to heat and mass transfer effects, using spatially resolved FTIR measurements to relate the period of the kinetic oscillations to fluctuations in CO coverage and local temperature at the catalyst surface.^{32, 33} The advances in characterisation techniques, particularly time-resolved x-ray techniques have provided convincing evidence that the oscillations cannot result from heat and mass transfer effects alone, and that physico-chemical changes to the catalyst must play a significant role.³⁴ More specifically, the reduction and oxidation bistabilities within

the reaction conditions for CO oxidation are suggested to be responsible for oscillating and non-linear reaction kinetics.

The oxidation-reduction mechanism was first proposed by Sales, Turner and Maple in the 1980s to explain oscillations in CO oxidation over a Pt catalyst.⁸⁻¹⁰ It was realised that the two reactants for CO oxidation, CO and O₂, may also act as reducing and oxidising agents, respectively, for the reduction and oxidation of the Pt catalyst surface. The oxidation and reduction of Pt with these agents were found to occur on the same timescale as the observed oscillations in CO oxidation reaction rate, and thus it was concluded that CO oxidation must proceed via two different kinetic pathways on the reduced and oxidised surfaces. Furthermore, the first step of the Langmuir Hinshelwood mechanism for CO oxidation involves the chemisorption of CO and dissociative chemisorption of oxygen, which are also the first steps, in the respective reduction and oxidation mechanisms of the metal surface. These theories were supported, at the time, with experimental evidence of phase transformations at the single crystal surface using Auger electron spectroscopy (AES)³⁵ and low energy electron diffraction (LEED).³⁶⁻³⁸ The first evidence of bulk oxidation and reduction of supported nanoparticle catalysts during CO oxidation was observed by *in situ* XRD experiments,²³ which further fuelled the theory for oxidation/reduction cycles to be responsible for the oscillating CO oxidation reaction kinetics, and demonstrated the advantage in using powerful X-ray techniques for time-resolved studies of real catalytic systems at atmospheric pressure.

Further characterisation of the supported nanoparticle catalysts (Pt, Pd, Rh) during the two kinetic regimes for CO oxidation have made use of XAFS in combination with IR, mass spectrometry and kinetic modelling calculations to reach the following conclusions; during the low activity regime, the catalyst exists as metallic nanoparticles with its surface blocked by adsorbed CO, as evidenced by FTIR^{22, 24, 25, 39-43} and high energy resolution XAFS⁴⁴, which inhibits the dissociative adsorption of O₂. Regardless of the particle size,⁴⁵ or the concentration of O₂ in the gas phase,^{22, 24} CO covered metallic nanoparticles are found to be the active surface species during this low activity regime. The desorption of CO_{ads} from the surface is therefore the rate determining step during this low temperature regime,⁴⁰ which is consistent with the original Langmuir Hinshelwood mechanism.^{16, 17} During the high temperature regime, the metal nanoparticle is found to exist in a partially oxidised state, with no evidence for adsorbed CO at the surface.^{24, 25, 40, 44-46} The reaction mechanism during this high activity regime is still of considerable debate, with some studies suggesting the formation of a surface oxide layer that participates in the oxidation of CO via a Mars-Van Krevelen mechanism,⁴⁷⁻⁵⁰ whereas others suggest the partial oxidation is due to a high surface coverage of atomic oxygen which permits the Langmuir Hinshelwood mechanism to proceed at a faster rate on the metal surface.^{22, 41, 51-53} Time-resolved measurements

that have followed the transition of the catalyst structure from the low activity phase to the high activity phase have reported a sharp change from the metal to a partially oxidised state⁴⁶, however, in some instances the extent of oxidation is found to exhibit oscillatory behaviour which results in the oscillating reaction kinetics.⁴⁷ In order to make direct links between the metal oxidation state and the surface reactivity, and to understand the conditions under which oscillating behaviour is observed, a combination of bulk and surface spectroscopic techniques must be used with sufficient time- and spatial- resolution to capture the dynamic changes.

For heterogeneous catalysts operating in plug-flow reactions conditions, concentration gradients and temperature gradients across the fixed catalyst bed mean that spatial resolution in spectroscopic techniques are essential to make meaningful conclusions for the catalyst structure-performance relationships.^{54, 55} Spatially resolved XAFS measurements were reported by van Bokhoven *et al.* in 2010, in the investigation of a Pt/Al₂O₃ catalyst during oscillating CO oxidation, which identified variation of Pt structure as a function of time and position within the catalytic reactor.⁴⁷ This work demonstrated the importance of using spatially resolved techniques for understanding the dynamic structure of the catalyst, showing that oscillating CO oxidation at the front of the bed had no consequence for structural transformations of the catalyst located at positions further downstream of the reactor. However, IR measurements that have been used to find the relationship between catalyst structure and surface reactivity, have investigated the catalyst as a self-supported pellet in a different reaction environment, meaning for a degree of uncertainty in structure-performance correlations. The spatial variation in local temperature, CO, O₂ and CO₂ gas concentrations across the length of a fixed catalyst bed of a Pd/Al₂O₃ catalyst during operation for CO oxidation have also been reported by Goguet *et al.* using the Spaci-FB instrumentation.³⁴ As expected, the change in reaction conditions at different spatial positions within the reactor were found to influence the structural properties of the Pd catalyst, measured by spatially resolved XAFS, and its reactivity. This study was the first to directly correlate the catalyst structure with the local gas concentration at each spatial position within a fixed-bed reactor, however, did not report the occurrence of any oscillating behaviour. Another spatially resolved study of a Pt/Al₂O₃ catalyst during CO oxidation was reported by Ganzler *et al.*, using XAFS spectroscopy to follow the Pt oxidation state at multiple positions along the length of a fixed-bed reactor, and used spatially resolved IR thermography to follow the evolution of the reaction exotherm.⁵⁶ In their work, the spectroscopic techniques were performed independently, with the catalyst contained in different reactors with different flow rates in each case, and so structure-activity correlations were again made with a degree of uncertainty. That said, the time and spatial resolution of the *operando* IR thermography measurements were successful in capturing the location of the CO oxidation hot spot within the fixed-bed reactor, and its change of location in relation to the applied temperature and integral

CO conversion; ignition of CO was found to occur initially at a position nearest to the reactor outlet, then propagate upstream with increasing temperature and CO conversion. The above mentioned spatially resolved studies confirmed the inhomogeneity of the supported Pt or Pd nanoparticle catalyst at different positions within the fixed catalyst bed, however, there is still lack of certainty in the relationship between catalyst structure and function at those positions that results in the oscillating behaviour. The correlation of XAFS and FTIR spectroscopy can provide information for structure-function relationships of the catalyst during oscillating CO oxidation, however, there is the need to perform both techniques simultaneously, with suitable spatial resolution, as well as time resolution, in order to characterise the catalyst and its dynamic properties during this process.

In this work, EDE and DRIFTS spectroscopy are performed simultaneously by using the new XAFS/DRIFTS reactor that has been reported in Chapter 5. The combination of EDE and DRIFTS performed at multiple positions along the axial length of a Pd/ γ - Al_2O_3 catalyst bed during oscillating CO oxidation are able to follow the change in Pd nanoparticle structure and surface adsorption, simultaneously. The evolution of the reaction front is also examined by using IR thermography imaging, and the integral catalytic activity measured by end-pipe mass spectrometry analysis. In this way, this work attempts to provide a more complete understanding of the operation of Pd/ γ - Al_2O_3 catalyst during oscillating CO oxidation by examining the entire catalyst bed and making links between nanoparticle structure, surface reactivity and catalytic performance.

6.2 Methods

6.2.1 Sample Preparation

The supported 3wt% Pd catalyst was prepared by incipient wetness impregnation of an acidified aqueous solution of tetraamminepalladium hydroxide (5.96 wt% Pd assay, Johnson Matthey) onto the commercial support, γ - Al_2O_3 (SASOL). Incipient wetness impregnation was carried out at room temperature. The impregnated support was subsequently dried at 100°C, then calcined in air at 500°C for 2 hours. Characterisation of the resulting PdO/ γ - Al_2O_3 catalyst is detailed in Chapter 2, with average particle size 1.1 nm (calculated from EXAFS Pd-Pd coordination number, using a method reported previously⁵⁷). The calcined catalyst was pelletized and sieved to a fraction 250 – 355 μm .

6.2.2 Spatially resolved, *operando* EDE/DRIFTS

Experiments were carried out on the I20-EDE, energy dispersive beamline, I20-EDE of Diamond Light Source. The experimental set-up and apparatus at the beamline are shown in Figure 6.1. Dispersive XAFS at the Pd K-edge (24358 eV) were collected in transmission mode using a Si(311) polychromator and a FReLoN CCD camera as the

x-ray detector. The reaction cell used for synchronous, spatially resolved EDE and DRIFTS measurements was reported in Chapter 5. The reaction cell was constructed from pure grade aluminium with a square cross sectional channel (5 mm x 5 mm) to contain the catalyst, thinned walls (250 μm) along the length of the reactor to allow the transmission of x-rays through the sample, and a rectangular CaF_2 window fitted on the top face of the reactor to allow IR transmission to and from the catalyst surface. Gas lines were fitted to both ends of the cell using Swagelok VCO fittings and a t-piece fitting was used at one end to accommodate a K-type Inconel thermocouple (1 mm diameter) that was inserted into the catalyst bed and sealed using a 1/16" Swagelok fitting. A heating plate was positioned beneath the reactor, and controlled by an external thermocouple. An Agilent Carey 680 FTIR Spectrometer was positioned in the experimental hutch and used a DaVinci arm accessory fitted with praying mantis optics to refocus the IR beam to the catalyst surface within the EDE/DRIFTS reactor. The outlet gas line from the reactor was connected directly to a Hiden QGA mass spectrometer for online end-pipe analysis.

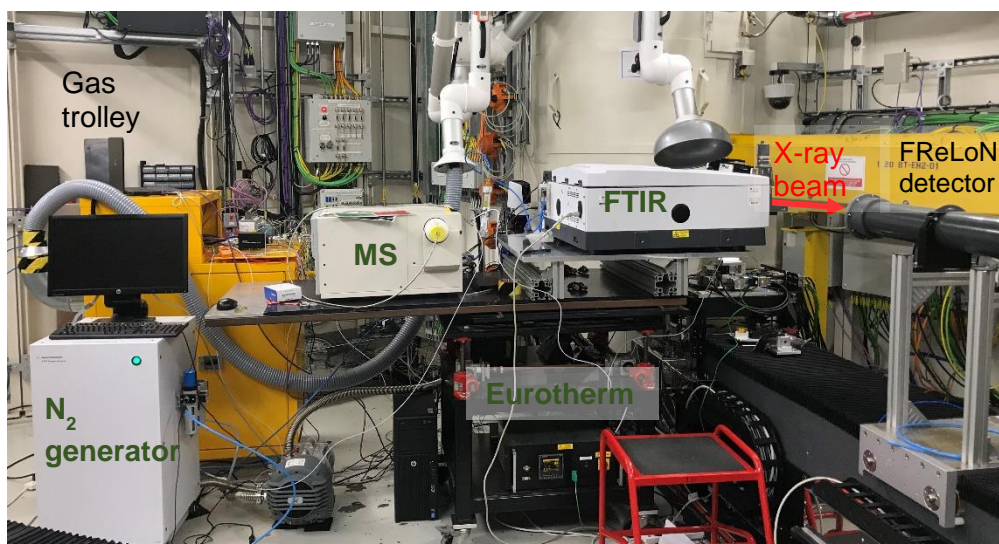


Figure 6.1. Annotated photograph of the experimental set-up at beamline I20-EDE, Diamond Light Source, showing the gas trolley with mass flow controllers, nitrogen generator, mass spectrometer, FTIR spectrometer, Eurotherm heater, X-ray detector and direction of the dispersive X-ray beam.

The experiment used a controlled flow of mixed gases into the reaction chamber at atmospheric pressure using Brooks mass flow controllers. 400 mg of the $\text{Pd}/\gamma\text{-Al}_2\text{O}_3$ catalyst and 200 mg of the bare $\gamma\text{-Al}_2\text{O}_3$ support material were sieved to a pellet fraction of 250-355 μm and loaded sequentially into the reactor so that the $\gamma\text{-Al}_2\text{O}_3$ portion of the bed sat upstream of the catalyst portion of the bed. The $\text{Pd}/\gamma\text{-Al}_2\text{O}_3$ and $\gamma\text{-Al}_2\text{O}_3$ fixed bed was contained between two quartz wool plugs. The bare $\gamma\text{-Al}_2\text{O}_3$ portion of the bed was used as a reference material to perform background measurements for DRIFTS spectra and I_0 measurements of the XAFS spectra, taking into account the absorption and scattering of the support material and reaction environment in each

case. The Pd/ γ -Al₂O₃ catalyst bed extended a length of 18 mm, and EDE/DRIFTS measurements were collected at 8 different spatial positions along its length; +0.4 mm, +1.8 mm, +5.2 mm, +7.1 mm, +8.7 mm, +10.4 mm, +12.5 mm and +14.6 mm from the front of the catalyst bed. The reactor was fixed via a bespoke mounting piece to a motorised stage which could be controlled remotely to move in the *x* and *y* directions with respect to the incident x-ray beam and IR beam. The catalyst was treated in 10% O₂/Ar at 135°C to clean the catalyst surface of adsorbates, then followed by treatment in 4% H₂/Ar at 135°C to return the catalyst the initial reduced state. The catalyst and reactor were then cooled to room temperature in Ar before repeating the experimental temperature ramp with reactant gases (CO and O₂) collecting EDE and DRIFTS measurements at the different spatial positions. The reactant gas feed used 1% CO, 3% O₂ and 96% Ar, at a total flow rate of 50 cm³ min⁻¹. The reactant feed was introduced to the sample at room temperature and allowed to reach steady state before ramping the temperature at a rate of 2°C min⁻¹ to 135°C, collecting EDE, DRIFTS and MS measurements continuously.

Each EDE spectrum was acquired in 4.8 ms (*k* range of 12 Å⁻¹) and 200 accumulations (~1 second) were used for EXAFS analysis. The EDE spectra were collected continuously throughout the duration of the ramp period, with *I*₀ measured from the bare γ -Al₂O₃ portion of the catalyst bed before and after each run. An averaged signal of the initial and final *I*₀ values were used to construct the resulting time-resolved EDE spectra during that period. The dispersive x-ray beam was focussed at the sample to a spot size of 0.5 mm horizontally and 0.15 mm vertically. The beam intensity was reduced by a factor of 5 by opening the wiggler gap to prevent radiation damage to the sample. To check that the X-rays were not causing photoreduction of the sample, EDE spectra were collected continuously at multiple positions under different gas environments. The EDE-XANES spectra in Figure 6.2 show that there were no observable changes in the Pd electronic structure after 500 seconds of beam exposure in the reactant gas environment (1% CO, 3% O₂, 96% Ar, 100°C), at three different spatial positions. DRIFTS spectra were collected taking 64 scans with a resolution of 4 cm⁻¹ (400 – 4000 cm⁻¹), at a time resolution of 25 seconds per spectrum. The background spectrum was collected from the bare γ -Al₂O₃ portion of the fixed bed in the reactant (CO/O₂/Ar) gas feed, which was subtracted from all acquired DRIFTS spectra of the catalyst. The composition of the effluent gas flow from the reactor was continuously measured by monitoring the *m/z* values by mass spectrometry; H₂ (*m/z* = 2), OH (*m/z* = 17), H₂O (*m/z* = 18), CO (*m/z* = 28), O₂ (*m/z* = 32), Ar (*m/z* = 40) and CO₂ (*m/z* = 44). The mass spectrometry signal was normalised relative to the Ar signal (*m/z* = 40) to account for any variation in the detector. The CO signal (*m/z* = 28) was corrected for contributions from CO₂ fragmentation in the MS by subtracting 10% of the value of *m/z* = 44.

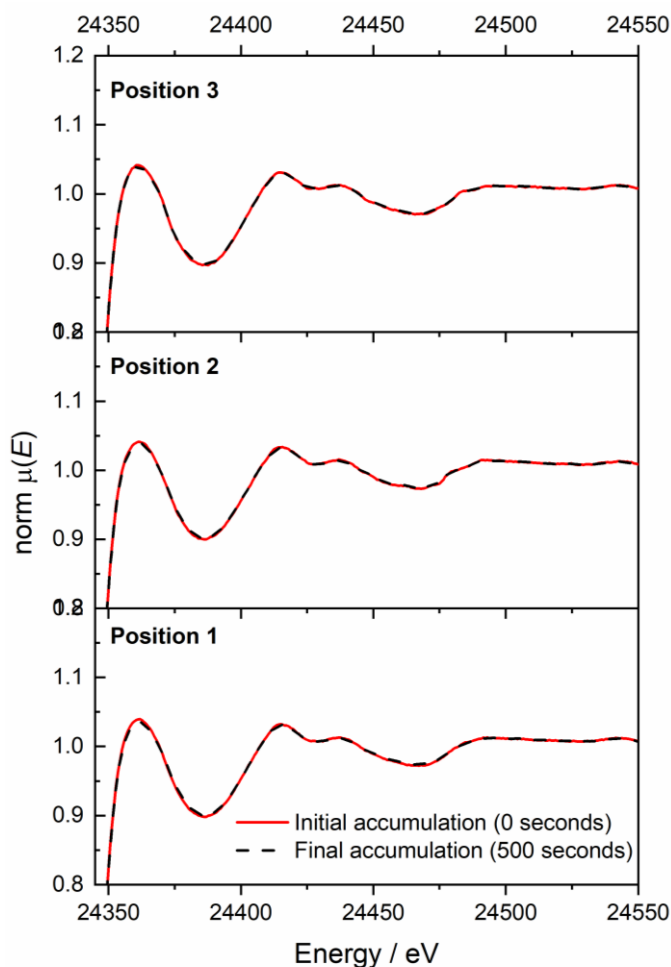


Figure 6.2. Pd K-edge XANES of calcined PdO/ γ -Al₂O₃ catalyst contained in operando XAFS/DRIFTS reactor under reactant (1%CO/3%O₂/Ar) gas feed at 100°C during exposure to reduced EDE beam intensity (reduced by a factor of 5) as a test for photoreduction, showing initial (0 secs, black dashed) and 500th (500 secs, red solid) accumulation at three different spatial positions.

6.2.3 EDE Data Processing

The time-resolved EDE data was processed using the DAWN software package for interpretation of XAFS spectra. A consistent method for energy calibration, cropping and normalisation was applied to all measured data: The x-ray energy for EDE spectra was calibrated using a Pd foil, and the edge energy was aligned as the maximum of the first derivative, E_0 , to the known value of 24358 eV. The upper and lower limits of the EDE spectra were cropped to an energy range of 24060 – 25365 eV ($k_{\text{max}} = 12 \text{ \AA}^{-1}$), to discard the poor data quality at the upper and lower wavenumbers of polychromatic beam. The spectra were then normalised by performing a pre-edge and post-edge subtraction. The calibrated and normalised spectra were then analysed using the linear profile function, which was able to plot the XAFS intensity as a function of temperature and time. For further analysis, selected EDE spectra were exported to Athena and Artemis (the Horae package). Athena was used to obtain difference XANES spectra, and Fourier transformed EXAFS spectra by using an appropriate k -range (3 - 11.3 \AA^{-1})

with k -weighting of 2.⁵⁸ The k -weighting of 2 was chosen for balanced scattering contribution from atomic neighbours with contrasting Z values (O and Pd). Athena was also used to perform linear combination fitting of the XANES region ($-20 < E_0 / \text{eV} < 50$), using two reference spectra for Pd⁽⁰⁾ and Pd^(II) i.e. the reduced Pd/ γ -Al₂O₃ catalyst and oxidised PdO/ γ -Al₂O₃ catalyst, respectively.

The Fourier transformed EXAFS data was fitted using Artemis. Fitting models used a single scattering path Pd-Pd (2.734 Å) of Pd foil, and Pd-O (2.018 Å) and Pd-Pd (3.030 Å) scattering paths of PdO. The amplitude reduction factor, S_0^2 , was derived by fitting the Pd K-edge EXAFS of the Pd foil (Figure 6.3) using a fixed Pd-Pd (2.734 Å) scattering path with a coordination number of 12 to give a value of 0.81.

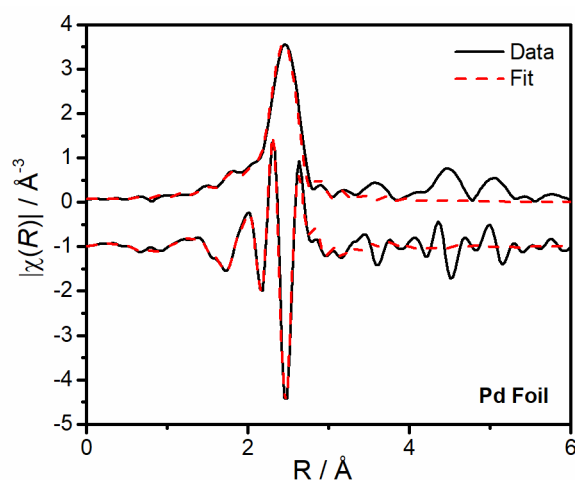


Figure 6.3. Magnitude and imaginary parts of Fourier transformed EXAFS data of Pd foil reference plotted with a fitting model constructed from a single Pd-Pd scattering path (coordination distance 2.734 Å; coordination number 12; σ^2 0.0053 \pm 0.0004 Å²; E_0 -7.2 \pm 4 eV; S_0^2 0.81 \pm 0.05). $3 < k / \text{Å}^{-1} < 11.3$.

6.2.4 IR Thermography Imaging

400 mg of the Pd/ γ -Al₂O₃ catalyst and 200 mg of the bare γ -Al₂O₃ support material were sieved to a pellet fraction of 250-355 μm and loaded sequentially into the XAFS/DRIFTS reactor in the same way as for the *operando* XAFS/DRIFTS measurements described above. The Pd/ γ -Al₂O₃ and γ -Al₂O₃ fixed bed was examined using an Optris PI 160 thermal imaging camera during the temperature ramping period for CO oxidation. The catalyst was cleaned and reduced with treatment in 4% H₂/Ar at 135°C and cooled to room temperature in Ar before repeating the experimental run with reactant gas feed (1% CO, 3% O₂ and 96% Ar,) at a total flow rate of 50 cm³ min⁻¹. The reactant feed was introduced to the sample at room temperature and allowed to reach steady state before ramping the temperature at a rate of 2°C min⁻¹ to 135°C. The IR camera was positioned 10 cm above the CaF₂ window of the reactor and was used to capture 2D colour maps showing the IR emission reaching the camera from the catalyst bed during the reaction period.

6.3 Results

6.3.1 Spatially resolved, *operando* EDE/DRIFTS

6.3.1.1 End-pipe Catalytic Activity

The concentration of reactant and product gases from the reactor exhaust during the *operando* EDE/DRIFTS temperature ramp experiments are shown in Figure 6.4. The same reaction profile was obtained upon repeating the experiment eight times with the same reaction conditions (gas feed; 1% CO, 3% O₂, ramp rate; 2°C min⁻¹), and using the same catalyst bed, showing that the catalytic reactivity was reproducible each time. The mass spectrometry measurements showed that upon increasing the temperature linearly from 100°C, there was an exponential increase in CO consumption and CO₂ formation until a critical temperature (114°C), at a reaction time of 500 seconds, when the CO signal dropped to zero indicating 100% CO conversion. This critical temperature will be referred to herein as the light-off point. At the light-off point, a large increase in CO₂ formation and O₂ consumption was observed. The normalised mass spectrometry signal for CO₂ formation in the period immediately after the light-off point reached a maximum value of 1.4, exceeding the value expected from the stoichiometry of the reaction with respect to the quantity of CO consumed *i.e.* 1 mole CO₂ formed for every 1 mole CO consumed. The normalised mass spectrometry signal for O₂ consumption was also greater than the value expected from the stoichiometry of the reaction. This period of high activity lasted for a duration of ~250 seconds, with the CO₂ formation and O₂ consumption decreasing logarithmically towards the stoichiometric values expected for 100% CO conversion to CO₂ (normalised value of 1 for CO₂ formation and normalised value of 0.8 for O₂ consumption). The excess of CO₂ formation and O₂ consumption in this period can be explained by ignition of additional CO molecules that were stored as CO_{ads} on the catalyst surface at low temperatures, as reported previously for a supported Pt catalyst.⁴⁷ At a reaction time of 750 seconds, when the global temperature of the reactor was increased ~20°C beyond the light-off point, the CO conversion remained at 100% but the O₂ consumption and CO₂ formation started to oscillate with a time period of ~50 seconds. During each oscillation there was a period of steady CO₂ formation and O₂ consumption at the stoichiometric values for 100% CO conversion, followed by a sharp increase in CO₂ formation to a normalised value >1, then followed by a decrease to return to the initial value. This was mirrored by the equivalent changes in O₂ consumption, however, the value for CO conversion showed no change during the oscillations. As the temperature was increased further, the amplitude of these oscillations decreased until the CO₂ formation and O₂ consumption plateaued at reaction time of 1000 seconds (reactor temperature 127°C), with normalised concentration of 1 and ~0.8 for CO₂ and O₂, respectively.

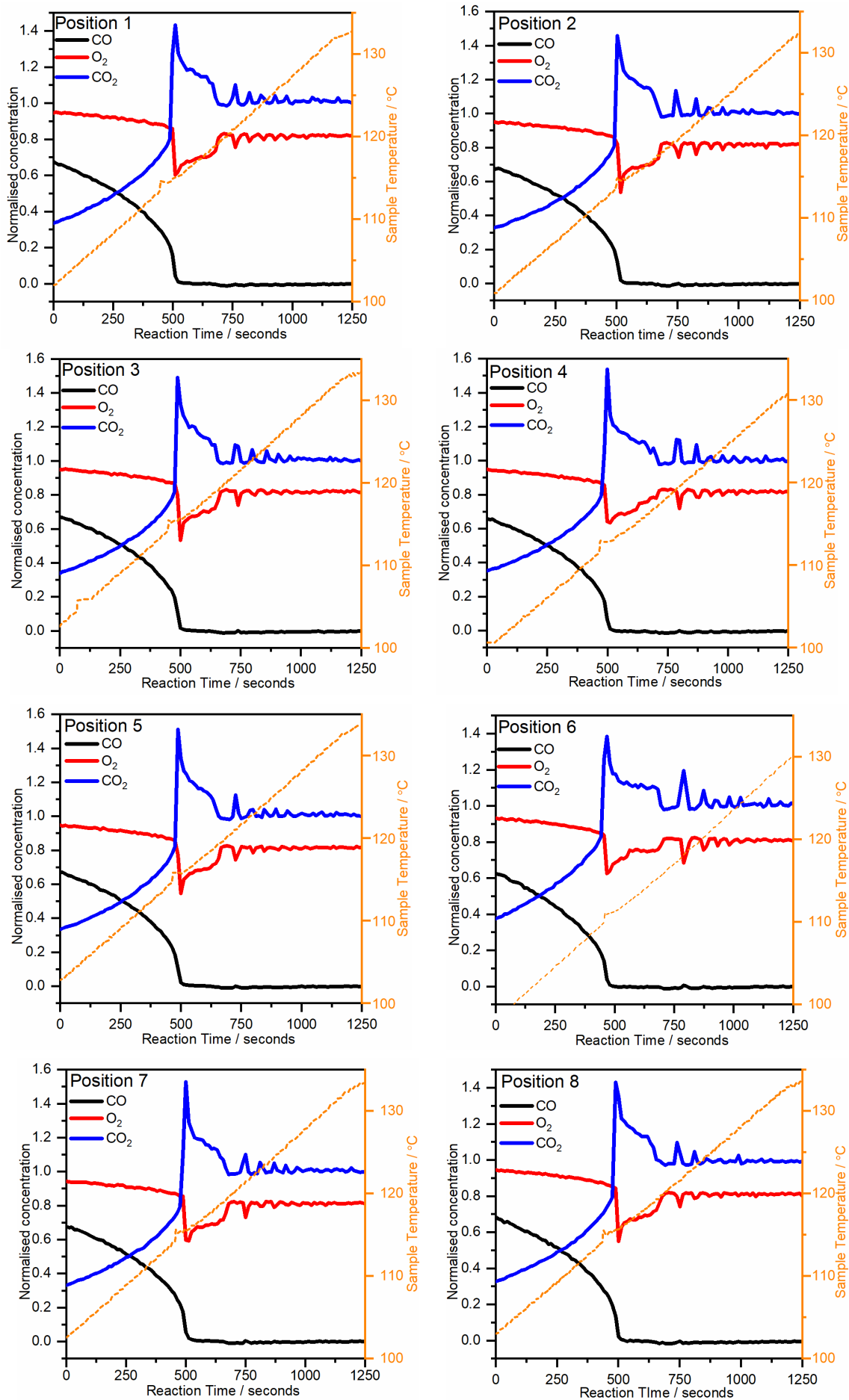


Figure 6.4. Mass spectrometry analysis of exhaust gas from plug-flow reactor during eight repeated CO oxidation temperature ramp experiments with 1%CO/3%O₂/Ar over the Pd/ γ -Al₂O₃ catalyst, showing CO consumption (black), O₂ consumption (red) and CO₂ formation (blue) calculated relative to the inlet CO signal, and the measured internal catalyst temperature (orange, dashed).

The sample temperature, measured by an internal thermocouple inserted into the end of the catalyst bed, is plotted alongside the mass spectrometry data in Figure 6.4. The temperature is shown to increase linearly as a function of time due to the temperature ramp rate of the heating plate beneath the reactor, however, a higher temperature was measured at a reaction time of 500 seconds in each experimental run. This increase in temperature must be a result of the heat released during the exothermic CO oxidation at the light-off point. The thermocouple was positioned at the same location in the catalyst bed in each experimental run, and so displayed the same temperature profile in each case, showing that the catalytic activity was reproducible.

6.3.1.3 Position 8 – End of the catalyst bed (+ 14.6 mm)

The Pd K-edge XANES spectra of the Pd/ γ -Al₂O₃ catalyst in the reactant gas feed (CO/O₂/Ar) were collected throughout the temperature ramp (80 - 135°C) at eight different spatial positions along the length of the 18 mm catalyst bed. The data collected from the end of the bed, nearest to the reactor outlet (+ 14.6 mm from the front of the catalyst bed) is discussed first.

The XANES spectrum of the Pd/ γ -Al₂O₃ catalyst collected in the reactant gas environment (CO/O₂) before and after the light-off point are plotted together in Figure 6.5(a). XANES spectra of the Pd/ γ -Al₂O₃ catalyst collected under a reducing (4% H₂, 100°C) and oxidising (10% O₂, 100°C) environment are also shown for reference. The XANES spectrum of the Pd/ γ -Al₂O₃ catalyst under reaction conditions before light-off matched that of the reference spectrum collected under the reducing (H₂) environment, showing that the Pd species initially exist in the metallic Pd⁽⁰⁾ oxidation state. After the light-off point, an increase in intensity of the main edge transition at 24370 eV was observed, due to increased electronic vacancies of Pd species in a higher oxidation state. The difference in Pd K-edge XANES features of the catalyst before and after light-off is made clearer by plotting the relevant difference spectrum, shown in Figure 6.5(b). The XANES spectrum of the catalyst collected after light-off could not be matched entirely to that of the reference spectrum that was collected in an oxygen only environment (O₂/Ar) or reducing (H₂/Ar) environment, but appeared to be a combination of both, which highlighted that only partial oxidation had occurred.

Performing a linear combination analysis of the XANES spectra collected over the light-off period showed that the final catalyst could be interpreted by a summation of Pd⁽⁰⁾ and Pd^(II) components, using reference XANES spectra of the reduced (Pd/ γ -Al₂O₃) and oxidised (PdO/ γ -Al₂O₃) catalyst, respectively. The Pd^(II) component increased from a fraction of 0.05 before light-off to 0.2 after light-off, and the Pd⁽⁰⁾ component decreased from a fraction of 0.95 before light-off to 0.8 after light-off, consistent with partial oxidation of the Pd nanoparticles. The change in Pd XANES from the metallic to partially oxidised state occurred rapidly at 114°C, consistent with the light-off

temperature reported from the mass spectrometry signals. The extent of Pd oxidation was also followed by the intensity of the XANES feature at 24370 eV, which showed the same sharp transition from the metallic to partially oxidised state (Figure 6.6).

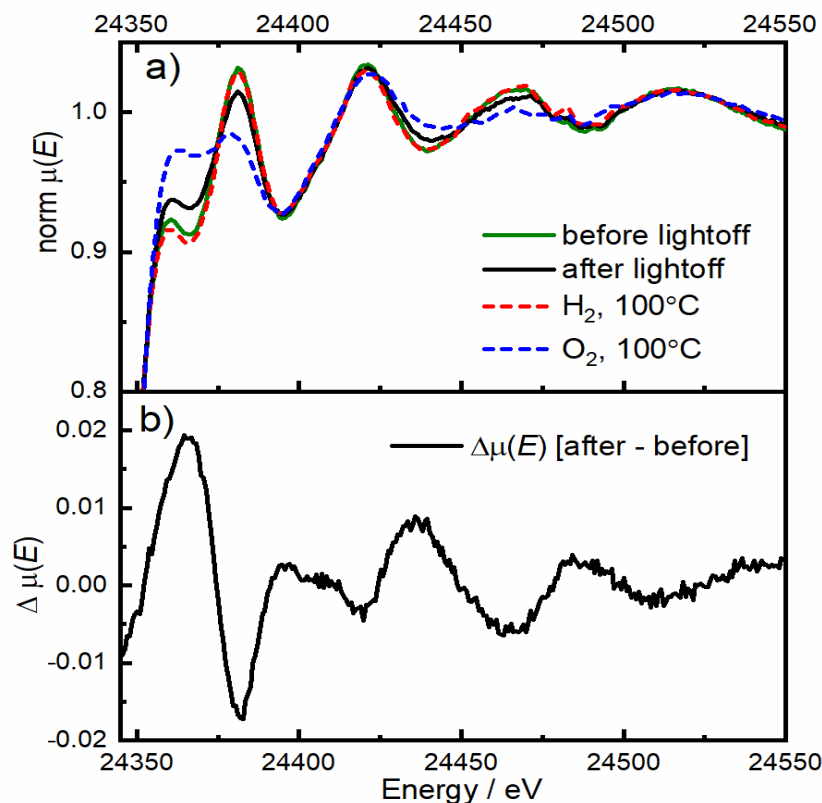


Figure 6.5. a) Pd K-edge XANES spectra of Pd/ γ -Al₂O₃ catalyst at position 8 (14.6 mm) in a plug-flow reactor under reactant (1% CO/3% O₂/Ar) gas feed, before (green) and after (black) ignition for CO oxidation. Plotted together with ex situ measurements of Pd/ γ -Al₂O₃ catalyst after reduction treatment in 4% H₂ at 100°C (red) and then exposure to 10% O₂ at 100°C (blue) and b) difference spectrum of Pd K-edge XANES before and after ignition for CO oxidation.

The extent of Pd nanoparticle oxidation could be understood further by examining the Fourier transformed EXAFS data collected of the catalyst before and after the light-off point. The Fourier transformed EXAFS data of the Pd/ γ -Al₂O₃ catalyst in the reducing (H₂) environment, and in the reactant gas environment before light-off (reaction time 433 seconds) are plotted in Figures 6.7(a) and 6.7(b), respectively. Both figures show similar EXAFS scattering features, which can be fitted using a model constructed from a single Pd-Pd scattering path of Pd foil (fitting parameters shown in Table 6.1). The Pd/ γ -Al₂O₃ catalyst before light-off is therefore found to have a Pd-Pd bond distance consistent with fcc Pd metal structure (2.732 Å) and a coordination number, 7.8.

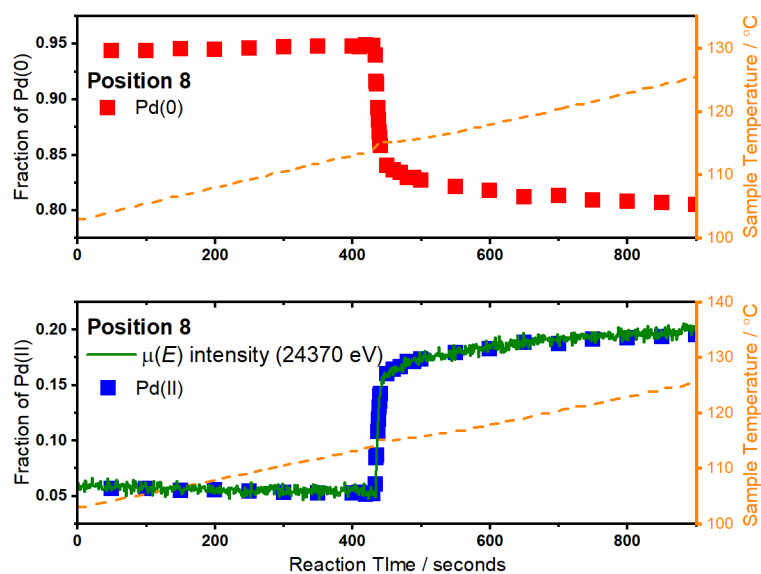


Figure 6.6. Linear combination analysis of Pd K-edge XANES spectra of Pd γ -Al $_2$ O $_3$ catalyst at the end of the catalyst bed (+14.6 mm), collected at multiple time points during the temperature ramp experiment for CO oxidation (1% CO, 3% O $_2$). Linear combination used two reference XANES spectra of the oxidised PdO/ γ -Al $_2$ O $_3$ and reduced Pd/ γ -Al $_2$ O $_3$ catalyst to represent Pd^(II) and Pd⁽⁰⁾, respectively. $\mu(E)$ intensity of XANES feature at 24370 eV plotted in bottom panel (green).

The Fourier transformed EXAFS data of the Pd/ γ -Al $_2$ O $_3$ catalyst during the light-off period (at reaction times 433 – 460 seconds) are shown in Figure 6.8(a). There is decrease in amplitude of the scattering feature at 2.5 Å, and change in the definition of the scattering features at low R (~1.8 Å). By fitting the Fourier transformed EXAFS data to a model using the Pd-Pd scattering path (2.734 Å) of Pd foil, and an additional Pd-O scattering path (1.98 Å) for coordination to oxygen atoms, the changes in EXAFS features during this period can be attributed to a decrease in Pd-Pd coordination and increasing coordination of Pd to oxygen atoms (fitting parameters shown in Table 6.1). The scattering features at higher R values remained consistent during this period, showing that there was no change to the bulk Pd nanoparticle structure at larger distances. Figure 6.8(b) shows that the Pd/ γ -Al $_2$ O $_3$ catalyst after light-off (reaction time 460 seconds) did not have the same local coordination environment as the catalyst in an oxygen only (O $_2$ /Ar) environment.

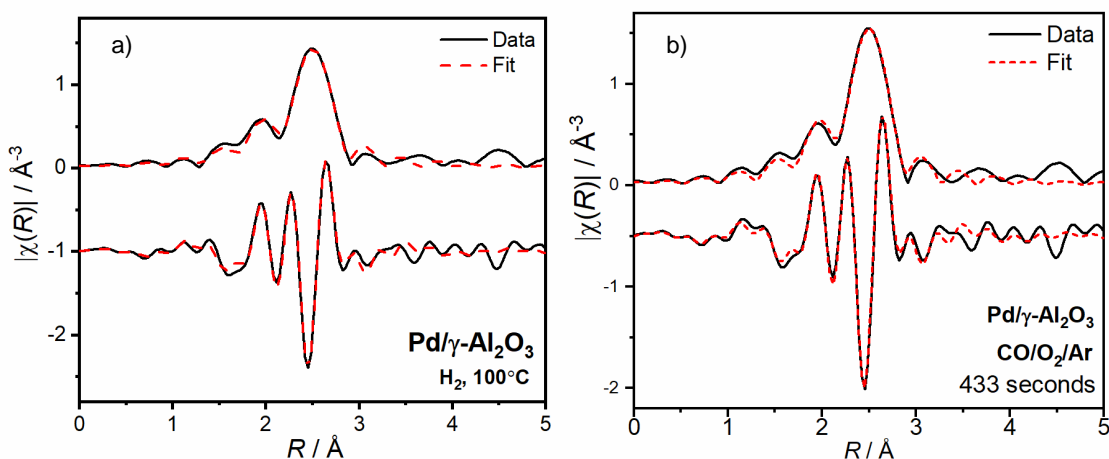


Figure 6.7. Non-phase corrected Fourier transformed Pd K-edge EXAFS data of Pd/γ-Al₂O₃ catalyst, showing magnitude (top) and imaginary (bottom) a) in a reducing (10%H₂/Ar) environment at 100°C, and b) at position 8 (near reactor outlet) in reactant (1%CO/3%O₂/Ar) gas feed at 114°C before light-off for CO oxidation, plotted with a fitting model constructed from a single Pd-Pd scattering path.

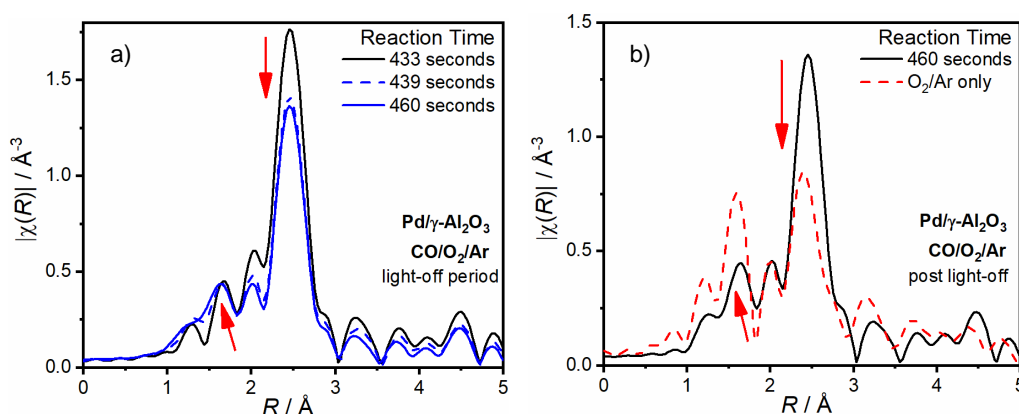


Figure 6.8. Non-phase corrected Fourier transformed EXAFS of Pd/γ-Al₂O₃ catalyst at position 8 (end of catalyst bed) a) during temperature ramp experiment in reactant gas feed (1% CO, 3% O₂) at reaction times 433, 439 and 460 seconds, b) during temperature ramp experiment in reactant gas feed (1% CO, 3% O₂) at reaction time 460 seconds (after light-off) and in O₂/Ar environment at 100°C (red, dashed).

The Fourier transformed EXAFS data of the Pd/γ-Al₂O₃ catalyst in an O₂/Ar environment, and in the reactant gas environment after light-off are plotted with the corresponding fitting models in Figures 6.9(a) and 6.9(b), respectively. The fitting models were constructed from two scattering paths for Pd coordination to neighbouring oxygen and palladium atoms, Pd-O and Pd-Pd respectively. For the Pd/γ-Al₂O₃ catalyst in O₂/Ar environment, the Pd-Pd distance remained at the value expected for Pd fcc crystal structure (2.73 Å) but with an additional path for high coordination of Pd to near neighbour oxygen atoms (coordination number, 1.9 ± 0.5), at a distance of 1.98 Å. A similar model was used to fit the EXAFS data of the Pd/γ-Al₂O₃ catalyst after light-off for CO oxidation (at reaction time 460 seconds) but was found to have lower coordination to near neighbour oxygen atoms (coordination number, 0.9 ± 0.1). The Pd-Pd distance at 2.73 Å is consistent with metallic Pd fcc crystal structure, and the absence of a Pd-Pd scattering path at ~3.0 Å for bulk PdO structure means that, even

in oxygen (O_2/Ar) environment, there was no evidence for the formation of a bulk oxide structure at that temperature. The formation of Pd-O coordination at the nanoparticle surface is known to be the first step in the formation of PdO nanoparticles, however the reaction temperature ($115^\circ C$) was below the temperature at which the formation of bulk PdO is expected to occur ($>200^\circ C$).⁵⁹ Thus partial oxidation, inferred from Pd K-edge XANES and EXAFS analysis, is suggested to be limited to the Pd nanoparticle surface, as reported previously for similar Pd K-edge EXAFS analysis of supported Pd nanoparticle catalysts in air.⁶⁰ The smaller Pd-O coordination number of 0.9 ± 0.1 found for the catalyst performing CO oxidation compared to 1.9 ± 0.5 for the same catalyst in O_2/Ar atmosphere shows that the Pd at the oxidised nanoparticle surface after light-off were not saturated with chemisorbed oxygen atoms. These results are consistent with Pd coordination numbers of previous *operando* EXAFS measurements of a Pd nanoparticle catalyst during CO oxidation.³⁴ In this previous work, the high activity regime of the CO oxidation reaction was suggested to proceed via a Langmuir Hinshelwood mechanism over a partially oxidised Pd surface dominated by chemisorbed oxygen.³⁴ However, the unsaturated coordination sites of a PdO surface have previously been attributed to the operation of a Mars Van-Krevelen reaction mechanism, whereby lattice oxygen at the surface participates in the reaction mechanism to leave a defect site at the surface,⁶¹ similarly to that reported for a Pt nanoparticle catalyst investigated during the high activity regime of CO oxidation.⁴⁷ The absence of any bulk PdO structural features in the EXAFS spectra of the Pd/ γ - Al_2O_3 catalyst in this work indicates that Pd oxidation is limited only to the Pd atoms at the nanoparticle surface, and that there is no PdO lattice formation for the Mars Van Krevelen mechanism to occur, thus the former theory for a Langmuir Hinshelwood reaction mechanism is suggested to occur in this case.

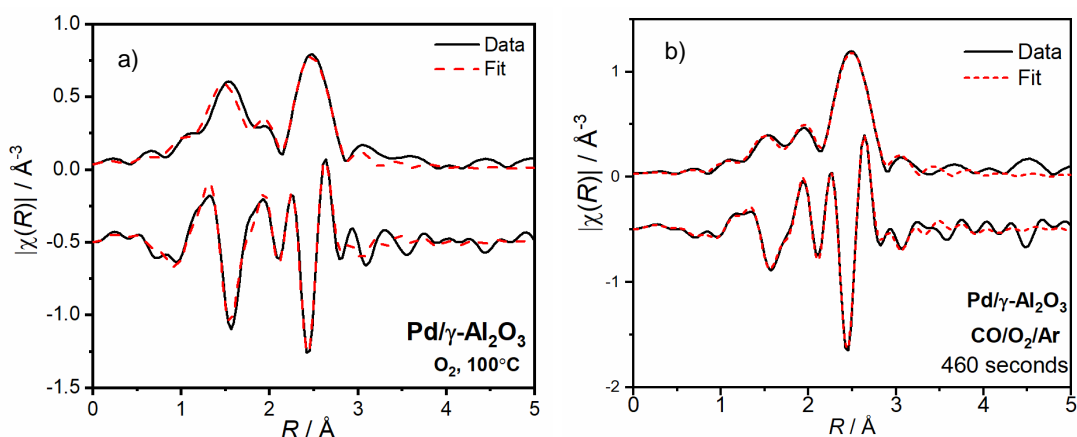


Figure 6.9. Non-phase corrected Fourier transformed Pd K-edge EXAFS data of Pd/ γ -Al₂O₃ catalyst, showing magnitude (top) and imaginary (bottom) a) in an oxidising (10% O₂/Ar) environment at 100°C, and b) at position 8 (near reactor outlet) in reactant (1%CO/3%O₂/Ar) gas feed at 114°C after light-off for CO oxidation, plotted with a fitting model constructed from Pd-Pd and Pd-O scattering paths.

Table 6.1. Pd K-edge EXAFS fitting parameters for Pd/ γ -Al₂O₃ catalyst at position 8 (end of catalyst bed) under different reaction environments. Fitting model used scattering paths Pd-Pd and Pd-O of Pd metal and PdO, respectively.

Gas Environment	Sample Temperature (Reaction Time)	Scattering Path	N	R / Å	$\sigma^2 / \text{Å}^2$	E_0 / eV	S_0^2	R_{factor}
10% H ₂	100°C	Pd-Pd	7.4(7)	2.735(3)	0.0069(7)	(-)3.3	0.81 (set)	0.01
10% O ₂	100°C	Pd-Pd	4.2(8)	2.717(7)	0.008(2)	(-)3.1(5)	0.81 (set)	0.03
		Pd-O	1.9(5)	1.98(1)	0.004(4)	(-)3.1(5)	0.81 (set)	0.03
1% CO/3% O ₂	114°C (433 secs)	Pd-Pd	7.8(6)	2.732(3)	0.0067(6)	(-)3.3(2)	0.81 (set)	0.009
1% CO/3% O ₂	115°C (439 secs)	Pd-Pd	6.8(2)	2.725(2)	0.0075(2)	(-)3.3(2)	0.81 (set)	0.004
		Pd-O	0.9(1)	1.98(1)	0.007(2)	(-)3.3(2)	0.81 (set)	0.004
1% CO/3% O ₂	115°C (441 secs)	Pd-Pd	6.7(2)	2.725(2)	0.0076(2)	(-)3.3(2)	0.81 (set)	0.005
		Pd-O	0.9(1)	1.99(1)	0.006(2)	(-)3.3(2)	0.81 (set)	0.005
1% CO/3% O ₂	115°C (460 secs)	Pd-Pd	6.5(2)	2.725(2)	0.0076(2)	(-)3.3(2)	0.81 (set)	0.005
		Pd-O	0.9(1)	1.99(1)	0.005(2)	(-)3.3(2)	0.81 (set)	0.005

Note: Fit range $3 < k / \text{Å}^{-1} < 11.3$, $1 < R / \text{Å} < 3$; number of independent points 10.

The DRIFTS spectra of the Pd/ γ -Al₂O₃ catalyst collected under reactant (CO/O₂) gas feed before, during and after light-off for CO oxidation are reported in Figure 6.10(a). The spectrum collected before light-off shows two characteristic absorption bands for CO adsorbed on a metallic Pd surface (CO_{ads}). The sharp band centred at 2064 cm⁻¹ is attributed to linear adsorption of CO, and the broad, asymmetric band with maximum at 1972 cm⁻¹ and a shoulder at 1928 cm⁻¹ is attributed to bridge-bonded and multi-coordinated CO adsorption at the Pd nanoparticle surface.⁶²⁻⁶⁶ Both linear and multi-coordinate CO adsorption bands were observed with high intensity in the DRIFTS spectrum before the light-off point for CO oxidation. This is in agreement with characterisation of the catalyst during the low activity regime to experience poisoning by CO_{ads} at the catalyst surface.^{22, 24, 43, 45} The DRIFTS spectrum collected at 114.7°C shows decreased intensity of all CO absorption bands, which were lost completely from the DRIFTS spectrum collected at 115.4°C meaning that the concentration of CO_{ads} at the catalyst surface after the light-off point was below the DRIFTS detection limit. The absorption bands at 1580 cm⁻¹ and 1458 cm⁻¹ can be attributed to carbonate species at the catalyst surface which were not removed after the light-off point.^{67, 68} These carbonate species may be strongly adsorbed to the γ -Al₂O₃ surface and, most likely, do not participate in catalysis at the Pd nanoparticle surface.⁶⁹ There was no evidence from these DRIFTS spectra for the adsorption of CO on Pd^(II) sites, nor evidence of dipole coupling that has previously been reported to shift the CO stretching frequency as a function of CO_{ads} coverage.^{45, 70} It is likely that the timescale for removal of CO_{ads} from the catalyst surface during the light-off period was too fast to induce any significant dipole moments for detection by DRIFTS. Time-resolved analysis of the DRIFTS spectra involved following the intensity of the CO absorption bands (1976 - 1940 cm⁻¹) as a function of reaction time. The intensity of the CO absorption bands are plotted in Figure 6.10(b), showing a sharp decrease in intensity at the light-off point. The intensity

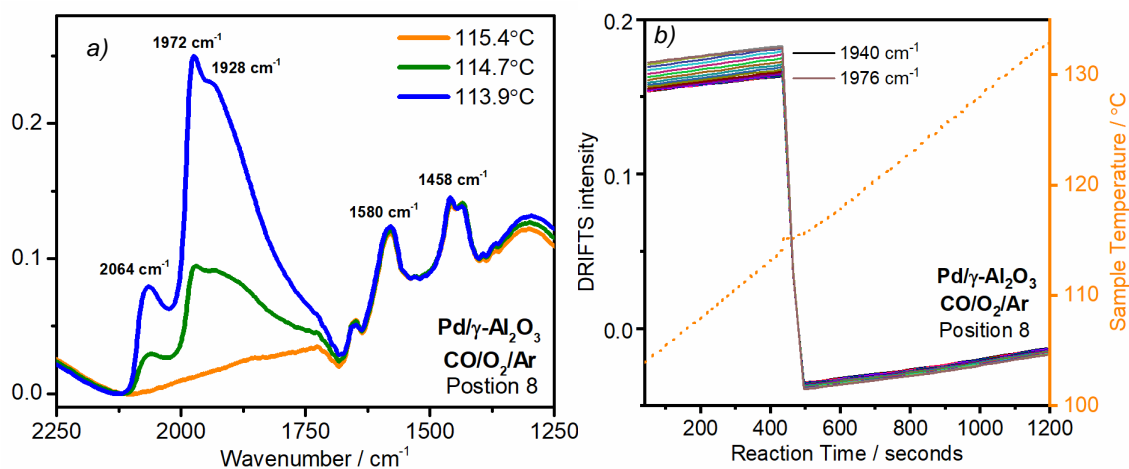


Figure 6.10. a) Operando DRIFTS spectra of Pd/ γ -Al₂O₃ in plug-flow reactor at position 8 (nearest the end of the catalyst bed) during CO oxidation (1%CO/3%O₂/Ar) at increasing temperatures. b) Intensity of DRIFTS CO absorption bands (1940 - 1976 cm⁻¹) as a function of time during temperature ramp experiment in reactant gas feed (1%CO/3%O₂/Ar).

of all CO bands decrease simultaneously to zero, showing that CO_{ads} is lost from linear and bridged adsorption sites at the same time.

The extent of Pd oxidation could be followed directly by the intensity of the main edge transition of the XANES spectra at 24370 eV, and the extent of CO_{ads} coverage followed by the intensity of the DRIFTS CO adsorption band at 1940 cm⁻¹. By plotting the time-resolved DRIFTS and XANES data on the same time scale (Figure 6.11), it is found that the sharp oxidation of Pd at the nanoparticle surface coincided with the sharp decrease in CO coverage at that particular spatial position in the catalyst bed. This observation is consistent with the widely accepted model which assumes that, beyond the light-off point, the catalyst surface is dominated by atomic oxygen and the reaction kinetics for combination of CO_{ads} with surface oxygen are so fast that the carbonyl surface concentration is too low to be detected by DRIFTS spectroscopy.^{24, 40, 71} The top panel of Figure 6.11 shows the normalised mass spectrometry signal from online end-pipe analysis of the reactor exhaust plotted on the same timescale as the time-resolved XANES and DRIFTS data. The decrease in CO coverage and oxidation of Pd species occur approximately 50 seconds before the sharp increase in mass spectrometry signal for CO₂ formation. The delay can be attributed to the residence time of CO₂ reaching the detector of the mass spectrometer from the reactor. (Time taken for gas flow of 50 cm³ min⁻¹ to travel ~80 cm length of a 1/16" tube.) Hence it can be found that the sharp increase in CO₂ formation can be attributed to ignition of CO_{ads} stored on the catalyst surface, which is mirrored by the simultaneous increase in consumption of O₂ which is both adsorbed to the Pd nanoparticle surface and used in the oxidation of CO_{ads} to CO₂. However, it must be noted that the end-pipe mass spectrometry signal provides information for the catalytic activity across the entire length of the catalyst bed, and so EDE and DRIFTS data at other spatial positions must be considered before interpreting the end-pipe catalytic activity, as discussed later.

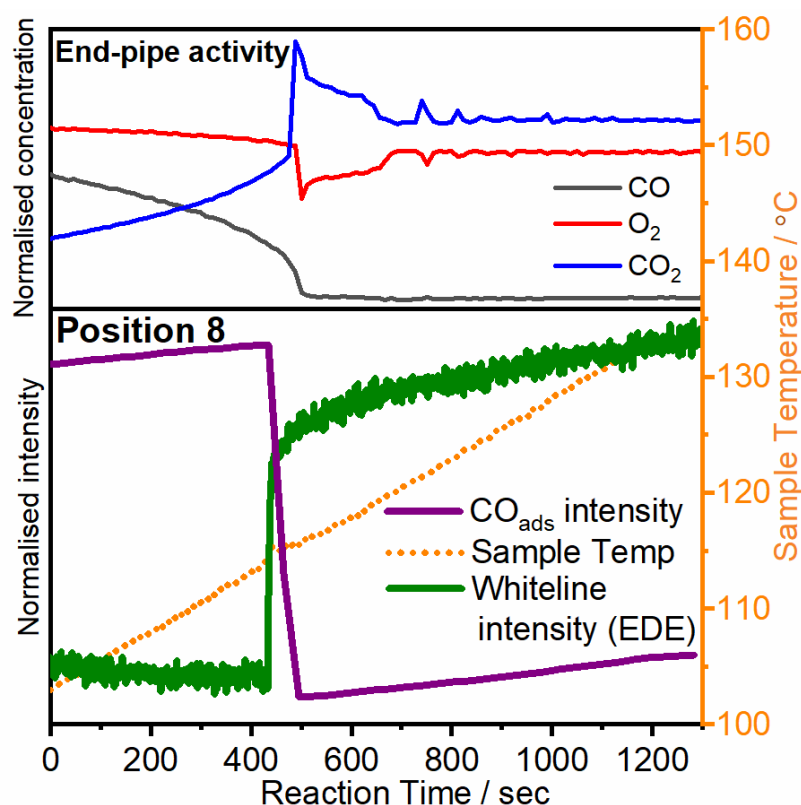


Figure 6.11. Bottom panel shows the Pd K-edge absorption intensity at 24370 eV (green), DRIFTS CO absorption intensity (purple) of the Pd/ γ -Al₂O₃ catalyst at the end of the catalyst bed (nearest the reactor outlet) and the internal reactor temperature (orange, dashed). Top panel shows the normalised end-pipe mass spectrometry signals for O₂ (red), CO (black) and CO₂ (blue) concentrations of the exhaust gas from the reactor.

6.3.1.4 Position 1 – Front of the catalyst bed (+ 0.4 mm)

The Pd K-edge XANES spectra of the Pd/ γ -Al₂O₃ catalyst measured at the axial position +0.4 mm from the front of the catalyst bed are shown in Figure 6.12. The XANES spectrum of the Pd/ γ -Al₂O₃ catalyst in reactant gas feed (CO/O₂) before light-off (reaction time of 600 seconds) was consistent with the XANES of Pd/ γ -Al₂O₃ in reducing atmosphere (H₂, 100°C). Similarly to the sample measured at the end of the catalyst bed, the XANES spectrum of the catalyst after light-off (reaction time of 1080 seconds) showed increased in absorption intensity of the main edge transition due to partial oxidation at the nanoparticle surface. The difference XANES spectra plotted in Figure 6.12b for the catalyst measured at the front and at the end of the catalyst bed show the similar extent of Pd oxidation before and after light-off.

The linear combination analysis of XANES spectra collected during the light-off period at the front of the bed are shown in Figure 6.13, plotted together with the XANES absorption intensity at 24370 eV. Similarly to the catalyst at the end of the bed, the fraction of Pd^(II) component increased from a near zero value before light-off to a final value of 0.2. However, during the light-off period at the front of the bed the transformation from the initial state of bulk metal nanoparticles to the final, partially oxidised state exhibited oscillating behaviour rather than a sharp, direct transition.

which was reached after extinction of the oscillating behaviour. The onset of Pd oxidation at position 1 was found to occur at a later reaction time (620 seconds) than that at position 8, which corresponds to a higher light-off temperature of 117.5°C. The first ‘oscillation’ can be described as a rapid increase in the fraction of Pd^(II) species from the initial value of 0.06 to a value of 0.14, before decreasing slowly to 0.10. During the second ‘oscillation’ the fraction of Pd^(II) species increased sharply to a maximum of 0.16 before decreasing slowly. The final state of each oscillation was more oxidised than the last, until the fraction of Pd^(II) and Pd⁽⁰⁾ components reached the same values (0.2 and 0.8, respectively) as those obtained for the final state of the catalyst at position 8. This final state of partial oxidation and extinction of oscillations was achieved at a reaction time of 1000 seconds, corresponding to the reactor temperature of 127°C.

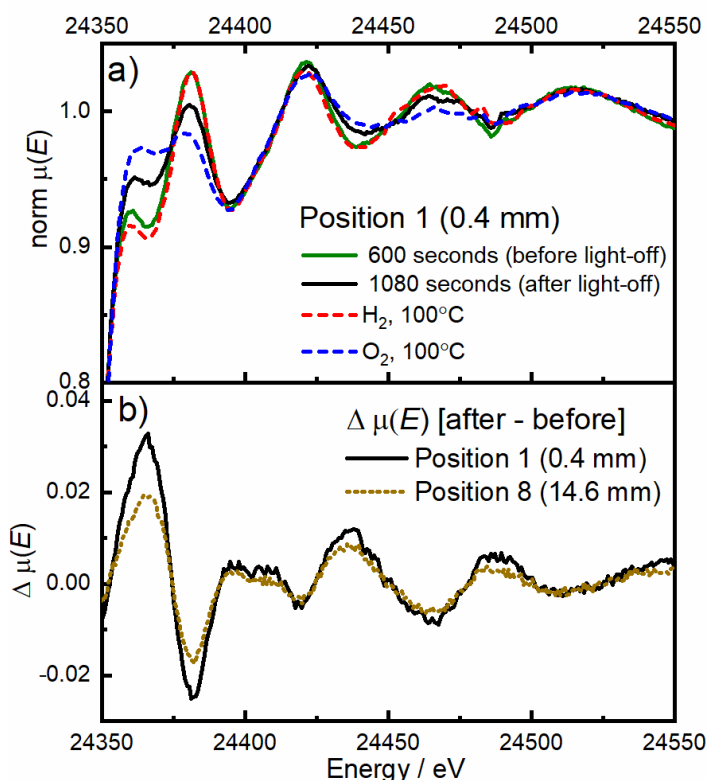


Figure 6.12. a) Pd K-edge XANES spectra of Pd/ γ -Al₂O₃ catalyst at position 1 (0.4 mm) in a plug-flow reactor under reactant (1% CO/3% O₂/Ar) gas feed, before (green) and after (black) ignition for CO oxidation. Plotted together with ex situ measurements of Pd/ γ -Al₂O₃ catalyst after reduction treatment in 4% H₂ at 100°C (red) and then exposure to 10% O₂ at 100°C (blue) and b) difference spectrum of Pd K-edge XANES before and after ignition for CO oxidation.

By plotting the absorption intensity of the XANES feature together with the absorption intensity of the CO stretching band (1940 cm⁻¹) of the time-resolved DRIFTS spectra (Figure 6.14), it is possible to observe that oscillations in the CO surface coverage occur as well as the surface oxide coverage. The top panel of Figure 6.14 shows the normalised mass spectrometry signal of the exhaust gases plotted on the same timescale as the DRIFTS CO intensity and XANES Pd oxidation intensity. It was found that the oscillations in Pd surface oxidation and CO surface coverage also coincided with the oscillations in the end pipe O₂ signal and CO₂ formation during the reaction

period between 650 seconds and 1000 seconds. The onset of oscillations in the mass spectrometry signals (reaction time of 748 seconds) were delayed by ~128 seconds after the onset of Pd oxidation. This can again be attributed to the residence time of CO₂ reaching the detector of the mass spectrometer from that position at the front of the catalyst bed.

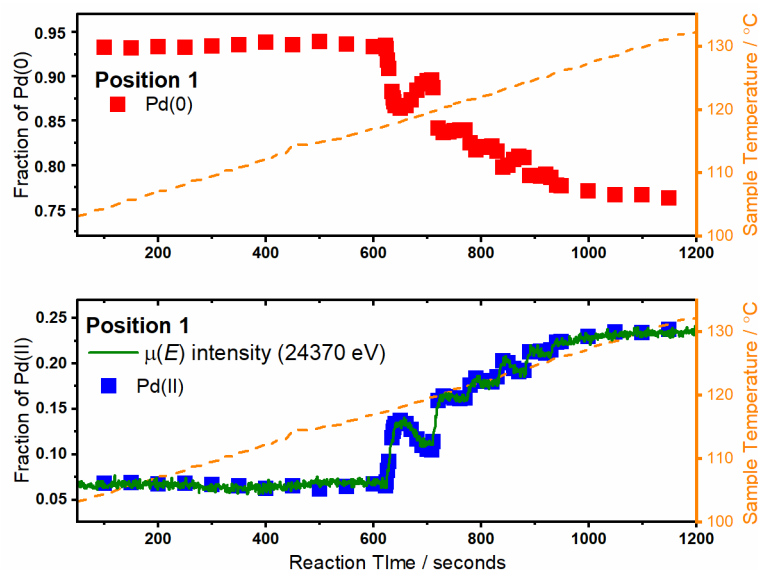


Figure 6.13. Linear combination analysis of Pd K-edge XANES spectra of Pd γ -Al₂O₃ catalyst at the front of the catalyst bed (+0.4 mm), collected at multiple time points during the temperature ramp experiment for CO oxidation (1% CO, 3% O₂). Linear combination used two reference XANES spectra of the oxidised PdO/ γ -Al₂O₃ and reduced Pd/ γ -Al₂O₃ catalyst to represent Pd^(II) and Pd⁽⁰⁾, respectively. $\mu(E)$ intensity of XANES feature at 24370 eV plotted in bottom panel (green).

During these oscillations a rise in CO₂ formation coincided with a decrease in CO surface coverage, which was followed immediately by a sharp increase in the extent of Pd oxidation. Following the sharp Pd oxidation there was a period of lower CO₂ formation and increase in surface CO coverage. With each cycle, the XANES absorption intensity reached a greater value (*i.e.* the Pd nanoparticle surface became increasingly oxidised) and the CO coverage decreased to a lower value until the catalyst eventually reached the final state of apparent zero CO coverage and partial Pd oxidation similar to that at the position at the end of the bed. Consequently, the overall behaviour in terms of temperature dependence of the CO conversion, Pd oxidation state and carbonyl coverage is similar to that observed at the position near the reactor outlet with the notable exception of the oscillating behaviour observed during the transition from initial to final states.

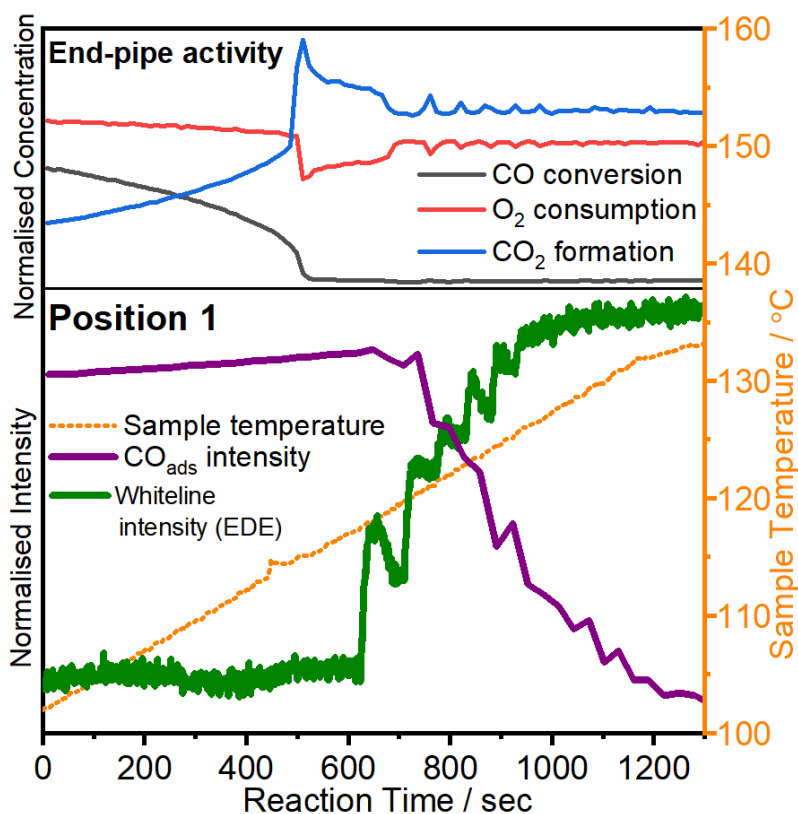


Figure 6.14. Bottom panel shows the Pd K-edge absorption intensity at 24370 eV (green), DRIFTS CO absorption intensity (purple) of the Pd/ γ -Al₂O₃ catalyst at the front of the catalyst bed (nearest the reactor inlet) and the internal reactor temperature (orange, dashed). Top panel shows the normalised end-pipe mass spectrometry signals for O₂ (red), CO (black) and CO₂ (blue) concentrations of the exhaust gas from the reactor.

6.3.1.4 Spatio-temporal analysis

In order to further examine the catalyst structure and surface reactivity across the entire catalyst bed, time-resolved EDE and DRIFTS data collected from eight different spatial positions along the length of the catalyst bed were compared. Figure 6.15 shows the extent of Pd oxidation (from normalised XANES absorption intensity at 24370 eV) and the extent of CO coverage (from DRIFTS absorption intensity at 1940 cm⁻¹) at multiple positions of the reactor during the temperature ramp experiment (100 - 135°C, 2°C min⁻¹) in reactant gas flow (CO/O₂). The top panel in Figure 6.15 refers to the position measured nearest to the reactor inlet (+0.4 mm from the front of the bed), and the positions measured at increasing distance from the reactor inlet are plotted in order vertically down the figure, with the position measured nearest to the reactor outlet (+14.6 mm from the front of the bed) shown in the bottom panel. The sharp increase in XANES absorption intensity corresponding to partial Pd oxidation is observed for all spatial positions downstream of position 2. The sharp transition in Pd oxidation occurred at the earliest reaction time (and thus lowest temperature) of 440 seconds (114°C) at position 8 – nearest to the reactor outlet. This was followed soon after by the sharp transition in Pd oxidation at positions 7 and 6 at 460 seconds (115°C), and then subsequently at positions 5 to 3 between reaction times of 500 to 530 seconds.

The CO coverage was found to sharply decrease in intensity at the same time as Pd oxidation at each position, which can be explained by the ignition of CO_{ads} to CO₂ which released free adsorption sites for dissociative adsorption of oxygen at the surface.

The onset of Pd oxidation at position 2 (+1.8 mm from the front of the catalyst bed) occurred at a similar reaction time as position 1 (620 seconds), after the oxidation of the catalyst at all other positions further downstream of the reactor. The XANES absorption intensity increased to a value close to that of the final partially oxidised state (as reached at positions 3 - 8), but then showed a small decrease before increasing again to reach the final partially oxidised state. The extent of CO coverage also showed a similar oscillating behaviour, in the same time frame, where the intensity of the CO adsorption band (at 1940 cm⁻¹) decreased by ~40%, then increased slightly before decreasing to a near-zero value, then increased slightly once more before falling to zero. This behaviour can be described as short-lived oscillations that occurred at the same time as the first three oscillations in Pd oxidation and CO coverage that were observed at position 1. Although the onset of oscillations at positions 1 and 2 occurred simultaneously, the amplitude and frequency of these oscillations did not match, as the oscillations at position 1 displayed a higher frequency, greater amplitude and longer duration than those at position 2.

The end-pipe mass spectrometry signal can be explained by collecting together information for the surface reactivity at multiple positions across the entire length of the catalyst bed. The reaction front was initiated at the end of the catalyst bed (nearest to the reactor outlet), which was evidenced by the earliest transition in Pd oxidation and loss of adsorbed CO from the catalyst surface at position 8. After the reaction front was initiated at the end of the catalyst bed (at the reaction time of 440 seconds), it propagated upstream consuming a large amount of oxygen for the ignition of stored CO_{ads} and adsorption of oxygen to the Pd surface. The large consumption of O₂ at the end and middle of the catalyst bed during this period of ignition (reaction period between 440 – 590 seconds) was observed in the normalised O₂ mass spectrometry signal and was mirrored by a large excess of CO₂ formation. After the ignition of the stored CO_{ads} from the end and middle of the catalyst bed (positions 3 – 8), the CO₂ formation and O₂ consumption fell towards the expected stoichiometric values for 100% CO conversion. The high CO conversion at that time period was achieved by catalysis at the middle and end of the catalyst bed where the Pd nanoparticles existed with a partially oxidised surface, while the front of the catalyst bed remained relatively inactive – where the Pd nanoparticles existed in metallic state with high concentration of CO_{ads} at the surface. The oscillations in O₂ consumption and CO₂ formation were observed by end-pipe analysis in the reaction period between 700 – 1000 seconds, which can be explained by the gradual ignition of CO_{ads} from positions 1 and 2 (within +1.8 mm from the front of the catalyst bed), at which time oscillations in CO coverage and Pd

oxidation were observed. At reaction times beyond 1000 seconds, the oscillations in CO₂ formation, O₂ consumption, CO coverage and Pd oxidation ceased, and 100% CO conversion to form CO₂ was maintained.

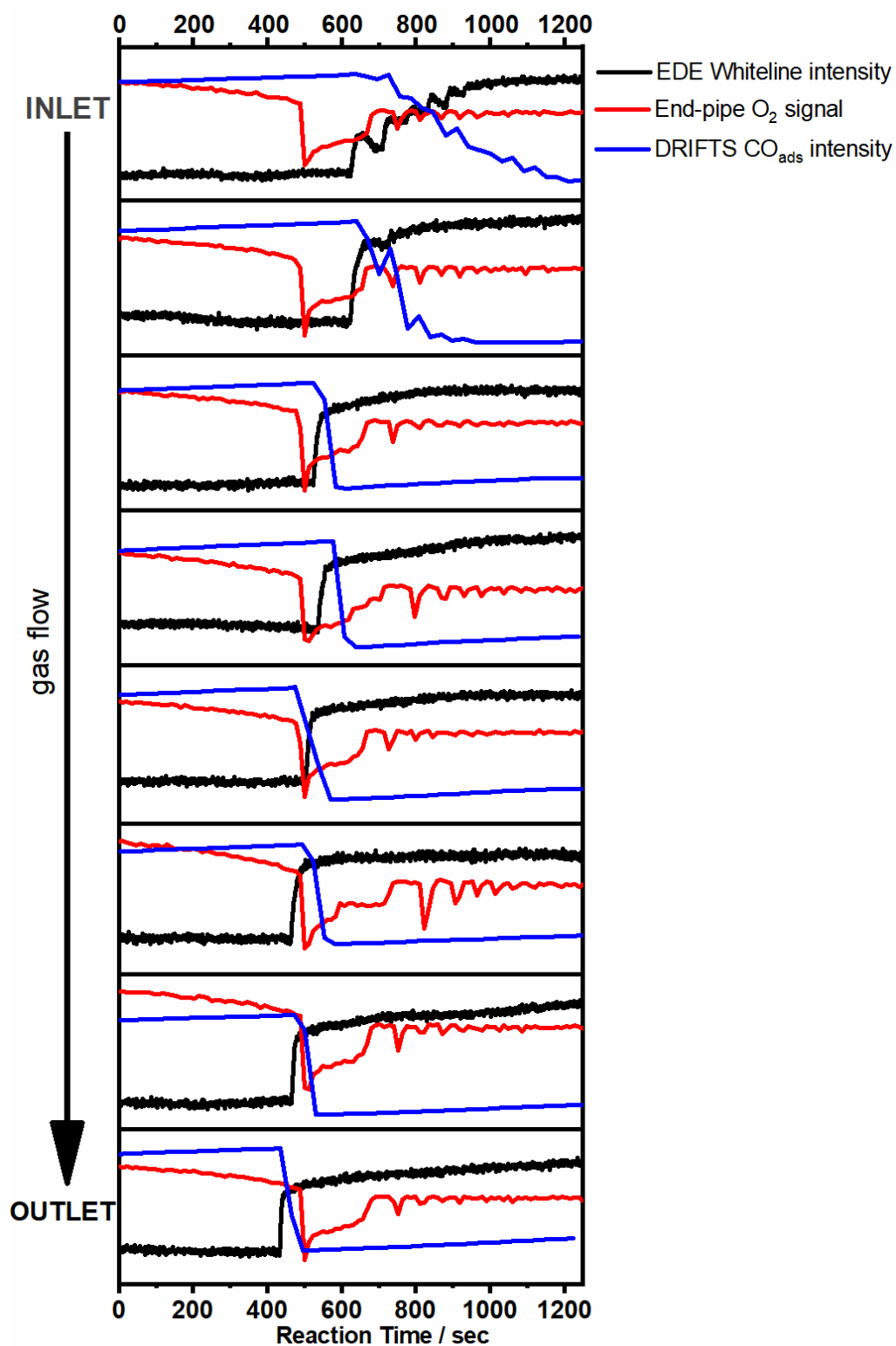


Figure 6.15. End-pipe mass spectrometry O₂ concentration (red), DRIFTS CO adsorption intensity (blue) and EDE Pd K-edge white line intensity (black) at multiple spatial positions in the Pd/ γ -Al₂O₃ fixed catalyst bed from the front/inlet (top panel) to the end/outlet (bottom panel) during each temperature ramp experiment (100°C - 135°C) during flow of reactant gas feed (1% CO/3% O₂/Ar).

6.3.2. Thermographic imaging

The oxidation of CO is an exothermic reaction ($\Delta H = -282 \text{ KJ mol}^{-1}$)¹⁵ and so the reaction front – the spatial position within the reactor that exhibits the highest reaction rate – generates a temperature hotspot that can be observed with an infrared camera. An infrared camera positioned above the EDE/DRIFTS reactor was able to follow the position of the reaction front in the Pd/ γ -Al₂O₃ catalyst bed during the CO oxidation reaction at increasing reactor temperatures. Figure 6.16 reports the thermographic IR images of the reactor, each panel showing a time slice of the catalyst bed at increasing reaction times during the temperature ramp experiment from a reaction time of 528 seconds (top panel) to 924 seconds (bottom panel). The first image, collected when the internal thermocouple measured 114°C, shows a moderate hotspot at an approximate distance +18 mm from the front of the catalyst bed. The position of this hotspot confirms that the CO is first ignited from a position nearest to the outlet of the reactor, in line with the spatially resolved measurements of CO coverage and Pd oxidation. As the reaction rate increased with increasing temperature, the temperature hotspot moved upstream, showing that the reaction front propagated towards the reactor inlet. These observations are again in line with the spatially resolved EDE and DRIFTS measurements which showed that the oxidation of Pd and ignition of CO moved upstream with increasing temperature. The hot spot eventually moved towards the front of the catalyst bed at a reaction time of ~700 seconds, which is the reaction time when oscillations were observed in the end-pipe O₂ consumption, CO₂ formation, and in the Pd oxidation and CO coverage at that position.

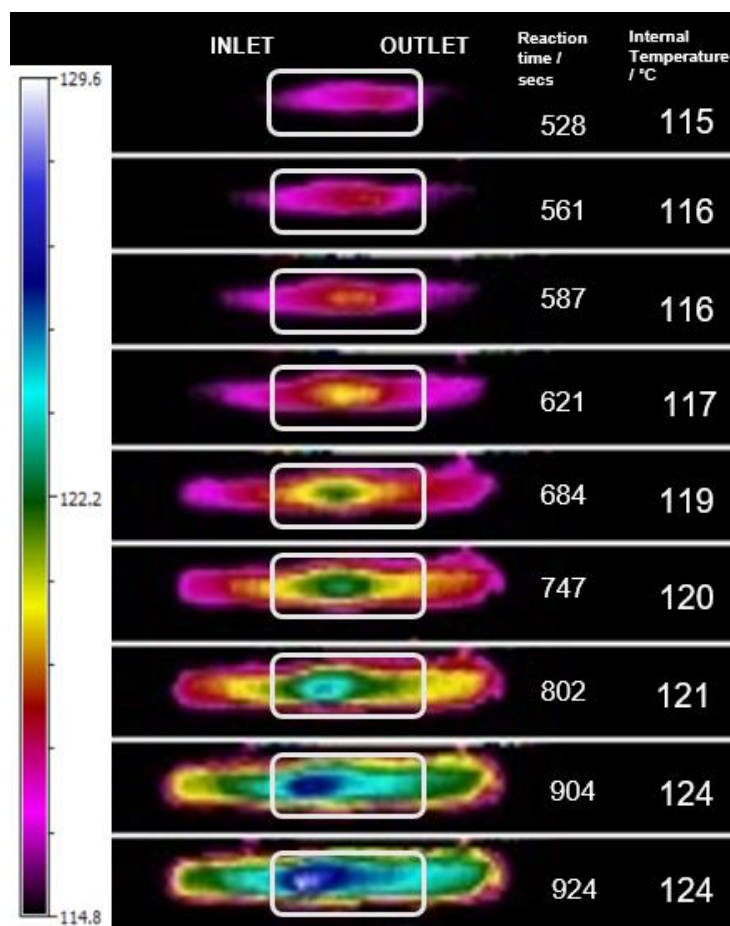


Figure 6.16. Thermographic IR images of reactor during CO oxidation (1%CO/3%O₂/Ar) at increasing temperatures (115°C - 124°C). Gas flow from inlet (left) to the outlet (right), annotated with the temperature read from the internal thermocouple positioned in the catalyst bed. The location of the catalyst bed within the reactor is outlined by a white box.

6.4 Discussion

The results obtained therefore confirm that the ignition of CO occurs initially at the end of the catalyst bed, nearest to the reactor outlet. This was confirmed with the location of the hotspot in IR thermography images both of the Pd/ γ -Al₂O₃ catalyst in this study, and the Pt/ γ -Al₂O₃ catalyst in a previously reported study.⁵⁶

Before ignition, the catalyst exists in its initial state as metallic Pd nanoparticles with a surface poisoned by a high concentration of CO_{ads} on linear, bridging and multi-coordinate adsorption sites, evidenced by DRIFTS measurements of the catalyst at all positions in the reactor at low temperatures (<114°C). This is in line with many previous studies, agreeing that a high concentration of poisoning CO_{ads} prevents the dissociative adsorption of oxygen.^{22, 24, 40, 43} This confirms that the Langmuir Hinshelwood mechanism operates during this low activity regime, with desorption of CO_{ads} being the rate limiting step.^{40, 72}

The ignition of CO oxidation at the end position of the catalyst bed was characterised by a sharp transition to the highly active state, where the catalyst was found to exist as metallic Pd nanoparticles with partial oxidation of Pd due to high Pd-O coordination at the surface. Unlike the Pt/ γ -Al₂O₃ catalyst in other investigations, there was no evidence for formation of an oxide structure,⁷³ and the surface was found not to have complete Pd-O coverage.⁴⁷ The fast reaction kinetics of CO oxidation over the partially oxidised Pd surface are therefore assumed to continue to operate via a Langmuir Hinshelwood mechanism; however the rapid combination of CO_{ads} and O_{ads} means that CO_{ads} are short lived and not present on the surface at concentrations enough to be observed by DRIFTS measurements.

The ignition of CO oxidation occurred initially at the end of the catalyst bed at a reactor temperature of 114°C. At this temperature there was low conversion of CO since the entire catalyst bed was operating in the low activity regime, creating a gradient in CO concentration across the bed. The lowest concentration of gas phase CO was therefore assumed to be at the end of the catalyst bed, as observed by previous spatially resolved measurements,³⁴ and heat released by the exothermic CO oxidation reaction thought to be carried downstream by the gas flow. It follows that the lowest CO concentration and highest local temperatures exist at the end of the catalyst bed during the low activity regime. This causes a greater rate of CO_{ads} desorption and thus releases more adsorption sites for the dissociative adsorption of oxygen at the end of the catalyst bed – facilitating the ignition of CO. The greater surface coverage of chemisorbed oxygen, resulted in greater conversion of CO, thus releasing even more adsorption sites in an autocatalytic process. This activity explains the sharp transition from the metallic state to the final partially oxidised state for the position at the end of the catalyst bed.

The ignition of CO oxidation at the end of the catalyst bed was shortly followed by propagation of the reaction front upstream. This was observed by the IR thermography images, EDE and DRIFTS measurements. The CO₂ formation measured at the reactor outlet during the light-off period of the end and middle of the catalyst bed was greater than the stoichiometric value for 100% CO conversion due to oxidation of stored CO_{ads}.

The catalyst located within the first +1.8 mm of the catalyst bed did not undergo a sharp transition from the low activity to high activity state, but displayed oscillations in Pd oxidation and CO coverage before eventually reaching that same final state as the catalyst downstream. Similarly to studies with a Pt/ γ -Al₂O₃ catalyst, the oscillations in Pd oxidation and CO coverage occurred after the end-pipe catalytic activity had displayed 100% CO conversion.⁴⁷ The end-pipe mass spectrometry signal showed variation in CO₂ and O₂ concentrations during the oscillating behaviour but not in CO concentration. From the EDE/DRIFTS measurements it is clear that oscillations in CO oxidation reaction kinetics occurred only at the front of the catalyst bed where the

catalyst exhibited oscillating Pd oxidation and CO coverage. Within each oscillation, the CO coverage dropped and CO₂ formation increased to a value greater than the stoichiometric value for 100% CO conversion, due to conversion of stored CO_{ads} to CO₂. This was followed by a sharp increase in Pd oxidation and decrease in CO₂ formation. Oscillations in catalytic CO oxidation can therefore be attributed to competition of CO adsorption and dissociative oxygen adsorption at the Pd surface following the release of surface adsorption sites. The low activity period is characterised by a high CO coverage, which prevents the dissociative adsorption of O₂. The high activity period is characterised by dissociative adsorption of oxygen and ignition of the stored CO_{ads}. At the front of the catalyst bed, where the temperature is lowest and the concentration of CO in the gas phase is highest, the release of adsorption sites following the oxidation of stored CO_{ads} is followed by competitive adsorption of either CO or O₂ from the gas phase. The oscillations decrease in amplitude as the reactor temperature is increased because the higher temperature promotes the dissociative adsorption of oxygen rather than the adsorption of CO, and so the extent of Pd oxidation increases with each oscillation. It has been reported that Pd catalysts may, under certain isothermal reaction conditions, exhibit self-sustained kinetic oscillations for CO oxidation.²⁵ The isothermal conditions for self-sustained oscillations must therefore be at CO concentrations and catalyst temperatures that permit this competitive adsorption of CO and O₂. Due to the different adsorption properties of metal surfaces with varying ratios of edge and terrace sites, the reaction conditions for self-sustained oscillating behaviour are likely to vary depending on the size and shape of the nanoparticle catalyst, as was observed for supported Pt catalysts of different particle size.⁴⁵

Although this experimental set-up for combined EDE and DRIFTS spectroscopies was able to make significant advances on previous combined, *operando* spectroscopic experiments, the limitations to this method must be mentioned. The different spatial positions were measured at different times, by cleaning the catalyst and repeating the reaction conditions. We have made the assumption in this work, from the consistent end-pipe mass spectrometry signal, that the catalytic activity was repeatable each time and the changes in catalyst structure were reversed in each cleaning cycle. The reduced time resolution of the DRIFTS data acquisition compared to the EDE technique meant that the CO coverage could not be followed on the same time scale as the Pd surface oxidation. The FTIR spectrometer used for this experiment was capable of achieving spectra with faster acquisition times, which should be considered in future experiments. Moreover the lack of spatial resolution in the mass spectrometry data means that only the integral, end-pipe catalytic activity could be assessed. For spatially resolved information of gas concentrations and temperature profiles within the catalyst bed, the XAFS/DRIFTS reactor should be coupled with a spatially resolved gas sampling technique such as the Spaci-FB.

6.5 Conclusions

The spatially resolved measurements of the metal oxidation state, from Pd K-edge EDE measurements, and surface speciation, from DRIFTS measurements, have been able to provide new insights for the operation of a Pd/ γ -Al₂O₃ catalyst bed during oscillating CO oxidation. The catalyst structure and surface properties have been linked to the catalytic activity at different spatial positions within a plug-flow reactor by using a newly designed XAFS/DRIFTS reactor for combined, *operando* EDE and DRIFTS spectroscopy.

The kinetic oscillations of CO oxidation over a supported Pd/Al₂O₃ catalyst are found to occur only within the front 1.8 mm of the catalyst bed. The rest of the catalyst bed shows a sharp transition from the low activity to high activity regime, due to an autocatalytic transition of surface speciation at the Pd nanoparticle surface. In the low kinetic regime, DRIFTS spectra show that the catalyst is characterized by a high coverage of adsorbed CO which prevents the dissociative adsorption of oxygen. In the high kinetic regime, Pd K-edge EXAFS show that the catalyst is characterized by a high surface coverage of atomic oxygen but no evidence of Pd oxide structure. The catalyst is therefore shown to continue to proceed via a Langmuir Hinshelwood reaction mechanism during the high activity regime, with a high surface coverage of atomic oxygen which facilitates faster CO oxidation reaction rate upon adsorption of CO to the metal surface.

The sharp transition of the catalyst from the low activity to high activity regime occurs initially at the end of the catalyst bed where there is the lowest concentration of CO and highest local catalyst temperature. The reaction front then propagates upstream and an excess of CO₂ formation is measured at the outlet due to conversion of the stored CO_{ads} to CO₂. The oxidation of CO_{ads} from the catalyst surface releases adsorption sites for the dissociative adsorption of oxygen, resulting in the sharp transition to the high activity state. However, at the front of the catalyst bed, higher concentrations of CO in the gas phase mean that the release of adsorption sites in the oxidation of CO_{ads} is followed by competitive adsorption of CO and O₂. For lower temperatures and high CO concentration, adsorption of CO is preferred, there is reformation of the low activity state, and kinetic oscillations are observed in the formation of CO₂.

Despite the lack of spatial resolution in the mass spectrometry methods, the correlation of the spatially resolved data with IR thermography images have meant that the integral catalytic activity could be related to the structure and function of the catalyst at different positions within the reactor. The successful collection of spatially resolved and time-resolved, simultaneous EDE and DRIFTS spectroscopy collected in this study

have therefore been able to provide a complete analysis of the change in nanoparticle structure and surface speciation during reaction conditions for CO oxidation.

6.6 References

1. MV Twigg, *Appl. Catal. B: Environmental*, 2007, **70**, 2-15.
2. J Lin, X Wang and T Zhang, *Chinese J. Catal.*, 2016, **37**, 1805-1813.
3. MP Cox, G Ertl and R Imbihl, *Phys. Rev. Lett.*, 1985, **54**, 1725-1728.
4. G Ertl, PR Norton and J Rüstig, *Phys. Rev. Lett.*, 1982, **49**, 177-180.
5. MM Slin'ko and NI Jaeger, Chapter 3 Oscillatory Behaviour in the Oxidation of CO. In *Oscillating Heterogeneous Catalytic Systems. Studies in Surface Science and Catalysis*, 1994, **86**, p. 47-120.
6. S Hong and HH Richardson, *J. Vac. Sci. Technol. A*, 1993, **11**, 1951-1956.
7. J Lauterbach, G Haas, HH Rotermund and G Ertl, *Surf. Sci.*, 1993, **294**, 116-130.
8. JE Turner, BC Sales and MB Maple, *Surf. Sci.*, 1981, **103**, 54-74.
9. BC Sales, JE Turner and MB Maple, *Surf. Sci.*, 1982, **114**, 381-394.
10. JE Turner and MB Maple, *Surf. Sci.*, 1984, **147**, 647-662.
11. O Chamberlain, *Adv. Automob. Eng.* 2016, **5**, 10000151.
12. European Union. Regulation (EU) No 64/2012 on emissions from heavy duty vehicles (Euro VI) 2012. Official Journal of the European Union. L 28.
13. E Rideal, C The, WA Bone, G Ingle-Finch, ECC Baly, WC McC. Lewis, *et al.*, *Trans. Faraday Soc.*, 1922, **17**, 655-675.
14. G Ertl, *Science*, 1991, **254**, 1750-1755.
15. CT Campbell, G Ertl, H Kuipers and J Segner, *J. Chem. Phys.*, 1980, **73**, 5862-5873.
16. J Rodriguez and D Wayne Goodman, *Surf. Sci. Rep.*, 1991, **14**, 1-107.
17. PJ Berlowitz, CHF Peden and DW Goodman, *J. Phys. Chem.*, 1988, **92**, 5213-5221.
18. T Engel and G Ertl, Elementary Steps in the Catalytic Oxidation of Carbon Monoxide on Platinum Metals. In: DD Eley, H Pines and PB Weez. *Advances in Catalysis*. United States: Academic Press. 1979, **28**, p. 1-78.
19. R. Farrauto, S. Hwang, L. Shore, W. Ruettinger, J. Lampert, T. Giroux, *et al.*, *Annu. Rev. Mater. Sci.*, 2003, **33**, 1-27.
20. H Beusch and E Wicke, *Adv. Chem. Ser.*, 1972, **1**(109), 615.
21. JE Turner, BC Sales and MB Maple, *Surf. Sci.*, 1981, **109**, 591-604.
22. TH Lindstrom and TT Tsotsis, *Surf. Sci.*, 1985, **150**, 487-502.
23. N Hartmann, R Imbihl and W Vogel, *Catal. Lett.*, 1994, **28**, 373-381.
24. P-A Carlsson, L Österlund, P Thormählen, A Palmqvist, E Fridell, J Jansson, *et al.*, *J. Catal.*, 2004, **226**, 422-434.

25. P-A Carlsson, VP Zhdanov and M Skoglundh, *Phys. Chem. Chem. Phys.*, 2006, **8**, 2703-2706.
26. AB Kroner, MA Newton, M Tromp, AE Russell, AJ Dent and J Evans, *Cat. Struct. React.*, 2017, **3**, 13-23.
27. HH Rotermund, W Engel, M Kordesch and G Ertl, *Nature*, 1990, **343**, 355.
28. NA Collins, S Sundaresan and YJ Chabal, *Surf. Sci.*, 1987, **180**, 136-152.
29. VA Burrows, S Sundaresan, YJ Chabal and SB Christman, *Surf. Sci.*, 1985, **160**, 122-138.
30. VA Burrows, S Sundaresan, YJ Chabal and SB Christman, *Surf. Sci.*, 1987, **180**, 110-135.
31. SJA Figueroa and MA Newton, *J. Catal.*, 2014, **312**, 69-77.
32. DJ Kaul and EE Wolf, *J. Catal.*, 1985, **91**, 216-230.
33. DJ Kaul and EE Wolf, *J. Catal.*, 1985, **93**, 321-330.
34. C Stewart, EK Gibson, K Morgan, G Cibir, AJ Dent, C Hardacre, *et al.*, *ACS Catal.*, 2018, DOI: 10.1021/acscatal.8b01509, 8255-8262.
35. RC Yeates, JE Turner, AJ Gellman and GA Somorjai, *Surf. Sci.*, 1985, **149**, 175-190.
36. MP Cox, G Ertl, R Imbihl and J Rüstig, *Surface Science Letters*, 1983, **134**, L517-L523.
37. R Imbihl, MP Cox, G Ertl, H Müller and W Brenig, *J. Chem. Phys.*, 1985, **83**, 1578-1587.
38. RJ Behm, PA Thiel, PR Norton and G Ertl, *J. Chem. Phys.*, 1983, **78**, 7437-7447.
39. G Ertl, *Surf. Sci.*, 1993, **287-288**, 1-11.
40. X Su, PS Cremer, YR Shen and GA Somorjai, *J. Am. Chem. Soc.*, 1997, **119**, 3994-4000.
41. FJ Gracia, L Bollmann, EE Wolf, JT Miller and AJ Kropf, *J. Catal.*, 2003, **220**, 382-391.
42. FJ Gracia, S Guerrero, EE Wolf, JT Miller and AJ Kropf, *J. Catal.*, 2005, **233**, 372-387.
43. DM Haaland and FL Williams, *J. Catal.*, 1982, **76**, 450-465.
44. J Singh, M Tromp, OV Safonova, P Glatzel and JA van Bokhoven, *Catal. Today*, 2009, **145**, 300-306.
45. J Singh and JA van Bokhoven, *Catal. Today*, 2010, **155**, 199-205.
46. J Singh, EMC Alayon, M Tromp, OV Safonova, P Glatzel, M Nachtegaal, *et al.*, *Angew. Chem. Int. Ed.*, 2008, **47**, 9260-9264.
47. J Singh, M Nachtegaal, EMC Alayon, J Stötzel and JA van Bokhoven, *ChemCatChem*, 2010, **2**, 653-657.
48. BLM Hendriksen, MD Ackermann, R van Rijn, D Stoltz, I Popa, O Balmes, *et al.*, *Nat. Chem.*, 2010, **2**, 730-734.

49. BLM Hendriksen, SC Bobaru and JWM Frenken, *Top. Catal.*, 2005, **36**, 43-54.
50. H Over, YD Kim, AP Seitsonen, S Wendt, E Lundgren, M Schmid, *et al.*, *Science*, 2000, **287**, 1474-1476.
51. R Burch and PK Loader, *Appl. Catal. A: General*, 1995, **122**, 169-190.
52. SM McClure and DW Goodman, *Chem. Phys. Lett.*, 2009, **469**, 1-13.
53. F Gao, Y Wang, Y Cai and DW Goodman, *J. Phys. Chem. C*, 2009, **113**, 174-181.
54. BM Weckhuysen, *Angew. Chem. Int. Ed.*, 2009, **48**, 4910-4943.
55. A Goguet, C Stewart, J Touitou and K Morgan, Chapter Three – In Situ Spatially Resolved Techniques for the Investigation of Packed Bed Catalytic Reactors: Current Status and Future Outlook of Spaci-FB. In: AG Dixon and O Deutschmann, *Advances in Chemical Engineering*. Academic Press, 2017, **50**, p. 131-160.
56. AM Gänzler, M Casapu, A Boubnov, O Müller, S Conrad, H Lichtenberg, *et al.*, *J. Catal.*, 2015, **328**, 216-224.
57. AM Beale and BM Weckhuysen, *Phys. Chem. Chem. Phys.*, 2010, **12**, 5562-5574.
58. DC Koningsberger, BL Mojet, GE van Dorssen and DE Ramaker, *Top. Catal.*, 2000, **10**, 143-155.
59. SC Su, JN Carstens and AT Bell, *J. Catal.*, 1998, **176**, 125-135.
60. SM Rogers, CRA Catlow, CE Chan-Thaw, A Chutia, N Jian, RE Palmer, *et al.*, *ACS Catal.*, 2017, **7**, 2266-2274.
61. J Rogal, K Reuter and M Scheffler, *Physical Review B*, 2008, **77**, 155410.
62. RP Eischens, SA Francis and WA Pliskin, *J. Phys. Chem.*, 1956, **60**, 194-201.
63. D Tessier, A Rakai and F Bozon-Verduraz, *J. Am. Chem. Soc., Faraday Trans.*, 1992, **88**, 741-749.
64. GC Cabilla, AL Bonivardi and MA Baltanás, *Catal. Lett.*, 1998, **55**, 147-156.
65. AM Bradshaw and F Hoffmann, *Surf. Sci.*, 1975, **52**, 449-454.
66. X Wang, H Shi, JH Kwak and J Szanyi, *ACS Catal.*, 2015, **5**, 6337-6349.
67. ND Parkyns, *J. Phys. Chem.*, 1971, **75**, 526-531.
68. J Szanyi and JH Kwak, *Phys. Chem. Chem. Phys.*, 2014, **16**, 15117-15125.
69. J Szanyi and JH Kwak, *Phys. Chem. Chem. Phys.*, 2014, **16**, 15126-15138.
70. AM Bradshaw and FM Hoffmann, *Surf. Sci.*, 1978, **72**, 513-535.
71. M Bowker, *Chem. Soc. Rev.*, 2008, **37**, 2204-2211.
72. T Engel and G Ertl, *J. Chem. Phys.*, 1978, **69**, 1267-1281.
73. R van Rijn, O Balmes, R Felici, J Gustafson, D Wermeille, R Westerström, *et al.*, *J. Phys. Chem. C*, 2010, **114**, 6875-6876.

Chapter Seven. Summary and Conclusions

7.1 Summary and Future Outlooks

There is no doubt that heterogeneous catalysis plays a significant role in industrial processes, and will continue to do so in the future. For the rational design of new heterogeneous catalyst materials, it is crucial to understand the nature of the active species and how they facilitate the catalytic pathway. In order to do this, this work has focussed on making improvements to advanced characterisation methods, using multiple techniques to simultaneously collect information about the catalyst properties in an *operando* approach. Due to the advances in synchrotron radiation techniques and beamline capabilities, XAFS measurements can be performed with high time resolution on the millisecond timescale (QEXAFS and EDE) and high spatial resolution on the micrometre length scale. The limitation in performing these measurements of a catalyst in *operando* is owed to the design of a suitable sample environment and experimental method – which is addressed in this work. The powerful combination of XAFS and DRIFTS has been particularly useful for studying supported metal nanoparticle catalysts – in understanding their formation from molecular precursors and their reactivity during catalytic operation.

By using a combined XAFS and DRIFTS approach, a thorough understanding of the preparation route to supported metal nanoparticle catalysts has been obtained. Time-resolved XAFS and DRIFTS spectroscopy, have been able to make links between the decomposition pathway of the molecular precursor (DRIFTS) and the nucleation and growth mechanism of the metal nanoparticle (XAFS). Although the results in Chapter 3 were reported only for the formation of PdO nanoparticles from two specific precursors, Pd(NO₃)₂ and Pd(NH₃)₄(OH)₂, there is scope to investigate the formation of a range of other supported metal nanoparticle catalysts from different impregnating precursor solutions. The constraints in this approach for studying metal nanoparticle formation are related to the X-ray absorption edge energy of the metal in question, and the provision for the metal precursor to contain at least one IR active molecular component (eg. NO₃, NH₃, CO₃, SO₄). The method could also be extended to investigate the role of promoter species in the preparation route, or for the investigation of bimetallic nanoparticle catalysts. The role of the Pd precursor in achieving the resulting PdO nanoparticle properties in Chapter 3 has implications for the preparation of supported metal nanoparticles catalysts in the future, such that the metal precursor can be chosen with intelligent reasoning. It would be interesting to investigate, using this combined XAFS and DRIFTS approach, whether the phenomena observed with the Pd precursors and γ -Al₂O₃ support in this study are consistent in the preparation of other supported metal nanoparticle catalysts. There is question as to whether other bidentate ligands would cause early nanoparticle formation, and whether other NH₃

containing salts, or NO gas, would create a similar stabilising environment for the suppression of nanoparticle growth. The modified Harrick XAFS/DRIFTS cell was able to provide a suitable sample environment for replicating the calcination treatment in the catalyst preparation route, as there was no requirement for plug-flow configuration and the changes in XAFS and DRIFTS spectral features occurred slowly enough to be captured with the spectral time resolution employed (2 spectra min⁻¹). The combined XAFS/DRIFTS approach was therefore found to be a useful method for understanding the preparation of supported metal nanoparticle catalysts, and has scope to be extended to investigate the formation of a number of other such catalysts.

Combined, *operando* XAFS/DRIFTS spectroscopy has been applied to understand the structure-function properties of Pd nanoparticle catalysts for selective ammonia oxidation (NH₃-SCO) in Chapter 4. The selectivity of NH₃-SCO to form N₂, rather than N₂O or NO, is crucial for its industrial application in diesel after-treatment systems and has been found to be attributed to a previously unidentified structural phase of the Pd nanoparticle catalyst, PdN_x. The PdN_x phase was only present under a defined set of reaction conditions, and so *in situ* techniques were essential for its characterisation; Pd K-edge XAFS, Pd L₃-edge XANES and XPS. In order to relate the change in Pd nanoparticle structure to change in the reactivity, time-resolved Pd K-edge XAFS and DRIFTS spectra were correlated with the end-pipe mass spectrometry analysis. Despite the limitations of the *operando* measurements performed with the Harrick XAFS/DRIFTS cell, the changes to Pd nanoparticle structure, surface speciation and end-pipe reactivity were observed with sufficient time resolution to be confidently correlated for an understanding of the catalyst structure-function relationships.

The limitations of previous combined XAFS/DRIFTS reaction cells for the *operando* spectroscopy have been outlined in Chapter 5; large dead volume, lack of spatial resolution in both spectroscopic measurements, ambiguous correlation between spectral information collected from the two techniques performed at different positions of the catalyst bed. The problems have been addressed by the design of a new, improved reactor affording spatially resolved XAFS and DRIFTS measurements of a catalyst contained as a fixed bed under plug-flow configuration. The reactor design resembles the configuration of a flow reactor and eliminates the problem for gas bypass and dead volume. The X-ray window and IR window extend the entire axial length of the catalyst bed meaning for an infinite number of measurements in the axial direction, depending on the spot size of the spectroscopy beam. The advantage of high spatial resolution and high time resolution achieved with this cell have been demonstrated by the investigation of a Pd/γ-Al₂O₃ catalyst during CO oxidation, reported in Chapter 6. The nanoparticle structure and surface coverage were followed by EDE and DRIFTS spectroscopy performed at multiple positions of the catalyst bed during kinetic oscillations of CO oxidation. The behaviour of the catalyst was found to depend on its

position within the reactor, which resulted in a propagating reaction front which could also be observed by IR thermography images. The end-pipe mass spectrometry signal could be interpreted by combining the information collected at multiple spatial positions. However, in order to improve the *operando* spectroscopy performed with this new reactor in future work, there is the potential to incorporate a spatially resolved mass spectrometry technique – such as the Spaci-FB instrumentation – which would complement the spatially resolved spectroscopic measurements with measurements of the local gas environment and temperature.

The improved cell design for combined, *operando* XAFS and DRIFTS spectroscopy has proved to be successful in achieving improved understanding of structure-function relationships of supported metal nanoparticle catalysts. The new XAFS/DRIFTS cell has so far only been used for the investigation of a Pd catalyst during CO oxidation, but there is scope for investigating a number of different catalysts operating for different catalytic reactions, *eg.* selective reduction of NO_x, CH₄ oxidation and selective NH₃ oxidation. Modifications to the reported cell design may need to be considered for future investigations of other catalytic systems that require higher reaction temperatures and pressures. The major advantage of the new XAFS/DRIFTS cell reported in this work is the opportunity to investigate catalytic reactions that are suspected to experience spatial variations, whereby different catalyst structures and reaction pathways exist at different positions of the catalyst bed.

7.2 Final Remarks

This work has shown that spatial resolution in spectroscopic measurements of heterogeneous catalyst materials is crucial when investigating a catalyst bed operating in plug-flow configuration. In order to truly understand the structure-function relationship of the catalyst, multiple spectroscopic techniques can be performed simultaneously, and on the same time- and length-scale such that the multiple datasets can be confidently correlated. Here, simultaneous XAFS and DRIFTS spectroscopy were combined for structure-function analysis of supported metal nanoparticle catalysts, but there is opportunity for other *operando* techniques to be performed with adequate time and spatial resolution, in the study of other industrial heterogeneous catalysts.